Biomechanical Modelling of Colorectal Crypt Formation and In-Vitro Replication

Martin R. Nelson, MMath.

Thesis submitted to The University of Nottingham
for the degree of Doctor of Philosophy

September 2010

Abstract

The colon's epithelial lining exhibits a number of invaginations into the underlying tissue, called the crypts of Lieberkühn. Housing stem cells at their bases, these crypts play an essential role in the maintenance of the epithelium; however, the processes by which crypts form are not conclusively understood. This study deploys mathematical and experimental modelling to validate one potential mechanism: that cellular growth in the developing epithelium causes a build up of compressive stresses, resulting in buckling instabilities which initiate crypt formation.

We begin with an extension to the model of Edwards & Chapman (2007), modelling the epithelium as a beam tethered to underlying tissue by a series of springs. Modelling growth parametrically as a sequence of equilibrium configurations attained by beams of increasing length, we demonstrate that competition between lateral supports and stromal adhesion determines buckling wavelength. We show how non-equilibrium relaxation of tethering forces affects post-buckled shapes, and illustrate that growth inhomogeneity has a much weaker influence upon buckled configurations than do variations of mechanical properties.

An *in-vitro* study, in which we culture intestinal epithelial cells upon a flexible substrate, demonstrates that the cells can exert sufficient force to induce buckling upon reaching confluence. A corresponding one-dimensional model is presented, in which a growing, confluent cell monolayer adheres to a thin compressible elastic beam. The model exhibits buckling via parametric growth. Cell–substrate adhesion and growth inhomogeneity have minimal influence upon configurations. Compressibility is important only in separating bifurcation points; large-amplitude shapes are accurately approximated by incompressible solutions. A two-dimensional analogue of this model, which extends von Kármán plate theory, is then given. Axisymmetric configurations are compared with an alternative shell theory model, highlighting discrepancies arising from constitutive assumptions. Examining configurations of an inhomogeneous plate reveals that generation of multiple crypts by targeted softening alone is difficult; however, attachment to an elastic foundation can bias high frequency configurations.

Acknowledgements

Firstly, I would like to thank my supervisors: Oliver Jensen, Sarah Waters, John King and Felicity Rose. The guidance which they have provided throughout this project is greatly appreciated. I am also thankful to the University of Nottingham, for providing funding for this project, and to the BBSRC and the EPSRC for funding experiments.

Regarding the experimental work of chapter 3, I gratefully acknowledge collaboration with Dr. Daniel Howard of the Tissue Engineering & Drug Delivery group at the University of Nottingham. Furthermore, I would like to thank Lloyd Hamilton and Isha Paik for their assistance with the surface modification of membranes discussed in section 3.1.3. Extended thanks go to Teresa Marshall, whose lab training and guidance throughout was invaluable. I would also like to thank all those members of the tissue engineering group that have offered advice and answered numerous queries over the last four years; their assistance made my time in the lab as pain-free as could ever have been hoped!

My thanks go to all those Theoretical Mechanics postgrads and postdocs with whom I have shared the last four years. Throughout this study, they have proved to be a valued source of japery, procrastination and (on particularly special occasions) academic insight. Particular thanks go to Reuben O'Dea for indulging me in more conversations about semi-colons than strictly necessary, and to Sara Jabbari – purveyor of kebabs and giggling in times of need.

Finally, I would like to extend my thanks to my family, and to Julia, for their continued support throughout, without which this project would not have been possible.

Contents

CHAPTER 1

Introduction

The structure and function of the digestive system have become increasingly well-studied in recent years, both experimentally and mathematically. With cancer of the large intestine (or colon) prevailing as the second-greatest cause of cancer-related mortality in developed countries (Stewart & Kleihues, 2003), much focus has been placed upon understanding the cellular dynamics of the colon and, in particular, the epithelial cell layer which forms its internal lining. In its capacity as a self-renewing tissue housing a 'stem cell niche', the colon is of great interest to stem cell biologists, while the growing benefits of transplant surgery motivate the interest of tissue engineers in recreating the tissue in the laboratory. Replication of intestinal tissue *in vitro* also has great potential in aiding the understanding of the underlying biology and for such clinical applications as drug testing and gene therapy. In this study we aim to couple theoretical modelling of the large intestine to the experimental research of Nottingham's Tissue Engineering group. Many of the concepts discussed in this thesis can be applied to both small and large intestine. Our choice to focus upon the large intestine is motivated by the greater availability of large intestinal tissue for experimental studies.

In this chapter we present an overview of the relevant background biology for this study, beginning with a discussion of the structure of gastrointestinal tissue. We then examine the gastrointestinal stem cell niche, its cellular dynamics and its important role in the constant regeneration and maintenance of the intestinal epithelium. We discuss some prevalent diseases of the large intestine, before introducing common tissue engineering techniques used to replicate intestinal tissue artificially. We then review previous modelling of the intestine and mathematical theory pertinent to this study, before closing this chapter with an overview of the contents of the remainder of this thesis.

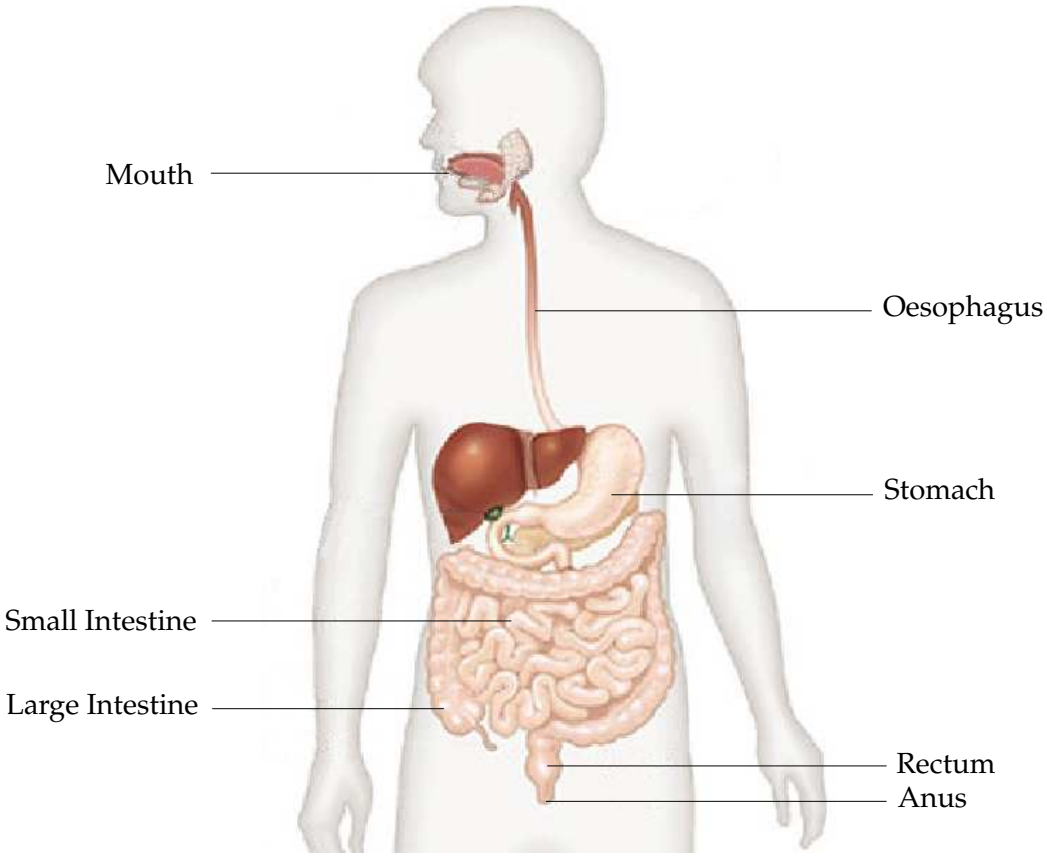

Figure 1.1: The digestive system. Image adapted from www.britannica.com.

1.1 The digestive system – background biology

The digestive system is responsible for performing the vital function of preparing food particles for use by the body's cells. When food particles initially enter the digestive system, they are too large to pass through cell membranes. They must, therefore, be broken down into molecules small enough to enter cells. This process of altering the physical and chemical composition of ingested food is called *digestion*. Once the food particles are small enough to pass into the blood stream and lymphatic system, they do so via a process termed *absorption*.

The main organs of the digestive system connect to form a tube-like structure known as the *gastrointestinal (GI) tract* (see figure 1.1). The walls of the GI tract consist (subject to local variations) of four tissue layers, as illustrated in figure 1.2. We discuss the structure and function of these layers here, focussing upon the details of the large intestine and omitting details of variations found in other areas of the tract.

The *serosa* is the most superficial layer of the GI tract wall. This connective tissue layer also forms part of the *peritoneum* – an external structure connected to the abdominal

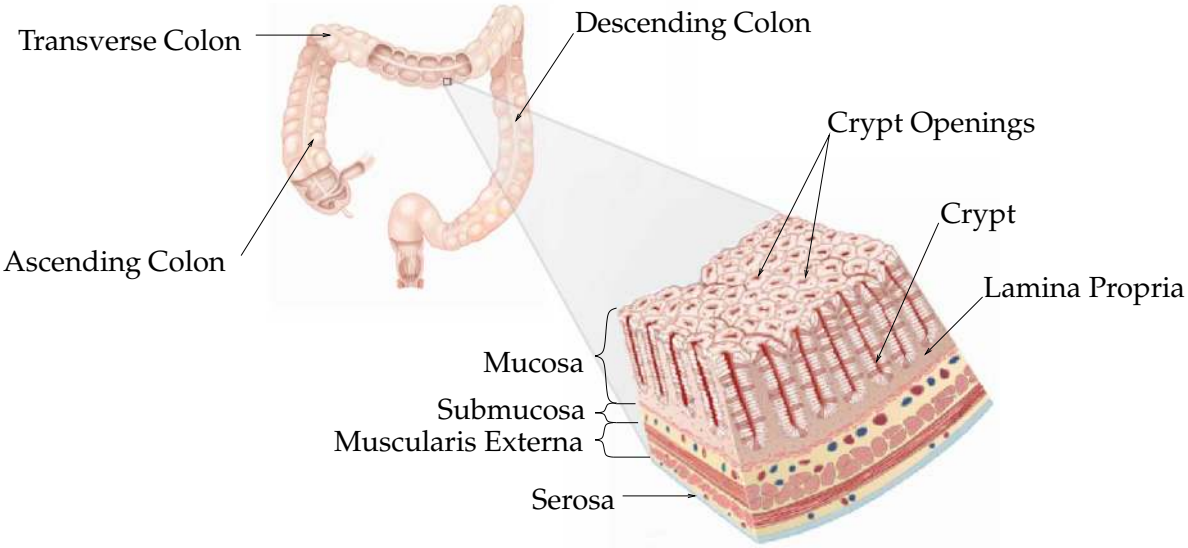

Figure 1.2: The geometry of the large intestine, and the constituent layers making up its wall. Image adapted from www.britannica.com

cavity which provides structure and support for the tract (Thibodeau & Patton, 2007; Tortora & Grabowski, 1996). Adjacent to the serosa is the *muscularis externa*, consisting of two thick layers of smooth muscle tissue. Cells in the innermost layer are arranged in a tight spiral, and the layer is referred to as 'circularly oriented'. Cells in the outermost layer, however, are oriented longitudinally. Between these two muscle layers is a thin layer of connective tissue which contains nerve cells, blood vessels and lymphatic vessels. Contractions of the inner muscle layer cause the compression and mixing of the intestine's contents by constricting the lumen. The longitudinal muscle layer, however, contracts in a slow rhythmic fashion causing *peristalsis* by which the contents of the lumen are propelled along the tract (Ross *et al.*, 2003). The next layer, the *submucosa*, mostly consists of dense, irregular connective tissue. Contained within this are larger blood vessels whose smaller branches reach the other layers of the tract wall, lymphatic vessels, nerves and occasional glands. The primary role of this layer is to innervate (provide nerves to) the smooth muscle layers of the tract wall (Ross *et al.*, 2003). The innermost layer of the tract wall is the *mucosa*, and is the focus of this study. The mucosa contains three sublayers: the *muscularis mucosa*, containing muscle which enables the mucosa to fold; the *lamina propria*, which contains blood and lymphatic vessels; and a monolayered columnar *epithelium*, a tightly packed layer of cells which lines the intestinal lumen to protect the underlying tissue from external substances.

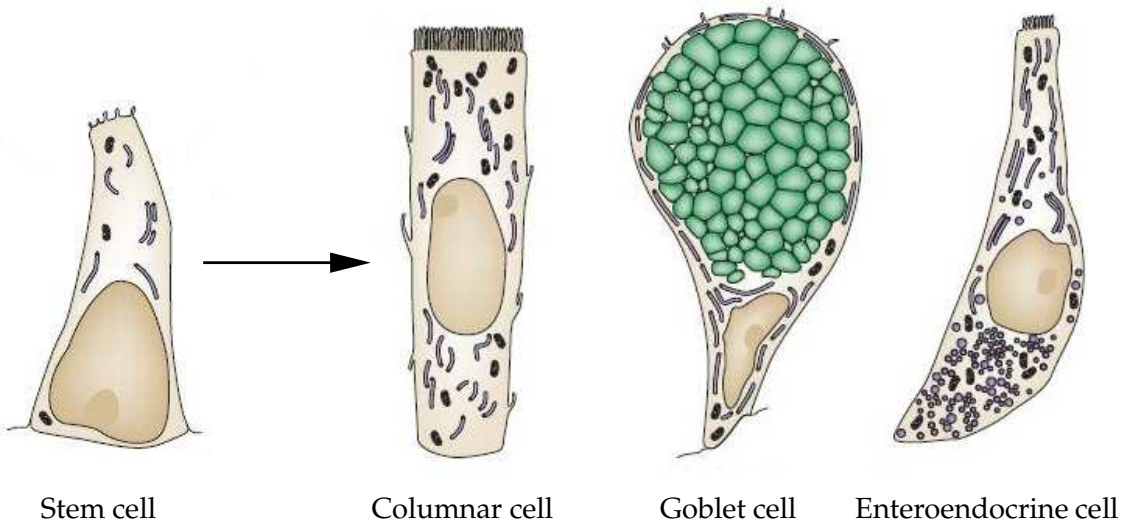

Figure 1.3: Cells of the large intestinal epithelium. Cells are oriented such that the apical surfaces of the cells lie at the top of the figure. Image adapted from Crosnier *et al.* (2006).

1.1.1 Cells of the intestinal mucosa

The gastrointestinal epithelium is comprised of a number of distinct cell types. We introduce some of these cells here, focussing on the cells of the large intestine, and give a brief description of their function. We also introduce intestinal subepithelial myofibroblast (ISEMF) cells (which reside immediately below the epithelium) since these cells are of potential importance for future tissue engineering models.

Also known as absorptive cells, columnar cells are the most abundant cells in the epithelial layer. In the large intestine they are specifically termed *colonocytes*. The primary function of these cells is to facilitate the absorption of nutrients from the intestinal lumen. As such, the apical surface of the cell (which is oriented towards the lumen) is lined with a dense array of microvilli which provide the cell with a large absorptive surface (Crosnier *et al.*, 2006; Ross *et al.*, 2003). Enteroendocrine cells are less abundant than columnar cells, accounting for approximately 1.5% of the epithelial population. Their role is to secrete peptide hormones which are important in the regulation of fluid and electrolyte transport. A large variety of enteroendocrine cells exist, facilitating the secretion of a large array of gut hormones (Crosnier *et al.*, 2006). Goblet cells serve to secrete mucus into the lumen to trap and expel micro-organisms (Brittan & Wright, 2004). Their apical cytoplasm is usually distended and packed with mucus-filled secretory granules (Crosnier *et al.*, 2006), as illustrated in figure 1.3.

The intestinal crypts are enclosed within a protective sheath of intestinal subepithelial myofibroblasts (ISEMFs), which reside in the lamina propria. These cells have a broad range of functions including mucosal protection, wound healing, regulation of water and electrolyte transport and, with greatest relevance to this study, regulation of epithelial proliferation and differentiation (Brittan & Wright, 2004; Powell *et al.*, 1999).

1.1.2 The crypts of Lieberkühn, stem cells & epithelial regeneration

The columnar epithelium which lines the lumen is folded to form a series of test-tubed shaped invaginations into the underlying mucosa known as the *crypts of Lieberkühn*, as illustrated in figure 1.2. In mice, these crypts are roughly 45 cells deep, 18 cells in circumference at the midpoint and each crypt contains 300–450 cells in total (Potten, 1998). Formation of the crypts is known to occur in mice around seven days after birth; prior to this the intestinal wall is smooth (Crosnier *et al.*, 2006; Barker *et al.*, 2008).

The crypts of Lieberkühn play a crucial role in the maintenance and regeneration of the epithelium as they house populations of gastrointestinal stem cells (Barker *et al.*, 2008; Crosnier *et al.*, 2006). A stem cell population may be defined as a population of proliferative cells which, on division, maintains its own numbers whilst also producing *pluripotent* daughter cells capable of differentiating down various other cell lineages (Marshman *et al.*, 2002). Determination of the precise location of stem cells within the crypt has long been hampered by the scarcity of suitable molecular markers (Barker & Clevers, 2007). In the ascending colon stem cells are thought to reside approximately half-way up the walls of the crypts (Karam, 1999; Brittan & Wright, 2002). In the descending colon and small intestine, however, stem cells are thought to reside towards the base of the crypts (Karam, 1999; Brittan & Wright, 2002; Crosnier *et al.*, 2006). Barker & Clevers (2010) recently identified the G-protein–coupled receptor Lgr5 as a suitable marker for stem cell capacity in the small intestine and were able to use this marker to provide further evidence for the above claim. As the daughter cells differentiate they migrate up the wall of the crypt. When they reach the top of the crypt they are fully differentiated and are ultimately shed into the intestinal lumen. This continuous production, differentiation, migration and loss of epithelial cells enables the epithelium to be constantly regenerated, with a full renewal of the layer occurring every 5–6 days in humans (Ross *et al.*, 2003).

The proliferation and differentiation of cells in the crypt is known to be strongly influenced by the expression of genes and signalling molecules in the *Wnt signalling pathway* (Pinto & Clevers, 2005). A critical component of the pathway is the protein β-catenin, which resides in the cytoplasm of the cell. Extracellular Wnt protein binds

to transmembrane 'frizzled' (Fz) and low density lipoprotein (LDL) receptors stimulating the overexpression of cytoplasmic β-catenin (Gordon & Nusse, 2006; Booth *et al.*, 2002). This results in the translocation of β-catenin from the cytoplasm to the nucleus where it binds with T-cell factor (TCF). TCF is a DNA-binding protein and transcription factor, which is activated upon its binding with β-catenin. The TCF-β-catenin complex is known to stimulate cell proliferation (Booth *et al.*, 2002). Such an increase in proliferation is linked to an upregulation of the transcription factor c-MYC and a repression of the growth inhibitor p21 (van de Wetering *et al.*, 2002; Booth *et al.*, 2002). In addition to this, there is evidence to suggest that extremely high levels of Wnt result in the stimulation of apoptosis (Wong, 2004). Extracellular Wnt proteins reside in abundance toward the base of the crypt and decrease in quantity towards the lumen. This Wnt signalling gradient is believed to be key in the maintenance of the crypt hierarchy, in which proliferation is restricted to the lower portion of the crypt and differentiation occurs further up the crypt axis (Wong, 2004).

Batlle *et al.* (2002) presented evidence that β-catenin/TCF signalling in the small intestine contributes to the control of cell positioning along the crypt axis via its regulation of EphrinB ligands and the associated EphB receptors. β-catenin is also known to play a role in cell adhesion. Its expression at the cell surface facilitates its interaction with α-catenin and E-cadherin, resulting in a reduced rate of cell migration (Wong *et al.*, 1998). Also playing a central role is *adenomatous poliposis coli* (APC), which competes with TCF in binding to β-catenin (Booth *et al.*, 2002). As such, high levels of APC act to suppress cell proliferation (Booth *et al.*, 2002), reduce cell growth and/or stimulate apoptosis (Morin *et al.*, 1996).

Other notable signalling pathways which have a role in regulating crypt cell dynamics include Notch, BMP and Hedgehog signalling. Notch receptors are activated by transmembrane ligands of the delta and jagged families expressed by neighbouring cells (Radtke & Clevers, 2005; Artavanis-Tsakonas *et al.*, 1999). Notch signalling has been shown to regulate many events during post-natal development, including proliferation, apoptosis and cell fate decisions (Wilson & Radtke, 2006; Artavanis-Tsakonas *et al.*, 1999). In self-renewing organs such as the intestine, Notch signalling is also linked to inhibition/induction of differentiation and lineage specification (Wilson & Radtke, 2006). BMP (bone morphogenetic protein) signalling molecules reside below the epithelium in the underlying tissue layers. Interactions between these molecules and the epithelium are known to regulate growth and differentiation in the epithelium (Batts *et al.*, 2006). Such authors as He *et al.* (2004) have examined the disruption of the BMP signalling pathway in mice, providing empirical evidence for

this. Playing an important role in the BMP signalling pathway is the BMP antagonist 'noggin', which is highly expressed in the vicinity of the crypts. When the BMP receptor (BMPR1A) is knocked out, or noggin is overexpressed, excessive quantities of crypt-like structures develop (Crosnier *et al.*, 2006). Secreted Hedgehog proteins act as morphogens during intestinal development, as they control cell fate specification in a concentration-dependent manner (Sancho *et al.*, 2004). Two members of the Hedgehog protein family have been identified as particularly important: Sonic Hedgehog (SHH) and Indian Hedgehog (IHH). Knocking out IHH in embryonic mice results in a multilayered epithelium which does not develop to exhibit the normal crypt morphology (van den Brink *et al.*, 2004). Studies of mutant mice reveal that hedgehog signalling deficiencies impact upon gut regionalisation, radial patterning of the GI tract and self-renewal of GI tissue from stem cells (Ramalho-Santos *et al.*, 2000). In the intestine in particular, SHH mutations have been linked with gut malrotation (in which the rotational symmetry of the gut is broken), while IHH mutations are thought to impact upon stem cell proliferation (Ramalho-Santos *et al.*, 2000).

The four signalling pathways discussed here are not mutually independent. For example, active Wnt signalling is known to have the ability to switch on Notch activity, suggesting that Wnt signalling drives the expression of Notch pathway components (Crosnier *et al.*, 2006). Wnt signalling is also known to be suppressed by an activation of either BMP (He *et al.*, 2004) or Hedgehog (van den Brink *et al.*, 2004).

1.2 Diseases of the intestine

Colorectal cancer ranks as the second most prevalent cancer in the developed world, both in terms of incidence and mortality (Stewart & Kleihues, 2003). The onset of colorectal cancer is commonly linked to a disruption of the cellular dynamics of the intestinal epithelium. The development of a cancerous tumour procedes according to the 'adenoma–carcinoma sequence'. Here, 'adenoma' refers to a benign growth while 'carcinoma' refers to a malignant, cancerous growth. The sequence is initiated with the formation of an aberrant crypt focus – a small lesion in the colonic epithelium. Such foci expand over time to form macroscopically visible adenomatous polyps, which may ultimately progress to carcinomas (Radtke & Clevers, 2005). The initial trigger in the series of genetic events which lead to colorectal cancer is generally regarded to be an activating mutation in the Wnt cascade, most commonly a loss of the tumour-suppressing gene APC (Reya & Clevers, 2005). Since APC reduces net proliferation through increased apoptosis (Morin *et al.*, 1996), its absence results in the on-

set of hyper-proliferation at the crypt base, an event which is commonly linked to tumour growth (Renehan *et al.*, 2002). Treatment of colorectal cancer commonly requires a colostomy – surgery in which the affected tissue is removed.

Inflammatory bowel disease (IBD) is another prevalent condition, caused by the inflammation of the gastrointestinal tract wall. The main forms of IBD are ulcerative colitis and Crohn's disease. Ulcerative colitis involves the inflammation of the mucosa of the colon or rectum, while Crohn's disease can affect any region of the tract and impacts upon all the layers of the tract wall (Bouma & Strober, 2003). Symptoms of IBD include vomitting, diarrhoea, rectal bleeding, abdominal pain and weight-loss. IBD can commonly be treated with the use of anti-inflammatory medication; however, more severe cases may require such surgery as bowel restriction or colostomy.

Short bowel syndrome is a condition which can be inherited, or more commonly follows the removal of a section of small intestine during treatment of *e.g.* Crohn's disease. The condition occurs when the length of the intestine is reduced substantially, resulting in an insufficient length for the absorption of nutrients (Vanderhoof & Langnas, 1997). Symptoms include abdominal pain, diarrhoea, weight-loss, malnutrition and fatigue. Treatments of this condition include medication and prescription of vitamins and mineral supplements; however, a notable alternative technique which has been trialled over recent years is intestinal transplantation from a donor (Vanderhoof & Langnas, 1997). Intestinal transplantation is hindered by both a shortage of donor organs and a high morbidity rate (Chen & Badylak, 2001; Chen & Beierle, 2004). This illustrates the importance of tissue engineering studies by which insight may be gained into the generation of tissue artificially, in such a manner as to maximise acceptance by the recipient. We further examine such procedures in the following section.

1.3 Tissue engineering

Tissue engineering was defined by Langer & Vacanti (1993) as "an interdisciplinary field that applies the principles of engineering and the life sciences toward the development of biological substitutes that restore, maintain or improve tissue function."

One fundamental strategy employed by tissue engineers is to implant cells onto a biodegradable scaffold which initially acts as a supporting structure for the cells and ultimately degrades or is metabolised as the cells produce extra-cellular matrix. The initial task, therefore, is to obtain a supply of cells from which to generate a tissue for implantation. A number of choices of cell source are available, each with advantages and disadvantages. Cells taken from the eventual recipient of the engineered tissue

are termed *autologous*. Such cells are highly immune-acceptable; however, depending on the specifics of the tissue, they may not be easily obtainable and their supply is commonly limited. Sourcing of autologous cells may include the use of the healthy cells which are removed alongside damaged tissue during surgery, as is commonly the case during intestinal tissue engineering, or may involve the culture of a cell population from a sample of the recipient's stem cells (Lanza *et al.*, 2007). Alternatively, tissue engineering procedures may utilise *allogenic* cells, which are obtained from another donor. Allogenic cells are more easily obtained; however, they may require a greater degree of engineering to facilitate immune-acceptance. *Xenogenic* cells originate from another species and, as such, are in much more abundant supply. However, the use of such cells raises concerns relating to immune acceptance, animal virus transmission and ethical issues (Lanza *et al.*, 2007). Over recent years, much interest has been placed in the use of stem cells to supply a diverse range of cells in the quantity required for tissue engineering applications. Stem cells may be collected from either autologous, allogenic or xenogenic sources (Griffith & Naughton, 2002) and their *in-vitro* culture conditions can be adjusted to favour differentiation down the desired lineage. To date, tissues which have been successfully recreated using stem-cell-based tissue engineering techniques include epithelia (skin, cornea and mucosal membranes) and skeletal tissues (Bianco & Robey, 2001).

Upon seeding of the cells onto the scaffold, the resulting constructs are allowed to mature either *in vitro* or *in vivo* (Rocha & Whang, 2004). *In-vitro* tissue engineering draws many parallels with transplant surgery. However, since the transplanted material is generated through the culture of cells upon a scaffold, the burden of organ-donation is avoided. The fundamental challenge, here, is the provision of a suitable physical environment to allow the cells to survive, proliferate and mature. Typically this task involves placing the cell–scaffold construct in some form of bioreactor, a device in which cells can be cultured in 3D subject to regulated external factors. Bioreactors are usually designed to perform some or all of the following functions:

- provide control over the initial distribution of cells over the scaffold;
- provide efficient transfer of gases, nutrients and regulatory factors to the tissue-engineered constructs during their cultivation;
- expose the developing construct to convective mixing, perfusion and/or mechanical conditioning

(Lanza *et al.*, 2007). Critically, the bioreactor must also provide an environment free of infection and contamination. Once the tissue has developed to the required de-

gree, it is removed from the laboratory culture environment and transplanted into the recipient's body in the appropriate manner. *In-vitro* tissue engineering exhibits the advantages of high throughput and accurate control of the microenvironment, at the expense of risking altering the phenotype of cultured cells and potentially obtaining a non-physiological tissue (Rocha & Whang, 2004). Examples of successful *in-vitro* tissue engineering include the development of tissue-engineered autologous bladders to replace those of patients with end-stage bladder disease (Atala *et al.*, 2006) and the clinical transplantation of a tissue engineered airway (Macchiarini *et al.*, 2008).

In-vivo tissue engineering, however, takes a contrasting approach in which a scaffold is placed (either with or without pre-seeded cells) into the recipient in an underdeveloped state. Effectively the recipient's body plays the role of the bioreactor in this technique, yielding the obvious and substantial advantage of providing the ideal conditions for cell development and, hence, maximising the chance of acceptance of the newly generated tissue. One approach to *in-vivo* tissue engineering, which has shown promising results in many animal trials, is to load cells into a gel which is then injected into the host. This technique offers a number of advantages over preformed scaffolds, including minimally invasive implantation, the ability to fill any desired shape and easy incorporation of therapeutic agents (Gutowska *et al.*, 2001). Examples of clinical applications of *in-vivo* tissue engineering in humans are scarce due to the associated risk of transplanting a tissue of limited (or zero) functionality. However, animal studies have shown promising progress in replicating tissues such as cartilage (Shieh *et al.*, 2004), bone (Stevens *et al.*, 2005) and intestine (see below).

1.3.1 Gastrointestinal tissue engineering

In recent years, the prevalence of short bowel disease and colonic cancer have stimulated much interest in engineering both small and large intestinal tissue, the ultimate goal being the generation of tissue for human transplantation. Here, we review recent advances toward achieving this goal. Where primary human cells are used, these are commonly sourced from healthy tissue which is removed from *e.g.* bowel cancer patients alongside defective tissue. However, studies are commonly carried out using cells sourced from murine intestine – a tissue whose use is advantageous in its ready supply and its high degree of similarity with the human intestine. The ultimate goal of many murine cell studies is the development of protocols which can be directly transferred to human tissue engineering.

Successful engineering of intestinal tissue *in vivo* was first reported by Vacanti *et al.* (1988), who sourced cells from minced fetal intestine, attached them to polymer scaf-

folds and implanted the scaffolds into host animals. Evans *et al.* (1992) later developed a protocol by which the small intestine of a rat can be removed from the body, and the epithelium be detached and broken down by enzymatic digestion, yielding either whole villi/crypt units (termed epithelial organoid units) or (after more prolonged digestion) a population of individual epithelial cells. The authors determined appropriate conditions for the culture of these cells *in vitro*, although the cell types cultured were never fully identified and characterised. Choi & Vacanti (1997) deployed these methods to isolate rat intestinal epithelial organoid units which were then placed upon tubular biodegradable scaffolds and transplanted into host rats. This tissue-engineered small intestine was shown to replicate many of the geometric and cellular characteristics of the healthy intestine, displaying crypt-villus-like structures and appropriate proportions of Paneth[1], goblet and columnar epithelial cells. Grikscheit *et al.* (2002) later deployed similar methods to engineer rat colon *in vivo*. On transplantation into host rats, the tissue-engineered colon was shown to recover many of the functions of the healthy colon.

Other examples of successful *in-vivo* gastrointestinal tissue engineering include many 'autologous patch models', in which a section of healthy tissue is used as a scaffold for the repair of a damaged portion of intestine. The patch is located at the damaged site and, over a number of weeks, becomes covered by the appropriate cell population which invades from neighbouring tissue. The reader is directed to Chen & Beierle (2004) for a review of numerous successful animal trials of such a method. Small intestinal submucosa (SIS) has also been identified as a suitable *in-vivo* scaffold for the repair of both small bowel and many other tissues (see Chen & Badylak (2001) and references therein).

In this study we focus upon *in-vitro* alternatives to the *in-vivo* gastrointestinal tissue engineering approaches described above. Successful replication of healthy intestinal tissue *in vitro* requires that the complex crypt structure be replicated in the final engineered tissue. Our primary goal is to determine whether this task requires the manufacture of a complex, preformed scaffold which imposes the crypt geometry, or whether the cells possess the inherent ability to generate crypts unaided (as suggested by the recent studies of Viney *et al.* (2009) and Sato *et al.* (2009)). Current research, upon which this study focuses, involves the construction of an experimental framework by which some of the mechanisms which potentially underlie crypt formation may be investigated. In particular, one hypothesis under consideration is that during the develop-

[1]Paneth cells are found at the base of crypts in the small intestine. Their primary function is to maintain mucosal immunity by secreting antimicrobial substances (Ross *et al.*, 2003). Paneth cells are not present in crypts of the large intestine.

ment of the intestine the growth of the epithelial layer generates compressive stresses within the layer itself, causing it to buckle forming crypts. We investigate this hypothesis in the laboratory framework through the culture of intestinal epithelial cells upon a flexible substrate. Under standard culture conditions upon a rigid surface, proliferation of these cells ceases due to contact inhibition as the cells become confluent. Upon our flexible substrate, we examine whether the confluent cell layer is able to generate sufficient force to deform the substrate, thus increasing the surface area and facilitating continued proliferation. Should the cells generate sufficient forces to drive deformation of the substrate, we may infer that future research should exploit this, allowing the requirement for a preformed scaffold to be relaxed in favour of a more simplistic, planar substrate which exhibits the required deformability. We provide further details of this work in chapter 3, and present corresponding *in-silico* models of this system in chapters 4–6.

1.4 Biomechanics in cellular development

Discher *et al.* (2005) presented a discussion of the manner in which cellular behaviour is affected by the mechanical properties of the substrate on which they sit. Tissue cells are usually anchorage dependent, by which we mean that their survival (both *in vitro* and *in vivo*) relies on adherence to a solid substrate. Contractile forces in adherent cells may be transmitted to the underlying substrate, potentially inducing deformations (Discher *et al.*, 2005). One common approach to estimating cellular expansion/contraction forces is to culture the cells of interest upon a flexible gel, allow the cells to contract, wrinkling the substrate and then use measurements of the wrinkles to calculate cell forces.

Fibroblasts have been shown to migrate in directions influenced by gradients of substrate rigidity. Lo *et al.* (2000) showed that 3T3 fibroblasts migrate preferentially toward stiffer areas of their substrate, generate stronger traction forces upon stiffer substrates and can be guided to migrate in a given direction by prescribing variations in the degree of substrate stretch. Solon *et al.* (2007) cultured fibroblasts upon a polyacrylamide gel to assess the effects of substrate stiffness upon cell stiffness. These fibroblasts were shown to adjust their cellular stiffness to match that of their substrate. Changes in the cell size were also observed as substrate stiffness was varied. Softer substrates have also been shown to reduce spreading of isolated smooth muscle cells (Engler *et al.*, 2004) and promote the aggregation of fibroblasts and epithelial cells into tissues (Guo *et al.*, 2006).

The elastic properties of the cell culture surface have also been shown to play a role in specifying the lineage selected by a differentiating stem cell population (Engler *et al.*, 2006). Culturing mesenchymal stem cells upon a gel whose rigidity could be altered, the authors were able to force differentiation along brain, muscle or bone lineages by increasing the gel's stiffness. Collinsworth *et al.* (2002) also observed similar variations in the stiffness of a differentiating population of skeletal muscle cells.

While many authors have examined the behaviours of individual cells in response to biomechanical inputs, few have examined the properties of multicellular assemblies. Saez *et al.* (2010), however, considered the traction forces generated by a sheet of epithelial cells. The authors cultured a population of Madin-Darby Canine Kidney (MDCK) cells upon a substrate whose surface was covered with micropillars, the deflections of which allowed cellular traction forces to be measured. They observed that traction forces were largest at the edge of the cell sheet, decaying rapidly towards the centre of the assembly. This suggests that the cell population exerts force as a whole, rather than on an individual cell basis; cell–cell adhesion seems to inversely modulate the traction exerted by the cell. Traction forces were also shown to vary linearly as a function of substrate stiffness. For the range of substrates examined, the magnitude of traction forces was between 1nN and 100nN. For a substrate with anisotropic stiffness, the direction of both traction forces and growth were shown to align with the stiffest direction.

1.5 Cell-based models of colorectal crypt dynamics

Here we examine previous mathematical models of proliferation, differentiation and migration of cells within a colorectal crypt. Such models can generally be categorised as either 'lattice-based' (in which cells are located in a regular array of rows and columns, and their movements are restricted as such) or 'lattice-free' (in which cellular movements are unrestricted). We examine each of these approaches in the following sections.

1.5.1 Lattice-based models

Many previous models have relied upon the assumption that the crypt can be considered cylindrical and can be unrolled and mapped onto a planar, rectangular 2D grid. Cells are considered rectangular also, and are arranged in a regular array of rows and columns. On the division of a cell, a new cell is inserted into the grid according to some model-specific set of rules. Neighbouring cells are pushed up the column or

across the row to accommodate this. Loeffler *et al.* (1986, 1988) assessed numerous insertion rules by comparison of their results with experimental data from cell-labelling assays. Specifically, the authors utilised labelling index (LI) data, which quantify the percentage of labelled versus unlabelled cells as a function of crypt row, and vertical run numbers (RUN), which quantify the number of labelled cell sequences per crypt column (van Leeuwen *et al.*, 2006). Together, LI and RUN data provide a quantified measure of both lateral and vertical cell displacements in the entire crypt; comparison with these data allows optimal insertion rules to be determined.

Paulus *et al.* (1993) extended the model of Loeffler *et al.* (1986) to incorporate the development of the goblet cell lineage. The 16×24 grid of cells used by Loeffler *et al.* (1986) was maintained; the authors presented simulations carried out in the presence of four stem cells whose locations were fixed close to the crypt base. The goblet cell lineage was introduced to the model through the assumption that a newly formed third-generation transit cell may acquire goblet cell properties with a likelihood of 5%. For reasons of simplicity the model does not allow the acquisition of such properties for cells of other generations (Paulus *et al.*, 1993). Goblet cell division rules were considered to be consistent with those of columnar cells of the same age. The results of the authors' simulations were assessed against experimental data obtained via the staining of goblet cells in the murine small intestinal crypt. The simulations yielded good agreement with goblet cell frequency in the lower half of the crypt and successfully captured the lateral displacement of cells towards the crypt opening. However, the experimental data illustrated a decline in goblet cell frequency at the top of the crypt which was not captured by the mathematical model. It was also observed that the model predicts too few goblet cell clusters, in comparison to the frequency of lone goblet cells. The authors claim that such discrepencies are rectifiable through a refined choice of cell migration parameters in the model. In particular, it is suggested that columnar and goblet cells exhibit distinct cell cycle characteristics, while in this model all parameters are obtained from the columnar cell lineage. The authors concluded that their model provides evidence in support of the claim that goblet cells and columnar cells arise from a common stem cell at the crypt base. This hypothesis was later proven experimentally by Bjerknes & Cheng (1999).

The lattice-based models discussed in this section rely on a number of unrealistic assumptions. Firstly, the geometry of the crypt is compromised by the assumptions that the crypt is perfectly cylindrical and that cells are rectangular, of regular size and arranged in a precise grid. The assumption that migration occurs in discrete cell-sized steps is also an area of simplification, resulting in the shifting of an entire column of

cells upon cell division. Many cell–cell interactions must be broken to incorporate new cells, which may be considered energetically unfavourable (van Leeuwen *et al.*, 2006). The lattice-free models discussed in the following section make some progress in overcoming these deficiencies.

1.5.2 Lattice-free models

Meineke *et al.* (2001) presented a model for cell division in a small-intestinal crypt in which cell location is not restricted to a grid framework, such as that of Loeffler *et al.* (1986). The discrete, stepwise migration of cells discussed above was replaced by a setting in which cells move continuously according to attractive/repulsive cellular forces. The model crypt is considered cylindrical once more; however, the consequences of this are minimised through the assumption that the tapering crypt-base is completely filled with non-proliferative Paneth cells. Each cell within the crypt was represented by a point on the planar crypt surface. The point is representative of the entire cell, but may be considered to be located at the centre of the cell nucleus. For a given number of points, termed *generators*, a Voronoi diagram is used to divide the plane into regions according to which of the generators each point on the plane lies closest to. Each region can be thought to represent one cell; the polygonal shape of the intestinal epithelial cell is, thus, recovered. Interactions between the cells are captured through a series of damped springs linking neighbouring generators. It is assumed that neighbouring cells will seek to establish equal distances from one another. Cells are not permitted to move out of the bottom of the crypt, while cells which move beyond the upper crypt boundary are removed from the system. Stem cells are assumed to reside directly above the Paneth cells and divide strictly asymmetrically in this model to yield one stem cell and one transit cell. Dividing transit cells undergo a fixed number of divisions before becoming mature, non-dividing cells. All cells are assumed to have identical mechanical properties. The authors found that their model exhibits best fit with experimental data when a complete ring of sixteen stem cells is considered to reside immediately above the Paneth cells. The (*in-vitro*) LI and RUN data of Kaur & Potten (1986) were reproduced with a high degree of success, suggesting that the intricate cell-sorting rules discussed by Loeffler *et al.* (1986) are not key in achieving biological accuracy.

Morel *et al.* (2001) utilised a similar Voronoi diagram approach in the formulation of a model for proliferation control in a generalised epithelium. The model couples this spatial representation of cells to a model for the molecular control of cell proliferation based upon the law of mass action. The cell proliferation model incorporates both intracellular and extracellular controls, including growth and differentiation factors.

The 2D simulations presented illustrate the influence of the microenvironment upon cell proliferation and could potentially be applied to intestinal tissue. However, the authors comment that these simulations are computationally expensive due to the large number of parameters involved.

A modular, multiscale model for proliferation in the intestinal crypt has been formulated by van Leeuwen *et al.* (2009). The authors combined the discrete spatial cell model of Meineke *et al.* (2001), an ODE model for the Wnt signalling pathway owing to van Leeuwen *et al.* (2007) and a cell-cycle model owing to Swat *et al.* (2004). A strong Wnt signal was considered to speed up the progression of the cell cycle, stimulating rapid division and differentiation; Wnt proteins are greatest in number near the crypt base and gradually decline towards the lumen, accounting for variations in cell division and maturity along the crypt axis. In contrast to Meineke *et al.* (2001), cell–cell adhesions were assumed non-uniform and proportional to the degree of contact between cell edges, while drag forces due to cell–matrix adhesion were assumed to be dependent upon the cell area. The direction of cell divisions was assumed random and the stem cells were permitted to move away from the base of the crypt subject to sufficient biomechanical force from their neighbours. The authors illustrated that stem cell motility enables monoclonal conversion of the crypt, *i.e.* the progeny of a single stem cell can ultimately populate the entire crypt. The model is able to predict intracellular localisation of β-catenin and, thus, enables the connections between Wnt signalling and cell–cell adhesion to be examined. The model can also be used to provide spatio-temporal information at the cell level, by analogy with the labelling experiments of Kaur & Potten (1986), for example.

An alternative to the 'cell-centre' approach of Meineke *et al.* is to represent each cell by vertices at cell junctions. For further details, and a comparison of these two approaches, the reader is directed to Walter (2009), Osborne *et al.* (2010) and references therein. Osborne *et al.* (2010) compared the results of a cell-centre model, a cell-vertex model and an analogous continuum model of cell proliferation and migration in the crypt. The three models each considered the competing proliferation of healthy and mutant cell populations within the crypt, with a view to examining relative cell division and migration characteristics and the extent to which the progeny of a single (mutant or stem) cell may populate the entire crypt. The authors found that, in most cases, conclusions were independent of the modelling approach. Cell-based models were shown to be more convenient for investigation of whether crypts are monoclonal or polyclonal; however, this approach is computationally expensive. While the continuum model is quicker and easier to implement, the authors comment that determining

the required parameters from available biological data is difficult.

While the lattice-free models discussed here are more realistic than the 2D-grid models of section 1.5.1, their construction still relies on a number of key simplifications. For example, these models assume that healthy crypts are all cylindrical and identical, and crypt size is considered constant throughout. While these assumptions are not entirely consistant with the observed crypt structure *in vivo*, they are justifiable on the grounds of making the models mathematically tractable. The results of Meineke *et al.* (2001) observed a movement of cells out of the crypt which briefly continued in the absence of cell division. Such behaviour is not observed in reality (van Leeuwen *et al.*, 2006). Many lattice-free models lack a detailed description of the impact of the mechanical properties of the connective tissue (although cell–matrix adhesion is considered by such authors as van Leeuwen *et al.* (2009), for example). To the author's knowledge, no model currently utilises a 2D, lattice-free description of the cells to study deformations of the underlying tissue.

In the above models, migration of cells up the crypt axis is considered to be driven by a combination of both external cellular signals, and forces exerted upon a cell from its neighbours. In particular, the rapid proliferation at the base of the crypt can be considered to place these cells under some compression, resulting in a pressure gradient which pushes cells up the crypt axis. Resistance to cell proliferation is considered to be lower in those regions which are less compressed (*i.e.* further up the crypt). We suggest that these cell-level mechanisms play a role in patterning the growth and mechanical properties of the cell layer, the effects of which are evident at the tissue-level. Rapidly proliferating regions are likely to be more heavily compressed and may buckle more readily; such variations may play a role in crypt formation during development. In this study, we examine the buckling of epithelia whose growth rates and mechanical properties vary spatially, as a result of cell-level patterning mechanisms such as these.

1.6 Pertinent mathematical theory

In this thesis we focus upon the cascade by which epithelial growth induces compressive stresses in the epithelium, the relief of which necessitates buckling. In turn, the buckling of the epithelium acts as a patterning mechanism which impacts upon crypt frequency and location. We will examine the manner in which an imposed patterning of the tissue's growth or mechanical properties controls the resulting distribution of colorectal crypts. Such a cascade has previously been postulated in numerous areas of biology. Authors including Green *et al.* (1996), Steele (2000) and Dumais (2007) have

studied the links between growth-induced buckling and pattern formation in plant leaves, stems and petals, while such authors as Dervaux & Ben Amar (2008) have examined buckling driven by growth in soft tissues. Ben Amar & Brener (1993) considered a similar mechanism for the control of pattern selection in dendritic crystals, pertinent to many natural processes including snowflake formation. Many such models involve either the buckling of nonlinear elastic shells (Ben Amar & Goriely (2005), for example) or modification of the Föppl–von Kármán equations for a deformed plate (*e.g.* Dervaux *et al.* (2009)). We review these two approaches in section 1.6.3; firstly, however, we discuss some of the fundamentals of elasticity theory and common approaches to modelling growth.

1.6.1 Elasticity

We begin our review of the mathematical theory required for this study with a brief summary of the equations which underpin solid mechanics. The fundamental goal in studying any problem in solid mechanics is to determine the relationship between applied force and material displacement. The resolution of this problem lies in identifying the appropriate relationship between the material's distribution of stresses (internal forces per unit area) and strains (measures of relative change in length of material elements in certain coordinate directions). The equations below will be presented in terms of Lagrangian coordinates $\mathbf{X}^* = \left(X_1^*, X_2^*, X_3^*\right)$, which map to Eulerian coordinates $\mathbf{x}^* = \left(x_1^*, x_2^*, x_3^*\right)$ in the deformed configuration. Throughout this thesis stars denote dimensional quantities. We relate the two coordinate systems via the *deformation gradient tensor*, denoted $\mathbf{F}$, with components defined according to

$$F_{ij} = \frac{\partial x_i^*}{\partial X_j^*}. \tag{1.1}$$

The determinant of $\mathbf{F}$ quantifies the relative change in volume of material elements upon deformation. Using (1.1), we can write any line element $\mathrm{d}x_i$ in the deformed configuration in terms of the equivalent line element in the undeformed configuration:

$$\mathrm{d}x_i^* = F_{ij}\mathrm{d}X_j^*. \tag{1.2}$$

We adopt the Einstein summation convention here, summing any term with a repeated index (such as the right-hand side of (1.2)) over values 1, 2 and 3.

When measuring stresses, we have a choice to work in either the Eulerian (current) configuration or the Lagrangian (reference) configuration. The symmetric *Cauchy stress tensor*, which we denote σ^*, measures stresses relative to the Eulerian frame. Considering a small volume element with sides parallel to the Eulerian coordinates (x_1, x_2, x_3),

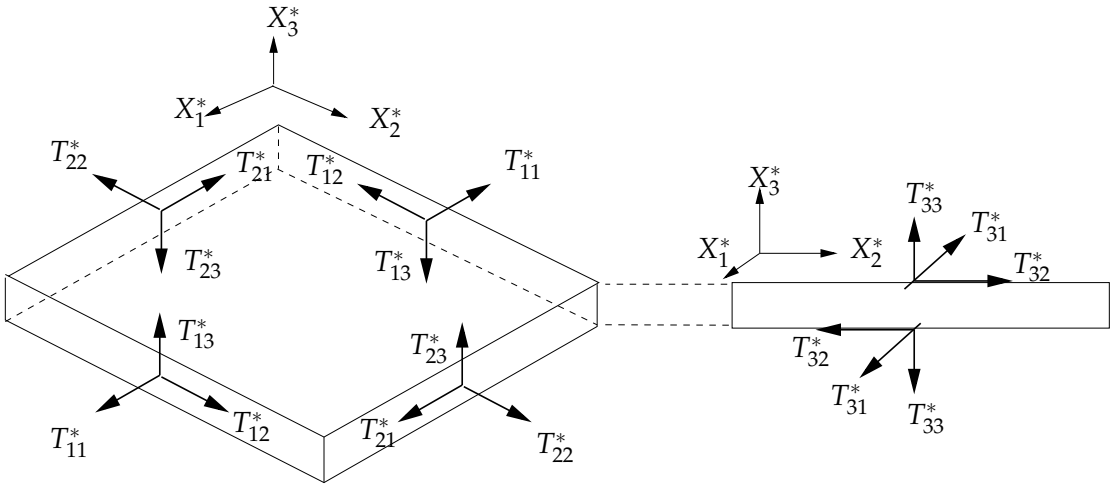

Figure 1.4: Distribution of stresses on a surface element, with respect to the Lagrangian frame of reference.

we interpret σ_{ij}^* as a stress acting upon the side whose normal is x_i^* due to internal forces directed in the x_j^* direction. However, it is often more convenient to present equations in terms of Lagrangian quantities. In the Lagrangian frame, stress is characterised by the first and second *Piola–Kirchhoff stress tensors*, which we denote $\mathbf{T}^*$ and $\mathbf{S}^*$ respectively. Figure 1.4 illustrates the interpretation of the components of $\mathbf{T}^*$, with reference to a small volume element with sides parallel to the Lagrangian coordinate directions.

Howell *et al.* (2009) consider the deformation of an arbitrary body to derive the following relationship between the first Piola–Kirchhoff stress tensor, $\mathbf{T}^*$, and the Cauchy stress tensor, $\boldsymbol{\sigma}^*$:

$$\mathbf{T}^* = \det(\mathbf{F})\boldsymbol{\sigma}^* \left(\mathbf{F}^\top\right)^{-1}. \tag{1.3}$$

In general, $\mathbf{T}^*$ is not symmetric; however, we can exploit the symmetry of $\boldsymbol{\sigma}^*$ to manipulate (1.3) and obtain the following identity:

$$\mathbf{T}^*\mathbf{F}^\top = \mathbf{F}\mathbf{T}^{*\top}. \tag{1.4}$$

The transpose of $\mathbf{T}^*$ is commonly referred to as the *nominal stress tensor* (Spencer, 1980).

The second Piola–Kirchhoff stress tensor, $\mathbf{S}^*$, is defined according to

$$\mathbf{S}^* = \mathbf{F}^{-1}\mathbf{T}^*, \tag{1.5}$$

and has no direct physical interpretation (Spencer, 1980). However, manipulating (1.3) to calculate $\mathbf{S}^{*\top}$, we can show that $\mathbf{S}^*$ is symmetric. It is, therefore, convenient to present equations in terms of $\mathbf{S}^*$ rather than $\mathbf{T}^*$.

Cauchy's equation for the conservation of momentum, written in terms of Eulerian

quantities, is

$$\rho^* \frac{\partial^2 x_i^*}{\partial t^{*2}} = \frac{\partial \sigma_{ij}^*}{\partial x_j^*} + \rho^* b_i^*, \tag{1.6}$$

where t^* is time, $\rho^*(t^*)$ is the density of the body and $\mathbf{b}^* = \left(b_1^*, b_2^*, b_3^*\right)$ captures any external body forces acting on the material, such as gravity. Equivalently, in terms of Lagrangian variables, (1.6) is

$$\rho_0^* \frac{\partial^2 x_i^*}{\partial t^{*2}} = \frac{\partial T_{ij}^*}{\partial X_j^*} + \rho_0^* b_i^*, \tag{1.7}$$

where $\rho_0^* = \det(\mathbf{F})\,\rho^*$ is the initial density of the body.

The deformation gradient tensor, $\mathbf{F}$, equips us with knowledge of changes in shape of volume elements upon deformation. However, since $\mathbf{F}$ is dependent upon the orientation of the body, it does not naturally lend itself to the quantification of material strains. To see this, consider a rigid body displacement of the deformed body, under which $\mathbf{x}^*$ is replaced by

$$\mathbf{x}'^* = \mathbf{a}^* + \mathbf{P}\mathbf{x}^*, \tag{1.8}$$

where $\mathbf{a}^*$ represents a translation and $\mathbf{P}$ is an orthogonal matrix representing a rotation. We expect no generation of strain under this displacement; however, with respect to the new Eulerian coordinates, the deformation gradient is replaced by $\mathbf{F}' = \mathbf{P}\mathbf{F}$. Consider instead the combination $\mathbf{C} = \mathbf{F}^\top\mathbf{F}$. Under the same rigid body displacement, we have

$$\mathbf{C}' = \mathbf{F}'^\top\mathbf{F}' = \mathbf{F}^\top\mathbf{P}^\top\mathbf{P}\mathbf{F} = \mathbf{F}^\top\mathbf{F} = \mathbf{C}, \tag{1.9}$$

which illustrates that, unlike $\mathbf{F}$, $\mathbf{C}$ is invariant under these transformations. Alternatively, a rotation of the Lagrangian coordinate system according to

$$\mathbf{X}'^* = \mathbf{a}^* + \mathbf{Q}\mathbf{X}^*, \tag{1.10}$$

(for orthogonal matrix $\mathbf{Q}$) implies that

$$\mathbf{F}' = \mathbf{F}\mathbf{Q}^\top, \qquad \mathbf{C}' = \mathbf{Q}\mathbf{C}\mathbf{Q}^\top, \tag{1.11}$$

illustrating that $\mathbf{C}$ obeys the transformation law of a second-rank tensor (Howell *et al.*, 2009). We refer to $\mathbf{C}$ as the *right Cauchy-Green deformation tensor*. Formulation of the problem in terms of $\mathbf{C}$ has the further advantage that, since $\mathbf{C}$ is symmetric, we have three fewer variables to consider. Note that under rigid-body motion $\mathbf{F}$ is orthogonal and $\mathbf{C} = \mathbf{I}$. This motivates the following definition of the *Lagrangian strain*, $\mathbf{e}$ (also called the *Green strain*):

$$\mathbf{e} = \frac{1}{2}(\mathbf{C} - \mathbf{I}) = \frac{1}{2}\left(\mathbf{F}^\top\mathbf{F} - \mathbf{I}\right). \tag{1.12}$$

Since $\mathbf{F}$ is non-singular, the polar decomposition theorem (Spencer, 1980) states the existence of an orthogonal matrix $\mathbf{M}$ and a positive definite, symmetric matrix $\mathbf{U}$ such that

$$\mathbf{F} = \mathbf{M}^\top \mathbf{U}, \tag{1.13}$$

and since $\mathbf{U}$ is positive definite, it is diagonalisable and can be written as

$$\mathbf{U} = \mathbf{R}^\top \mathbf{\Lambda} \mathbf{R}, \quad \text{where} \quad \mathbf{\Lambda} = \begin{pmatrix} \lambda_1 & 0 & 0 \\ 0 & \lambda_2 & 0 \\ 0 & 0 & \lambda_3 \end{pmatrix}, \tag{1.14}$$

and $\mathbf{R}$ is orthogonal. The decomposition in (1.13) separates rotational effects (via $\mathbf{M}$) from changes in volume (given by $\mathbf{U}$). Note that the entries of $\mathbf{\Lambda}$ are precisely the eigenvalues of $\mathbf{U}$. Since the eigenvectors of $\mathbf{\Lambda}$ are simply the coordinate axes, the eigenvalues λ_i ($i = 1, 2, 3$) represent stretches of the material in these directions. We refer to the λ_i as the *principal stretches*.

Without loss of generality, we can choose our Lagrangian coordinate system such that $\mathbf{R} \equiv \mathbf{I}$. Since (1.9) and (1.13) imply that $\mathbf{C} = \mathbf{U}^2$, this choice results in $\mathbf{C}$ being of diagonal form with eigenvalues given by the diagonal entries λ_i^2 ($i = 1, 2, 3$). It then follows from (1.12) that $\mathbf{e}$ is also diagonal with non-zero entries given by

$$e_i = \frac{1}{2}\left(\lambda_i^2 - 1\right), \tag{1.15}$$

termed the *principal strains*. The characteristic polynomial of $\mathbf{C}$, in terms of some arbitrary independent variable ζ, is as follows

$$\det\left(\zeta \mathbf{I} - \mathbf{C}\right) = \left(\zeta - \lambda_1^2\right)\left(\zeta - \lambda_2^2\right)\left(\zeta - \lambda_3^2\right) = \zeta^3 - I_1\zeta^2 + I_2\zeta - I_3, \tag{1.16}$$

where

$$I_1 = \lambda_1^2 + \lambda_2^2 + \lambda_3^2, \qquad I_2 = \lambda_1^2\lambda_2^2 + \lambda_2^2\lambda_3^2 + \lambda_3^2\lambda_1^2, \qquad I_3 = \lambda_1^2\lambda_2^2\lambda_3^2, \tag{1.17}$$

(Howell *et al.*, 2009). Since the eigenvalues and characterstic polynomial of $\mathbf{C}$ are unchanged under an orthogonal transformation of Eulerian coordinate axes, the quantities I_1, I_2 and I_3 are independent of choice of Eulerian coordinates. Thus, these are termed *strain invariants*. Equivalently, we can write (1.17) as

$$I_1 = \mathrm{Tr}\left(\mathbf{C}\right), \qquad I_2 = \frac{1}{2}\left(\mathrm{Tr}\left(\mathbf{C}\right)^2 - \mathrm{Tr}\left(\mathbf{C}^2\right)\right), \qquad I_3 = \det\left(\mathbf{C}\right). \tag{1.18}$$

Note that for an incompressible material $I_3 \equiv 1$.

Given (1.12), the task of relating stresses and strains reduces to that of determining $\mathbf{T}^*$ as a function of $\mathbf{F}$. Howell *et al.* (2009) explain that conservation of energy as an

arbitrary body deforms requires the existence of a function $W^*(\mathbf{F})$, termed the *strain energy density*, such that

$$T^*_{ij} = \frac{\partial W^*}{\partial F_{ij}}. \tag{1.19}$$

Hereafter, we will use the following notation for differentiation by a tensor to write (1.19) more compactly:

$$\mathbf{T}^* = \frac{\partial W^*}{\partial \mathbf{F}}. \tag{1.20}$$

We can regard W^* as a measure of the stored elastic energy per unit volume, the elastic energy of the whole body $\mathcal{B}$ being

$$\mathcal{E}^*_{\text{elast}} = \iiint_{\mathcal{B}} W^* \mathrm{d}\mathbf{V}. \tag{1.21}$$

This justifies the requirement that W^* is strictly positive, except when $\mathbf{F} = \mathbf{I}$. Further restrictions upon the choice of W^* can also be justified; however, we omit the details here. Materials for which there exists a suitable strain energy density function satisfying (1.20) are termed *hyperelastic*.

The strain energy density function must be unchanged under rigid-body rotations and, hence, must satisfy

$$W^*(\mathbf{F}) = W^*(\mathbf{PF}), \tag{1.22}$$

for any orthogonal matrix $\mathbf{P}$. Deploying the decomposition of (1.13) we require

$$W^*(\mathbf{F}) = W^*(\mathbf{PM}^\top \mathbf{U}), \tag{1.23}$$

for any orthogonal matrices $\mathbf{P}$ and $\mathbf{M}$. In particular, the case $\mathbf{P} = \mathbf{M}$ yields the requirement that W^* can be considered as a function of $\mathbf{U}$ alone. Since there is a one-to-one correspondence between $\mathbf{U}$ and $\mathbf{C}$, we can regard W^* as $W^*(\mathbf{C})$ (Spencer, 1980; Atkin & Fox, 1980). The second Piola–Kirchhoff tensor is then given by

$$S^*_{ij} = \frac{\partial W^*}{\partial C_{ij}} + \frac{\partial W^*}{\partial C_{ji}}, \tag{1.24}$$

(Spencer, 1980), or equivalently by

$$\mathbf{S}^* = 2\frac{\partial W^*}{\partial \mathbf{C}}, \tag{1.25}$$

since $\mathbf{C}$ is symmetric (Howell *et al.*, 2009). We can further simplify the problem by writing W^* in terms of the strain invariants, so that

$$\mathbf{S}^* = 2\frac{\partial W^*}{\partial I_k}\frac{\partial I_k}{\partial \mathbf{C}}, \tag{1.26}$$

the expansion of which is aided by the following identities (Howell *et al.*, 2009):

$$\frac{\partial I_1}{\partial \mathbf{C}} = \mathbf{I}, \qquad \frac{\partial I_2}{\partial \mathbf{C}} = I_1\mathbf{I} - \mathbf{C}, \qquad \frac{\partial I_3}{\partial \mathbf{C}} = I_3\mathbf{C}^{-1}. \tag{1.27}$$

Since $\mathbf{C}$ satisfies its own characteristic polynomial, we can use (1.16) to write $\mathbf{C}^{-1}$ in terms of higher powers of $\mathbf{C}$ in (1.27). Expanding (1.26) then gives

$$\mathbf{S}^* = 2\left(\frac{\partial W}{\partial I_1} + I_1\frac{\partial W}{\partial I_2} + I_2\frac{\partial W}{\partial I_3}\right)\mathbf{I} - 2\left(\frac{\partial W}{\partial I_2} + I_1\frac{\partial W}{\partial I_3}\right)\mathbf{C} + 2\frac{\partial W}{\partial I_3}\mathbf{C}^2. \tag{1.28}$$

The requirement that W^* is minimised when $\mathbf{F} = \mathbf{I}$ is equivalent to ensuring a global minimum when $\lambda_i = 1$, for all i. Furthermore, for isotropic materials we require W^* to be invariant under permutation of the λ_i. Taking the limit $\lambda_i \to 1$ for all i, in which principal stretches (and, hence, principal strains) are small, we expect the dominant terms in W^* to be of the form

$$W^* \sim \mu^* \sum_{i=1}^{3} (\lambda_i - 1)^2 + \frac{\lambda^*}{2} \sum_{i,j=1}^{3} (\lambda_i - 1)\left(\lambda_j - 1\right), \tag{1.29}$$

for constants λ^* and μ^* (Howell *et al.*, 2009). Substitution of (1.29) into (1.28) gives

$$\mathbf{S}^* = \lambda^* \mathrm{Tr}(\mathbf{e})\mathbf{I} + 2\mu^*\mathbf{e}, \tag{1.30}$$

which is the constitutive stress–strain relationship of *linear elasticity*. The constants λ^* and μ^* are known as the *Lamé constants* and act as measures of a material's resistance to elastic deformation. They must satisfy $\mu > 0$ and $3\lambda + 2\mu > 0$ to ensure that W^* is positive definite (Howell *et al.*, 2009).

Authors including Fung (1967), Demiray (1972) and Holzapfel *et al.* (2000) have illustrated that the deformation of soft tissues is generally governed by a nonlinear relationship between applied stresses and material strains. However, despite this, the simplicity and familiarity of linear elasticity theory has led many authors to apply these methods to soft tissues directly (Humphrey, 2003; Fung, 1967). We note that, while these methods are suitable in the limit of small strains, the study of larger deflections requires the deployment of a nonlinear theory. One property exhibited by many biological tissues is an effective stiffening as strains increase (Goriely *et al.*, 2006).

The strain energy function is commonly decomposed into an isochoric component (capturing volume-preserving effects) and a volumetric component (which accounts for changes in volume). Accordingly, we write

$$\mathcal{W}^*(I_1, I_2, I_3) = \mathcal{W}^*_{\mathrm{iso}}(I_1, I_2) + \mathcal{W}^*_{\mathrm{vol}}(I_3). \tag{1.31}$$

Numerous forms of $\mathcal{W}^*_{\mathrm{vol}}$ have been proposed in the literature (see Doll & Schweizerhof (2000) and references therein), the key feature being that $\mathcal{W}^*_{\mathrm{vol}}$ attains a minimum as $I_3 \to 1$. We consider the following form here:

$$\mathcal{W}^*_{\mathrm{vol}} = c^*(I_3 - 1)^2 + d^* \log I_3, \tag{1.32}$$

where c^* and d^* are constants.

Table 1.1 lists the forms of the isochoric components of the strain energy functions corresponding to a number of nonlinear theories. Those of Ogden, Fung and Gent are particularly appropriate for biological materials which exhibit strain-stiffening behaviour. We briefly discuss the neo-Hookean strain energy function here, motivated by its relevance to forthcoming models (*c.f.* section 1.6.3 and chapters 5 and 6). For a neo-Hookean material, consider a strain energy function of the form

$$\mathcal{W}^* = \frac{\mu^*}{2}\left(I_1 - 3\right) + c^*\left(I_3 - 1\right)^2 + d^* \log I_3. \tag{1.33}$$

Substitution of (1.33) into (1.28) yields

$$\mathbf{S}^* = \mu^* \mathbf{I} + \left(2c^*\left(I_3 - 1\right) + \frac{d^*}{I_3}\right)\left(2I_2\mathbf{I} - 2I_1\mathbf{C} + 2\mathbf{C}^2\right). \tag{1.34}$$

Now let us consider small strains, $\mathbf{e} = \delta\hat{\mathbf{e}}$, for some $0 < \delta \ll 1$. It follows that

$$\mathbf{C} = \mathbf{I} + 2\delta\hat{\mathbf{e}} \tag{1.35}$$

and

$$I_1 = 3 + 2\delta \mathrm{Tr}\left(\hat{\mathbf{e}}\right) + O\left(\delta^2\right), \tag{1.36a}$$

$$I_2 = 3 + 4\delta \mathrm{Tr}\left(\hat{\mathbf{e}}\right) + O\left(\delta^2\right), \tag{1.36b}$$

$$I_3 = 1 + 2\delta \mathrm{Tr}\left(\hat{\mathbf{e}}\right) + O\left(\delta^2\right). \tag{1.36c}$$

Substituting (1.35) and (1.36) into (1.34), we have

$$\mathbf{S}^* = \left[\mu^* + 2d^* + 8\delta c^* \mathrm{Tr}\left(\hat{\mathbf{e}}\right)\right]\mathbf{I} - 4d\delta\hat{\mathbf{e}} + O\left(\delta^2\right). \tag{1.37}$$

Under the assumption that the material is unstressed in its reference state, we require $d^* = -\mu^*/2$. Writing $c^* = \lambda^*/8$, for consistency with linear elasticity, and setting $\mathbf{S}^* = \delta\hat{\mathbf{S}}^*$ we then have

$$\hat{\mathbf{S}}^* = \lambda^* \mathrm{Tr}\left(\hat{\mathbf{e}}\right)\mathbf{I} + 2\mu^*\hat{\mathbf{e}} + O\left(\delta\right), \tag{1.38}$$

which recovers (1.30). The neo-Hookean formulation thus provides a hyperelastic theory which is valid for large strains, but recovers linear elasticity for small strains.

1.6.2 Growth

Taber (1995) defines growth as the addition of mass occurring due to such processes as cell division, cell enlargement and secretion of extracellular matrix. Analogously, negative growth (termed *atrophy*) occurs due to processes including cell death, cell shrinkage and resorption. Mathematical models of growing biological organisms have been

Name	Definition	Properties
Neo-Hookean	$\mathcal{W}^*_{\text{iso}} = \frac{\mu^*}{2}(I_1 - 3)$	Linear response initially, followed by a transition to a less stiff linear response.
Mooney–Rivlin	$\mathcal{W}^*_{\text{iso}} = c_1^*(I_1 - 3) + c_2^*(I_2 - 3)$	Linear response initially, followed by a transition to a less stiff linear response.
Varga	$\mathcal{W}^*_{\text{iso}} = 2\mu^*(\lambda_1 + \lambda_2 + \lambda_3 - 3)$	Failure for finite value of applied force.
Ogden	$\mathcal{W}^*_{\text{iso}} = \frac{2\mu^*}{\alpha}\left(\lambda_1^\alpha + \lambda_2^\alpha + \lambda_3^\alpha - 3\right)$	For $\alpha < 1$ force reaches a maximum (as a function of strain) and decays to zero, giving failure of the material for finite force. For $1 < \alpha < 2$ behaviour is similar to Mooney-Rivlin. For $\alpha > 2$ the stiffness always increases with increasing strain. Appropriate for soft tissues for $\alpha \geq 9$.
Fung	$\mathcal{W}^*_{\text{iso}} = \frac{k^*}{2\alpha}\left(\exp\left(\alpha(I_1 - 3)\right) - 1\right)$	Exponential stiffening as a function of strain. Applicable to soft tissues for $3 < \alpha < 20$.
Gent	$\mathcal{W}^*_{\text{iso}} = -\frac{k^*}{2\beta}\ln\left(1 - \beta(I_1 - 3)\right)$	Limited extensibility as a function of strain. Applicable to soft tissues for $0.4 < \beta < 3$.

Table 1.1: A selection of nonlinear strain energy functions, where α, β, μ^*, c_1^*, c_2^* and k^* are positive constants. Sources: Howell *et al.* (2009); Goriely *et al.* (2006, 2008) and references therein. The above properties are determined in the aforementioned references via direct computation of the stress–strain relationship corresponding to each choice of $\mathcal{W}^*$. 'Failure' refers to unbounded strain for finite applied stress.

published since the 1940's by such authors as Thompson (1942) (Taber, 1995). Many early studies focused purely upon deploying arguments of geometry to track the displacements and velocities of material points as functions of some prescribed growth rate, examples include the study of growing cartilage by Cox & Peacock (1978, 1979). In such models the interaction between growth and mechanical factors (such as stress) are not considered.

While such authors as Hsu (1968) and Cowin & Hegedus (1976) considered some specific problems regarding the mechanical loading of tissues, it was not until the early 1980's that the study of coupled growth and deformation was placed within the rigorous framework of nonlinear elasticity. Skalak (1980) suggested that the growth and deformation of an initially unstressed, unloaded body can be considered as distinct processes, happening concurrently and linked via some hypothetical intermediate configuration. After a few refinements, the model was presented in detail by Rodriguez *et al.* (1994); figure 1.5 illustrates the proposed decomposition of growth and deformation. Consider an elastic body whose initial configuration is deformed according to a deformation gradient tensor $\mathbf{F}$. Skalak's suggested approach states that we decompose $\mathbf{F}$ as

$$\mathbf{F} = \mathbf{F}_g \cdot \mathbf{F}_e, \tag{1.39}$$

where $\mathbf{F}_g$ is a growth tensor and $\mathbf{F}_e$ is an elastic deformation gradient tensor. Starting with the unstressed configuration at time t_0, which we denote $\mathcal{B}(t_0)$, initially purely the growth of the body is considered. Applying $\mathbf{F}_g$ to $\mathcal{B}(t_0)$ yields an intermediate, hypothetical configuration, $\tilde{\mathcal{B}}(t_1)$, which is enlarged and stress-free. In general we can write $\mathbf{F}_g$ as

$$\mathbf{F}_g = \mathbf{R}_g \mathbf{U}_g, \tag{1.40}$$

where $\mathbf{R}_g$ captures any rotational growth behaviour and $\mathbf{U}_g$ is the growth stretch tensor. However, Rodriguez *et al.* show that we can assume $\mathbf{R}_g$ to be the identity without loss of generality; any rotational effects are simply incorporated in the elastic deformation phase. We, thus, consider $\mathbf{F}_g$ as a pure stretching of material elements. The mapping $\mathcal{B}(t_0) \mapsto \tilde{\mathcal{B}}(t_1)$ imposes no restrictions upon the compatibility of growth, a condition which is usually imposed to ensure a single-valued displacement field upon deformation of the body. Given an incompatible growth regime, the enlarged stress-free body would exhibit discontinuities or overlappings.

The second mechanism considered is that which acts to instantaneously deform the new stress-free configuration, $\tilde{\mathcal{B}}(t_1)$, into its final configuration $\mathcal{B}(t_1)$. This mapping is determined by $\mathbf{F}_e$ alone. If applicable, $\mathbf{F}_e$ must also correct for those discontinuities generated by the growth phase. Taber (1995) considers that the correction of incom-

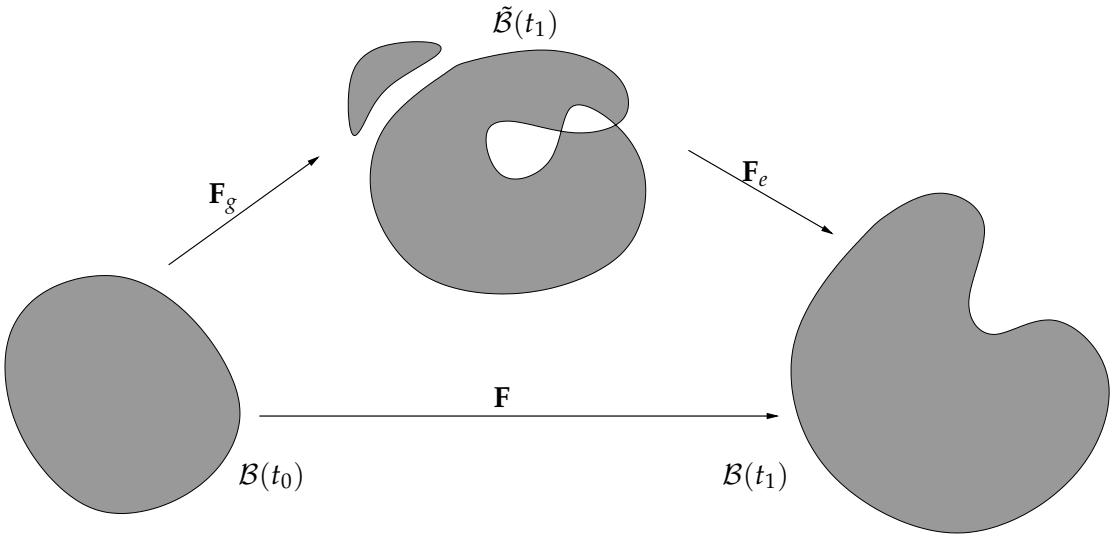

Figure 1.5: A schema of the model of Rodriguez *et al.* (1994), in which the growth and elastic deformation of an initially unstressed body are considered. The initial configuration, $\mathcal{B}(t_0)$, is first considered to undergo growth according to the growth tensor $\mathbf{F}_g$, which maps the body into an intermediate configuration $\tilde{\mathcal{B}}(t_1)$. The growth regime may be incompatible, suggesting that $\tilde{\mathcal{B}}(t_1)$ may be discontinuous or have overlappings. The intermediate configuration then experiences elastic deformation, $\mathbf{F}_e$, correcting the consequences of incompatible growth (if necessary) and giving rise to residual stresses.

patibilities can be further decoupled, via a second intermediate configuration which is single-valued. We omit this here. After elastic deformation, the body lies in configuration $\mathcal{B}(t_1)$, which is now both expanded and deformed, is continuous and is under residual stress.

This framework has since been utilised for studying the growth of both hard and soft tissues. Growth of hard tissues (such as bone, horns *etc.*) occurs via deposition of new mass upon the surfaces of the body, while that of soft tissues occurs via the generation of mass internally. The latter is commonly termed *volumetric growth*; previous studies have considered such a mechanism in application to such biological processes as tumour growth (Ambrosi & Mollica, 2002) and vascular mechanics (authors include Taber (1998) and Rachev *et al.* (1998)).

While the formalism described above has been deployed extensively by numerous authors, Humphrey & Rajagopal (2002) argue that the theory merely accounts for the consequences of growth rather than the precise nature of the underlying processes. They suggest that a preferred approach is to use mixture theory to account for the production and removal of the individual constituents of the tissue. Such a theory would better account for microscale inhomogeneities; however, it would require more detailed knowl-

edge of reaction kinetics and rate parameters than is currently available (Humphrey, 2003).

For further details of soft tissue growth and remodelling, the reader is directed to the reviews of Taber (1995), Humphrey (2003), Cowin (2004) and Goriely *et al.* (2008).

1.6.3 Reductions of 3D elasticity

In this study we will consider deformations of bodies which are thin in comparison to their in-plane dimensions. The theory obtained upon reducing the equations of general elasticity in this limit is termed *shell theory*. Moreover, if the reference configuration is flat, further simplification yields *plate theory*.

Let us assume that the body is thin in the X_3^*-direction. We denote the upper/lower surfaces of the plate by $X_3^* = \pm h^*/2$. Our discussions will now proceed in terms of *stress resultants* (rather than stresses) derived by averaging the stress components across the thickness of the layer. Denoting stress resultants by $\bar{T}_{ij}^*$, we have

$$\bar{T}_{ij}^* = \int_{-h^*/2}^{h^*/2} T_{ij}^* \, \mathrm{d}X_3^*. \tag{1.41}$$

We will discuss deformations of the body in terms of *bending moments*, which capture variations in the distribution of stresses across the thickness of the layer, *i.e.*

$$M_{ij}^* = \int_{-h^*/2}^{h^*/2} T_{ij}^* X_3^* \, \mathrm{d}X_3^*, \tag{1.42}$$

the senses of which are illustrated in figure 1.6. We regard M_{ij} as a bending moment which acts upon the side of a surface element whose normal is X_i^*, owing to internal forces directed parallel to X_j^*. Those bending moments for which $i = j$ arise due to normal stresses and those for which $i \neq j$ arise due to shear stresses. The latter are sometimes referred to as 'twisting moments', to reflect the differing geometric change to the surface elements upon which they act (Brush & Almroth, 1975). Note that the conventions used to define bending moments vary between authors. With the exception of appendix B, in which we discuss an existing model by Pamplona & Calladine (1993), all model derivations presented in this thesis refer to bending moments as defined by (1.42).

Beam theory

Prior to discussion of common approaches to modelling deforming plates, let us consider the further simplification attained by adopting the plane strain assumption. In

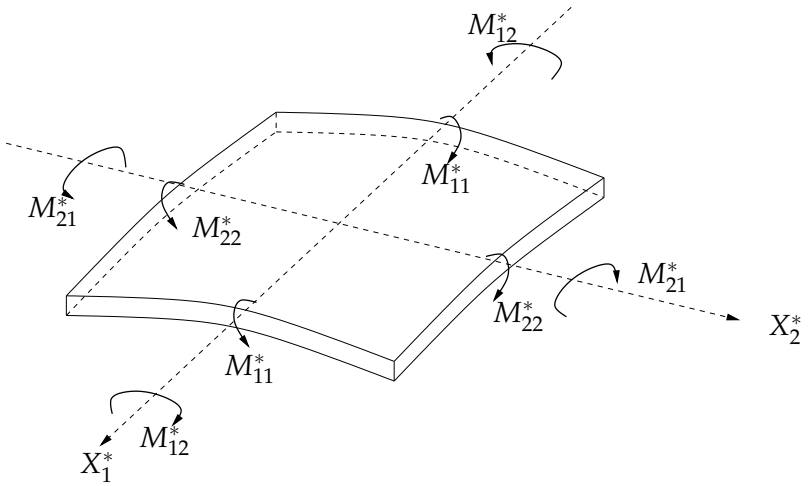

Figure 1.6: Moments acting upon a surface element.

this limit we can characterise deformations by a cross-section of the plate (oriented in the X_1^*-direction, say). The resultant theory is termed *beam theory*. All mechanical quantities are now considered to be taken per unit length in the X_2^*-direction; we refer to stress resultants per unit length (which have dimensions of stress) and bending moments per unit length. Under plane strain we have only one non-zero bending moment (*i.e.* that whose action is in the (X_1^*, X_3^*)-plane); we denote this bending moment by M^* in this section.

Fundamentally, the development of a comprehensive beam theory dates back to Euler and Bernoulli, who observed that the primary distortion of a beam upon application of a bending moment is a proportional change in curvature (Calladine, 1989), *i.e.*

$$M^* = -D^*\kappa^*. \tag{1.43}$$

The above is now known as the *Euler–Bernoulli relation*. Historically, determination of the constant of proportionality, D^*, in (1.43) has proved difficult. The key step was made by Kirchhoff in 1850 in his study of deforming elastic plates. His approach was to make the following assumptions, now termed the *Kirchhoff assumptions*:

1. normals to the plate's central plane remain straight, normal and inextensible during deformation;

2. out-of-plane stresses are small in comparison to in-plane stresses,

(Brush & Almroth, 1975; Calladine, 1989). The assumption that normals to the plate's central plane are inextensible requires that out-of-plane normal strains vanish, which

in turn justifies the following expression for the *bending stiffness* of the layer:

$$D^* = \frac{E^* h^{*3}}{12\,(1-\nu^2)}, \tag{1.44}$$

(Calladine, 1989). In the above, the constants E^* and ν are respectively the Young's modulus and Poisson's ratio of the material under consideration. The Young's modulus captures proportionality between the magnitude of applied stresses and the magnitude of the strains which they induce. The Poisson's ratio describes the extent to which extention of the material in one principal direction induces contraction in the other two directions. These measures of the material's deformability are related to the Lamé constants of (1.30) via

$$\lambda^* = \frac{\nu E^*}{(1+\nu)\,(1-2\nu)}, \qquad \mu^* = \frac{E^*}{2\,(1+\nu)}. \tag{1.45}$$

On dimensional grounds, we require $-1 < \nu \leq 0.5$; the lower bound being required to enforce convexity of the strain energy function, while the upper bound is approached in the limit of incompressibility (*i.e.* as $\lambda^* \to \infty$) (Howell *et al.*, 2009). For incompressible materials, $\nu = 0.5$ and the expression for λ^* in (1.45) breaks down. In problems regarding incompressible materials, we must be careful to ensure that the stress–strain relationship is regular in the limit $\nu \to 0.5$; we will return to this issue in chapter 5.

The Euler–Bernoulli relation has been widely deployed in previous models. A common problem is to consider the deformation of a beam under the action of tangential and normal forces (T_0^* and N_0^* respectively) applied at the boundaries. Performing a force-balance to determine M^* yields the following ODE for the angle of inclination of the beam, θ, as a function of arclength, s^*:

$$D^* \frac{\mathrm{d}^2\theta}{\mathrm{d}s^{*2}} = T_0^* \sin\theta - N_0^* \cos\theta, \tag{1.46}$$

(Howell *et al.*, 2009). Commonly used boundary conditions include imposing either clamping at the beam ends (for which θ vanishes) or simply supported ends which are stress free (*i.e.* the derivative of θ vanishes). Without loss of generality, we may assume $s^* = 0$ in the centre of the beam. For small displacements we may linearise (1.46) about the flat configuration. Taking one derivative of (1.46) yields the linear beam equation in terms of the out-of-plane displacement $u_3^*(x_1^*)$:

$$D^* \frac{\mathrm{d}^4 u_3^*}{\mathrm{d}x_1^{*4}} = T_0^* \frac{\mathrm{d}^2 u_3^*}{\mathrm{d}x_1^{*2}}, \tag{1.47}$$

where we have used the fact that for small deflections s^* is x_1^* to leading order. Many authors have deployed (1.46) or (1.47) in a wide variety of applications. Examples include vibration problems (Morgul (1992) and Diken (2000), for example) and studies

of fracture and mechanical failure (Caddemi & Caliò, 2008). Flaherty & Keller (1973) extended (1.46) to study contact problems in buckling beams. Euler–Bernoulli beam theory has also been applied to mechanobiology, including models of buckling epithelia (such as that of Edwards & Chapman (2007), which we discuss in more detail in section 1.7).

Von Kármán's equations

In this study, we will examine two broad approaches to deriving models of a deforming plate. The first of these is the direct use of the von Kármán equations[2], derived from the general theory of elasticity through application of the Kirchhoff assumptions described above. The derivation of von Kármán's equations assumes a neo-Hookean strain energy function; the material is assumed linearly elastic (*i.e.* there exists a linear relationship between stresses and strains, as in (1.38)); however, the theory is geometrically weakly nonlinear since strains are not assumed to be linearly related to displacement gradients (Stoker, 1942; Howell *et al.*, 2009).

Howell *et al.* (2009) present a derivation of von Kármán's equations under the assumption that the upper/lower surfaces of the plate remain stress-free throughout buckling. In terms of appropriately nondimensionalised variables, the resulting equations, in the absence of inertia and body forces, are

$$\nabla^4\Phi + \frac{1}{2}[w,w] = 0, \tag{1.48a}$$

$$\nabla^4 w = 12\left(1-\nu^2\right)[w,\Phi], \tag{1.48b}$$

for (dimensionless) out-of-plane displacement w and Airy stress function Φ, defined according to

$$\bar{T}_{11} = \frac{\partial^2\Phi}{\partial X_2^2}, \qquad \bar{T}_{22} = \frac{\partial^2\Phi}{\partial X_1^2}, \qquad \bar{T}_{12} = -\frac{\partial^2\Phi}{\partial X_1\partial X_2}, \tag{1.49}$$

chosen in such a manner to ensure that the conservation of momentum equations are satisfied automatically. In the above, $[f,g]$ represents the following commutator:

$$[f,g] = \frac{\partial^2 f}{\partial X_1^2}\frac{\partial^2 g}{\partial X_2^2} + \frac{\partial^2 f}{\partial X_2^2}\frac{\partial^2 g}{\partial X_1^2} - 2\frac{\partial^2 f}{\partial X_1\partial X_2}\frac{\partial^2 g}{\partial X_1\partial X_2}. \tag{1.50}$$

Of particular significance is the quantity $[w,w]/2$, which is the surface's *Gaussian curvature*, *i.e.* the product of the surface's two principal curvatures. A plate which is deformed without being stretched will always have zero Gaussian curvature, *i.e* one of its principal curvatures will be zero. Once bent in one direction, deformation of a plate

[2]Interchangeably termed the "Föppl–von-Kármán equations" in some literature.

in a second direction will be difficult since generating a non-zero Gaussian curvature requires that a certain stretching energy be overcome. Since this can be energetically expensive, the configuration will often stretch only in isolated regions; deformation of the rest of the structure is purely bending. In these regions form pointlike structures (termed *developable cones*) or ridges (Boudaoud *et al.*, 2000). A deformed surface is described as *developable* if it can be induced without the generation of in-plane strain (Howell *et al.*, 2009).

Von Kárman's equations have been deployed in a number of applications, including the buckling of swelling gels (Mora & Boudaoud, 2006) and viral shells (Lidmar *et al.*, 2003). Mansfield (1962) added terms proportional to an imposed temperature gradient to (1.48) for his analysis of the bending, buckling and curling of a heated thin plate.

In chapter 5, we present this derivation in more detail, incorporating material inhomogeneities and growth-induced stresses upon the surfaces.

Nonlinear elastic shell models

Many authors have formulated plate/shell buckling models by combining balances of forces and moments (which yield equilibrium equations) with geometric constraints and constitutive assumptions, relating bending moments to changes in curvature and stress resultants to material stretches, for example. Such an approach has the advantage that the rigorous (and often complex) analytical reduction of the full three-dimensional elasticity equations can be avoided. The fundamental challenge in this technique lies in selecting the appropriate constitutive assumptions, often from a choice of many. Preston *et al.* (2008) and Reboux *et al.* (2009) review a number of such assumptions in their studies of the buckling of compressed spherical vesicles (subcellular, fluid-filled capsules). The authors referenced below all adopted an alternative convention to (1.42) when defining bending moments, in which positive bending moments induce positive curvatures. We use calligraphic notation here to highlight that bending moments are defined differently to (1.42); assuming axisymmetry[3], meridional and azimuthal bending moments are denoted by $\mathscr{M}_\theta^*$ and $\mathscr{M}_\varphi^*$ respectively.

Let us consider, firstly, the manner in which the generation of bending moments induces a change in the curvature of the shell. In two-dimensional models, we have a choice of a number of constitutive assumptions with which we can replace (1.43). Evans & Skalak (1980) proposed a constitutive assumption in which the two bending

[3]Note that the assumption of axisymmetry implies that all twisting moments vanish.

moments are isotropic and proportional to the mean curvature, *i.e.*

$$\mathscr{M}_\theta^* = \mathscr{M}_\varphi^* = D^* \left(\kappa_\theta^* + \kappa_\varphi^*\right), \tag{1.51}$$

where subscripts denote quantities measured in the principal directions of a spherical polar coordinate system. The authors suggest that (1.51) is particularly appropriate when the layer exhibits a high resistance to change in area (Preston *et al.*, 2008). This constitutive assumption has since been deployed by authors including Pamplona & Calladine (1993), Parker & Winlove (1999), Preston *et al.* (2008) and Reboux *et al.* (2009). Alternatively, Pozrikidis (2003) suggested the following:

$$\mathscr{M}_\varphi^* = D^* \left(\kappa_\varphi^* - \tilde{\kappa}_\varphi^*\right), \qquad \mathscr{M}_\theta^* = D^* \left(\kappa_\theta^* - \tilde{\kappa}_\theta^*\right), \tag{1.52}$$

where tildes denote the principal curvatures of the reference configuration. Pozrikidis claims that (1.52) is valid for membranes comprised of thin elastic sheets whose thicknesses change on deformation.

We will commonly also require a constitutive relationship between principal stress resultants and principal stretches. Evans & Skalak (1980) deployed thermodynamic arguments to justify the following:

$$F_\varphi^* - F_\theta^* = H^* \left(\lambda_\varphi^2 - \lambda_\theta^2\right), \tag{1.53}$$

for stress resultants F_φ^* and F_θ^* and principal stretches λ_φ and λ_θ. The constant of proportionality, H^*, captures the resistance to changes in shape in the plane of of the membrane. Pamplona & Calladine (1993) and Parker & Winlove (1999) adopt a similar assumption of the form

$$F_\varphi^* - F_\theta^* = H^* \left(\lambda_\varphi - \lambda_\theta\right); \tag{1.54}$$

however, as discussed by Preston *et al.* (2008), for small deflections stretches are small and the differences between (1.53) and (1.54) are of little significance. The models of Pamplona *et al.* (2005), Preston *et al.* (2008) and Reboux *et al.* (2009) assume that the membrane is area-incompressible, writing the principal stretches as

$$\lambda_\varphi = \frac{1}{\lambda_\theta} = \frac{1}{\lambda}, \tag{1.55}$$

for some λ. Under this assumption it is convenient to write the stress resultants in terms of their isotropic counterpart, F^*. It follows from (1.54) that

$$F_\varphi^* = F^* + \frac{H^*}{\lambda}, \qquad F_\theta^* = F^* + H^* \lambda^*. \tag{1.56}$$

The constitutive assumptions above, termed by some authors the "first approximation" shell theory equations, assume no direct coupling between bending moments

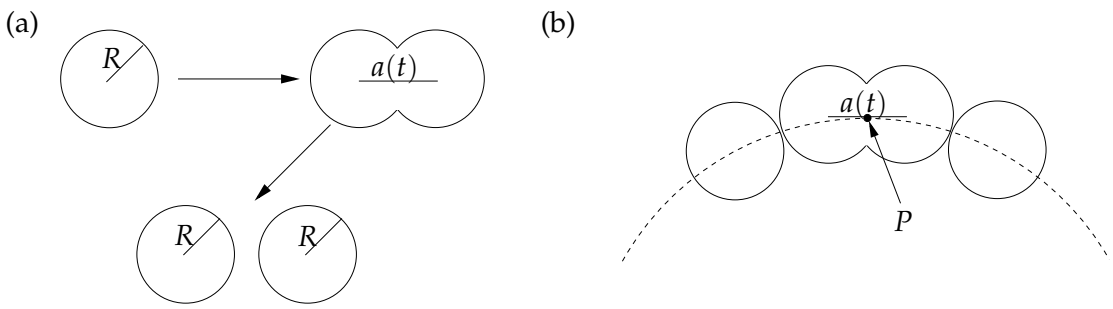

Figure 1.7: Schema of the cell division and placement algorithm used in Drasdo (2000). In (a) a spherical cell of radius R deforms into a dumbbell by progressively increasing the length of its axis, a, from $a = 0$ to $a = 2R$. Having enlarged into a dumbbell with radius $2R$ the cell divides, leaving behind two spherical daughter cells. In (b), the optimal orientation of a non-spherical cell is illustrated. The central cell attempts to align its axis with the tangent to the larger circle at the point P (representing the local tangent to the epithelial layer at P).

and stretching effects. The independence of these effects is appropriate for a shell with a flat reference state; however, these equations are commonly applied to the study of non-flat shells. Pamplona *et al.* (2005) suggest that (1.51) and (1.54) ought to contain additional terms which introduce such a coupling, accounting for the non-zero curvature of the reference state. Considering a spherical reference configuration, in which $\tilde{\kappa}^*_\varphi = \tilde{\kappa}^*_\theta = \kappa^*_0$, the authors propose the following in place of (1.51) and (1.54):

$$\mathscr{M}^*_\theta = \mathscr{M}^*_\varphi = D^* \left(\kappa^*_\theta + \kappa^*_\varphi - 2\kappa^*_0 \right) \equiv \mathscr{M}, \tag{1.57a}$$

$$F^*_\varphi - F^*_\theta = H^* \left(\lambda^{-1} - \lambda \right) + \mathscr{M} \left(\kappa^*_\theta - \kappa^*_\varphi \right). \tag{1.57b}$$

For a shell whose thickness is significantly smaller than its width, the contribution of these extra terms is negligible (Pamplona *et al.*, 2005). Reboux *et al.* (2009) showed that if resistance to bending is much smaller than resistance to in-plane shearing, the inclusion of these additional terms is insignificant to leading order.

It is noteworthy that the constitutive assumptions above are based around the assumption that the shell is linearly elastic. As such, we regard the applicability of any of these expressions to be questionable for the study of large strains (Parker & Winlove, 1999).

1.7 Epithelial buckling

We now review previous mathematical models of epithelial buckling, many of which have deployed the theories of elasticity and growth discussed above.

Drasdo (2000) considered a vertical cross-section of a colorectal crypt to investigate epithelial buckling. Individual cells were considered to be linked in a chain, held together by attractive forces between neighbouring cells. Each cell in the chain was modelled as spherical initially, deforming into a dumbbell shape upon mitosis. It was assumed that nonspherical cells look to attain their optimal orientation (which is favourable energetically), and that this corresponds to alignment of the cell axis with the local tangent to the epithelial layer (as illustrated in figure 1.7). Cells were allowed to grow and divide provided that this does not cause strong cellular deformations or compressions (*c.f.* contact inhibition). Thus, constant division and growth must be coupled to the migration of either individual cells or the entire layer. The author showed that the resulting geometry of the tissue is determined by the competition of destabilising cell growth and the stabilising bending energy of the tissue layer, which locally confines cell movements perpendicular to the layer. As the tissue grows above a certain size, the bending energy becomes too small to stabilise the local undulations occurring due to mitosis. If this occurs prior to the prevention of mitosis by the aforementioned rules, cell number increases exponentially. Such behaviour is dependent upon the cell cycle time being sufficiently large and the bending rigidity of the layer being specifically small. The ensuing buckling is reminiscent of a classical Euler buckling instability. In subsequent papers, this model was used to explore the dependence of crypt fission upon cell cycle time (Drasdo & Loeffler, 2001) and to examine cleavage, blastulation and gastrulation processes in the developing embryo (Drasdo & Forgacs, 2000; Drasdo & Loeffler, 2001).

Galle *et al.* (2005) presented a three-dimensional adaptation of the Drasdo (2000) model to assess the effect of variations in cell proliferation and apoptosis upon epithelial growth dynamics. The dependence of growth control mechanisms upon such cellular properties as cell–substrate adhesion and cell cycle time was examined. The specific mechanisms of focus were cell contact inhibition, substrate-contact-dependent cell-cycle arrest and programmed cell death upon removal of the cell from the substrate (anoikis). The authors concluded that, in the presence of a full complement of these growth-regulating mechanisms, a monolayer is yielded given that cell–cell anchorage is stronger than cell–substrate anchorage. In the absence of anoikis, however, the monolayer structure relies upon weak cell anchorage. If growth is independent of cell anchorage, it transpires that a mono-layer culture cannot be obtained. For arbitrary cell properties, it is shown that the absence of contact inhibition has a destabilising effect upon the monolayered cell structure.

Edwards & Chapman (2007) presented a biomechanical model for colorectal crypt budding and fission; processes commonly associated with the onset of colorectal cancer by

which deviations from the healthy crypt morphology occur. A two-dimensional, vertical cross-section of the intestinal epithelium was 'unfolded' and modelled as a beam connected to the underlying tissue by a series of springs. The authors considered the hypothesis that epithelial buckling is directly driven by the growth of the epithelium, and examined the consequences of a genetic mutation in the Wnt cascade which causes the cells at the base of the crypt to hyperproliferate or change their motility or adhesion properties. To incorporate the dynamic detachment and reattachment of cells as they migrate up the crypt wall, the springs were considered viscoelastic.

Buckling of the layer is governed by a nonlinear PDE system which is first-order in time and sixth-order in a space; however, analysis is restriced to the small deflection regime (for which the problem is linear). Growth is captured through the function $\gamma(x)$, where x is a spatial coordinate running along the layer. Specifically, the authors choose

$$\gamma(x) = e^{-\lambda_p x^6}, \tag{1.58}$$

which prescribes a proliferative compartment at the base of the crypt (or equivalently, the centre of the beam), the size of which is controlled by λ_p. For a healthy crypt, the authors set $\lambda_p = 65$, which yields a 60% proliferative region such as that found *in vivo* (Bach *et al.*, 2000). The model is also dependent on two further dimensionless parameters, namely λ_0 which captures the relative stiffnesses of beam and springs, and λ_T which captures the relative timescales of growth and viscous relaxation of spring stresses. To determine whether the crypt will deform after a genetic mutation, the authors examined whether the corresponding change in these three parameters destabilises the flat steady-state solution. This allowed a surface to be determined in $(\lambda_0, \lambda_T, \lambda_p)$-space, below which the healthy crypt geometry is maintained and above which buckling occurs.

The downstream effects of an activating mutation in the Wnt cascade are: increasing the size of the proliferative compartment (*i.e.* reducing λ_p), increasing the net proliferation rate (*i.e.* reducing λ_T), altering attachment properties between the epithelium and the lamina propria (λ_0) and stimulating changes of cell motility (λ_T). The authors claim that an increase in the net proliferation rate (corresponding to a decrease in λ_T) can initiate buckling independently of the other parameters, while enlargement of the proliferative compartment can only initiate buckling given a sufficiently large λ_0. The model presented here does not include any remodelling of the underlying tissue. In reality the buckling of the epithelium would cause a permenant deformation of the lamina propria. The study of budding and fission beyond their initiation requires the additional consideration of this interaction (Edwards & Chapman, 2007).

Jones & Chapman (2009) presented a model for epithelial buckling driven by *apical con-*

striction – a process through which a change in the shape of individual cells results in a change to the preferred curvature of the epithelium as a whole. Close to the apical surface of an epithelial cell lies a band of fibres termed the *apical bundle*. Fibres are oriented both across the cross section of the cell and circumferentially around the perimeter. In response to an activation in some genetic pathway, the apical bundle can contract leading to a reduction in the size of the apical surface. To preserve the cell's area, this contraction is accompanied by an expansion of the basal surface. Previous modelling of apical constriction by Odell *et al.* (1981) considered each cell as a series of viscoelastic struts, one of which (*i.e.* that in the region of the apical bundle) is allowed to contract. Other models have neglected the details of individual cells, modelling the epithelial layer as continuum materials. These models commonly exploit the thinness of the layer, characterising deformations as functions of the central surface. Jones & Chapman argue that such an approach forfeits the knowledge of elastic inhomogeneities across the thickness of the layer afforded by the apical bundle itself. They presented a model based upon shell theory in which the epithelium is viewed as a linearly elastic sheet with an embedded surface at a prescribed distance from the central plane, via which the forces exerted by contractions of the apical bundle are transmitted to the rest of the tissue. The governing equations are simplified significantly through focussing upon flat, cylindrical and spherical reference states. In the former case the model incorporates Föppl–von-Kármán plate theory. The authors presented numerical results for the prolonged buckling of the shell as the prescribed degree of apical constriction is increased.

Many authors have considered the manner in which buckling instabilities (and the resulting patterns) can be mediated by elastic, viscous or viscoelastic attachment to a neighbouring material. Pocivavsek *et al.* (2008) demonstrated that if a thin sheet is placed upon a liquid or gelatinous foundation, the primary buckling is of a sinusoidal nature; fold localisation only occurs under greater forcing. Sultan & Boudaoud (2008) considered a thin swelling gel attached to a compliant substrate modelled as a Winkler foundation (*i.e.* a network of elastic springs attached to a rigid layer at a finite distance below the gel). The presence of the foundation yields wrinkled configurations with wavelengths and amplitudes proportional to the gel thickness; observations which were in agreement with an analogous experimental setup. Consistent with Pocivavsek *et al.* (2008), configurations reminiscent of a 'single crypt' in models such as that of Edwards & Chapman (2007) were not observed in the presence of the foundation. Coman (2010) presents a multiscale analysis of a similar model, incorporating inhomogeneities in the stiffness of the foundation. Both linear and weakly nonlinear analyses are used to determine the primary buckling instability and configurations

of the post-buckling regime. These weakly nonlinear approximations are validated against numerical simulations of the full nonlinear model. Huang & Suo (2002) considered the temporal evolution of an initially wrinkled layer upon a viscous foundation, illustrating that wrinkling occurs as a balance between the driving force of stored elastic energy and the induction of viscous flow. For short-wavelength wrinkles, the elastic energy cost is too high and wrinkles decay. For long-wavelength initial conditions, effects of viscous flow are smaller and shape transitions occur only very slowly. Audoly & Boudaoud (2008) considered a similar two-dimensional analysis, deploying the Föppl–von Kármán equations to model a plate attached to an elastic substrate. The authors examined the resulting patterns, illustrating that the primary configuration is striped while in-plane compression is below a given threshold. Above this threshold, stripes are destabilised in favour of such patterns as checkerboards and hexagons.

1.8 Thesis overview

The remainder of this thesis is structured as follows. In chapter 2, we consider some extensions of the model presented by Edwards & Chapman (2007), discussed above. We shift the focus of the model's application from crypt budding and fission to crypt formation, examining perturbations to the initially flat epithelium as cellular growth generates compression. The model utilises the theories of sections 1.6.2 and 1.6.3, modelling the epithelium as a growing, incompressible beam which buckles under appropriate conditions. We extend Edwards and Chapman's analysis to incorporate nonlinearity, while the modelling of growth is developed through a deeper consideration of non-uniformity. We examine the degree to which patterning of growth or material properties affects the resulting configuration.

In chapter 3, we present an *in-vitro* study which assesses the validity of the proposed buckling mechanism. A population of intestinal epithelial cells is cultured to confluence upon a flexible substrate. Since the cells exhibit contact inhibition, continued proliferation requires that the substrate be deformed to increase the available surface area. The profile of the substrate is monitored over a number of days, allowing the force exerted by the cells to be inferred. Furthermore, we examine the manner in which the addition of a growth factor (which increases cell proliferation rate) can affect the configuration, and the extent to which this configuration is compromised upon lysis of the cells. In chapter 4, we present a mathematical model of this system. We model deflections of the substrate using the beam theory of section 1.6.3 and incorporate a simple model for the cell layer, regarding the cells as a series of identical springs. We deploy

a parametric model of growth, progressively increasing the unstressed lengths of the springs. As buckling is induced, we monitor the sequence of equilibrium configurations attained. We assess the role of cell–substrate adhesion in determining buckled shapes and examine the extent to which the substrate's compressibility causes results to differ from those of chapter 2.

In chapter 5, we derive a two-dimensional analogue of the cell–substrate model of chapter 4. Our model presents an extension to von Kármán plate theory (see section 1.6.3) which accounts for material inhomogeneities and distributions of surface stresses due to proliferating cell layers thereon. In chapter 5 we focus upon the homogeneous case, but move beyond planar geometries by examining axisymmetric deformations of a circular substrate. The model is then compared with that of Pamplona & Calladine (1993), the derivation of which combines a thin-shell balance-of-forces approach with selection of appropriate constitutive assumptions. We compare the results of the two models, both at the onset of buckling and at large amplitude. In chapter 6, we examine fully two-dimensional buckling modes for an inhomogeneous substrate. We examine the manner in which patterning of the substrate's material properties can be used to control the geometry of the deformed configuration.

In chapter 7, we summarise the conclusions of the above models and discuss directions for future investigations.

CHAPTER 2

In-vivo Buckling of a Developing Intestinal Epithelium

In this chapter, we introduce a model which considers the buckling of a one-dimensional cross-section of the developing intestinal epithelium. We consider the hypothesis that, during development, the growth of cells in the epithelium generates compressive stresses within the layer causing it to buckle. We consider that this buckling is a contributing mechanism in the formation of the crypts of Lieberkühn. We take as our theoretical starting point the model presented by Edwards & Chapman (2007) in which the epithelial layer is modelled as a beam attached to the underlying stroma by a series of springs.

We present two models in this chapter. In section 2.1, we begin by considering a simplified problem in which buckling is driven by a compressive force applied at the beam ends. Growth is omitted initially; however, in section 2.1.4 we adapt the model to include a parametric description of growth which describes the temporal evolution of the beam's configuration as a series of equilibrium configurations attained by beams of increasing length. In this initial model, we consider cellular attachments to behave as linear springs. In section 2.2 we further develop the model by adding a kinematic description of growth. We also capture the effects of cellular migration up the crypt wall by allowing the cellular attachments to exhibit viscous relaxation of stress. We examine the dependence of the buckled geometry upon spatial variations in the growth profile, focussing upon the comparison of uniform growth with regimes in which growth is restricted to a central portion of the beam (analogous to the proliferative compartment at the crypt base *in vivo*), stimulated by deep invagination (perhaps due to some underlying chemical signalling gradient) or restricted by high in-plane compression (*c.f.* contact inhibition). Finally, we examine the extent to which the shape and distribution

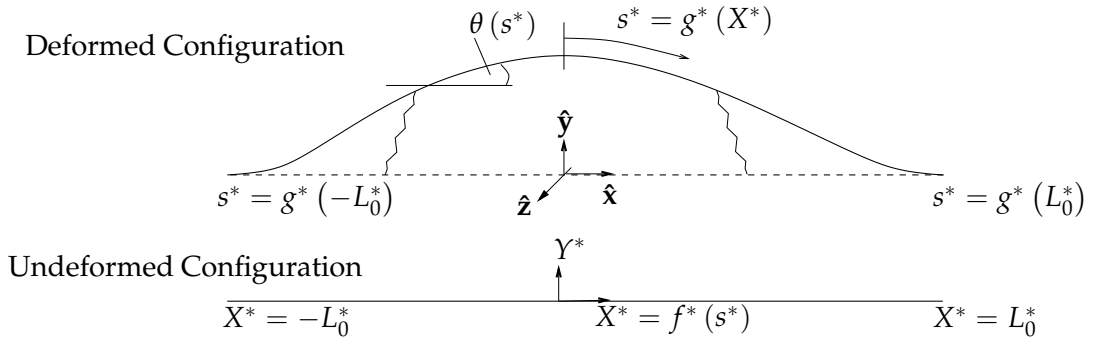

Figure 2.1: The geometry of the model of section 2.1.

of crypts are influenced by inhomogeneities in the tissue's growth or mechanical properties. Variations in mechanical properties are incorporated into the model by allowing the beam's bending stiffness to vary as a function of position.

2.1 Buckling due to imposed lateral compression

Prior to the introduction of epithelial growth, we consider a simpler problem in which buckling is driven by compressive forces applied at the ends of the beam.

2.1.1 Model derivation

We model the thin epithelial layer as a beam whose undeformed, unstressed configuration is flat and of length $2L_0^*$ (figure 2.1). The beam has thickness h^*, Young's modulus E^*, Poisson's ratio ν and bending stiffness $D^* = E^*h^{*3}/12(1-\nu^2)$. Assuming $h^* \ll L_0^*$, we characterise the profile of the beam by that of its centreline. We assume that cellular attachments to the underlying lamina propria behave as springs with stiffness parameter k^* (with dimensions of force/length^4).

We characterise the profile of the beam when deformed using coordinates s^* and $\theta(s^*)$, which are the arc-length from the centre of the beam and the local angle of inclination of the beam's centreline to the horizontal respectively. Cartesian coordinates in the reference and physical frames are denoted X^*, Y^* and x^*, y^* respectively, as illustrated in figure 2.1. In the reference frame the beam is flat and we regard X^* as a measure of arc-length. We define the mappings $g^* : X^* \mapsto s^*$ and $f^* : s^* \mapsto X^*$ between the arc-length coordinates in the two configurations.

We assume that the Euler–Bernoulli relation holds, so that the beam's curvature, κ^*, is

proportional to the bending moment, M^*,

$$\kappa^* = \frac{\mathrm{d}\theta}{\mathrm{d}s^*} = -\frac{M^*}{D^*}. \tag{2.1}$$

We relate $M^*(s^*)$ to beam stress resultants and spring stresses via consideration of the forces acting upon a small beam element of arc-length $\mathrm{d}s^*$, as illustrated in figure 2.2. We begin by defining Cartesian unit vectors $\hat{\mathbf{x}}$, $\hat{\mathbf{y}}$ and $\hat{\mathbf{z}}$, together with the vectors $\hat{\mathbf{n}}$ normal to the beam and $\hat{\mathbf{t}}$ tangential to the beam. In terms of the Cartesian vectors, $\hat{\mathbf{n}}$ and $\hat{\mathbf{t}}$ are given explicitly by

$$\hat{\mathbf{n}} = -\sin\theta\hat{\mathbf{x}} + \cos\theta\hat{\mathbf{y}}, \tag{2.2a}$$

$$\hat{\mathbf{t}} = \cos\theta\hat{\mathbf{x}} + \sin\theta\hat{\mathbf{y}}. \tag{2.2b}$$

Conversely, we have

$$\hat{\mathbf{x}} = \cos\theta\hat{\mathbf{t}} - \sin\theta\hat{\mathbf{n}}, \tag{2.3a}$$

$$\hat{\mathbf{y}} = \sin\theta\hat{\mathbf{t}} + \cos\theta\hat{\mathbf{n}}. \tag{2.3b}$$

It follows from (2.2) that

$$\frac{\mathrm{d}\hat{\mathbf{t}}}{\mathrm{d}s^*} = \frac{\mathrm{d}\theta}{\mathrm{d}s^*}\frac{\mathrm{d}\hat{\mathbf{t}}}{\mathrm{d}\theta} = \kappa^*\hat{\mathbf{n}}, \tag{2.4a}$$

$$\frac{\mathrm{d}\hat{\mathbf{n}}}{\mathrm{d}s^*} = \frac{\mathrm{d}\theta}{\mathrm{d}s^*}\frac{\mathrm{d}\hat{\mathbf{n}}}{\mathrm{d}\theta} = -\kappa^*\hat{\mathbf{t}}. \tag{2.4b}$$

We formulate equilibrium equations via consideration of the moments and forces acting tangentially and normally to the beam. We denote the in-plane and out-of-plane stress resultants per unit length by $F_T^*(s^*)$ and $F_N^*(s^*)$ respectively. The bending moment, $M^*(s^*)$, acts in a right-handed sense about the $\hat{\mathbf{z}}$ axis.

Noting (2.4), we can express the net force per unit length acting on the beam element due to variations in F_T^* as follows:

$$\begin{aligned}\left(F_T^*\hat{\mathbf{t}}\right)\Big|_{s^*+\mathrm{d}s^*} - \left(F_T^*\hat{\mathbf{t}}\right)\Big|_{s^*} &= \mathrm{d}s^* \cdot \frac{\mathrm{d}}{\mathrm{d}s^*}\left(F_T^*\hat{\mathbf{t}}\right) + O\left(\mathrm{d}s^{*2}\right) \\ &= \mathrm{d}s^*\left(\frac{\mathrm{d}F_T^*}{\mathrm{d}s^*}\hat{\mathbf{t}} + F_T^*\kappa^*\hat{\mathbf{n}}\right) + O\left(\mathrm{d}s^{*2}\right).\end{aligned} \tag{2.5}$$

Similarly, the net force per unit length due to variations in F_N^* is

$$\begin{aligned}\left(F_N^*\hat{\mathbf{n}}\right)\Big|_{s^*+\mathrm{d}s^*} - \left(F_N^*\hat{\mathbf{n}}\right)\Big|_{s^*} &= \mathrm{d}s^* \cdot \frac{\mathrm{d}}{\mathrm{d}s^*}\left(F_N^*\hat{\mathbf{n}}\right) + O\left(\mathrm{d}s^{*2}\right), \\ &= \mathrm{d}s^*\left(\frac{\mathrm{d}F_N^*}{\mathrm{d}s^*}\hat{\mathbf{n}} - F_N^*\kappa^*\hat{\mathbf{t}}\right) + O\left(\mathrm{d}s^{*2}\right).\end{aligned} \tag{2.6}$$

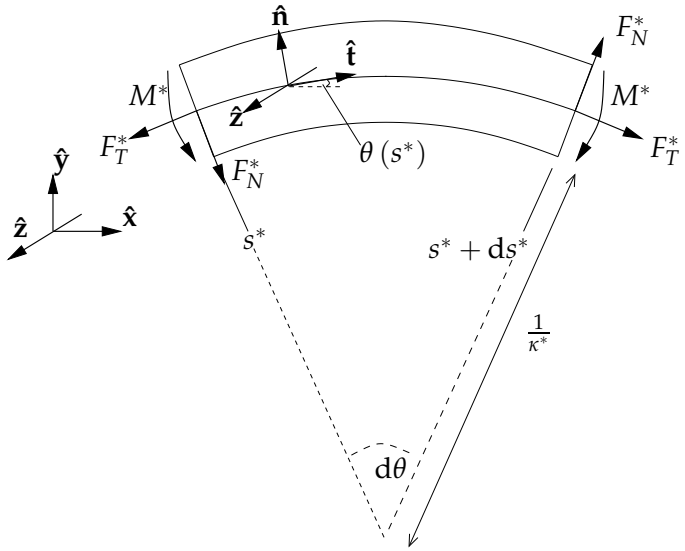

Figure 2.2: Forces and moments on a line element of length $\mathrm{d}s^*$ and curvature $\kappa^* < 0$. Clockwise arrows indicate bending moments acting the negative $\hat{\mathbf{z}}$-direction.

We also have an additional force per unit length appearing due to the cellular attachments which connect the beam to the underlying layer:

$$-T_N^* \mathrm{d}s^* \hat{\mathbf{n}} - T_T^* \mathrm{d}s^* \hat{\mathbf{t}}, \tag{2.7}$$

where $T_N^*(s^*)$ and $T_T^*(s^*)$ denote the normal and tangential components of spring stress per unit length respectively. Setting the sum of (2.5–2.7) to zero, we obtain

$$\frac{\mathrm{d}F_T^*}{\mathrm{d}s^*} - F_N^* \kappa^* - T_T^* = 0, \tag{2.8a}$$

$$\frac{\mathrm{d}F_N^*}{\mathrm{d}s^*} + F_T^* \kappa^* - T_N^* = 0. \tag{2.8b}$$

We now relate the net bending moment acting upon the line element to the normal component of force, as follows:

$$(M^* \hat{\mathbf{z}})\Big|_{s^* + \mathrm{d}s^*} - (M^* \hat{\mathbf{z}})\Big|_{s^*} = F_N \mathrm{d}s^* \hat{\mathbf{z}}. \tag{2.9}$$

Taylor expanding, and truncating at $O(\mathrm{d}s^*)$, we obtain

$$\frac{\mathrm{d}M^*}{\mathrm{d}s^*} = F_N^*. \tag{2.10}$$

For consistency of notation with the linear analysis presented by Edwards & Chapman (2007), we now resolve the forces into horizontal and vertical components, $F_x^*(s^*)$ and $F_y^*(s^*)$ respectively. It follows from (2.3) that

$$F_T^* = F_x^* \cos\theta + F_y^* \sin\theta, \tag{2.11a}$$

$$F_N^* = F_y^* \cos\theta - F_x^* \sin\theta, \tag{2.11b}$$

with similar expressions holding for the spring stress components. Substituting (2.11b) into (2.1) and (2.10) we obtain the dimensional beam equation

$$\frac{\mathrm{d}^2\theta}{\mathrm{d}s^{*2}} + \frac{1}{D^*}\left(F_y^* \cos\theta - F_x^* \sin\theta\right) = 0, \tag{2.12}$$

while from (2.8) we obtain

$$\frac{\mathrm{d}F_x^*}{\mathrm{d}s^*}\cos\theta + \frac{\mathrm{d}F_y^*}{\mathrm{d}s^*}\sin\theta - T_x^*\cos\theta - T_y^*\sin\theta = 0, \tag{2.13a}$$

$$\frac{\mathrm{d}F_y^*}{\mathrm{d}s^*}\cos\theta - \frac{\mathrm{d}F_x^*}{\mathrm{d}s^*}\sin\theta - T_y^*\cos\theta + T_x^*\sin\theta = 0. \tag{2.13b}$$

Since (2.13) holds for any θ, we can equate coefficients of $\sin\theta$ and $\cos\theta$ to zero, yielding

$$\frac{\mathrm{d}F_x^*}{\mathrm{d}s^*} = T_x^*, \qquad \frac{\mathrm{d}F_y^*}{\mathrm{d}s^*} = T_y^*. \tag{2.14}$$

Following Edwards & Chapman (2007), we assume that cellular attachments to the lamina propria behave as linear springs anchoring each material point to its location in the undeformed configuration. We note that the x^* and y^* coordinates of a material point can be found through the relations

$$\frac{\mathrm{d}x^*}{\mathrm{d}s^*} = \cos\theta, \qquad x^*(g^*(0)) = 0, \tag{2.15a}$$

$$\frac{\mathrm{d}y^*}{\mathrm{d}s^*} = \sin\theta, \qquad y^*(g^*(-L_0^*)) = 0, \tag{2.15b}$$

where the boundary conditions follow from assuming symmetry in x^* and clamping of the beam ends respectively. It is, hence, appropriate to define the spring tensions $T_{x,y}^*$ according to

$$T_x^* = k^*\left(\int_{g^*(0)}^{s^*} \cos\theta \mathrm{d}s^* - f^*(s^*)\right), \tag{2.16a}$$

$$T_y^* = k^*\int_{g^*\left(-L_0^*\right)}^{s^*} \sin\theta \mathrm{d}s^*, \tag{2.16b}$$

where the right-hand sides of (2.16) are the spring constant k^* multiplied by the horizontal and vertical deflections of the material point whose original location was $(f^*(s^*), 0)$.

It remains to determine the mapping $f^*(s^*)$ (and hence $g^*(X^*)$). We make the constitutive assumption that the in-plane component of force is proportional to the stretch of the element. It follows that

$$\int_{s^*}^{s^*+\mathrm{d}s^*} F_T^*(\bar{s}^*)\mathrm{d}\bar{s}^* = \beta_1^*\left([(s^*+\mathrm{d}s^*) - s^*] - [(f^*(s^*+\mathrm{d}s^*) - f^*(s^*)]\right). \tag{2.17}$$

In the limit $\mathrm{d}s^* \to 0$, we obtain the following expression for $f^*(s^*)$:

$$F_x^* \cos\theta(s^*) + F_y^* \sin\theta(s^*) = \beta_1^* \left(1 - \frac{\mathrm{d}f^*}{\mathrm{d}s^*}\right). \tag{2.18}$$

By definition, the Young's modulus E^* is the constant of proportionality between stress and strain of a material. However, since our model is formulated in terms of quantities averaged across the thickness of the beam, we have $\beta_1^* = E^* h^*$.

We consider that the beam is subject to a compressive, horizontal force of magnitude F_0^* applied at the beam ends. As such, the seventh order ODE system given by (2.12), (2.14–2.16) and (2.18) is solved subject to 'clamped' boundary conditions, given by

$$F_x^* = -F_0^*, \quad \frac{\mathrm{d}F_y^*}{\mathrm{d}s^*} = 0, \quad \theta = 0 \quad \text{at } f^*(s^*) = \pm L_0^*, \tag{2.19}$$

together with the symmetry condition $f^*(0) = 0$. In (2.19) the boundary condition on F_y^* enforces zero vertical displacement at the beam ends (as is evident from substitution of (2.16b) and (2.15b) into (2.14b)).

We nondimensionalise this system via the following scalings:

$$\{s^*, X^*, Y^*, f^*, g^*\} = L_0^* \{s, X, Y, f, g\}, \tag{2.20a}$$

$$\left\{F_x^*, F_y^*, F_0^*\right\} = k^* L_0^{*2} \left\{F_x, F_y, F_0\right\}, \tag{2.20b}$$

$$\left\{T_x^*, T_y^*\right\} = k^* L_0^* \left\{T_x, T_y\right\}. \tag{2.20c}$$

We now consider s in the range $[g(-L_0), g(L_0)]$, and we recover the dimensionless system of governing equations presented in Edwards & Chapman (2007),

$$\frac{\mathrm{d}^2\theta}{\mathrm{d}s^2} + \beta_0 \left(F_y \cos\theta - F_x \sin\theta\right) = 0, \tag{2.21a}$$

$$\frac{\mathrm{d}^2 F_x}{\mathrm{d}s^2} = \cos\theta - \frac{\mathrm{d}f}{\mathrm{d}s}, \tag{2.21b}$$

$$\frac{\mathrm{d}^2 F_y}{\mathrm{d}s^2} = \sin\theta, \tag{2.21c}$$

$$F_x \cos\theta + F_y \sin\theta = \beta_1 \left(1 - \frac{\mathrm{d}f}{\mathrm{d}s}\right), \tag{2.21d}$$

which is dependent upon two dimensionless parameters: $\beta_0 = k^* L_0^{*4}/D^*$, which characterises the force required to extend the springs relative to the force required to bend the beam, and $\beta_1 = E^* h^*/k^* L_0^{*2}$ which captures the resistance to extension of the beam relative to that of the springs. The model is solved subject to dimensionless boundary conditions given by

$$F_x = -F_0, \quad \frac{\mathrm{d}F_y}{\mathrm{d}s} = 0, \quad \theta = 0 \quad \text{at } f(s) = \pm 1, \tag{2.22}$$

together with $f(0) = 0$.

For the remainder of this section we assume that the beam is approximately incompressible. In this limit $\beta_1 \gg 1$ and dependent variables can be expanded in powers of β_1^{-1}. To leading order, $f(s) = s$ and the boundaries are fixed at $s = \pm 1$. Setting $f(s) = s + \beta_1^{-1}\hat{f}(s)$, the local stretch can be computed as

$$-\frac{\mathrm{d}\hat{f}}{\mathrm{d}s} = F_x \cos\theta + F_y \sin\theta, \tag{2.23}$$

with $\hat{f}(0) = 0$. For an incompressible beam, the leading-order problem is given by

$$\frac{\mathrm{d}^2\theta}{\mathrm{d}s^2} + \beta_0 \left(F_y \cos\theta - F_x \sin\theta\right) = 0, \tag{2.24a}$$

$$\frac{\mathrm{d}^2 F_x}{\mathrm{d}s^2} = \cos\theta - 1, \tag{2.24b}$$

$$\frac{\mathrm{d}^2 F_y}{\mathrm{d}s^2} = \sin\theta, \tag{2.24c}$$

subject to

$$F_x = -F_0, \quad \frac{\mathrm{d}F_y}{\mathrm{d}s} = 0, \quad \theta = 0 \quad \text{at } s = \pm 1. \tag{2.25}$$

We show in appendix A.1.1 that, under the assumption of incompressibility, the corresponding energy of equilibrium states is given by

$$\mathcal{E} = \frac{1}{2}\int_{-1}^{1} \left(\frac{\mathrm{d}F_x}{\mathrm{d}s}\right)^2 + \left(\frac{\mathrm{d}F_y}{\mathrm{d}s}\right)^2 + \frac{1}{\beta_0}\left(\frac{\mathrm{d}\theta}{\mathrm{d}s}\right)^2 + F_0\frac{\mathrm{d}x}{\mathrm{d}s}\mathrm{d}s, \tag{2.26}$$

which incorporates contributions from stretching of the springs, bending of the beam and work done at the boundaries respectively.

Assuming incompressibility, the behaviour of this system is characterised by the two dimensionless parameters β_0 and F_0. Since insufficient data is available to determine parameter values *in vivo*, we present analytical and numerical solutions for a range of parameter values below. We classify a solution of (2.24–2.25) as 'type n' if it exhibits n local extrema in the region $s \in (-1, 1)$. Since the model exhibits a symmetry under the transformation $\theta \mapsto -\theta$ (under which we also have $F_x \mapsto F_x$ and $F_y \mapsto -F_y$), we can further subcategorise type n solutions as either type n^+ or type n^-, where the superscript reflects the sign of θ close to the left hand boundary. For n odd we obtain a solution even in x, while for n even we obtain a solution odd in x. For later bifurcation analysis, we define the output variables X_0 and Y_0 to be the horizontal distance between the beam endpoints and the amplitude of the first peak/trough respectively, as illustrated in figure 2.3.

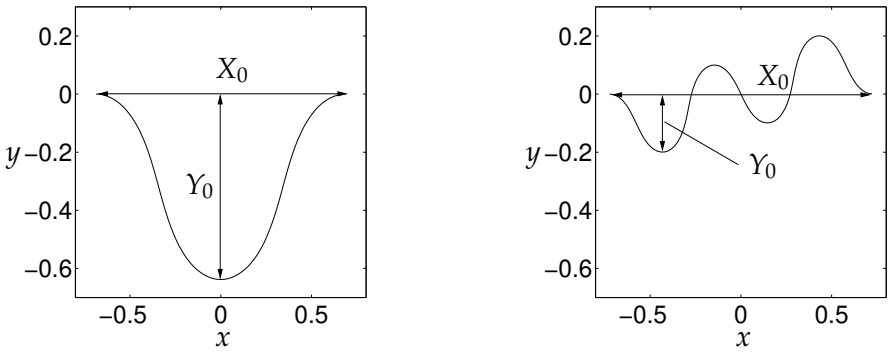

(a) Type 1^-

(b) Type 4^-

Figure 2.3: Features tracked during bifurcation analysis: solution amplitude, Y_0, and width, X_0.

2.1.2 Analysis of the linearised problem

We now consider (2.24–2.25) in the small deflection limit, rescaling according to $\theta = \varepsilon\bar{\theta}$ and $F_y = \varepsilon\bar{F}_y$, for $0 < \varepsilon \ll 1$. To leading order in ε, the linearisation of (2.24) gives

$$\frac{\mathrm{d}^2\bar{\theta}}{\mathrm{d}s^2} + \beta_0\left(\bar{F}_y - \bar{\theta}F_x\right) = 0, \tag{2.27a}$$

$$\frac{\mathrm{d}^2F_x}{\mathrm{d}s^2} = 0, \tag{2.27b}$$

$$\frac{\mathrm{d}^2\bar{F}_y}{\mathrm{d}s^2} = \bar{\theta}. \tag{2.27c}$$

It follows from (2.27b) and (2.25a) that $F_x = -F_0$ to leading order. The linearisation of the remaining boundary conditions gives

$$\bar{\theta} = 0, \qquad \frac{\mathrm{d}\bar{F}_y}{\mathrm{d}s} = 0 \qquad \text{at } s = \pm 1. \tag{2.28}$$

For convenience we re-express (2.27–2.28) in terms of $y(x)$. Since deflections are small it is appropriate to rescale $y = \varepsilon\bar{y}$. From (2.15) we have that $s = x$ and $\bar{\theta} = \mathrm{d}\bar{y}/\mathrm{d}x$ to leading order. Noting that $F_x = -F_0$, we differentiate (2.27a) to obtain

$$\frac{\mathrm{d}^4\bar{y}}{\mathrm{d}x^4} + \beta_0\left(\frac{\mathrm{d}^2\bar{F}_y}{\mathrm{d}x^2} + F_0\frac{\mathrm{d}^2\bar{y}}{\mathrm{d}x^2}\right) = 0, \tag{2.29}$$

into which we substitute (2.27c), yielding

$$\frac{\mathrm{d}^4\bar{y}}{\mathrm{d}x^4} + \beta_0F_0\frac{\mathrm{d}^2\bar{y}}{\mathrm{d}x^2} + \beta_0\bar{y} = 0. \tag{2.30}$$

We solve (2.30) subject to the following boundary conditions, analogous to (2.28):

$$\bar{y} = \frac{\mathrm{d}\bar{y}}{\mathrm{d}x} = 0 \quad \text{at } x = \pm 1. \tag{2.31}$$

Solutions to (2.30) are of the form

$$\bar{y}(x) = \sum_{i=1}^{4} A_i e^{m_i x}, \tag{2.32}$$

where the m_i are the four solutions of the quartic equation

$$m^4 + \beta_0 F_0 m^2 + \beta_0 = 0, \tag{2.33}$$

and the A_i are consants of integration which satisfy

$$\begin{bmatrix} e^{m_1} & e^{m_2} & e^{m_3} & e^{m_4} \\ e^{-m_1} & e^{-m_2} & e^{-m_3} & e^{-m_4} \\ m_1 e^{m_1} & m_2 e^{m_2} & m_3 e^{m_3} & m_4 e^{m_4} \\ m_1 e^{-m_1} & m_2 e^{-m_2} & m_3 e^{-m_3} & m_4 e^{-m_4} \end{bmatrix} \begin{bmatrix} A_1 \\ A_2 \\ A_3 \\ A_4 \end{bmatrix} = 0. \tag{2.34}$$

For the remainder of this section the bars upon rescaled variables are omitted. We obtain a non-flat solution of (2.30–2.31) for those values of β_0 and F_0 which result in the matrix in (2.34) having zero determinant. It follows from the linearisation of (2.26) that $\mathcal{E} = F_0 + O\left(\varepsilon^2\right)$ and, for a given β_0, the solution which corresponds to the smallest value of F_0 is energetically favourable. The first three neutral curves are plotted in figure 2.4, alongside the corresponding type 1^-, type 2^- and type 3^- eigenfunctions. Illustrations of the type n^+ solutions are omitted here for brevity. For sufficiently small β_0 the neutral curves are well-ordered. We thus label the neutral curves according to their ordering in the small β_0 limit; labelling the curve with lowest F_0 as 1, *etc.* We define the terminology 'mode n' to describe an eigenmode pertaining to the n^{th} neutral curve. Examination of the eigenmodes reveals that a 'mode n' solution is also of 'type n' for sufficiently small β_0. The ordering of the neutral curves is preserved until β_0 is increased to approximately 55, at which point the lowest two neutral curves cross and type 2 buckling becomes energetically favourable.

For $\beta_0 \ll 1$ the beam bending stiffness dominates the stiffness of the springs and buckling becomes independent of cellular attachment. In this limit, the problem reduces to that of a classical Euler strut. The wavelength of the buckled profile is controlled entirely by external forcing, and we expect the dominant terms in (2.30) to exhibit no explicit dependence on k^*, *i.e.* we expect (2.30) to become independent of β_0. The dominant balance of terms in (2.30) suggests that $F_0 \sim 1/\beta_0$ as $\beta_0 \to 0$, and it is hence convenient for the analysis of this limit to denote the product $\beta_0 F_0 = K^2$, where $K^2 = O(1)$,

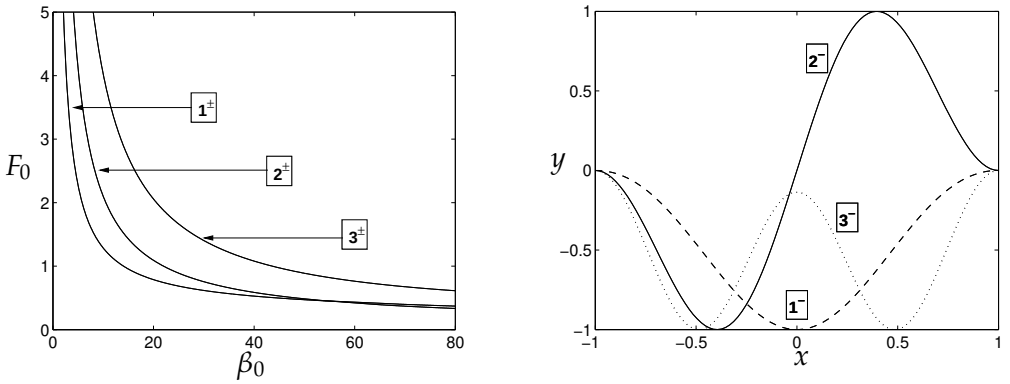

(a) (b)

Figure 2.4: In (a), the first three neutral curves of the linearised system given by (2.30–2.31) are shown, illustrating the force (F_0) required to yield buckling instabilities to modes 1, 2 and 3 as a function of material parameters (β_0). The eigenmodes corresponding to these neutral curves are shown in (b) for $\beta_0 = 20$.

yielding:

$$\frac{\mathrm{d}^4 y}{\mathrm{d}x^4} + K^2 \frac{\mathrm{d}^2 y}{\mathrm{d}x^2} = 0. \tag{2.35}$$

Solution of (2.35) subject to (2.31) yields the following expression for $y(x)$:

$$y(x) = \begin{cases} C_n \left(-\cos K_n + \cos(K_n x)\right) & \text{for profiles of type } (2n-1), \\ C_n \left(-x \sin(K_n) + \sin(K_n x)\right) & \text{for profiles of type } 2n, \end{cases} \tag{2.36}$$

where the C_n are arbitrary constants, $K_n = n\pi$ for odd-type profiles, and K_n is the n^{th} positive root of $K = \tan(K)$ for even-type profiles. For small β_0, the neutral curves are precisely

$$F_0 = \frac{K_n^2}{\beta_0}, \qquad n = 1, 2, 3, \ldots \tag{2.37}$$

For $\beta_0 \gg 1$ (*i.e.* for a long domain, for example) local buckling becomes independent of the force exerted at the boundaries. Wavelength is instead controlled entirely by the springs. In this limit, we expect $F_0 \sim 1/\beta_0^{1/2}$ so that dimensional force scales as $(D^*_{\max} k^*)^{1/2}$, which is independent of L_0^*. We examine the behaviour in the regime of large β_0 via a WKBJ analysis. We adopt notation consistent with that of Edwards & Chapman, rewriting (2.30) as

$$\frac{\mathrm{d}^4 y}{\mathrm{d}x^4} + \alpha k^2 \frac{\mathrm{d}^2 y}{\mathrm{d}x^2} + k^4 y = 0, \tag{2.38}$$

where $\alpha k^2 = \beta_0 F_0$, $k^4 = \beta_0$ and $k \gg 1$. We seek a solution to (2.38) of the form

$$y = e^{k\Phi(x)}, \tag{2.39}$$

where

$$\Phi(x) = \varphi_0(x) + \frac{1}{k}\varphi_1(x) + \frac{1}{k^2}\varphi_2(x) + \ldots, \tag{2.40}$$

and the φ_i are all $O(1)$. We also adopt a similar expansion for α. Considering terms of $O(k^4)$ in (2.38), we find that

$$\varphi_0'^4 + \alpha_0\varphi_0'^2 + 1 = 0, \tag{2.41}$$

and hence

$$\varphi_0 = \pm\sqrt{\frac{-\alpha_0 \pm \sqrt{\alpha_0^2 - 4}}{2}}x + C_0, \tag{2.42}$$

for arbitrary constant C_0. Considering terms of $O(k^3)$, and noting that $\varphi_0'' = 0$, we have

$$\varphi_1'\left(\pm\sqrt{\alpha_0^2 - 4}\right) + \alpha_1\varphi_0'^2 = 0. \tag{2.43}$$

For non-trivial solutions which satisfy (2.31), (2.43) requires that $\alpha_0 = 2$ and $\alpha_1 = 0$. From (2.42) we, therefore, have

$$\varphi_0 = \pm ix + C_0. \tag{2.44}$$

At $O(k^2)$ we obtain

$$\frac{\mathrm{d}^2\varphi_1}{\mathrm{d}x^2} + \left(\frac{\mathrm{d}\varphi_1}{\mathrm{d}x}\right)^2 + \frac{\alpha_2}{4} = 0. \tag{2.45}$$

We solve (2.45) via the transformation $\bar{\varphi}_1 = \exp(\varphi_1)$, to yield the solution

$$\bar{\varphi}_1(x) = A\sin\left(\sqrt{\frac{\alpha_2}{4}}x\right) + B\cos\left(\sqrt{\frac{\alpha_2}{4}}x\right), \tag{2.46}$$

for arbitrary constants of integration A and B. Noting our original WKBJ ansatz, the solution for $y(x)$ is

$$\begin{aligned} y(x) &= \bar{\varphi}_1(x)e^{\pm ikx}, \\ &= \left(A\sin\left(\sqrt{\frac{\alpha_2}{4}}x\right) + B\cos\left(\sqrt{\frac{\alpha_2}{4}}x\right)\right)e^{\pm ikx}, \end{aligned} \tag{2.47}$$

where C_0 has been absorbed into A and B. For (2.47) to satisfy the boundary conditions we must have either $A = 0$ and $\alpha_2 = (2n-1)^2\pi^2$, or $B = 0$ and $\alpha_2 = 4n^2\pi^2$ (for some $n \in \mathbb{N}$). The resulting expression for $y(x)$, having taken real parts, is hence

$$y(x) = \begin{cases} \left(\Re(A_n)\cos\left(\beta_0^{1/4}x\right) - \Im(A_n)\sin\left(\beta_0^{1/4}x\right)\right)\sin\left(n\pi x\right), \\ \left(\Re(B_n)\cos\left(\beta_0^{1/4}x\right) - \Im(B_n)\sin\left(\beta_0^{1/4}x\right)\right)\cos\left(\frac{(2n-1)\pi x}{2}\right), \end{cases} \tag{2.48}$$

while the neutral curves converge toward

$$F_0 = \frac{2}{\sqrt{\beta_0}} + \frac{n^2\pi^2}{\beta_0}, \tag{2.49}$$

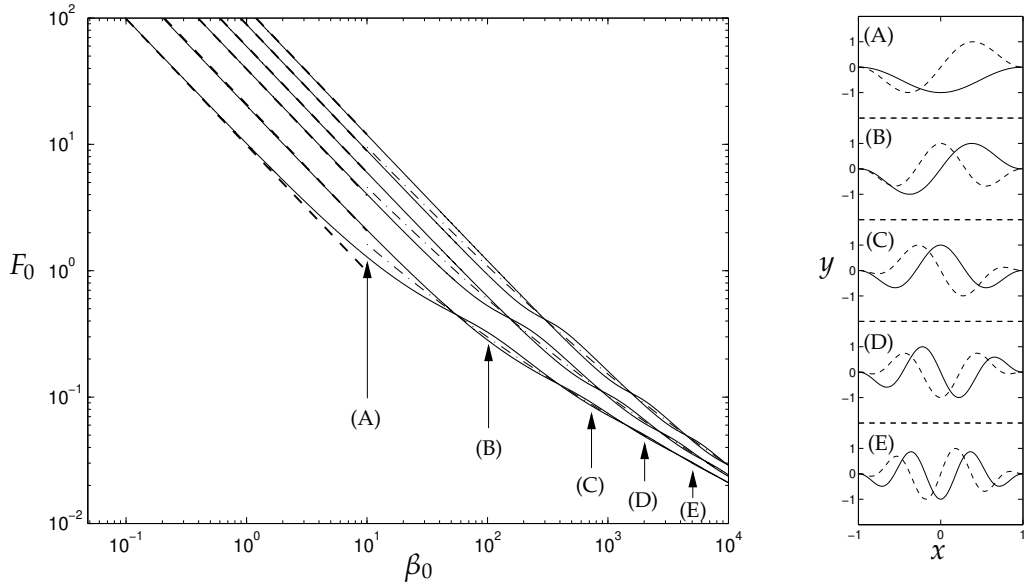

Figure 2.5: (a) The first six neutral curves, pertaining to the lateral compression problem of section 2.1. Dashed lines illustrate the asymptotic limit for $\beta_0 \ll 1$ (2.37), while dash-dotted lines illustrate the asymptotic limits for large β_0 (2.49). (b) The buckling types associated with the lowest eigenmode (solid line) and second eigenmode (dashed line), illustrated at $\beta_0 = 10$ (A), $\beta_0 = 100$ (B), $\beta_0 = 700$ (C), $\beta_0 = 2000$ (D) and $\beta_0 = 5000$ (E).

for some $n \in \mathbb{N}$. The neutral curves are plotted over a large range of β_0 in figure 2.5. Inspection of the eigenmodes reveals that as β_0 increases a series of symmetry-preserving type-transitions occurs. The first eigenmode, for example, is of type 1 for small β_0. As β_0 increases this mode becomes type 3, followed by type 5 *etc.* Similarly the second mode changes from type 2 to type 4, *etc.* These transitions of type correspond exactly to the crossing of the neutral curves illustrated in figure 2.5; as the mode 1 solution becomes type 3, it becomes more energetically expensive than the type 2 solution on the second neutral curve, and the curves cross. This type 2 solution remains energetically favourable until a transition to type 4 occurs, at which point the neutral curves cross again and type 3 configurations become energetically favoured. Thus, the most energetically favourable buckling type changes progressively from type 1, to type 2, to type 3 *etc.* as β_0 is increased. For sufficiently large β_0 a type 1 profile is no longer obtainable and buckling yields a highly wrinkled configuration.

2.1.3 Large-amplitude buckling

We seek solutions of (2.24–2.25) using the MATLAB boundary value solver 'bvp4c', which implements a collocation method to obtain a fourth-order accurate solution, as detailed in Kierzenka & Shampine (2001). In those regions of parameter space which facilitate buckled profiles of multiple types, we control configuration selection by starting the collocation with a functional form close to the desired profile. Numerical results are validated primarily via comparison with the previous linear analysis, ensuring that bifurcations from the flat state occur only for choices of β_0 and F_0 lying on the neutral curves of figure 2.5. While mesh-refinement tests are not directly appropriate since the solver automatically refines the mesh until a default tolerance is met, we ensure that numerical solutions are accurate through monitoring of the residual errors reported by the solver. Should the solver report errors deemed too large (relative to a pre-defined threshold), the algorithm is restarted with more rigorous bounds placed upon the minimum number of mesh points used. As a confirmation of the algorithm's stability, we ensure that a smooth transition of solutions occurs as we traverse parameter-space. Finally, numerical results are validated through examination of the physical quantities associated with each configuration, as discussed below.

The type 1^- solutions obtained upon fixing $\beta_0 = 10$ and varying F_0 are illustrated in figure 2.6. We observe that as F_0 is increased from zero, initially the layer resists buckling and remains in its flat configuration. When F_0 is increased to some critical value, F_0^{B1}, the layer exhibits type 1 buckling. The forces required for the onset of buckling agree with those predicted by the linear analysis above; for $\beta_0 = 10$ (as in figure 2.6), $F_0^{B1} \simeq 1.3$. Since we assume incompressibility, the length of the beam is unchanged to leading order in β_1^{-1}. Further increasing of F_0 results in the continued development of this type 1 profile, as illustrated, until contact occurs between two distinct points of the beam at $F_0 = F_0^{C1}$. For the choice of parameters illustrated, $F_0^{C1} \simeq 2.1$. Type 1 solutions for $F_0 > F_0^{C1}$ are ignored since they require either buckling out of the (x, y)-plane, or explicit consideration of the forces exerted at the contact point. For larger values of F_0 we also obtain solutions of higher modes. Consistant with the linear analysis, we find that on fixing $\beta_0 \gtrsim 55$ and increasing F_0 from zero, we primarily obtain type 2 buckling.

Figure 2.7 illustrates the beam stress resultants and spring stresses corresponding to the type 1 buckling of figure 2.6. We examine these distributions as a means of code validation. In particular, we confirm that the boundary conditions on F_x and F_y are enforced, and that the spring stresses T_x and T_y are precisely the displacements $x - X$ and y respectively. In the flat configuration, we observe that F_x is uniform and equal

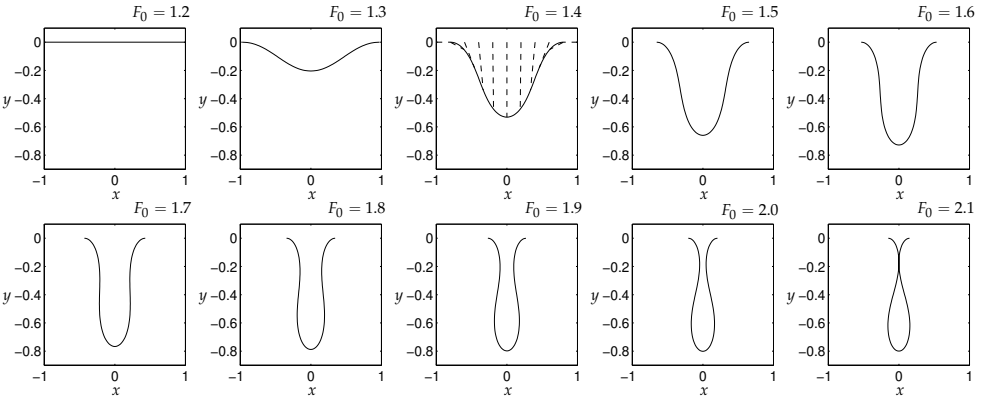

Figure 2.6: Type 1^- solutions of (2.24–2.25) for $\beta_0 = 10$, obtained using MATLAB. The onset of buckling occurs when $F_0 = F_0^{B1} \simeq 1.3$, as predicted by figure 2.5. For increasing force, the profiles continue to develop until opposite-wall contact occurs for $F_0 = F_0^{C1} \simeq 2.1$. Dashed lines illustrate typical spring locations.

to $-F_0$ across the beam. This is consistent with our linear analysis. As F_0 is increased, stimulating buckling, we see that F_x decreases globally. We note that $F_T < 0$ corresponds to compressive stresses within the beam. Thus, as F_0 is increased buckling acts as a mechanism to releave compression, illustrated by a reduction in the magnitude of F_T over the majority of the beam. Figure 2.7 illustrates that while most of the beam remains compressed for large amplitude configurations, some regions in which bending is minimal are actually under slight tension. Since springs are anchored to the original locations of material points in the results presented here, the horizontal component of spring stress becomes large as boundaries are displaced inwards. As we examine the growth of the beam in subsequent parts of this chapter, we refine the boundary conditions and the details of the spring model to improve upon this.

We observe similar behaviour on holding F_0 fixed and increasing β_0, corresponding to increasing the flexibility of the beam relative to that of the springs. Figure 2.8 illustrates the solution types obtained for a wider choice of F_0 and β_0.

We further examine the behaviour of the system through consideration of the bifurcation structure. We track the solution width, X_0, and amplitude, Y_0, as we adjust β_0 or F_0. Figure 2.9 illustrates the resultant bifurcation diagrams. In figure 2.9(a,c) we see that, for fixed β_0, the system undergoes supercritical pitchfork bifurcations at each of the points $F_0 = F_0^{Bi}$ ($i \in \mathbb{R}$). Amplitude and width data on non-trivial branches are plotted until we reach $F_0 = F_0^{Ci}$, at which point the solutions self-intersect and are rejected. In figure 2.9(b,d) we observe a similar bifurcation structure for fixed F_0 and varying β_0.

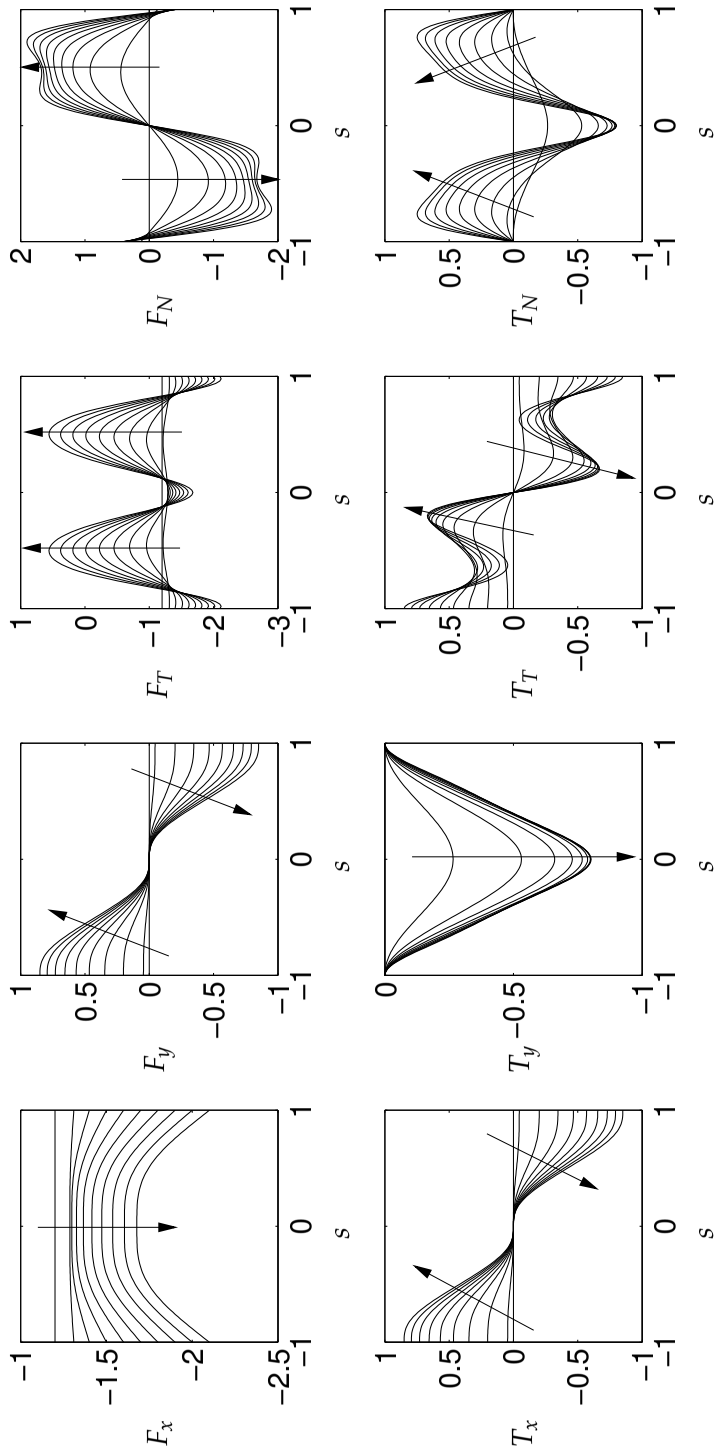

Figure 2.7: Beam stress resultants and spring stresses corresponding to the type 1^- profiles of figure 2.6. Arrows indicate the direction of increasing F_0. Examination of F_T illustrates that buckling acts as a mechanism to releave in-plane compression in the beam.

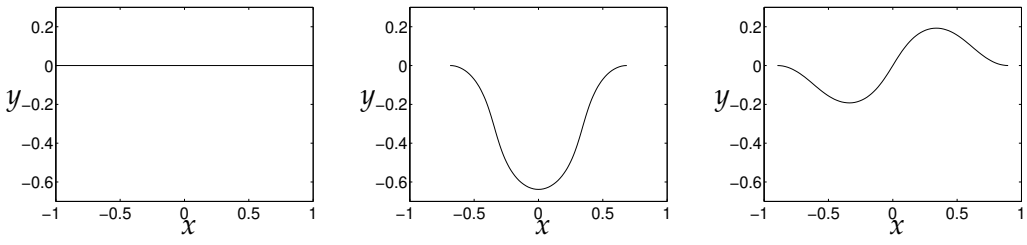

(a) Type 0 (b) Type 1^- (c) Type 2^-

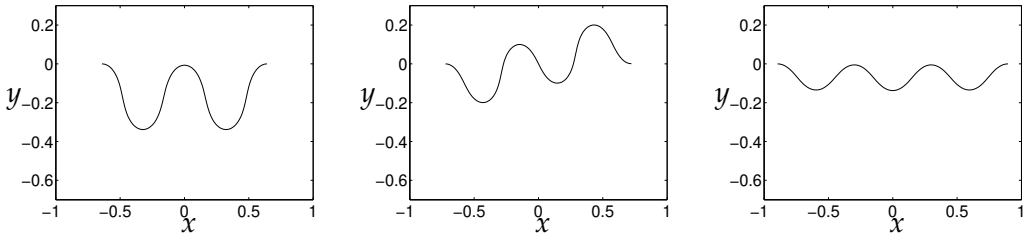

(d) Type 3^- (e) Type 4^- (f) Type 5^-

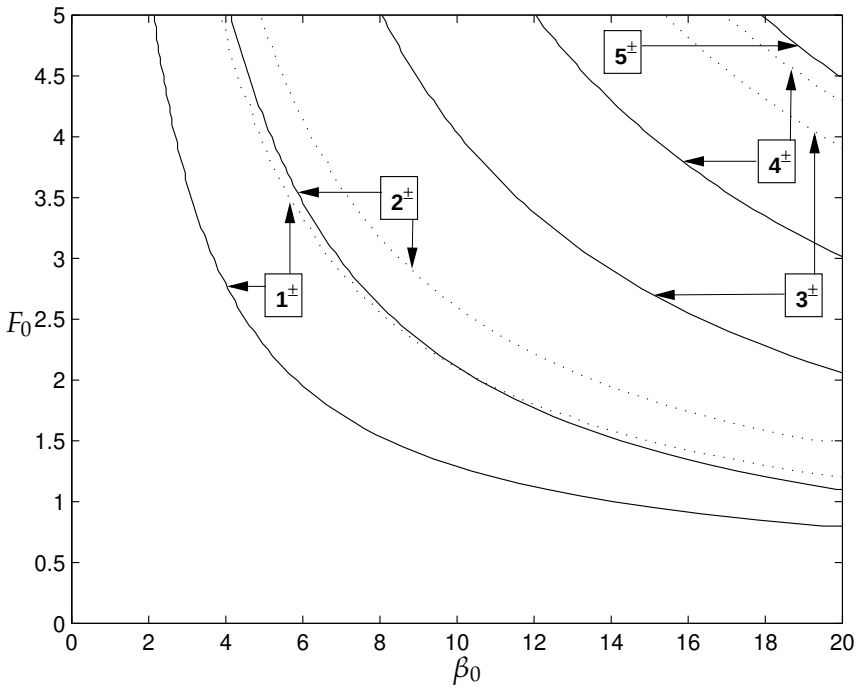

(g) Solutions obtained for varying β_0 and F_0.

Figure 2.8: Typical type 0–5 solutions (a-f) and an illustration of the values of F_0 and β_0 for which they are obtained (g). In (g), solid lines represent $F_0^{Bi}(\beta_0)$, while dotted lines represent $F_0^{Ci}(\beta_0)$ for $i \in [1,5]$.

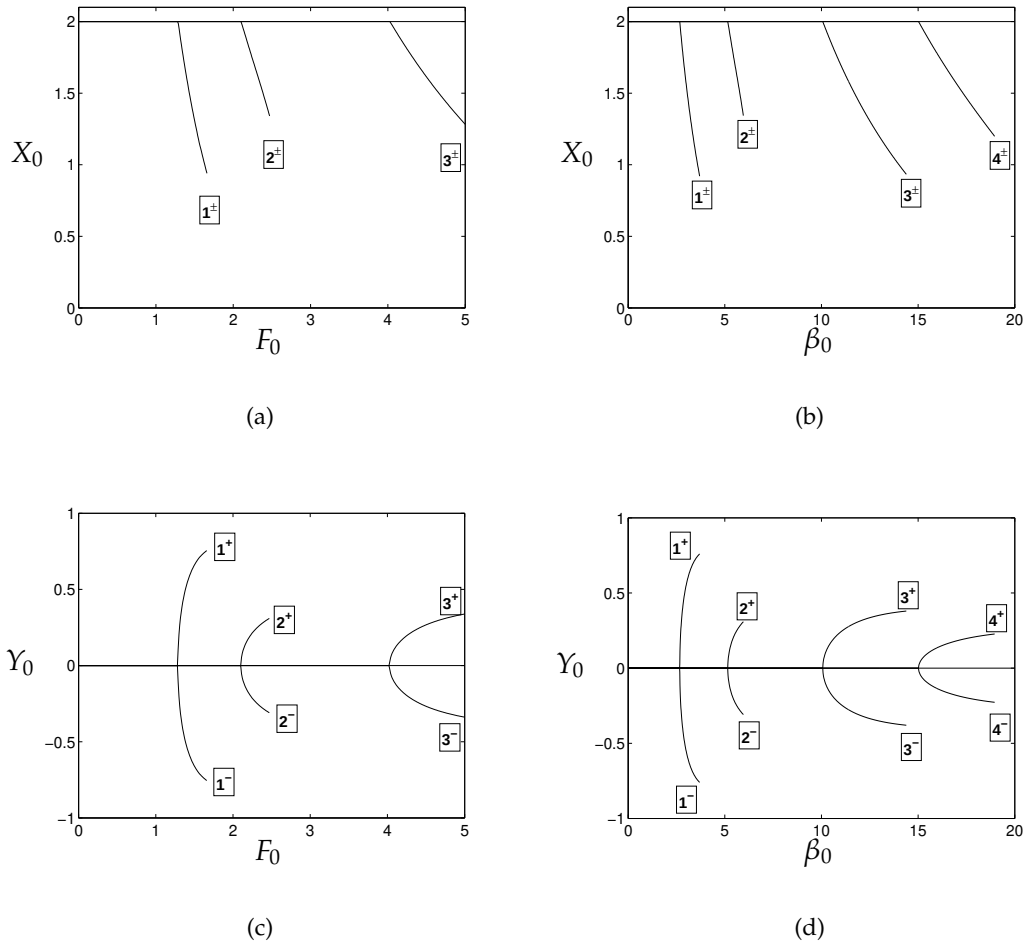

Figure 2.9: Bifurcation diagrams illustrating the evolution of (a) X_0 and (c) Y_0 for fixed $\beta_0 = 10$ and increasing F_0; and (b) X_0 and (d) Y_0 for fixed $F_0 = 4$ and increasing β_0. Branches are truncated at the point for which opposite-wall contact occurs.

2.1.4 Parametric growth

As an approach to modelling epithelial growth, we consider the question of how a beam of arbitrary length L^* can be confined between boundaries located at $x^* = \pm L_0^*$. We consider a sequence of beams of increasing length, starting with the undeformed configuration for which $L^* = L_0^*$. As L^* is increased above L_0^*, all beams must be deformed so as to satisfy the boundary conditions. We no longer place a restriction upon the magnitude of force applied at the beam ends. We refer to this approach, in which we examine a sequence of equilibrium configurations, as 'parametric growth'.

Nondimensionalising in a manner consistent with section 2.1.1, scaling all lengths against L_0^*, we now consider a dimensionless arclength, s, in the range $[-L, L]$ (where

$L = L^*/L_0^*$). To ensure that the points of spring anchorage remain independent of the beam length under consideration, we replace our original spring stress law of (2.16) by the following:

$$T_x = x - \hat{s}, \qquad T_y = y, \tag{2.50}$$

where $\hat{s} = s/L$ is a measure of arc-length in the reference configuration. The above ensures that anchorage points always remain in the region $x \in [-1, 1]$. Combining (2.50) with the dimensionless analogues of (2.12), (2.14) and (2.15), rescaling dependent variables according to

$$\{\hat{x}, \hat{y}\} = \frac{1}{L}\{x, y\}, \qquad \{\hat{F}_x, \hat{F}_y\} = \frac{1}{L^2}\{F_x, F_y\}, \tag{2.51}$$

and rewriting in terms of $\hat{s}$ yields:

$$\frac{\mathrm{d}^2\theta}{\mathrm{d}\hat{s}^2} + \hat{\beta}_0\left(\hat{F}_y\cos\theta - \hat{F}_x\sin\theta\right) = 0, \tag{2.52a}$$

$$\frac{\mathrm{d}^2\hat{F}_x}{\mathrm{d}\hat{s}^2} = \cos\theta - \frac{1}{L}, \qquad \frac{\mathrm{d}^2\hat{F}_y}{\mathrm{d}\hat{s}^2} = \sin\theta. \tag{2.52b}$$

where $\hat{\beta}_0 = \beta_0 L^4$. The appropriate boundary conditions, subject to which (2.52) are solved, are as follows:

$$\theta = 0, \qquad \frac{\mathrm{d}\hat{F}_x}{\mathrm{d}\hat{s}} = 0, \qquad \frac{\mathrm{d}\hat{F}_y}{\mathrm{d}\hat{s}} = 0 \qquad \text{on } \hat{s} = \pm 1, \tag{2.53}$$

which impose clamping and zero horizontal and vertical displacements at the beam ends respectively.

In appendix A.1.2 we show that the energy corresponding to this system is given by

$$\mathcal{E} = \frac{1}{2}\int_{-1}^{1}\left(\frac{\mathrm{d}\hat{F}_x}{\mathrm{d}\hat{s}}\right)^2 + \left(\frac{\mathrm{d}\hat{F}_y}{\mathrm{d}\hat{s}}\right)^2 + \frac{1}{\hat{\beta}_0}\left(\frac{\mathrm{d}\theta}{\mathrm{d}\hat{s}}\right)^2 \mathrm{d}\hat{s}, \tag{2.54}$$

and that for small deflections (2.54) reduces to

$$\mathcal{E} = 2\,(L-1)\,F_0, \tag{2.55}$$

where F_0 is the force on the boundary. From (2.55) we see that for small deflections the energy of equilibrium configurations is simply given by the total work done at the boundaries; F_0 effectively represents the force required to move the ends of the beam by a distance $(L-1)$, from their locations in the flat configuration to those of the boundaries of the problem.

Keeping fixed the material properties of beam and springs (k^*, D^*) and the distance between the boundaries (L_0^*), we examine solutions for fixed β_0 and increasing L. As L is increased, $\hat{\beta}_0$ increases as L^4. Bifurcation diagrams describing solutions obtained

for $\beta_0 = 1$ and $\beta_0 = 10$ are presented in figure 2.10, together with plots of the corresponding energies. Since the beam is inextensible, no solutions exist for $L < 1$ (since this corresponds to a beam shorter than the region to which it is confined). When $L = 1$ the only available solution is the flat configuration. At $L = 1$ lies an infinite family of bifurcations which give rise to all of the solutions described in the previous section. Solutions can be characterised, for L close to 1, by the magnitude of force exerted on the boundaries; that which exerts the least force is regarded as the preferred configuration energetically. For $\beta_0 = 1$ the preferred configuration is of type 1 initially. As L is increased this configuration develops, increasing in amplitude, and remains the lowest energy state until the point at which two parts of the beam come into contact. At this point, numerical simulations of this mode are terminated and the mode 2 configuration is regarded as preferred. Similar behaviour is observed on the branches corresponding to other modes. For $\beta_0 = 10$, however, we find that the developing type 1^- (respectively type 1^+) solution enters into the region $y > 0$ (respectively $y < 0$) as L is increased to approximately 1.85 (see figure 2.10(f)). For $L \gtrsim 1.85$ this eigenmode displays type 3 characteristics. These transitions of type act to minimise the extension of any given spring, particularly those close to the centre of the beam. A wrinkled configuration enables stresses to be distributed more uniformly across all of the springs than does a 'crypt-like' configuration (plots of spring stresses are omitted for brevity). For relatively stiff springs, obtaining a crypt-like profile will commonly be more difficult than obtaining a wrinkled configuration; we revisit this notion in the following section as we incorporate viscous relaxation of spring stresses into the model. Transitions of type were not observed for $\beta_0 = 1$ since beam self-intersection occurs more rapidly. Depending on our choice of β_0, we are also able to see changes of type occurring on higher modes. Consistent with the analysis of section 2.1.2, for $\beta_0 \gtrsim 55$ we find that type 1 solutions are not attainable, regardless of the choice of L. Plots are omitted for brevity. For sufficiently large L (and suitable choice of β_0) energy curves can cross, allowing mode 2 solutions to become the lowest energy state (see figure 2.10(d)).

2.2 Kinematic description of epithelial growth

We now extend the previous model by considering stress to be generated through the growth of the epithelial layer itself, rather than by an externally applied force. We also incorporate the effects of the movement of cells along the lamina propria and the consequent relaxation of stress in the layer. Tissue growth is prescribed by the dimensional growth rate function $\gamma^*(X^*)$. The derivation below builds upon the dimensionless framework of the previous section. As discussed in appendix A.3, we nondimension-

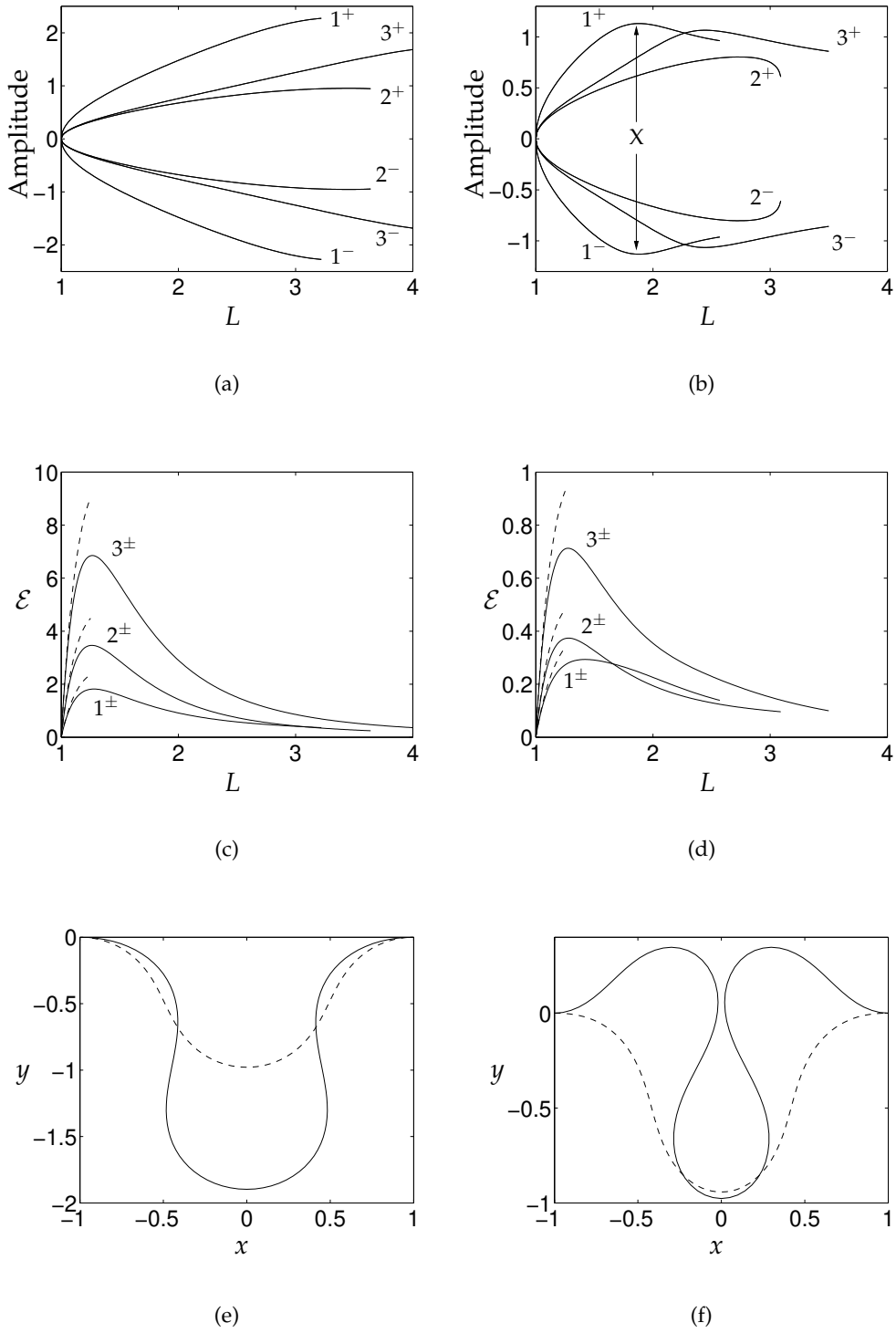

Figure 2.10: Results of parametric growth simulations for (a,c,e) $\beta_0 = 1$ and (b,d,f) $\beta_0 = 10$. (a) and (b) show bifurcation diagrams illustrating amplitude as a function of L for the first three modes. (c) and (d) show the corresponding energies ((2.54), solid line) and the small L asymptote ((2.55), dashed line). In (b), 'X' marks the point at which mode 1 solutions change from type $1^{\pm}$ to type $3^{\pm}$. In (e) and (f), mode 1 profiles are plotted for $L = 1.5$ (dashed) and $L = 2.5$ (solid).

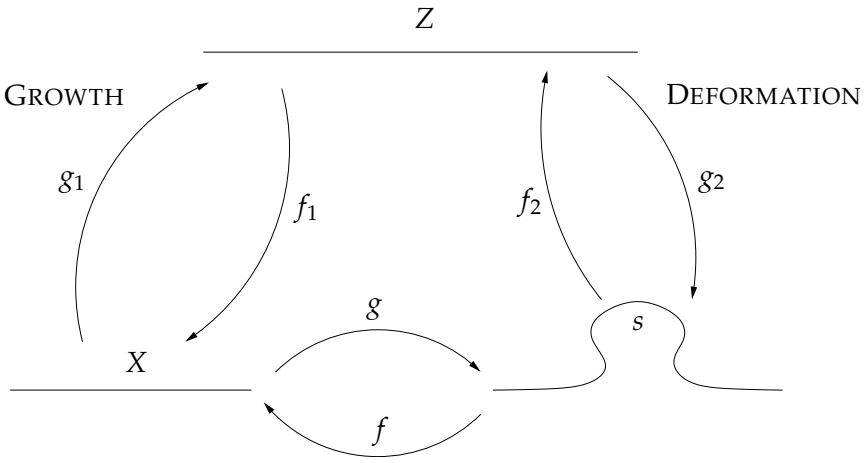

Figure 2.11: Schema showing the decomposition of growth and deformation, as described by Skalak (1980) and Rodriguez *et al.* (1994) (*c.f.* section 1.6.2). The unstressed configuration is first mapped (via mapping g_1) into a hypothetical, flat intermediate configuration. This intermediate configuration is then deformed (via g_2) so as to satisfy boundary conditions. The net deformation is given by $g = g_2(g_1)$. Inverses of g, g_1 and g_2 are denoted f, f_1 and f_2 respectively.

alise by scaling γ^* against its maximal value, $\gamma^*_{\max}$, and time against $1/\gamma^*_{\max}$.

2.2.1 Model development

We derive the equations which govern the growth of the tissue following the framework presented by Skalak (1980) and Rodriguez *et al.* (1994), as discussed in section 1.6.2. We first allow the nondimensionalised reference configuration (X, τ) to grow into an enlarged flat configuration (Z, τ) defined by the spatial mapping $g_1 : X \mapsto Z$. We then map this enlarged configuration into the domain $x \in [-1, 1]$. As a result the layer is forced to buckle. The coordinates (s, t) in this final configuration are arrived at through the spatial mapping $g_2 : Z \mapsto s$. A schema of this process is illustrated in figure 2.11. We note that a mapping analogous to $g(X)$ in the previous section may be defined through the relation $g(X, \tau) = g_2(g_1(X, \tau), \tau)$. For later use, we also define the inverses of g_1, g_2 and g as f_1, f_2 and f respectively.

As discussed in appendix A.3, conservation of mass requires the following expression for $g_1(X, \tau)$:

$$\frac{\partial^2 g_1}{\partial \tau \partial X} = \gamma(X) \frac{\partial g_1}{\partial X}, \tag{2.56}$$

which is solved subject to the symmetry condition $g_1(0, \tau) = 0$ and the condition imposing the initial length, $g_1(X, 0) = X$. On forcing the beam, we obtain the following

expression, analogous to the previous stretch condition (2.21d):

$$F_x \cos\theta + F_y \sin\theta = \beta_1 \left(\frac{\partial g_2}{\partial Z} - 1 \right), \tag{2.57}$$

subject to $g_2(0,\tau) = 0$; β_1 captures the compressibility of the layer and is defined as following (2.21).

Under the assumption that the layer is essentially incompressible, we have that $\beta_1 \gg 1$ and it follows from (2.57) that

$$g_2(Z,\tau) = Z + \frac{1}{\beta_1}\hat{g}_2(Z,\tau), \tag{2.58}$$

for some $O(1)$ function $\hat{g}_2(Z,\tau)$. In particular, we have

$$g(X,\tau) = g_2(g_1(X,\tau),\tau) = g_1(X,\tau) + \frac{1}{\beta_1}\hat{g}_2(g_1(X,\tau),\tau), \tag{2.59}$$

and so to leading order $g(X,\tau) = g_1(X,\tau)$. Again, we can evaluate the local stretch according to

$$\frac{\partial \hat{g}_2}{\partial Z} = F_x \cos\theta + F_y \sin\theta. \tag{2.60}$$

From here onwards we consider only the leading-order problem and, owing to (2.59), the remainder of the derivation proceeds in terms of $g(X,\tau)$.

We look to capture the effects of cell migration, and the resultant relaxation of stresses in the layer, through the assumption that the springs attaching the epithelium to the underlying layer are viscoelastic, with viscosity ν^*. Following Edwards & Chapman (2007), we choose a Maxwell constitutive law for T_x and T_y, motivated by the expectation that the layer will exhibit elastic behaviour over short timescales. The equations governing the evolution of T_x and T_y, which replace (2.16a) and (2.16b), are derived in appendix A.2. The results are

$$\frac{\partial T_x}{\partial \tau} + \beta_T T_x = \frac{\partial}{\partial \tau}\int_0^{g(X,\tau)} \cos\theta\left(s',t\right) \mathrm{d}s', \tag{2.61a}$$

$$\frac{\partial T_y}{\partial \tau} + \beta_T T_y = \frac{\partial}{\partial \tau}\int_{-1}^{g(X,\tau)} \sin\theta\left(s',t\right) \mathrm{d}s', \tag{2.61b}$$

which are solved subject to the conditions of zero stress initially,

$$T_x(X,0) = 0, \quad T_y(X,0) = 0. \tag{2.62}$$

The dimensionless parameter $\beta_T = k^*/\nu^*\gamma^*_{\max}$ captures the ratio of the growth timescale to the timescale for the viscous relaxation of the attachments.

Equations (2.61–2.62) have been written with respect to the reference configuration, whereas the remainder of the governing equations in section 2.1 are written with respect to the deformed configuration. Thus, we must consider a change of variable to

the (s,t)-frame. Denoting derivatives of f and g by subscripts, we have that

$$g_X = f_s^{-1}, \quad g_\tau = -f_t\,(f_s)^{-1}, \tag{2.63}$$

and hence, (2.61) can be written in the physical frame as

$$\frac{\partial T_x}{\partial t} - \frac{f_t}{f_s}\frac{\partial T_x}{\partial s} + \beta_T T_x = \frac{\partial}{\partial t}\int_0^s \cos\theta\,(s',t)\,\mathrm{d}s' - \frac{f_t}{f_s}\frac{\partial}{\partial s}\int_0^s \cos\theta\,(s',t)\,\mathrm{d}s', \tag{2.64a}$$

$$\frac{\partial T_y}{\partial t} - \frac{f_t}{f_s}\frac{\partial T_y}{\partial s} + \beta_T T_y = \frac{\partial}{\partial t}\int_{-1}^s \sin\theta\,(s',t)\,\mathrm{d}s' - \frac{f_t}{f_s}\frac{\partial}{\partial s}\int_{-1}^s \sin\theta\,(s',t)\,\mathrm{d}s', \tag{2.64b}$$

with $T_x(s,0) = 0$ and $T_y(s,0) = 0$. Similarly, (2.56) becomes

$$-\frac{\partial f}{\partial s}\frac{\partial^2 f}{\partial s \partial t} + \frac{\partial^2 f}{\partial s^2}\frac{\partial f}{\partial t} = \left(\frac{\partial f}{\partial s}\right)^2 \gamma(s), \tag{2.65}$$

with $f(0,t) = 0$ and $f(s,0) = s$, from which we obtain

$$-\left(\frac{f_t}{f_s}\right)_s = \gamma(s). \tag{2.66}$$

Owing to (2.66), we rewrite (2.64) as

$$\frac{\partial T_x}{\partial t} + \Gamma(s)\frac{\partial T_x}{\partial s} + \beta_T T_x = \frac{\partial}{\partial t}\int_0^s \cos\theta\,(s',t)\,\mathrm{d}s' + \Gamma(s)\frac{\partial}{\partial s}\int_0^s \cos\theta\,(s',t)\,\mathrm{d}s', \tag{2.67a}$$

$$\frac{\partial T_y}{\partial t} + \Gamma(s)\frac{\partial T_y}{\partial s} + \beta_T T_y = \frac{\partial}{\partial t}\int_{-1}^s \sin\theta\,(s',t)\,\mathrm{d}s' + \Gamma(s)\frac{\partial}{\partial s}\int_{-1}^s \sin\theta\,(s',t)\,\mathrm{d}s', \tag{2.67b}$$

where $\Gamma(s)$ is the cumulative growth function defined by

$$\Gamma(s) = \int_0^s \gamma(s')\mathrm{d}s'. \tag{2.68}$$

Thus, denoting the integrals in (2.67) by $x(s,t)$ and $y(s,t)$ respectively, the full system of governing equations is

$$\frac{\partial^2\theta}{\partial s^2} + \beta_0\left(F_y\cos\theta - F_x\sin\theta\right) = 0, \tag{2.69a}$$

$$\frac{\partial F_x}{\partial s} = T_x, \qquad \frac{\partial F_y}{\partial s} = T_y, \tag{2.69b}$$

$$\frac{\partial x}{\partial s} = \cos\theta, \qquad \frac{\partial y}{\partial s} = \sin\theta, \tag{2.69c}$$

$$\frac{\partial T_x}{\partial t} + \Gamma(s)\frac{\partial T_x}{\partial s} + \beta_T T_x = \frac{\partial x}{\partial t} + \Gamma(s)\frac{\partial x}{\partial s}\,, \tag{2.69d}$$

$$\frac{\partial T_y}{\partial t} + \Gamma(s)\frac{\partial T_y}{\partial s} + \beta_T T_y = \frac{\partial y}{\partial t} + \Gamma(s)\frac{\partial y}{\partial s}\,, \tag{2.69e}$$

and is solved subject to the boundary conditions

$$\theta(\pm L,t) = 0, \qquad x(\pm L,t) = \pm 1, \qquad y(\pm L,t) = 0, \tag{2.70}$$

and the initial conditions

$$T_x(s,0) = 0, \qquad T_y(s,0) = 0, \qquad L(0) = 1, \tag{2.71}$$

where $L(t)$ denotes the right-hand moving boundary.

2.2.2 Reduction to the growth-free model of section 2.1

We demonstrate, below, that imposing zero growth ($\Gamma(s) = 0$) on (2.69–2.71) we recover the model of section 2.1 at short times. We note that (2.69a-c) are unchanged from section 2.1. Omitting growth from the model, (2.69d) and (2.69e) become

$$\frac{\partial T_x}{\partial t} + \beta_T T_x = \frac{\partial}{\partial t}\int_0^s \cos\theta\left(s',t\right)\mathrm{d}s', \tag{2.72a}$$

$$\frac{\partial T_y}{\partial t} + \beta_T T_y = \frac{\partial}{\partial t}\int_{-1}^s \sin\theta\left(s',t\right)\mathrm{d}s'. \tag{2.72b}$$

As discussed in appendix A.2, a Maxwell viscoelastic material behaves as a linearly elastic material over short times; *i.e.* if the timescale over which growth occurs is much shorter than the relaxation time of the layer, viscous effects are negligible. In this regime we have $\beta_T \ll 1$ and we obtain the following expression for spring stresses, which is valid over short times:

$$\frac{\partial T_x}{\partial t} = \frac{\partial}{\partial t}\int_0^s \cos\theta\left(s',t\right)\mathrm{d}s', \tag{2.73a}$$

$$\frac{\partial T_y}{\partial t} = \frac{\partial}{\partial t}\int_{-1}^s \sin\theta\left(s',t\right)\mathrm{d}s'. \tag{2.73b}$$

Integrating (2.73), we obtain

$$T_x = \int_0^s \cos\theta\left(s',t\right)\mathrm{d}s' + A(s), \tag{2.74a}$$

$$T_y = \int_{-1}^s \sin\theta\left(s',t\right)\mathrm{d}s' + B(s), \tag{2.74b}$$

where $A(s)$ and $B(s)$ are arbitrary functions of s. Requiring the right-hand sides of (2.74) to be the components of displacement of the point s fixes $A(s) = -f(s)$ and $B(s) = 0$, which recovers (2.21b-c). The model of section 2.1 is thus regained.

2.2.3 Code formulation and validation

We develop an iterative method to solve (2.69–2.71) numerically. Given the initial data corresponding to the flat solution, we first use (2.69d-e) to determine the forms of T_x and T_y at the next timestep. We then substitute this information into (2.69a-c) to determine the profile of the beam at this step. We describe this numerical scheme in greater detail below.

We obtain solutions to (2.69d-e), and track the growth of the domain, via consideration of the characteristics of the system. Firstly, we consider changes of variable defined as follows

$$\mathcal{T}_x = T_x - x, \qquad \mathcal{T}_y = T_y - y. \tag{2.75}$$

Under this change of variable (2.69d-e) become

$$\frac{\partial \mathcal{T}_x}{\partial t} + \Gamma(s)\frac{\partial \mathcal{T}_x}{\partial s} + \beta_T \mathcal{T}_x = -\beta_T x, \tag{2.76a}$$

$$\frac{\partial \mathcal{T}_y}{\partial t} + \Gamma(s)\frac{\partial \mathcal{T}_y}{\partial s} + \beta_T \mathcal{T}_y = -\beta_T y. \tag{2.76b}$$

We parameterise the characteristics with variable ρ defined according to

$$\frac{\partial t}{\partial \rho} = 1, \qquad \frac{\partial s}{\partial \rho} = \Gamma(s). \tag{2.77}$$

We impose the initial conditions of (2.71) by setting

$$s = X, \quad t = 0, \quad \mathcal{T}_x = -X, \quad \mathcal{T}_y = 0 \tag{2.78}$$

on $\rho = 0$. It follows from (2.77–2.78) that $\rho = t$, and the following equations thus govern the evolution of $\mathcal{T}_x$ and $\mathcal{T}_y$ along characteristics:

$$\frac{\mathrm{d}\mathcal{T}_x}{\mathrm{d}t} + \beta_T \mathcal{T}_x = -\beta_T x, \tag{2.79a}$$

$$\frac{\mathrm{d}\mathcal{T}_y}{\mathrm{d}t} + \beta_T \mathcal{T}_y = -\beta_T y. \tag{2.79b}$$

Noting (2.77) we see that the characteristics themselves satisfy

$$\frac{\mathrm{d}s}{\mathrm{d}t} = \Gamma(s), \tag{2.80}$$

from which we deduce that each characteristic represents the path traced out by a material point as the layer grows. Since $\Gamma(s)$ is monotonic, the characteristics cannot cross and each material point lies on a unique characteristic. As a consequence of (2.80), we track the moving boundaries at $s = \pm L(t)$ according to

$$\frac{\mathrm{d}L}{\mathrm{d}t} = \Gamma(L). \tag{2.81}$$

We initiate our numerical solver with a discrete growth step. Applying a forward-Euler finite difference approximation to (2.80), we obtain

$$s^{i+1} = s^i + \Delta t \Gamma\left(s^i\right), \tag{2.82}$$

where Δt is our timestep size and the i-superscript denotes that s is evaluated at the i^{th} timestep. We then apply a similar discretisation to (2.79), yielding

$$\frac{\mathcal{T}_x^{i+1} - \mathcal{T}_x^i}{\Delta t} + \beta_T \mathcal{T}_x^i = -\beta_T x^i, \tag{2.83a}$$

$$\frac{\mathcal{T}_y^{i+1} - \mathcal{T}_y^i}{\Delta t} + \beta_T \mathcal{T}_y^i = -\beta_T y^i. \tag{2.83b}$$

Manipulation of (2.83) yields the following equations,

$$\mathcal{T}_x^{i+1} = \mathcal{T}_x^i - \beta_T \Delta t \left(\mathcal{T}_x^i + x^i \right), \tag{2.84a}$$

$$\mathcal{T}_y^{i+1} = \mathcal{T}_y^i - \beta_T \Delta t \left(\mathcal{T}_y^i + y^i \right), \tag{2.84b}$$

which govern the evolution of $\mathcal{T}_x$ and $\mathcal{T}_y$ from the i^{th} timestep to the $(i+1)^{\text{th}}$ timestep. Having determined $\mathcal{T}_x^{i+1}$ and $\mathcal{T}_y^{i+1}$, it remains to determine the beam profile at the $(i+1)^{\text{th}}$ timestep. From (2.69a-c) we have

$$\frac{\partial^2 \theta^{i+1}}{\partial s^2} + \beta_0 \left(F_y^{i+1} \cos\theta^{i+1} - F_x^{i+1} \sin\theta^{i+1} \right) = 0, \tag{2.85a}$$

$$\frac{\partial F_x^{i+1}}{\partial s} = \mathcal{T}_x^{i+1} + x^{i+1}, \tag{2.85b}$$

$$\frac{\partial F_y^{i+1}}{\partial s} = \mathcal{T}_y^{i+1} + y^{i+1}, \tag{2.85c}$$

$$\frac{\partial x^{i+1}}{\partial s} = \cos\theta^{i+1}, \tag{2.85d}$$

$$\frac{\partial y^{i+1}}{\partial s} = \sin\theta^{i+1}, \tag{2.85e}$$

which we solve subject to the boundary conditions of (2.70) using MATLAB's boundary value solver as described in section 2.1.3.

In addition to the code validation methods discussed in section 2.1.3, we perform the following checks to ensure that the numerical solutions are accurate. The code is validated initially through examination of the results obtained when $\beta_T = 0$. In this limit we recover purely elastic spring behaviour, and hence we expect $T_x = x - X$ and $T_y = y$. Testing of the code reveals that numerical results are consistant with this. For $\beta_T > 0$ our springs exhibit some viscous relaxation. For short times we expect the springs to exhibit elastic behaviour. Comparison of the results which we obtain for $\beta_T = 0$ and $\beta_T = 100$ for early timesteps confirms that this short-time elastic behaviour is present. Since increasing β_T results in the relaxation of spring stresses, we further validate the code by ensuring that T_x and T_y are bounded by $x - X$ and y respectively, and we observe that as t increases we see a global decay in the magnitude of T_x and T_y.

2.2.4 Uniform growth

Considering uniform growth we set $\gamma(s) \equiv 1$, and hence $\Gamma(s) = s$. It follows from (2.81) that the moving boundaries satisfy

$$L(t) = e^t, \tag{2.86}$$

which illustrates that in the case of uniform growth we obtain an exponential increase in domain size.

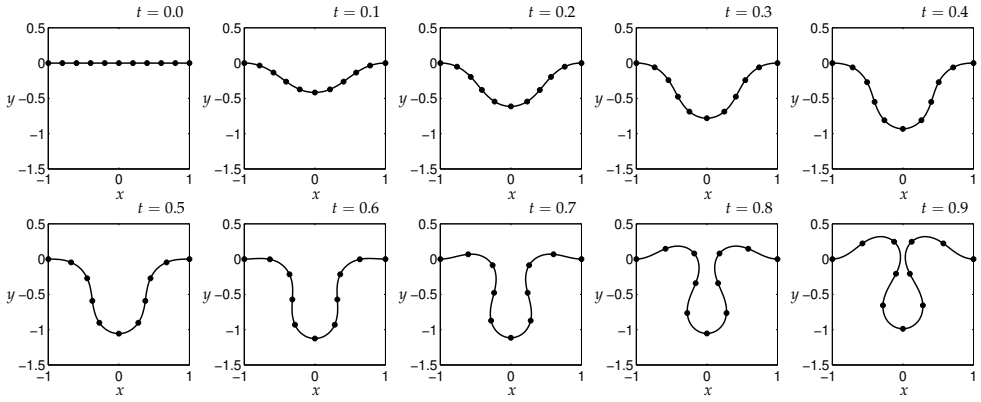

Figure 2.12: Evolution of an initially type 1^- profile for $\beta_0 = 10$, under uniform growth with no relaxation of tethering forces ($\beta_T = 0$). Dots illustrate the progression of material points.

Figure 2.12 illustrates the temporal evolution of a typical solution profile, obtained for $\beta_0 = 10$ and $\beta_T = 0$. We note that choosing $\beta_T = 0$ corresponds to switching off viscous relaxation of spring stresses; beam profiles are then qualitatively similar to those of section 2.1. The illustrated solution is of type 1 initially; however, we may also obtain solutions of higher modes. We observe that as time evolves our type 1 profile lifts into the region $y > 0$, resembling type 3. This is explained by the springs in the centre of the beam being highly stretched in comparison to those elsewhere and, hence, it being energetically favourable to transfer the resulting stress to those springs closer to the boundaries. As such, large deviations from the line $y = 0$ are prevented. This behaviour suggests a favouring of wrinkling over crypt-like buckling for large time, and recovers the equivalent observation in the parametric growth approximation of section 2.1.4.

The components of beam and spring stresses are shown in figure 2.13. We observe that as the beam buckles the stresses in the springs are increased in magnitude, owing to the displacement of material points from their original locations and consequent stretching of the springs. We also note that in the centre of the beam where bending is greatest, we have that $F_T \to 0$ as $t \to \infty$, illustrating that buckling acts as a mechanism to resist compression. This observation is consistant with the results of section 2.1.3.

Figure 2.14 illustrates the evolution of a similar type 1 profile with $\beta_0 = 10$ and $\beta_T = 100$, corresponding to the limit in which viscous relaxation dominates the evolution of spring stresses. We see that the beam profile no longer enters the region $y > 0$ and the solution remains type 1 for all time. This behaviour is consistent with the spring stress relaxation facilitating more greatly extended springs in the centre of the

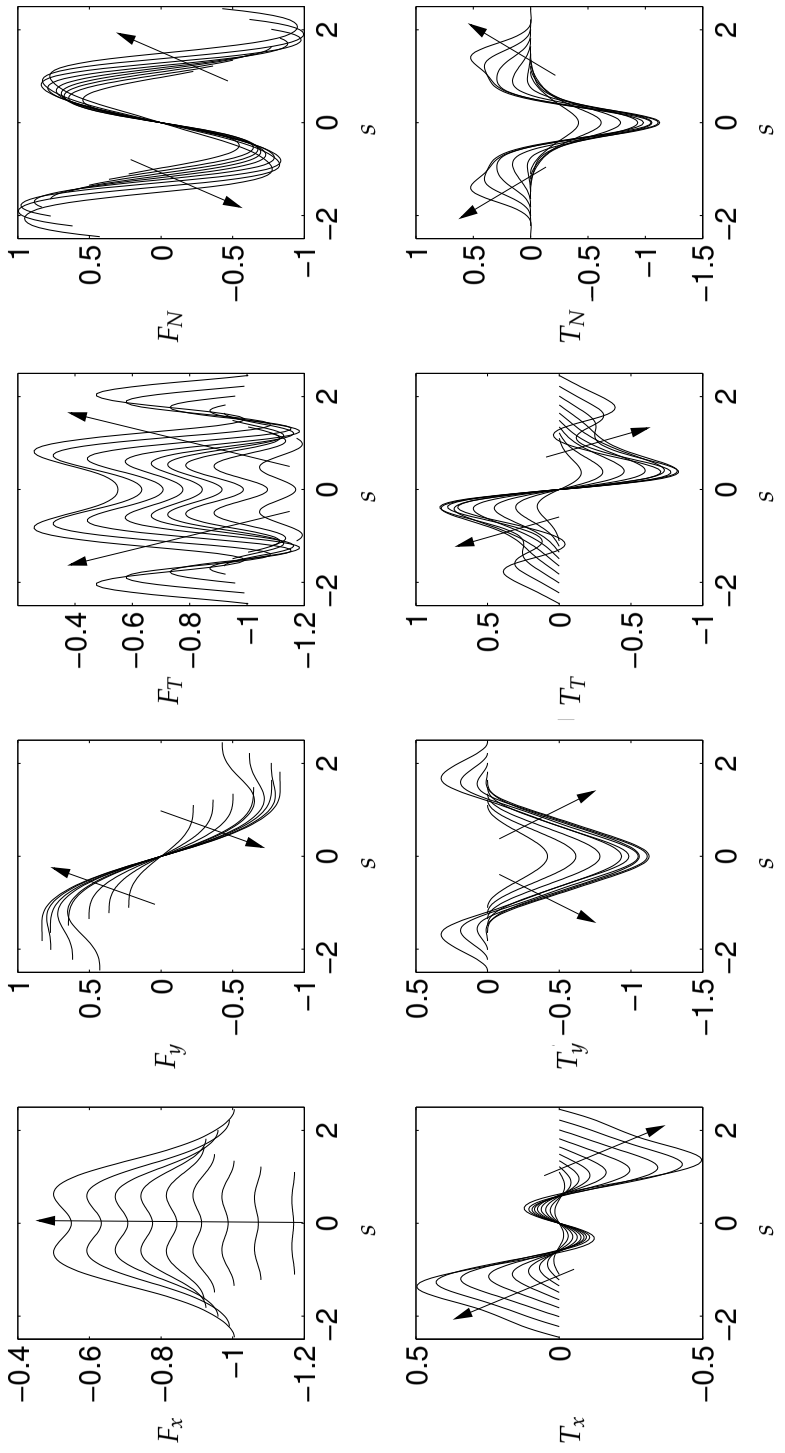

Figure 2.13: Evolution of beam stress resultants and spring stresses for the configurations of figure 2.12 ($\beta_0 = 10, \beta_T = 0$), attained in the regime of uniform growth. Arrows indicate the progression of time.

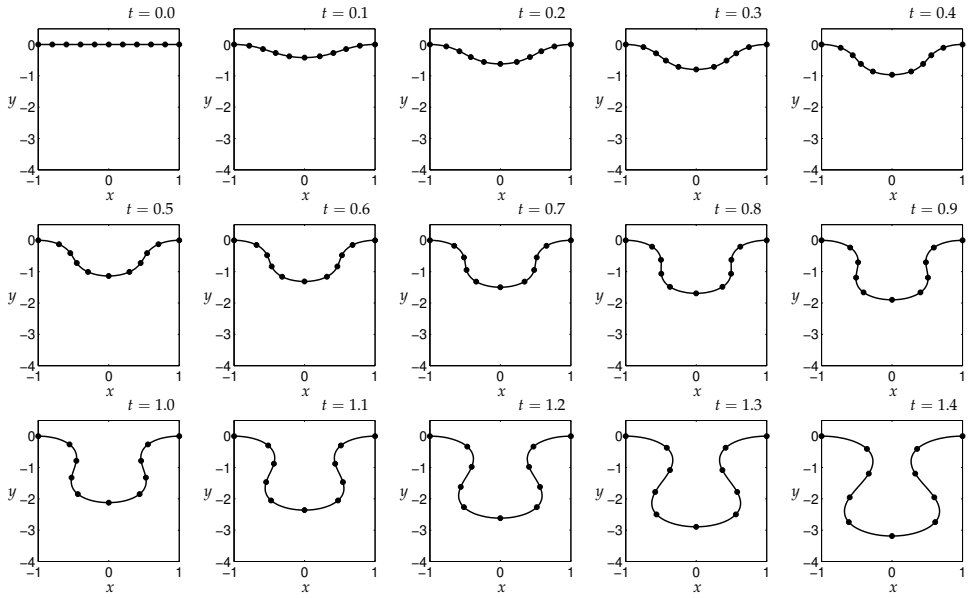

Figure 2.14: Evolution of an initially type 1^- profile for $\beta_0 = 10$, under uniform growth with rapid relaxation of tethering forces ($\beta_T = 100$). Dots illustrate the progression of material points.

beam. Since viscous relaxation permits a greater deviation from the linear state, we can allow the beam to grow for a more lengthy period of time before self-intersection occurs. As a result we obtain deeper and broader crypts than in the linear spring regime ($\beta_T = 0$). We observe, in figure 2.15, that increasing β_T results in a global reduction in the magnitude of all components of the beam stress resultants and spring stresses. In figure 2.16 we compare solutions for $\beta_T = 1$ (intermediate spring stress relaxation) and $\beta_T = 100$ (rapid spring stress relaxation). We allow both beams to grow uniformly until $t = 1$, at which point growth is stopped. We observe that the two profiles become indistinguishable as the spring stresses relax; both solutions converge to the solution obtained in the viscous-dominated limit.

2.2.5 Growth confined to a central region

We now consider a regime in which growth occurs only within the region $s \in [-s_0, s_0]$, for some constant $0 < s_0 < 1$. Inside this region growth is considered uniform. We may liken such behaviour to that of the proliferative compartment at the base of a crypt. The

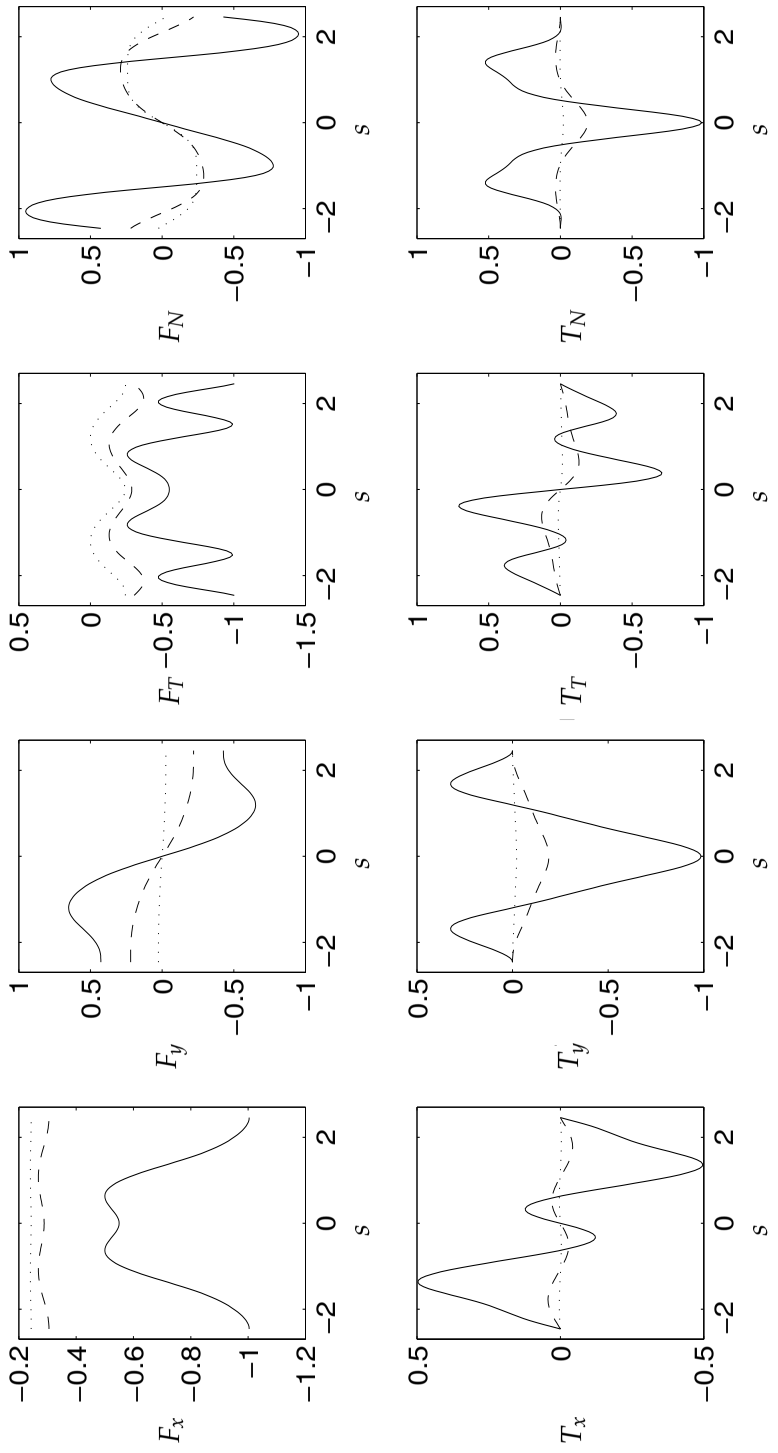

Figure 2.15: Beam stress resultants and spring stresses in the regime of uniform growth for $\beta_0 = 10$ and $\beta_T = 0$ (solid line), $\beta_T = 10$ (dashed line) and $\beta_T = 100$ (dotted line). These data are plotted at $t = 1.08$; the last time point at which all three solutions are viable.

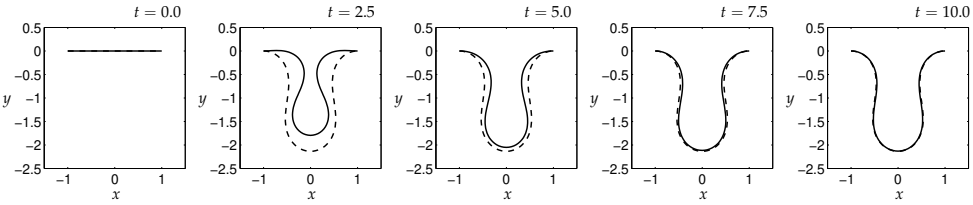

Figure 2.16: Here we observe the long-time profile obtained when growth is switched off at $t = 1$. We compare the beam profile obtained when spring stresses are dominated by viscous relaxation ($\beta_T = 100$; dotted line), against that of a more gradual relaxation of spring stresses ($\beta_T = 1$; solid line). Both profiles refer to uniformly growing layers with $\beta_0 = 10$. We observe that the profile corresponding to the slowly relaxing regime converges to that of the viscous-dominated regime for large time.

appropriate definitions of the growth functions are as follows:

$$\gamma(s) = \begin{cases} 0 & s < -s_0, \\ 1 & -s_0 \leq s \leq s_0, \\ 0 & s > s_0, \end{cases} \qquad \Gamma(s) = \begin{cases} -s_0 & s \leq -s_0, \\ s & -s_0 \leq s \leq s_0, \\ s_0 & s \geq s_0. \end{cases} \tag{2.87}$$

It follows from (2.81) that

$$L(t) = s_0 t + 1, \tag{2.88}$$

and the size of the domain increases linearly in this regime.

Figures 2.17 and 2.18 illustrate the evolution of type 1 profiles for $\beta_T = 0$ and $\beta_T = 100$ respectively, with $\beta_0 = 10$ and $s_0 = 0.25$. We observe that the geometry of the solutions is qualitatively similar to that of the uniform growth regime. In the linear spring limit ($\beta_T = 0$), the type 1 beam profile develops type 3 characteristics once more. Through the introduction of viscous relaxation in the spring stresses ($\beta_T > 0$), we enable greater deviations from $y = 0$ and the solutions do not display such behaviour. Since larger amplitude solutions are then attainable, more prolonged growth is possible prior to opposite wall contact occurring. Figures 2.17 and 2.18 show that the crypt-like geometry is maintained when restricting growth to the centre of the beam (or equivalently the base of the crypt). We see from the figures that the results now make progress towards capturing the hierarchical nature of the cells in the crypt, as older cells effectively remain close to the intestinal lumen while younger cells reside at the base of the crypt. Such behaviour is more consistent with that found *in vivo*, although our model does not incorporate the loss of cells from the top of the crypt due to apoptosis or shedding. Plots of beam and spring stresses are omitted for brevity; however, examination of these reveals that the characteristics observed under uniform growth are maintained under the transition to this 'proliferative compartment' model. In particular, the degree

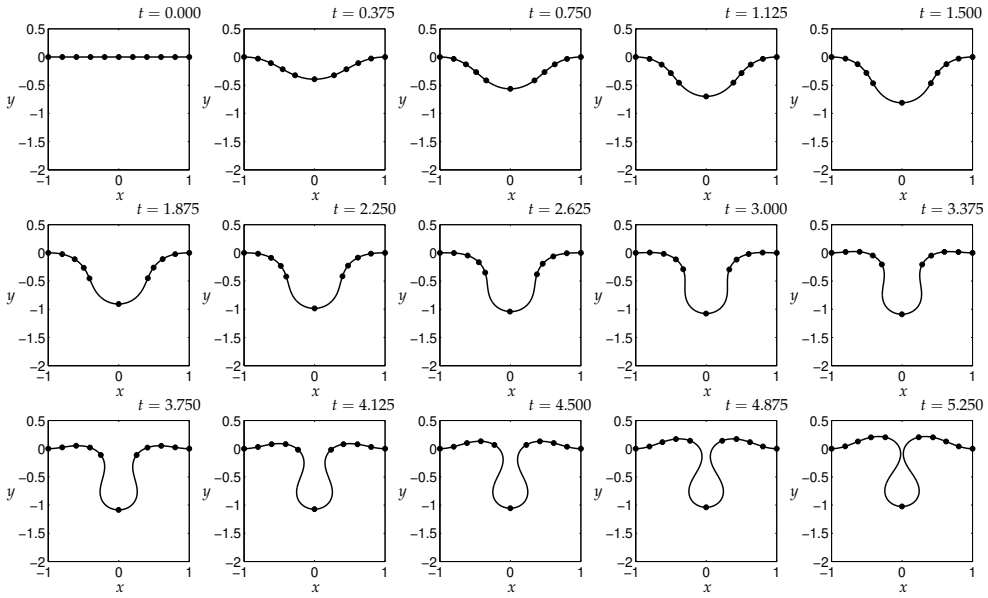

Figure 2.17: Evolution of an initially type 1 profile corresponding to a beam whose growth is confined to a central proliferative region, for $\beta_0 = 10$, $\beta_T = 0$ and $s_0 = 0.25$. Dots illustrate the progression of material points.

to which the beam is compressed is reduced upon buckling, and increasing β_T yields a notable reduction in all spring and beam stresses.

Comparing the large-time profiles illustrated in figures 2.12 and 2.14 to those of figures 2.17 and 2.18, we see that confining growth to the centre of the beam has the effect of delaying beam self-intersection, enabling simulations to be run for longer and yielding deeper crypts. This observation is exaggerated in figure 2.19, in which we compare the results of this growth regime to the profiles of equal length obtained for uniform growth. We see that, in general, confining growth to a central compartment ultimately results in a straighter-walled crypt with less of a narrowing at the neck and a less bulbous base. As the figure illustrates, the extent to which the geometry differs between the growth regimes is strongly dependent on β_0. For large β_0 (corresponding to stiff springs) the change in geometry is significant, as illustrated in figures 2.19(d-f). However, for smaller β_0 the bending stiffness of the beam dominates spring stiffness and buckling is largely independent of the springs. As such, the increased flexibility in the springs counter-acts the dependence on the exact location of growth and the two geometries become rather similar. We also observe that the distinctions between the two solutions are much more slight for large β_T. In this limit the springs exhibit rapid viscous relaxation of stresses, and the geometry of the buckled profile becomes independent of the springs once more. As such, an explicit dependence on the nature of

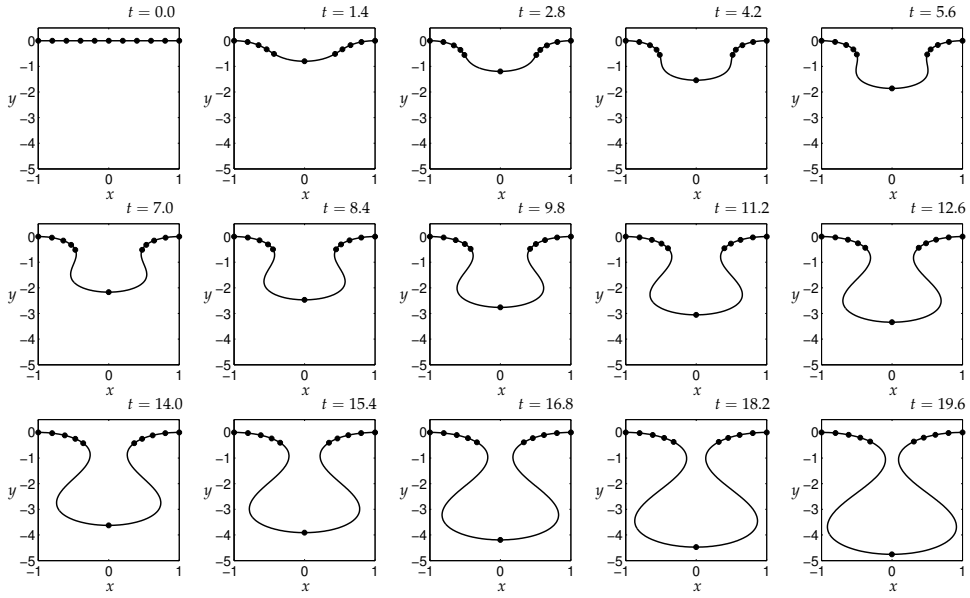

Figure 2.18: Evolution of a type 1 profile corresponding to a beam whose growth is confined to a central proliferative region, for $\beta_0 = 10$, $\beta_T = 100$ and $s_0 = 0.25$. Dots illustrate the progression of material points.

growth is lost once more. In figures 2.19(b) and 2.19(e) we see a marked difference in the results obtained for $\beta_T = 1$, for which growth occurs over a similar timescale to spring stress relaxation. We observe a transition from the wrinkled configurations obtained under uniform growth to deeper, straighter-sided configurations reminiscent of colorectal crypts.

2.2.6 Coupling of growth to geometry

Here we consider the dependence of growth upon the geometry of the configuration into which the beam has buckled, or associated physical quantities. In general, we consider that $\gamma = \gamma(s, \theta, x, y, F_x, F_y)$. Since the growth rate now evolves with the buckling of the beam, γ^* exhibits an implicit dependence upon time. In the nondimensionalisation of γ^*, we regard $\gamma^*_{\max}$ to represent the maximal value of γ^* when the beam is in its flat configuration.

In this section we focus upon two such growth regimes. Firstly, we consider growth to be stimulated by the depth of invagination. This may model a chemical gradient (such as Wnt, for example) which acts to stimulate proliferation towards the base of the crypt. We choose γ to have an exponential dependence upon y, as follows:

$$\gamma = \gamma(y) = e^{-\alpha y}. \tag{2.89}$$

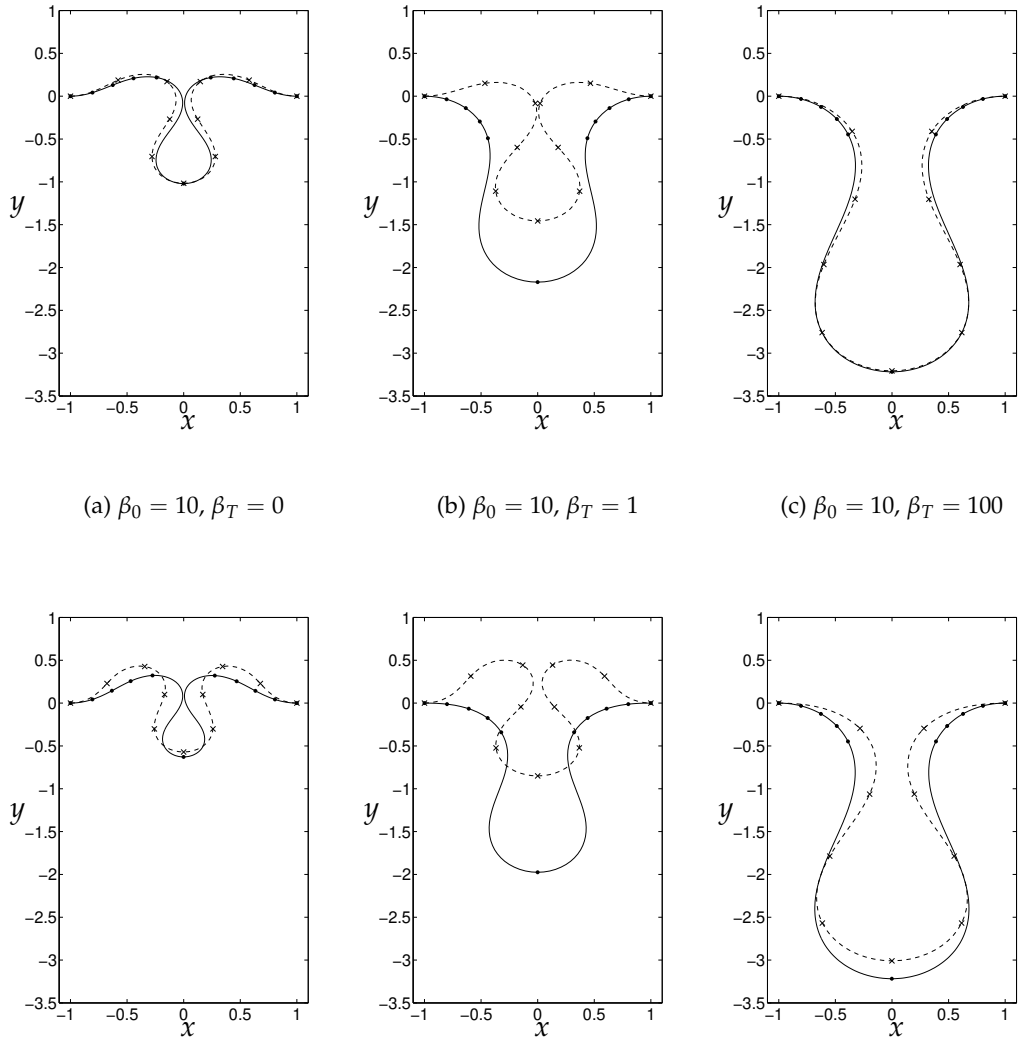

(a) $\beta_0 = 10$, $\beta_T = 0$ (b) $\beta_0 = 10$, $\beta_T = 1$ (c) $\beta_0 = 10$, $\beta_T = 100$

(d) $\beta_0 = 50$, $\beta_T = 0$ (e) $\beta_0 = 50$, $\beta_T = 1$ (f) $\beta_0 = 50$, $\beta_T = 100$

Figure 2.19: Comparison of buckled profiles in the uniform growth regime (dashed lines) against those of equivalent lengths obtained when growth is confined to a central proliferative region of half-width $s_0 = 0.25$ (solid lines). Dots and crosses represent material points which were equally spaced in the undeformed configuration.

Here α is a dimensionless parameter which governs the strength of dependence of the growth profile upon the depth of invagination. With γ prescribed by (2.89), those regions of the beam which buckle downwards will undergo a rapid acceleration of growth, while those regions which pertrude into $y > 0$ experience a sharp decay in their growth rate.

Secondly, we consider growth to be restricted by compression of the beam. Such a growth regime draws parallels with contact inhibition, a property exhibited by epithelial cells which causes them to stop proliferating on reaching confluence (Quaroni *et al.*, 1979). We consider γ to depend upon the in-plane component of beam stress, F_T, as follows:

$$\gamma = \gamma(F_T) = e^{\alpha F_T}. \tag{2.90}$$

We recall from section 2.2.3 that the system's characteristics have gradient $\mathrm{d}t/\mathrm{d}s = 1/\Gamma(s)$. Our growth rate formulae (2.89–2.90) have been chosen to be non-negative functions so that $\Gamma(s)$ remains monotonic. This is sufficient to ensure that the characteristics do not cross in these growth regimes.

In figures 2.20 and 2.21 the profiles obtained under the two growth regimes described above are compared to those of equivalent lengths obtained in the uniform growth regime. We find that differences between the beam shapes are minimal. Some local variation in the displacements of material points is observed; however, such variations are not substantial. Increasing α exaggerates the dependence of the growth rate upon the geometry of the solutions; however, numerical simulations reveal that this does not yield significantly different buckled profiles to those attained under uniform growth.

2.2.7 Patterning of growth and tissue stiffness

We now examine the manner in which the patterning of growth, γ, or beam stiffness, D, can be manipulated to generate multiple crypts. Since we regard the beam's bending stiffness as a function of position, we solve (2.1), (2.10) and (2.11b) in favour of (2.69a). We redefine $\beta_0 = k^* L_0^{*4}/D^*_{\max}$ to account for the dependence of D^* upon s^*, allowing the governing equations to be written in terms of dimensionless bending stiffness $D = D^*/D^*_{\max}$. The resulting system of equations is as follows:

$$\frac{\partial \theta}{\partial s} = -\beta_0 \frac{M}{D}, \tag{2.91a}$$

$$\frac{\partial M}{\partial s} = F_y \cos\theta - F_x \sin\theta, \tag{2.91b}$$

$$\frac{\partial F_x}{\partial s} = T_x, \qquad \frac{\partial F_y}{\partial s} = T_y, \tag{2.91c}$$

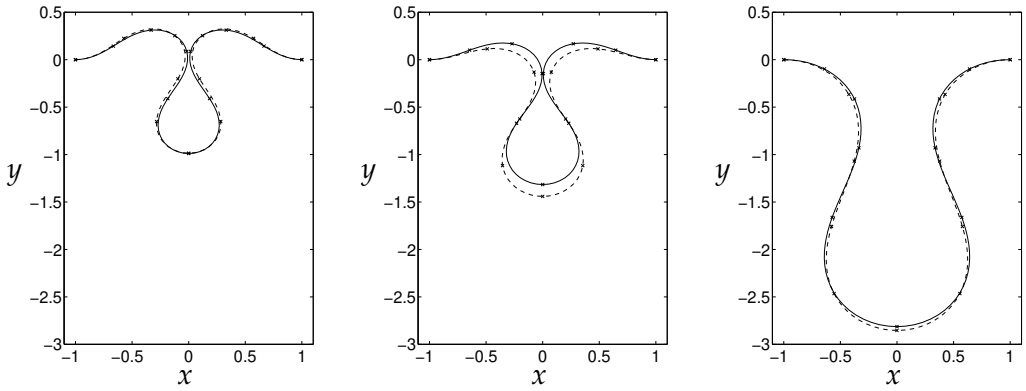

(a) $\beta_0 = 10$, $\beta_T = 0$ (b) $\beta_0 = 10$, $\beta_T = 1$ (c) $\beta_0 = 10$, $\beta_T = 100$

Figure 2.20: Comparison of buckled profiles in the uniform growth regime (dashed lines) against those of equivalent lengths obtained when growth is stimulated by depth of invagination with $\alpha = 1$ (solid lines).

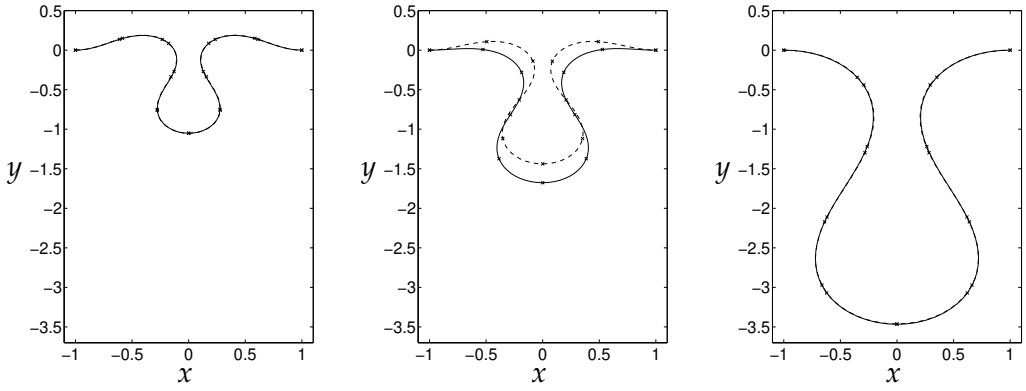

(a) $\beta_0 = 10$, $\beta_T = 0$ (b) $\beta_0 = 10$, $\beta_T = 1$ (c) $\beta_0 = 10$, $\beta_T = 100$

Figure 2.21: Comparison of buckled profiles in the uniform growth regime (dashed lines) against those of equivalent lengths obtained when growth is restricted by compression with $\alpha = 1$ (solid lines).

$$\frac{\partial x}{\partial s} = \cos\theta, \qquad \frac{\partial y}{\partial s} = \sin\theta, \tag{2.91d}$$

$$\frac{\partial T_x}{\partial t} + \Gamma(s)\frac{\partial T_x}{\partial s} + \beta_T T_x = \Gamma(s)\frac{\partial x}{\partial s} + \frac{\partial x}{\partial t}\,, \tag{2.91e}$$

$$\frac{\partial T_y}{\partial t} + \Gamma(s)\frac{\partial T_y}{\partial s} + \beta_T T_y = \Gamma(s)\frac{\partial y}{\partial s} + \frac{\partial y}{\partial t}\,, \tag{2.91f}$$

together with the boundary conditions

$$\theta(\pm L, t) = 0, \qquad x(\pm L, t) = \pm 1, \qquad y(\pm L, t) = 0, \tag{2.92}$$

and the initial conditions

$$T_x(s, 0) = 0, \qquad T_y(s, 0) = 0, \qquad L(0) = 1. \tag{2.93}$$

We prescribe variations of γ and D inside two patches initially separated a distance $2L_1$ and initially of width L_2 (for $0 < L_1, L_2 < 1$). In the grown configuration we denote the location of the patches by $s^- \leq |s| \leq s^+$ (where $s^+ > s^-$), with s^- and s^+ evolving according to

$$\frac{\mathrm{d}s^-}{\mathrm{d}t} = \Gamma\left(s^-\right), \quad s^-(0) = L_1, \tag{2.94a}$$

$$\frac{\mathrm{d}s^+}{\mathrm{d}t} = \Gamma\left(s^+\right), \quad s^+(0) = L_1 + L_2. \tag{2.94b}$$

We consider two regimes here, independently varying growth and beam stiffness from the uniform configuration. Firstly, we consider a regime in which growth occurs uniformly ($\gamma \equiv 1$) and beam stiffness is significantly reduced to $D = D_P \ll 1$ inside the patches, *i.e.*

$$D(s) = \begin{cases} D_P & s^- \leq |s| \leq s^+, \\ 1 & \text{otherwise.} \end{cases} \tag{2.95}$$

We compare the resulting buckling to that of a second regime in which the beam stiffness is uniform ($D \equiv 1$) but growth is restricted to the patches described above. Inside the patches, growth is considered uniform, *i.e.*

$$\gamma(s) = \begin{cases} 1 & s^- \leq |s| \leq s^+, \\ 0 & \text{otherwise.} \end{cases} \qquad \Gamma(s) = \begin{cases} 0 & 0 \leq |s| \leq s^-, \\ \mathrm{sgn}(s)\,(s - s^-) & s^- \leq |s| \leq s^+, \\ \mathrm{sgn}(s)\,(s^+ - s^-) & \text{otherwise.} \end{cases} \tag{2.96}$$

Figure 2.22 illustrates the buckling attained in each of these regimes. The parameters used in the figure are selected to best illustrate obtainable crypt profiles. Varying L_1 and keeping L_2 fixed, we observe that in the regime of non-uniform beam stiffness (figure 2.22(a-c)) we obtain a single crypt for $L_1 = 0$ and a transition to a two-crypt profile for $L_1 > 0$. As L_1 is increased, the crypts are pushed away from each other towards the

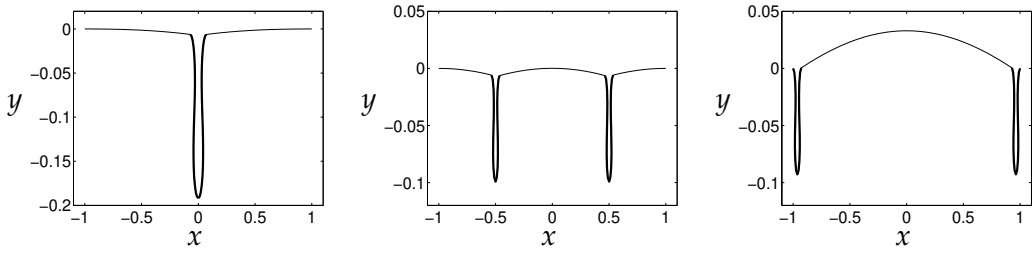

(a) $L_1 = 0$ (b) $L_1 = 0.4$ (c) $L_1 = 0.8$

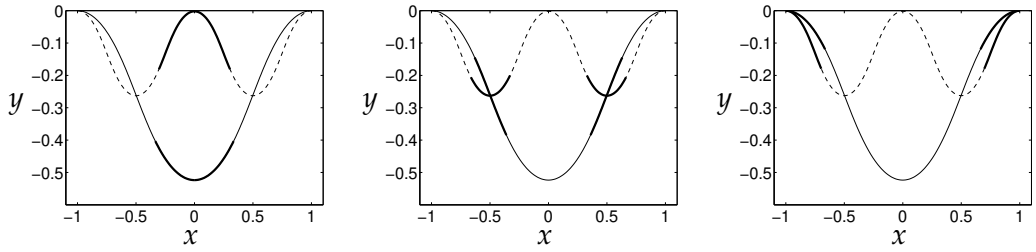

(d) $L_1 = 0$ (e) $L_1 = 0.4$ (f) $L_1 = 0.8$

Figure 2.22: Buckling obtained under patterning of growth and beam stiffness, for $\beta_0 = \beta_T = 1$ and $L_2 = 0.2$. In (a-c) we pattern beam stiffness, with $D_P = 0.001$, yielding a transition from a single-crypt profile for $L_1 = 0$ (a) to two-crypt profiles for $L_1 = 0.4$ (b) and $L_1 = 0.8$ (c). Profiles are plotted at $t = 0.15$, heavier lines represent more flexible regions. In (d-f) we impose a patterning of growth, with $D \equiv 1$. Profiles of mode 1 (solid lines) and mode 3 (dashed lines) are plotted at $t = 0.59$ for (d) $L_1 = 0$, (e) $L_1 = 0.4$ and (f) $L_1 = 0.8$; heavier lines represent growing regions.

boundaries. Buckling is primarily confined to those regions which exhibit the greatest flexibility. When considering a patterning of growth, however, such two-crypt profiles are not obtainable. Solutions corresponding to modes 1 and 3 are illustrated in figure 2.22(d-f); we see that the shapes of these configurations are largely independent of the location of growth. We conclude, therefore, that the modulation of growth is not a sufficient mechanism to control the buckling wavelength. Modulating the stiffness of the beam, however, has the desired effect.

2.3 Summary

In this chapter, we have adapted the model for crypt budding and fission presented by Edwards & Chapman (2007) to consider colorectal crypt formation. In doing so we

have built upon the linear analysis presented by Edwards & Chapman to illustrate that buckling in the nonlinear regime yields profiles reminiscent of colorectal crypts. We have illustrated the family of buckling modes obtained and have shown how the model parameters determine selection of configuration type. Our analysis revealed that (as demonstrated by Edwards & Chapman (2007)) the wavelength of the primary buckling mode is determined by the relative stiffnesses of beam and springs (β_0); stronger attachment to the underlying stroma results in a highly wrinkled configuration.

In section 2.2, we developed the model of epithelial growth presented by Edwards & Chapman to yield a system of governing equations capable of assessing the effects of a non-uniform growth pattern upon the buckled epithelial profile. To allow for substrate remodelling due to cellular migration, we also incorporated viscoelastic relaxation of cellular attachments. We illustrated that this viscoelastic stress relaxation is key to the obtaining of a crypt-like geometry, rather than the 'wrinkled' configuration which is ultimately yielded in the regime of linear springs. Our studies of uniform and non-uniform growth patterns illustrated that buckled states are relatively insensitive to patterning of growth. Crypt-like profiles are maintained upon the confinement of growth to a central portion of the layer (analogous to the proliferating compartment which resides at the crypt base *in vivo*), and upon allowing growth to be stimulated by deep invagination or restricted by high compression (analogous to the effects of a chemical gradient and contact inhibition respectively). Buckling due to growth in a central compartment was shown to delay the pinching-off of the crypt opening and, hence, we were able to generate longer crypts within the confines of this model's validity. The crypt walls were also shown to be straighter in this growth regime, to an extent dependent upon the relative stiffnesses of beam and springs (β_0). Studies of spatial patterning of growth and mechanical properties provided significant evidence that crypt frequency cannot be controlled by patterning of growth. Imposing variations in tissue stiffness, however, can act as an effective mechanism for the control of crypt distribution.

We note here that the model presented in this chapter exhibits some short-comings. Primarily, the model fails to capture the deformation of the sub-epithelial mucosa. As such, the spring model of cellular attachment could be considered unrealistic since the points of attachments of the springs are not altered as the epithelium buckles. This motivates further consideration of how best to model the substrate. We revisit this issue in chapter 4. Also, we were not able to examine the epithelial geometry once two distinct points of the epithelium come into contact; this may play an important role in determining the shape of buckled profiles *in vivo*.

CHAPTER 3

In-Vitro Analysis of Cell Proliferative Forces

In this chapter, we discuss an *in-vitro* study to investigate the hypothesis that colorectal crypts form due to a build up of compressive stresses in the developing epithelium. Our approach is to culture a population of intestinal epithelial cells upon a flexible substrate until confluent. Under standard culture conditions upon a rigid surface, proliferation would be halted due to contact inhibition once the cell layer reached confluence. We examine whether the cells are able to exert sufficient force to deform the flexible substrate as they approach confluence. Deformation of the substrate would yield a greater surface area, perhaps allowing proliferation to continue. We elect to work with the rat intestinal epithelial cell line IEC6, since these cells are readily available, form a regular "cobblestone" monolayer which is highly similar to the human intestinal epithelium, and exhibit the required contact inhibition behaviour (Quaroni *et al.*, 1979; Beauchamp *et al.*, 1996).

Formulation of a suitable experimental protocol was hindered by a number of technical challenges. Primarily, the cell culture surface must be sufficiently flexible to allow cells to induce deformations, while being sufficiently robust to facilitate manipulation during culture and imaging. Some materials were identified to have the required mechanical properties, but their use was not practical since they were not amenable to the culture of this particular cell line (often resulting in an abnormal cell morphology). The final challenge lies in measuring deformations. Ideally, we would measure substrate deflections via a side-on microscope image of the substrate. However, with the equipment available, we were only able to take microscope images from above. Other techniques, such as X-ray microtomography, were considered; however, these were not practical due to the size of the samples and the fact that cells would be killed upon

scanning, potentially disrupting substrate deflections. A number of experimental approaches were trialled, including fabrication of substrates from agarose, glucose and collagen gels for subsequent analysis using histology; however, these methods were unsuccessful. We omit further details of this preliminary work here.

The experimental protocol discussed below was designed in collaboration with Dr. Daniel Howard (Tissue Engineering & Drug Delivery Group, School of Pharmacy, University of Nottingham) and was based upon similar work by Feinberg *et al.* (2007) in which rat ventricular cardiomyocytes were cultured upon a flexible polydimethylsiloxane (PDMS) membrane. Feinberg *et al.* (2007) showed that these cardiomyocytes were able to generate membrane deformations. We note, however, that cardiomyocytes are able to actively contract to drive these deformations. This is in strong contrast to the study presented here, in which we focus upon the forces resulting from expansion of the cell layer against fixed boundaries.

The protocol of Feinberg *et al.* required extensive modification prior to this study, primarily focused upon functionalisation of the substrates for IEC6 cell culture and creation of a supporting structure in which the substrates could be held. Having completed this preliminary work, the remaining time available was only sufficient for preliminary data to be collected. However, the data presented below do act as a proof of the principle that in-plane compression in the epithelial cell layer can be sufficient to induce buckling in the developing intestine *in vivo*.

3.1 Methods

Our experimental approach can broadly be divided into four tasks: (i) fabrication of substrates, (ii) modification of the substrates' surfaces to facilitate cell adhesion, (iii) cell culture, and (iv) measurement of substrate deflections. For the former, we follow the protocol of Feinberg *et al.* (2007) to produce substrates made from PDMS, a silicon-based elastomer (further details are given in section 3.1.1). Several standard surface modification techniques were trialled, we briefly discuss the optimal strategy in section 3.1.3. Cell culture methods followed published guidelines (see section 3.1.4). The deflection measurement techniques discussed in section 3.1.5 were designed specifically for this study.

3.1.1 Casting substrates

PDMS substrates were fabricated by depositing a prescribed quantity of Sylgard 184 silicone elastomer (PDMS; Dow Corning, density 1.09 g/cm^3, prepared as per the manufacturer's instructions) upon glass disks and spinning at high speed using a Laurell WS-650SX-23NPP/LITE spin coater.

Prior to coating, circular glass disks of 22mm diameter were cleaned with a 0.01% (*w/v*) solution of sodium dodecyl sulphate (SDS, a detergent) before extensively rinsing with reverse osmosis (RO) water (filtered with resistance of 18MΩ to remove impurities). These disks were then coated with a 30% (*w/v*) solution of poly-vinyl alcohol (PVA), spun at 3000rpm and left flat to dry overnight. This PVA coating forms a sacrificial layer which can be dissolved to facilitate release of the PDMS from the glass.

A 2ml deposit of PDMS was then added to the PVA-coated disks, which were then spun at high speed and cured overnight, level in a 50°C oven. Varying the spin speed enabled the thickness of the PDMS layer to be controlled. An optimal speed of 8000rpm was selected, which produces a PDMS layer of $12.22 \pm 0.97\mu$m thickness. This substrate thickness was chosen since the study of Feinberg *et al.* (2007) showed that membranes of thickness less than 25μm are amenable to deformation (albeit by a different cell line).

A nylon washer of 6.5mm internal diameter, 13mm external diameter and 1.5mm thickness was attached to the cured substrate using a 50μm deposit of PDMS and cured in position. The substrate and washer were then removed from the glass by incubating the substrate in water at 37°C over 3 days to remove the PVA layer and then leaching for a further day to remove excess PVA. A second nylon washer was then attached to the other side of the substrate by repeating this process.

3.1.2 Mechanical testing of substrates

The final substrates were mechanically tested using a Stable Microsystems TA HD plus texture analyser equipped with a Peltier temperature control system. Substrates were submerged in a phosphate buffered saline (PBS) solution and kept at $37°C$ to mimic experimental conditions. A spherically-tipped probe (of radius $R^* = 2.5$mm) was moved into the membrane from above, inducing substrate stretching; the resistive force upon the probe was recorded as a function of indentation distance. The substrate was held in a clamp designed to allow free movement of solution around the sample and the probe tip was submerged prior to the test to avoid surface-tension effects. The probe was moved into the substrate at 0.1mm/s and the resistive force was measured by a 5kg load cell.

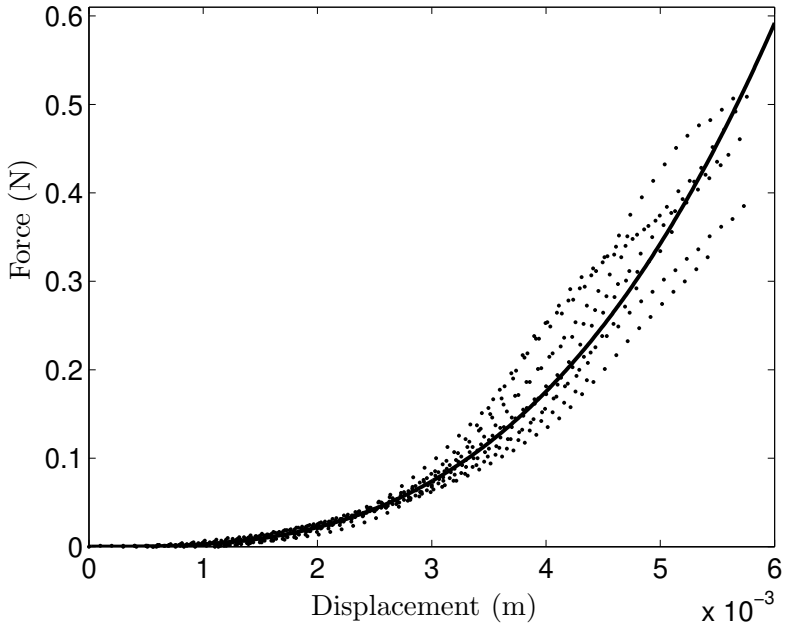

Figure 3.1: Force–displacement data for PDMS substrates with $L^* = 3.25$mm, $h^* = 12$mm and $R^* = 2.5$mm (dotted). The line of best fit (solid) corresponds to (3.1) with $E^* = 1.41$MPa.

We compare our force–displacement data to a theoretical model of the same system presented by Begley & Mackin (2004). The authors model the substrate as an incompressible neo-Hookean material which is linearly elastic for small strains (see section 1.6.1). Deformations are assumed axisymmetric. Taking a membrane approximation, the substrate's bending stiffness is considered negligible compared to its stretching stiffness. In the limit of zero pre-stretch, the following relationship between applied force, $\mathcal{F}^*$, and vertical displacement, δ^*, is deduced:

$$\mathcal{F}^* = E^* h^* R^* \frac{9\pi}{16} \left(\frac{R^*}{L^*}\right)^{9/4} \left(\frac{\delta^*}{R^*}\right)^3, \tag{3.1}$$

where $L^* = 3.25$mm is the radius of the substrate, $h^* = 12\mu$m is the substrate's thickness and E^* its Young's modulus. We fit (3.1) to our raw data via a least-squares regression to determine E^* (see figure 3.1). Based upon 12 sets of raw data, we estimate the Young's modulus of the substrate to be $E^* = 1.41 \pm 0.21$MPa.

3.1.3 Surface modification

Cell–substrate attachment relies on interactions between cells and proteins embedded in the substrate surface. Since PDMS does not contain any cell attachment peptides and is strongly hydrophobic, which limits protein interaction, the PDMS substrates do

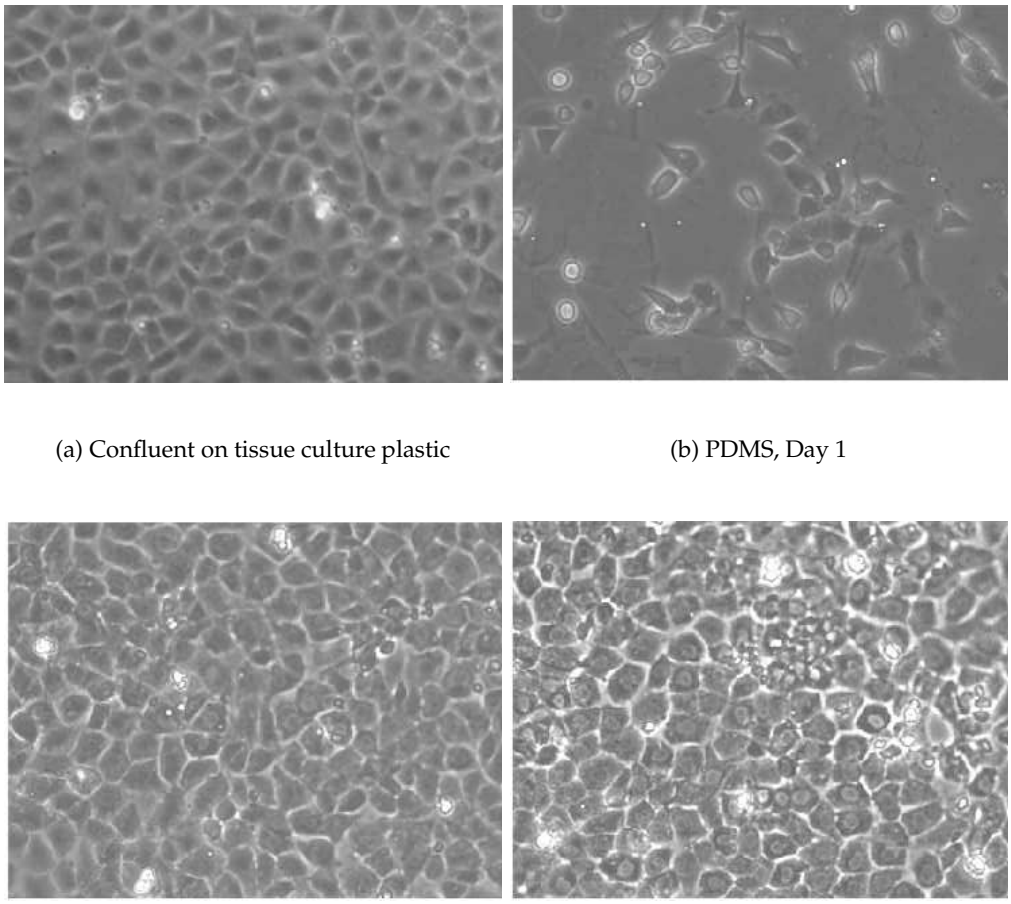

(a) Confluent on tissue culture plastic

(b) PDMS, Day 1

(c) PDMS, Day 6

(d) PDMS, Day 14

Figure 3.2: Adherence and coverage of IEC6 cells on PDMS after surface modification (b-d) in comparison with their normal morphology on tissue culture plastic (a).

not lend themselves well to cell culture. Trials revealed that, when placed upon untreated PDMS, cells will either fail to adhere or will change their morphology, losing the desired cobblestone monolayer conformation. A number of surface modification processes were investigated, to improve the cell adhesion properties. The most effective strategy was found to be coating the PDMS with a 350nm layer of plasma polymerised allyl amine, previously shown to increase cell adherence (Barry *et al.*, 2005; Dehili *et al.*, 2006; Zelzer *et al.*, 2008). As figure 3.2 illustrates, IEC6 cells will adhere to the PDMS substrates after treatment and the characteristic cobblestone morphology is maintained.

3.1.4 IEC6 cell culture and addition to the substrates

IEC6 cells were cultured in Dulbecco's modified eagle medium (DMEM) supplemented with 5% (v/v) fetal bovine serum, one ITS supplement (providing final concentrations of 10μg/ml insulin, 5.5μg/ml human transferrin and 5ng/ml sodium selenite), 2mM L-glutamine and antibiotic solution (giving final concentrations of 100 units penicillin, 0.1mg/ml streptomycin and 500μg/ml gentamicin), as per the guidelines of the European Collection of Cell Cultures (ECACC). When the cells reached approximately 70% confluence they were 'passaged' as follows. Cells were removed from the culture surface by addition of a trypsin solution, incubated at 37°C until detached, isolated by centrifugation, placed in fresh media (where the serum inactivates the trypsin), diluted and added to new flasks to facilitate continued proliferation.

Surface-modified PDMS substrates were added to culture media (5ml per substrate) one hour prior to the addition of the cells, and placed in an incubator at 37°C to temperature stabilise. Cells were removed from the source culture flask with with trypsin as described above, pelleted by centrifugation, resuspended in fresh IEC6 culture media and counted manually using a haemocytometer. Approximately 27,000 cells were added to each substrate, representing an approximate surface coverage of 80% (substrate surface area: 33,166,250μm^2, cell area: 989μm^2, total coverage requires approximately 33,535 cells). Cells were maintained in culture at 37°C for a period of 21 days. For each substrate, 2ml of the culture media was replaced with fresh stock every two days.

To confirm that membrane deformation was attributable to the cells, two further assays were carried out in which cell proliferation was either exaggerated or arrested and substrate deflections were compared. To one strongly deformed substrate, upon which cells were confluent, we added (on day 14) a 200ng/ml supplement of basic fibroblast growth factor (bFGF2) to the culture medium. This growth factor is known to stimulate epithelial cell proliferation *in vitro* (Hu *et al.*, 2009) and was used in this study to assess the effect of enhanced cell proliferation on membrane deformation. Cells were allowed to proliferate for a further 7 days and membrane deformation measurements taken before and after treatment were compared.

A second strongly deformed substrate was treated (on day 21) with a cell lysis buffer, comprising 1% (v/v) Triton X-100, 150mM NaCl, 50mM EDTA, 10mM TRIS-HCl (pH 7.6). The lysis buffer contains a detergent which disrupts lipids such as those in the cell membranes, effectively killing the cells. Pre-treatment deflections were compared with deflections 30 minutes after treatment, allowing the extent to which the membrane

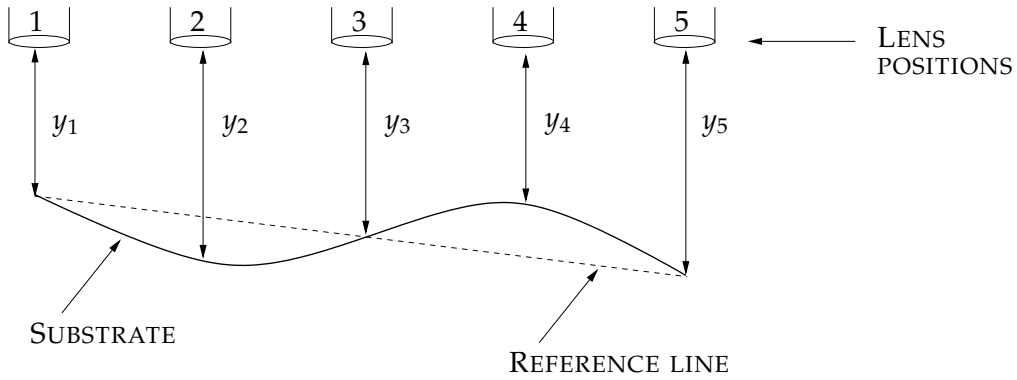

Figure 3.3: Schema of the substrate imaging process. Images are taken at five points along an arbitrary diameter and the focal distance of each image ($y_1, \ldots, y_5$) is recorded. Taking the difference between y_1 and y_5, we can identify a reference line (dashed) to account for any inaccuracies in sample orientation. In forthcoming figures, the deflections plotted refer to the differences between the solid and dashed lines above.

flattens in the absence of the cells to be quantified.

3.1.5 Image analysis and measurement of membrane deflection

Substrates and cells were observed using a Leica DM-RBE cell culture microscope equipped with an environmental chamber (images and measurements were taken at 37°C to avoid any temperature effects). As figure 3.3 illustrates, images were taken at five equidistant points along an arbitrary diameter. At each point the lens was re-focused and the focal distance was recorded using Volocity 5 image analysis software. The magnitude of substrate deflections was calculated by taking the difference in focal distance between the five points, having corrected the data to set the measurements on the boundary to zero (accounting for any small errors in the orientation of the sample). Substrate height could be measured to within an accuracy of $\pm 8.1\mu$m (calculated by refocussing the lens on 2μm fluorescent beads of known position).

3.2 Results

Figure 3.4 illustrates the substrate deflections observed after fourteen days in culture. From figure 3.4(a) we confirm that the proliferation of the IEC6 cells is able to generate sufficient cellular compression to drive substrate deformations. We compare these configurations to control substrates illustrated in figure 3.4(b), which were placed under

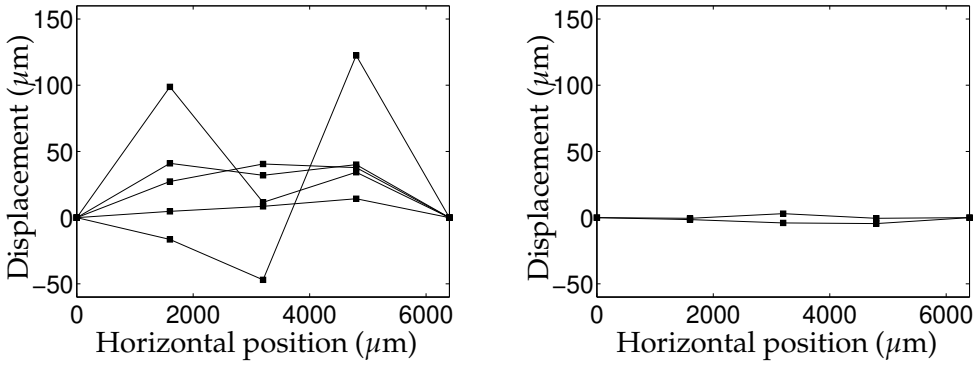

(a) (b)

Figure 3.4: (a) Deflections of five substrates after 14 days (each line represents one substrate). (b) Control membranes under identical conditions, but in the absence of cells. The horizontal axis represents lens position along a diameter, zero being defined on the disc's circumference.

identical environmental conditions but with no cells added. Deflections of the control substrates were negligibly small (within the experimental error of the measurement process), giving us a sound basis to attribute deformations to the action of the cells.

As figure 3.4(a) illustrates, both the magnitude of deflections and the shape of adopted configurations varied greatly between substrates. In the terminology of chapter 2, we see configurations which broadly resemble types 1, 2 and 3; the maximal deflection being 122.5μm. We will revisit the issue of configuration selection mathematically in the model of chapter 4.

In figures 3.5 and 3.6 we briefly expand upon the connection between proliferation rate and substrate deflection. In figure 3.5 we add a basic fibroblast growth factor (bFGF2) to a strongly deformed substrate on day 14, promoting cell proliferation. We allow the cells to continue to proliferate for a further seven days. Comparing figures 3.5(b) and 3.5(c), we see that the cells are more densely packed and are greater in number after addition of the growth factor. The deflection of the substrate is shown to increase with cell density (figure 3.5(a)).

In figure 3.6 we take a strongly deformed substrate on day 21 and add a lysis buffer, which effectively kills the cells by disrupting their cell membranes. In figure 3.6(b) we see a region in which cells are in focus and a region in which cells are out of focus, indicating a difference in the height of the substrate across this image. Thirty minutes after the addition of the lysis buffer, we see (figure 3.6(c)) that all cells have now moved out

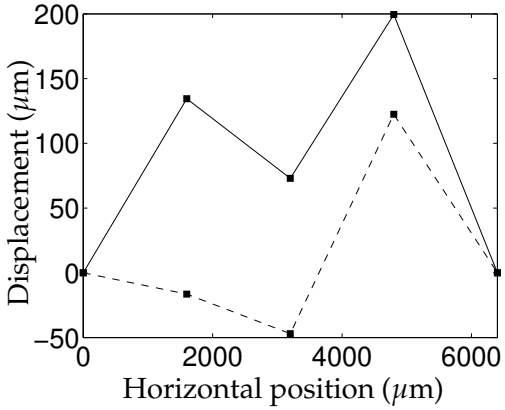

(a) Substrate deflection before (dashed line) and after (solid line) addition of bFGF2.

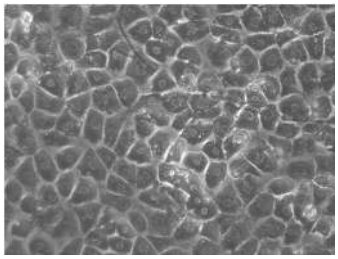

(b) Before bFGF2 (day 14).

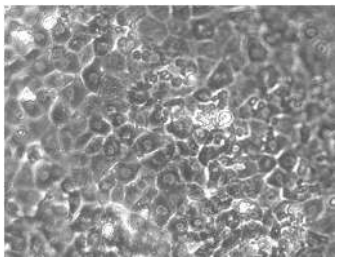

(c) After bFGF2 (day 21).

Figure 3.5: Increased cell density and exaggerated substrate deflection after addition of growth factor bFGF2 on day 14.

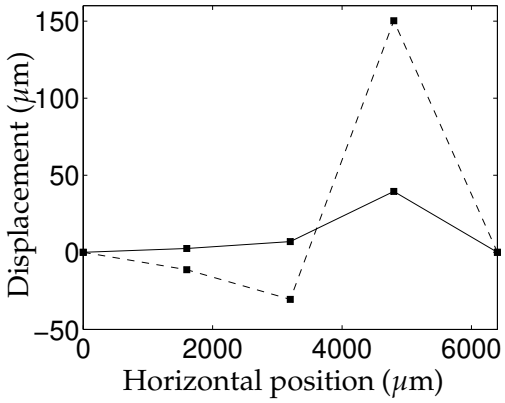

(a) Substrate deflection before (dashed line) and after (solid line) addition of lysis buffer.

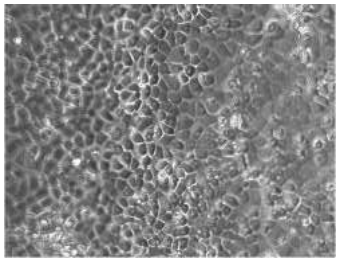

(b) Before lysis (day 21).

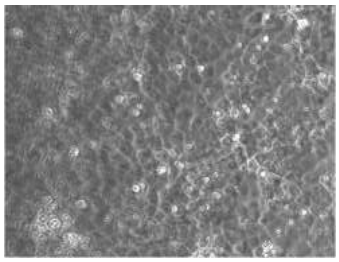

(c) After lysis (+30 mins).

Figure 3.6: Flattening of a substrate 30 minutes after addition of a cell lysis buffer.

of focus as the substrate flattens (the focal distance of the microscope is unchanged between these two images). The substrate approximately returns to its flat configuration, as shown in figure 3.6(a).

3.3 Discussion

While the results above must be regarded as preliminary, given the small sample size, we do have sufficient evidence to validate the proposed buckling mechanism. Comparison with controls suggests that substrate deflections are solely due to cellular proliferation, given that in the absence of the cells significant deflections are not observed. The magnitude of deflections seems to be dependent upon proliferation rate: configurations are exaggerated by the addition of a growth factor and significantly reduced when cells are lysed *in situ*.

Our results suggest that replication of colorectal crypts *in vitro* may not require the fabrication of a complex tissue engineering scaffold with a prescribed crypt-like geometry. We suggest that, given a sufficiently flexible substrate, it may be possible for the epithelial cell population to form crypts unaided. A rigorous examination of how best to facilitate the required framework remains as further work.

One immediate direction for future work would be to repeat the procedure described here to generate data from a greater number of samples. Time constraints prevented the collection of further data for this study. It would be interesting to compare these data with a parallel experiment in which a population of intestinal sub-epithelial myofibroblasts (ISEMFs) is cultured upon the underside of the membrane, replicating the organisation of these cell types *in vivo* (see section 1.1.1). Comparison of the buckling in each setup may yield insight into the role of communication between the epithelial cells and those of the lamina propria in the onset of buckling.

CHAPTER 4

A One-Dimensional Model for Cell Culture upon a Deformable Substrate

In this chapter, we present a mathematical model of the experimental study of chapter 3. We model a cross-section of the silicon substrate via Euler–Bernoulli beam theory, as in chapter 2. The upper surface of the beam is assumed to be covered by a confluent monolayer of n identical cells from the outset (figure 4.1). Cells are modelled as rigid springs connecting at cell boundaries. Cellular growth is incorporated parametrically via prescribed increases in the springs' unstressed lengths. Growth of the cell layer generates compressive stresses therein, which may induce bending and stretching of the substrate under appropriate conditions.

While the formulation of this model is motivated by *in-vitro* work, we may also draw analogy with an epithelium attached to underlying tissue *in vivo*. The model below can, therefore, be thought to improve upon the model of the lamina propria in chapter 2, incorporating large-amplitude deformations thereof. This model separately accounts for stresses in the two layers: while the cell layer is under compression, the underlying buckled material is under extension. This presents an extension to chapter 2, in which the effects of the material's extensibility upon buckled configurations were not studied.

The silicon substrate is modelled as an extensible beam of undeformed, unstressed length $2L^*$ and thickness h^*. Once more, we assume that $h^* \ll L^*$ and characterise the profile of the substrate by that of its centreline. The substrate bending stiffness is denoted $D^* = E^* h^{*3}/12(1-\nu^2)$, for Young's modulus E^* and Poisson's ratio ν. The cells' resistance to expansion is characterised by spring stiffness parameter k^*, with dimensions of force per unit area. We assume that, to leading order, the cells remain

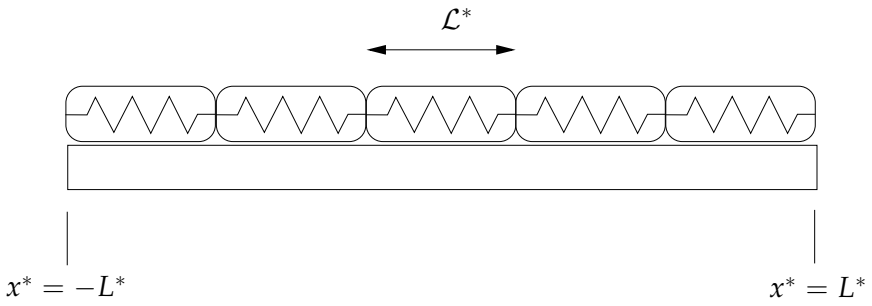

Figure 4.1: Schema of a cell layer upon a deformable substrate. The cell layer is modelled as n linear springs connecting at cell junctions, while the substrate is modelled as an Euler–Bernoulli beam.

flat during deformation. The length of the j^{th} cell is denoted $\mathcal{L}_j^*$, and in the undeformed configuration $\mathcal{L}_j^* = 2L^*/n$ for any $j \in [1, n]$. Preserving the notation of chapter 2, we denote Cartesian coordinates by x^* and y^*, respectively oriented horizontally and vertically. In the reference configuration, the substrate lies along the line $y^* = 0$. The inclination of the substrate to the horizontal is denoted by $\theta(s^*)$, where s^* is the arc-length from the centre of the substrate in the deformed configuration. In-plane and out-of-plane substrate stress resultants are denoted F_T^* and F_N^* respectively and the tension in the cell layer is denoted T^*. The curvature of the substrate is denoted by κ^*.

4.1 Model derivation

4.1.1 Force balances in the cell layer

We begin with a discrete representation of the cells in the cell layer. Cells are treated as straight line elements, as illustrated in figure 4.2. Denoting the angle of inclination of cell j to the horizontal by θ_j, we define unit vectors $\mathbf{t}_j$ and $\mathbf{n}_j$ to lie tangentially and normally to cell j, so that

$$\mathbf{t}_j = \left(\cos\theta_j, \sin\theta_j\right), \tag{4.1a}$$

$$\mathbf{n}_j = \left(\sin\theta_j, -\cos\theta_j\right). \tag{4.1b}$$

Since frictional forces between the substrate and the cell layer result in variations in tension across the length of a cell, we introduce the notation T_j^{-*} and T_j^{+*} to denote the tensions at the left and right boundaries of cell j respectively. We consider that cell j is under the action of forces (per unit length) generated by tensions in neighbouring cells, T_{j-1}^{+*} and T_{j+1}^{-*}, and due to friction and normal reaction with the substrate, Q_j^* and R_j^* respectively, which have dimensions of force per unit area and are assumed to act

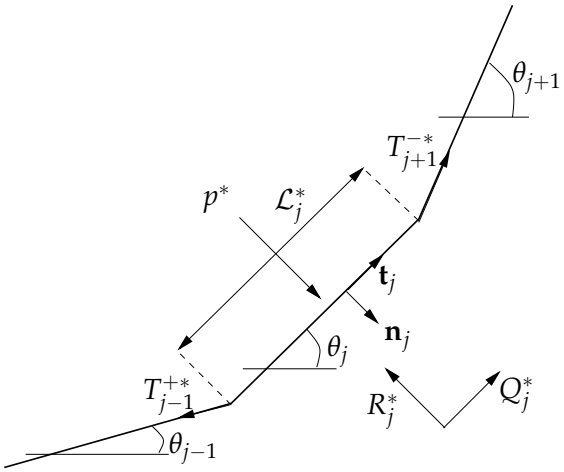

Figure 4.2: Schema showing the forces acting upon cell j owing to neighbouring cells, the substrate and pressure p^*, which acts to deform the layer downwards.

uniformly along the length of the cell to leading order. Furthermore, we incorporate a constant pressure p^* (with dimensions of force per unit area) which acts normally to the layer from above, as illustrated in figure 4.2. The net force per unit length upon cell j, denoted $\mathbf{F}_j^*$, is given by

$$\mathbf{F}_j^* = T_{j+1}^{-*}\mathbf{t}_{j+1} - T_{j-1}^{+*}\mathbf{t}_{j-1} + Q_j^*\mathcal{L}_j^*\mathbf{t}_j - R_j^*\mathcal{L}_j^*\mathbf{n}_j + p^*\mathcal{L}_j^*\mathbf{n}_j. \tag{4.2}$$

Assuming that the angle of inclination, θ, is slowly varying between neighbouring cells, we can write $\mathbf{t}_{j\pm1}$ in terms of $\mathbf{t}_j$ and $\mathbf{n}_j$ as follows. We expand the trigonometric functions in (4.1a) as functions of θ_j, treating $(\theta_j - \theta_{j\pm1})$ as a small parameter, yielding

$$\begin{aligned}\mathbf{t}_{j\pm1} &= \left(\cos\theta_{j\pm1}, \sin\theta_{j\pm1}\right) \\ &= \left(\cos\theta_j + \left(\theta_j - \theta_{j\pm1}\right)\sin\theta_j, \sin\theta_j - \left(\theta_j - \theta_{j\pm1}\right)\cos\theta_j\right) + O\left(\left(\theta_j - \theta_{j\pm1}\right)^2\right) \\ &= \mathbf{t}_j + \left(\theta_j - \theta_{j\pm1}\right)\mathbf{n}_j + O\left(\left(\theta_j - \theta_{j\pm1}\right)^2\right).\end{aligned} \tag{4.3}$$

Thus, neglecting terms of $O((\theta_j - \theta_{j\pm1})^2)$, (4.2) becomes

$$\mathbf{F}_j^* = \left(T_{j+1}^{-*} - T_{j-1}^{+*} + Q_j^*\mathcal{L}_j^*\right)\mathbf{t}_j + \left(T_{j+1}^{-*}\left(\theta_j - \theta_{j+1}\right) + T_{j-1}^{+*}\left(\theta_{j-1} - \theta_j\right) + \left(p^* - R_j^*\right)\mathcal{L}_j^*\right)\mathbf{n}_j. \tag{4.4}$$

If the cell layer is in equilibrium, (4.4) yields

$$Q_j^*\mathcal{L}_j^* = T_{j-1}^{+*} - T_{j+1}^{-*}, \tag{4.5a}$$

$$R_j^*\mathcal{L}_j^* = T_{j+1}^{-*}\left(\theta_j - \theta_{j+1}\right) + T_{j-1}^{+*}\left(\theta_{j-1} - \theta_j\right) + p^*\mathcal{L}_j^*. \tag{4.5b}$$

4.1.2 Continuum approximation of the cell layer

We wish to couple (4.5) to the substrate equations given in chapter 2. Since the substrate equations are given in terms of continuous variables, we now formulate a continuum approximation to the system of discrete equations given above by re-writing in terms of continuous, smoothly varying functions. The process by which we obtain a continuum model below is based upon that of Fozard *et al.* (2010). To avoid confusion between continuous dependent variables and their discrete counterparts, we denote continuous dependent variables with hats.

We define the appropriate continuous variables in terms of the independent variable v, which replaces the cell index j above. We regard variables evaluated between $v = j$ and $v = j + 1$ to refer to cell j in the discrete system. Since Q_j^*, R_j^* and θ_j are constant along the length of cell j, we have the freedom to define their continuous analogues such that they are exact at the cell-centre, denoted $v = j + 1/2$. Thus, we set

$$Q_j^* \mapsto \hat{Q}^*\Big|_{v=j+1/2}, \qquad R_j^* \mapsto \hat{R}^*\Big|_{v=j+1/2}, \qquad \theta_j \mapsto \hat{\theta}\Big|_{v=j+1/2}. \tag{4.6}$$

We define the continuous analogue of $\mathcal{L}_j^*$ in a corresponding manner, setting

$$\mathcal{L}_j^* \mapsto \hat{\mathcal{L}}^*\Big|_{v=j+1/2}. \tag{4.7}$$

When approximating T^* by its continuous counterpart, we define $\hat{T}^*$ such that

$$T_j^{-*} \mapsto \hat{T}^*\Big|_{v=j}, \qquad T_j^{+*} \mapsto \hat{T}^*\Big|_{v=j+1}. \tag{4.8}$$

For convenience we scale v against the number of cells in the system, n, setting

$$v = n\bar{v}, \tag{4.9}$$

which facilitates the following Taylor expansions of $\hat{T}^*$ about the centre of the j^{th} cell, $\bar{v} = j/n + 1/2n$, treating $1/2n$ as a small parameter:

$$\hat{T}^*\Big|_{v=j} = \hat{T}^*(\bar{v}) - \frac{1}{2n}\frac{\mathrm{d}\hat{T}^*}{\mathrm{d}\bar{v}} + O\left(\frac{1}{n^2}\right), \tag{4.10a}$$

$$\hat{T}^*\Big|_{v=j+1} = \hat{T}^*(\bar{v}) + \frac{1}{2n}\frac{\mathrm{d}\hat{T}^*}{\mathrm{d}\bar{v}} + O\left(\frac{1}{n^2}\right), \tag{4.10b}$$

where all quantities on the right-hand sides of (4.10) are evaluated at $\bar{v} = j/n + 1/2n$. Similar expansions hold for θ_{j+1} and θ_j. In terms of continuous variables, (4.5) becomes

$$\hat{Q}^*\hat{\mathcal{L}}^* = -\frac{1}{n}\frac{\mathrm{d}\hat{T}^*}{\mathrm{d}\bar{v}}, \tag{4.11a}$$

$$\hat{R}^*\hat{\mathcal{L}}^* = p^*\hat{\mathcal{L}}^* - \frac{1}{n}\frac{\mathrm{d}\hat{\theta}}{\mathrm{d}\bar{v}}\hat{T}^*, \tag{4.11b}$$

having neglected terms of $O(1/n^2)$ and smaller. We now write (4.11) in terms of the geometric variable $\hat{s}^*$, which measures distance from the centre of the substrate, in preference to the cell number variable $\bar{v}$. We denote the position of the centre of cell j by

$$\hat{s}^*\Big|_{\bar{v}=\frac{j}{n}+\frac{1}{2n}}. \tag{4.12}$$

Given that the $\hat{s}^*$-locations of the edges of cell j satisfy

$$\hat{s}^*\Big|_{\frac{j+1}{n}} - \hat{s}^*\Big|_{\frac{j}{n}} = \mathcal{L}_j^*, \tag{4.13}$$

we have

$$\frac{\mathrm{d}\hat{s}^*}{\mathrm{d}\bar{v}} = n\hat{\mathcal{L}}^*, \tag{4.14}$$

having neglected terms of $O(1/n^2)$. Under this change of variable (4.11) becomes

$$\hat{Q}^* = -\frac{\mathrm{d}\hat{T}^*}{\mathrm{d}\hat{s}^*}, \tag{4.15a}$$

$$\hat{R}^* = p^* - \hat{\kappa}^*\hat{T}^*, \tag{4.15b}$$

where the curvature, $\hat{\kappa}^*$, of the layer is given by

$$\hat{\kappa}^* = \mathrm{d}\hat{\theta}/\mathrm{d}\hat{s}^*. \tag{4.16}$$

In the forthcoming sections, all variables are continuous and we omit hats for brevity.

4.1.3 Substrate equations

It remains to couple the force balances from above to the equations governing the forces and moments acting upon the substrate (as illustrated in figure 4.3). We once more assume the Euler–Bernoulli relation (2.1), alongside the moment balance on the substrate given in (2.10):

$$\kappa^* = -\frac{M^*}{D^*}, \qquad \frac{\mathrm{d}M^*}{\mathrm{d}s^*} = -F_N^*, \tag{4.17}$$

which we combine to yield

$$\frac{\mathrm{d}\kappa^*}{\mathrm{d}s^*} - \frac{1}{D^*}F_N^* = 0, \tag{4.18}$$

which is analogous to (2.12). Performing a force balance upon an element of the substrate of length $\mathrm{d}s^*$, we have

$$\left(F_T^*\hat{\mathbf{t}} + F_N^*\hat{\mathbf{n}}\right)\Big|_{s^*+\mathrm{d}s^*} - \left(F_T^*\hat{\mathbf{t}} + F_N^*\hat{\mathbf{n}}\right)\Big|_{s^*} - \mathrm{d}s^*Q^*\hat{\mathbf{t}} + \mathrm{d}s^*R^*\hat{\mathbf{n}} = \mathbf{0}. \tag{4.19}$$

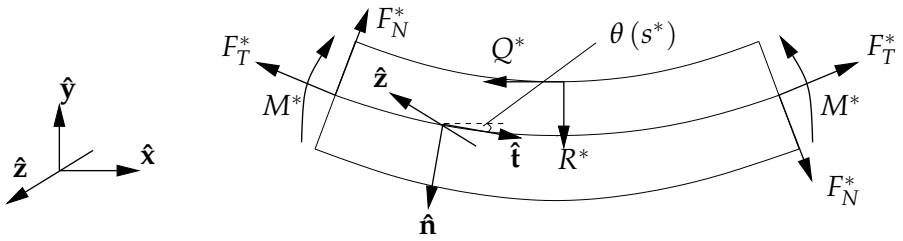

Figure 4.3: Distribution of forces (per unit length) along an element of the substrate, and the resultant stresses and bending moments. Internal forces Q^* and R^* are equal and opposite to those acting in the cell layer in figure 4.2. Clockwise arrows indicate bending moments acting the negative $\hat{\mathbf{z}}$-direction.

We Taylor expand (4.19), noting the following expressions for the derivatives of the unit vectors:

$$\frac{\mathrm{d}\hat{\mathbf{t}}}{\mathrm{d}s^*} = -\kappa^*\hat{\mathbf{n}}, \qquad \frac{\mathrm{d}\hat{\mathbf{n}}}{\mathrm{d}s^*} = \kappa^*\hat{\mathbf{t}}. \tag{4.20}$$

Resolving into tangential and normal components, the resulting equations are

$$\frac{\mathrm{d}F_T^*}{\mathrm{d}s^*} + \kappa^* F_N^* - Q^* = 0, \tag{4.21a}$$

$$\frac{\mathrm{d}F_N^*}{\mathrm{d}s^*} - \kappa^* F_T^* + R^* = 0, \tag{4.21b}$$

to leading order. From (4.15), it follows that

$$\frac{\mathrm{d}F_T^*}{\mathrm{d}s^*} = -\kappa^* F_N^* - \frac{\mathrm{d}T^*}{\mathrm{d}s^*}, \tag{4.22a}$$

$$\frac{\mathrm{d}F_N^*}{\mathrm{d}s^*} = \kappa^* F_T^* - p^* + \kappa^* T^*. \tag{4.22b}$$

We also have the following relations between $\theta(s^*)$ and the Cartesian coordinate system (x^*, y^*)

$$\frac{\mathrm{d}x^*}{\mathrm{d}s^*} = \cos\theta, \qquad \frac{\mathrm{d}y^*}{\mathrm{d}s^*} = \sin\theta. \tag{4.23}$$

It will be convenient to rewrite the system in terms of the Lagrangian arc-length, denoted $\tilde{s}^*$. We define the in-plane stretch, λ, according to

$$\lambda = \frac{\mathrm{d}s^*}{\mathrm{d}\tilde{s}^*}. \tag{4.24}$$

We quantify the substrate stretch in a manner consistent with Edwards & Chapman (2007) and (2.18), via the assumption that material strains are proportional to in-plane stresses:

$$F_T^* = E^* h^* (\lambda - 1). \tag{4.25}$$

4.1.4 The composite system

To close the system, it remains to prescribe a constitutive assumption for T^*. We restrict our analysis to two cases: that in which cells are fully adhered to the substrate ($Q^* \to \infty$) and that in which cells experience no resistance to sliding along the substrate ($Q^* = 0$). If cells are fully adhered, the stretch of the cells is equal to that of the substrate and we prescribe T^* according to

$$T^* = k^* \left(\lambda - \lambda_G\right), \tag{4.26}$$

where k^* captures the stiffness of the springs and λ_G is a dimensionless parameter which relates the unstressed length of the cells to the stretch of the substrate. For $\lambda_G = 1$, the cell layer is stress-free when the substrate is unstretched (*i.e.* is flat). With the exception of the limiting cases examined in section 4.5, we regard λ_G as spatially invariant. We model cellular growth parametrically by successively increasing λ_G from unity, requiring that the substrate must stretch (and hence buckle) to relieve stresses in the cell layer.

In the absence of friction between the layers ($Q^* = 0$) the stretches in the cell layer and the substrate will, in general, differ. We expect the stretch in the cell layer to be uniform in this regime and, since the two layers must remain the same length, the cellular stretch is simply the average of the substrate stretch across the layer, denoted

$$\bar{\lambda} = \frac{1}{2L^*} \int_{-L^*}^{L^*} \lambda \mathrm{d}\tilde{s}^*. \tag{4.27}$$

The corresponding equation for T^* in this regime is

$$T^* = k^* \left(\bar{\lambda} - \bar{\lambda}_G\right). \tag{4.28}$$

Note that for uniform cell growth $\bar{\lambda}_G = \lambda_G$.

We further simplify the equations by writing in terms of a composite in-plane stress resultant, $F^* = F_T^* + T^*$. Together with a change of variable to the Lagrangian frame, (4.16), (4.17), (4.22) and (4.23) become

$$\frac{\mathrm{d}\theta}{\mathrm{d}\tilde{s}^*} = \lambda\kappa^*, \tag{4.29a}$$

$$\frac{\mathrm{d}\kappa^*}{\mathrm{d}\tilde{s}^*} = \frac{\lambda}{D^*} F_N^*, \tag{4.29b}$$

$$\frac{\mathrm{d}F^*}{\mathrm{d}\tilde{s}^*} = -\lambda\kappa^* F_N^*, \tag{4.29c}$$

$$\frac{\mathrm{d}F_N^*}{\mathrm{d}\tilde{s}^*} = \lambda\left(\kappa^* F^* - p^*\right), \tag{4.29d}$$

$$\frac{\mathrm{d}x^*}{\mathrm{d}\tilde{s}^*} = \lambda\cos\theta, \tag{4.29e}$$

$$\frac{\mathrm{d}y^*}{\mathrm{d}\tilde{s}^*} = \lambda \sin\theta, \tag{4.29f}$$

with λ prescribed by

$$F^* = E^* h^* (\lambda - 1) + k^* (\lambda - \lambda_G), \tag{4.30}$$

in the limit of strong cell–substrate adhesion, or by

$$F^* = E^* h^* (\lambda - 1) + k^* \left(\bar{\lambda} - \bar{\lambda}_G\right), \tag{4.31}$$

in the absence of cell–substrate adhesion.

We solve the sixth-order system (4.29) subject to the following boundary conditions. We impose that the ends of the substrate are held clamped, so that

$$\theta(\pm L^*) = 0, \tag{4.32}$$

and we prescribe the (x^*, y^*) coordinates of the endpoints according to

$$x^*(\pm L^*) = \pm L^*, \qquad y^*(\pm L^*) = 0. \tag{4.33}$$

4.1.5 Nondimensionalisation

We nondimensionalise the governing equations by scaling all lengths against L^*, stress resultants against k^* and pressure against k^*/L^*. Under these scalings (4.29) yields

$$\frac{\mathrm{d}\theta}{\mathrm{d}\tilde{s}} = \lambda\kappa, \tag{4.34a}$$
$$\frac{\mathrm{d}\kappa}{\mathrm{d}\tilde{s}} = \alpha_0 \lambda F_N, \tag{4.34b}$$
$$\frac{\mathrm{d}F}{\mathrm{d}\tilde{s}} = -\lambda\kappa F_N, \tag{4.34c}$$
$$\frac{\mathrm{d}F_N}{\mathrm{d}\tilde{s}} = \lambda(\kappa F - p), \tag{4.34d}$$
$$\frac{\mathrm{d}x}{\mathrm{d}\tilde{s}} = \lambda \cos\theta, \tag{4.34e}$$
$$\frac{\mathrm{d}y}{\mathrm{d}\tilde{s}} = \lambda \sin\theta. \tag{4.34f}$$

In the regime of strong cell–substrate adhesion, F is given by

$$F = \frac{\lambda - 1}{\alpha_1} + \lambda - \lambda_G, \tag{4.35}$$

while in the absence of cell–substrate adhesion

$$F = \frac{\lambda - 1}{\alpha_1} + \bar{\lambda} - \bar{\lambda}_G, \qquad \bar{\lambda} = \frac{1}{2}\int_{-1}^{1} \lambda \mathrm{d}\tilde{s}. \tag{4.36}$$

The appropriate dimensionless boundary conditions (which follow from (4.32) and (4.33)) are

$$\theta(\pm 1) = 0, \qquad x(\pm 1) = \pm 1, \qquad y(\pm 1) = 0. \tag{4.37}$$

The system is dependent upon two dimensionless parameters: $\alpha_0 = k^* L^{*2}/D^*$, which captures the resistance to cellular extension relative to substrate bending resistance, and $\alpha_1 = k^*/E^* h^*$, which quantifies the resistance to cellular extension relative to substrate stretching resistance. Noting that $D^* = E^* h^{*3}/12\left(1-\nu^2\right)$, we have

$$\alpha_0 = 12\left(1-\nu^2\right)\left(\frac{L^*}{h^*}\right)^2 \alpha_1, \tag{4.38}$$

and it follows that $\alpha_0 \gg \alpha_1$ and a thin substrate will seek to bend in preference to stretching.

It was not possible to measure directly the stiffness of the cell layer (k^*) used in the experiments of chapter 3. However, if we assume that cells generate a typical force of 1–10nN (Du Roure *et al.*, 2005), acting over a typical cell height of 2μm, then we are able to estimate $k^* \simeq 5 \times 10^{-4}\mathrm{Nm}^{-1}$. Given the dimensions and Young's modulus of the substrates used in the *in-vitro* study of chapter 3, and assuming incompressibility ($\nu = 0.5$), we calculate the bending stiffness of the substrates as $D^* = (2.71 \pm 0.40) \times 10^{-10}\mathrm{Nm}$. It follows that α_0 lies in the approximate range 20–200, while α_1 is either $O\left(10^{-5}\right)$ or $O\left(10^{-4}\right)$. These values are only approximate, being sensitive to both our estimation of the magnitude of cell forces and the preliminary nature of our experimental data. For this reason, and to ensure that we present a thorough catalogue of the mathematical behaviour of this model, we present numerical results below for a range of characteristic parameter values. Simplified versions of (4.34–4.37), exploiting the limit $\alpha_0 \gg \alpha_1$, are presented in section 4.5.

4.2 Linear analysis

In order to establish the parameter values for which a departure from the flat configuration first occurs, we linearise (4.34–4.37) about the reference state. Below, we restrict attention to uniform cellular growth, so that $\bar{\lambda}_G = \lambda_G$. For small deflections, $\lambda = 1$ to leading order and we set

$$\lambda = 1 + \varepsilon \check{\lambda} \tag{4.39}$$

for some small parameter $0 < \varepsilon \ll 1$. In the regime of no cell–substrate adhesion, we also have

$$\bar{\lambda} = 1 + \frac{1}{2}\varepsilon \int_{-1}^{1} \check{\lambda} \mathrm{d}\tilde{s} = 1 + \varepsilon \bar{\check{\lambda}}. \tag{4.40}$$

Thus, in either adhesion regime, assuming $\varepsilon \ll \alpha_1$, it follows from (4.35) that F is constant to leading order and given by

$$F = 1 - \lambda_G + O(\varepsilon). \tag{4.41}$$

We, thus, linearise (4.34) via the following rescalings:

$$\theta = \varepsilon\check{\theta}, \quad \kappa = \varepsilon\check{\kappa}, \quad F = 1 - \lambda_G + \check{F}, \quad F_N = \varepsilon\check{F}_N, \quad p = \varepsilon\check{p}, \tag{4.42a}$$

$$x = \tilde{s} + \varepsilon\check{x}, \quad y = \varepsilon\check{y}, \quad \lambda = 1 + \varepsilon\check{\lambda}, \tag{4.42b}$$

under which the leading-order terms in (4.34) yield

$$\frac{\mathrm{d}\check{\theta}}{\mathrm{d}\tilde{s}} = \check{\kappa}, \tag{4.43a}$$

$$\frac{\mathrm{d}\check{\kappa}}{\mathrm{d}\tilde{s}} = \alpha_0\check{F}_N, \tag{4.43b}$$

$$\frac{\mathrm{d}F}{\mathrm{d}\tilde{s}} = 0, \tag{4.43c}$$

$$\frac{\mathrm{d}\check{F}_N}{\mathrm{d}\tilde{s}} = \check{\kappa}(1 - \lambda_G) - \check{p}, \tag{4.43d}$$

$$\frac{\mathrm{d}\check{y}}{\mathrm{d}\tilde{s}} = \check{\theta}, \tag{4.43e}$$

Rearrangement of (4.43) yields the following equation for the substrate profile $\check{y}(x)$:

$$\frac{\mathrm{d}^4\check{y}}{\mathrm{d}x^4} + \alpha_0\left(\lambda_G - 1\right)\frac{\mathrm{d}^2\check{y}}{\mathrm{d}x^2} + \alpha_0\check{p} = 0. \tag{4.44}$$

The corresponding linearised boundary conditions, which follow from (4.37), are

$$\check{y} = \frac{\mathrm{d}\check{y}}{\mathrm{d}x} = 0 \qquad \text{on } x = \pm 1. \tag{4.45}$$

A solution to (4.44) is of the form

$$\check{y}(x) = A + Bx - \left(\frac{\check{p}}{2\left(\lambda_G - 1\right)}\right)x^2 + C\cos\left(\xi x\right) + G\sin\left(\xi x\right), \tag{4.46}$$

where

$$\xi = \sqrt{\alpha_0\left(\lambda_G - 1\right)}, \tag{4.47}$$

and A, B, C, G are arbitrary constants of integration. Imposing that $\check{y}$ must vanish at the ends of the substrate determines two of the constants as

$$A = -C\cos\xi + \frac{\check{p}}{2\left(\lambda_G - 1\right)}, \tag{4.48a}$$

$$B = -G\sin\xi. \tag{4.48b}$$

Imposing the derivative conditions gives the following further restrictions:

$$\xi C\sin\xi = -\frac{\check{p}}{\lambda_G - 1}, \tag{4.49a}$$

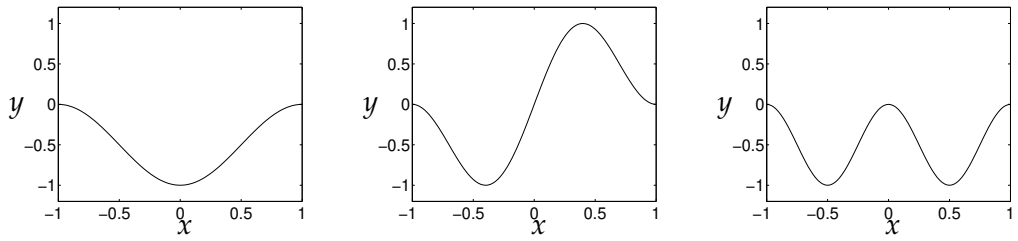

(a) $n = 1$ (b) $n = 2$ (c) $n = 3$

Figure 4.4: The first three eigenfunctions obtained in the absence of pressure, given by (4.52). In the terminology of chapter 2, these configurations correspond to 'type n^-'. The equivalent 'type n^+' configurations can be obtained by reflecting the curves about $y = 0$. Illustrations of these are omitted for brevity.

$$\xi G \cos \xi = G \sin \xi. \tag{4.49b}$$

If $\breve{p} = 0$, (4.49) implies one of the following pairs of constraints. For non-trivial solutions, either

$$G = 0, \qquad \xi = m\pi, \tag{4.50}$$

for some integer m, or

$$C = 0, \qquad \tan \xi = \xi. \tag{4.51}$$

The resulting expression for $\breve{y}(x)$ recovers (2.36):

$$\breve{y}_n(x) = \begin{cases} C_n \left(\cos\left(\xi_n x\right) - \cos \xi_n\right) & \text{for } n \text{ odd}, \\ G_n \left(\sin\left(\xi_n x\right) - x \sin \xi_n\right) & \text{for } n \text{ even}, \end{cases} \tag{4.52}$$

where $\xi_n = (n+1)\pi/2$ for n odd and ξ_n is the $(n/2)^{\text{th}}$ positive root of $\xi = \tan(\xi)$ for n even. The profiles which (4.52) describe for $n = 1, 2, 3$ are illustrated in figure 4.4. We denote by $\lambda_G^{(n)}$ the values of λ_G for which a solution of the form (4.52) is attainable, with values given by

$$\lambda_G^{(n)} = 1 + \frac{\xi_n^2}{\alpha_0}. \tag{4.53}$$

For non-zero $\breve{p}$ and any choice of ξ such that $\xi \neq m\pi$ (for integer m), we have a solution for which $G \equiv 0$ and C is non-zero and given by

$$C = -\frac{\breve{p}}{(\lambda_G - 1)\, \xi \sin \xi}. \tag{4.54}$$

The resulting expression for $\breve{y}(x)$ is, thus

$$\breve{y}(x) = \frac{\breve{p}}{(\lambda_G - 1)\, \xi \sin \xi} \left(\cos \xi - \cos\left(\xi x\right)\right) + \frac{\breve{p}}{2\left(\lambda_G - 1\right)} \left(1 - x^2\right), \tag{4.55}$$

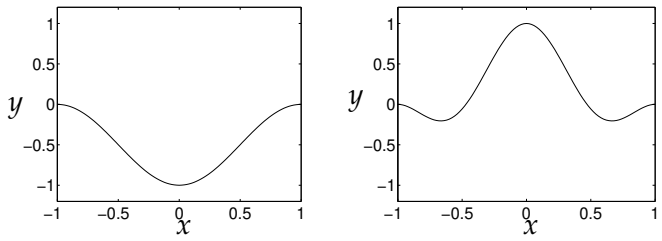

(a) $\lambda_G = 2$ (type 1^-). (b) $\lambda_G = 4$ (type 3^-).

Figure 4.5: Configurations corresponding to (4.55) for $\alpha_0 = 10$ and $\breve{p} = 0.01$.

with ξ given by (4.47). In the terminology of chapter 2, (4.55) defines deformed configurations of odd type. As $\xi \to m\pi$ the amplitudes of these solutions become exponentially large. When $\xi = m\pi$, solutions of odd type are not attainable, the only viable solutions being either flat or of even type, as discussed below. For small ξ (or equivalently λ_G close to 1) (4.55) defines a deformed configuration of type 1. As ξ (or λ_G) increases, this solution's wavelength decreases and the configuration exhibits a series of transitions from type 1 to type 3, followed by type 5, *etc.* Examples of these linear solutions are illustrated in figure 4.5.

For choices of ξ such that $\xi = \tan(\xi)$ (*i.e.* $\xi = \xi_n$ for even n) we have a series of additional solutions of the form

$$\breve{y}_n(x) = G\left(\sin\left(\xi_n x\right) - x\sin\xi_n\right) + \frac{\breve{p}}{(\lambda_G - 1)}\left(\frac{\cos\xi_n - \cos\left(\xi_n x\right)}{\xi_n \sin\xi_n} + \frac{1 - x^2}{2}\right). \qquad (4.56)$$

The linear solutions defined by (4.56) are of even type, and those for which $n = 2$ are illustrated in figure 4.6. In the absence of pressure, setting $n = 2$ in (4.52) yields deformed configurations which exhibit both lateral and vertical reflection symmetries. Prescribing a non-zero pressure, however, results in configurations defined by (4.56) in which the vertical symmetry is broken and most of the substrate is moved in a downward direction.

Buckling is driven by compressive stresses generated in the cell layer as the growth of cells seeks to extend the layer. Mathematically, this is equivalent to increasing λ_G gradually from one or, equivalently, increasing ξ from zero. In the absence of pressure there exists a critical degree of growth, $\lambda_G = \lambda_G^{(1)}$, prior to which the substrate will remain in its flat configuration. The linear analysis shows that when this critical value of λ_G is reached the substrate will buckle into a type 1 configuration. Prolonged growth facilitates the substrate adopting configurations of higher types; for $\lambda_G \gg 1$ the substrate may become highly wrinkled. For $\alpha_0 \gg 1$, which is equivalent to a very small

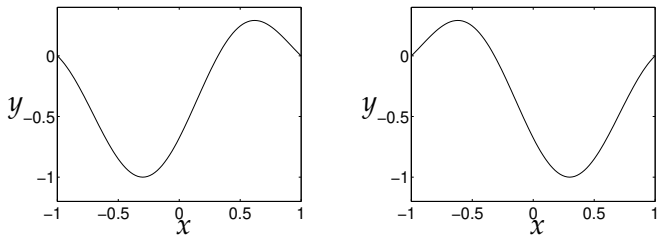

(a) Type 2^-. (b) Type 2^+.

Figure 4.6: Type 2 configurations corresponding to (4.56) for $\alpha_0 = 10$, $\check{p} = 0.01$, $\lambda_G = 2.5$ and $G = \pm 0.005$.

substrate bending stiffness, the values of the $\lambda_G^{(n)}$ are reduced (as per (4.53)) and bifurcations from the flat configuration occur more readily. With a pressure difference acting across the construct, the linear analysis has shown that the substrate can be deformed in a downward direction regardless of the action of the cells. However, selection of configurations of higher types is still dependent upon the cells being able to generate sufficient compression within the cell layer. Figure 4.7 summarises the attainable deformed configurations across λ_G-space and illustrates the manner in which the vertical symmetry is broken for $\check{p} > 0$.

4.3 Strong cell–substrate adhesion – nonlinear analysis

We begin our numerical study with the assumption that cell–substrate adhesion is sufficiently strong to prevent any sliding of cells along the substrate. For convenience we use (4.35) to eliminate F from (4.34), and seek solutions to the following sixth-order ODE system,

$$\frac{\mathrm{d}\theta}{\mathrm{d}\tilde{s}} = \lambda\kappa, \tag{4.57a}$$

$$\frac{\mathrm{d}\kappa}{\mathrm{d}\tilde{s}} = \alpha_0\lambda F_N, \tag{4.57b}$$

$$\frac{\mathrm{d}\lambda}{\mathrm{d}\tilde{s}} = -\frac{\alpha_1}{\alpha_1+1}\lambda\kappa F_N, \tag{4.57c}$$

$$\frac{\mathrm{d}F_N}{\mathrm{d}\tilde{s}} = \lambda\kappa\left(\frac{1}{\alpha_1}(\lambda-1)+\lambda-\lambda_G\right)-\lambda p, \tag{4.57d}$$

$$\frac{\mathrm{d}x}{\mathrm{d}\tilde{s}} = \lambda\cos\theta, \tag{4.57e}$$

$$\frac{\mathrm{d}y}{\mathrm{d}\tilde{s}} = \lambda\sin\theta, \tag{4.57f}$$

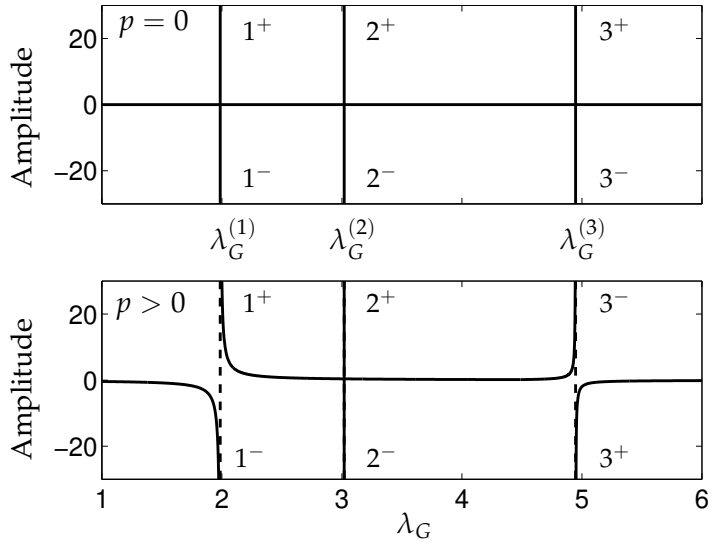

Figure 4.7: The locations of bifurcations in λ_G-space for $\alpha_0 = 10$, as determined by the linear analysis (4.52, 4.55, 4.56). The non-trivial branches above are labelled according to the corresponding deformed configuration type. Solutions corresponding to (4.52) or (4.56) have arbitrary amplitude, and as such are illustrated by vertical lines. In the upper panel, $p = 0$ and the system exhibits vertical symmetry. In the lower panel, however, $p = 1$ and bifurcations are imperfect.

subject to the boundary conditions of (4.37). Solutions to (4.57) are determined through the use of the MATLAB boundary value solver 'bvp4c', which uses a collocation algorithm to successively refine a prescribed approximate solution until the governing equations and boundary conditions are satisfied. Once a non-trivial solution is determined, it is passed back to the solver for use as the starting point for the algorithm at the next value of λ_G. This approach defines a continuation method by which we are able to track the development of non-trivial branches as λ_G is increased. Numerical solutions are validated as discussed in section 2.1.3. For small amplitudes, we also verify that configurations recover the results of the linear analysis of section 4.2, with bifurcations from the flat state occurring for values of λ_G given by (4.53) for $p = 0$.

Figure 4.8 illustrates the solutions obtained for $\alpha_0 = 10$, $\alpha_1 = 1$ and $p = 0$, while figure 4.9 illustrates the corresponding distribution of stresses and substrate stretch for a typical type 1^- configuration. Figure 4.9(a) confirms that compression in the cell layer is relieved through generation of a tension in the substrate; buckling thus acts as a mechanism to minimise the composite in-plane stress-resultant. The development of each configuration type is most easily observed via a bifurcation diagram, plotting solution amplitude as a function of λ_G. Figure 4.10 shows two examples of such diagrams, for

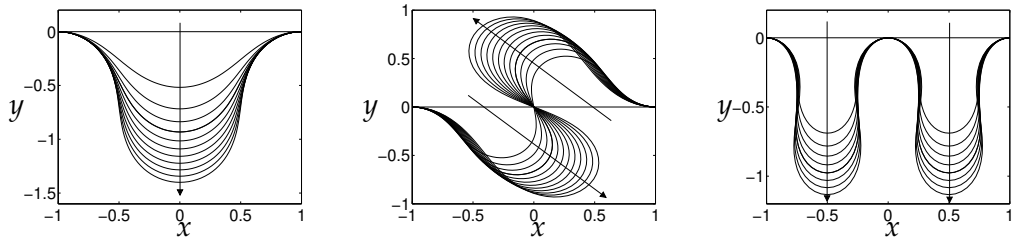

(a) Type 1^- solutions. (b) Type 2^- solutions. (c) Type 3^- solutions.

Figure 4.8: Profiles obtained in the regime of strong cell–substrate adhesion for $\alpha_0 = 10$, $\alpha_1 = 1$, $p = 0$ and increasing λ_G (indicated by arrows).

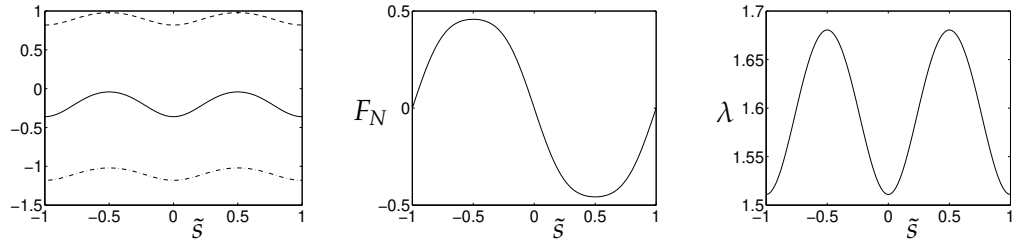

(a) (b) (c)

Figure 4.9: Stresses corresponding to the extremal configuration of figure 4.8(a), obtained for $\alpha_0 = 10$, $\alpha_1 = 1$, $p = 0$ and $\lambda_G = 3$. (a) In-plane stress in the substrate (dashed line), the cell layer (dash-dotted line) and the composite (solid line). (b) Normal stress in the substrate. (c) Substrate stretch (which equals the cellular stretch since cells are fully bound to the substrate).

two parameter choices. As shown in the figures, as λ_G is increased from one (analogous to the onset of cellular growth in the upper layer) the substrate initially remains in its flat configuration. A series of pitchfork bifurcations is observed, the locations of which agree with the linear analysis above. Analysis of the full, nonlinear system reveals that the criticality of these bifurcations is dependent upon parameter choice.

For a parameter choice which results in subcritical pitchfork bifurcations (figure 4.10(a)), numerical simulations show that the corresponding branches each exhibit one turning point, resulting in the existence of a series of saddle-node bifurcations. Departure from the substrate's flat configuration does not occur until λ_G is increased to a value at which a bifurcation lies. For the parameter choices corresponding to figures 4.8 and 4.10(a) this occurs at $\lambda_G \simeq 2$, at which point the configuration rapidly changes

to that of a well-developed type 1^+ or type 1^- profile. As λ_G is further increased these profiles continue to develop, increasing in amplitude. For higher λ_G we are able to also obtain configurations of higher types, such as those illustrated in figure 4.4.

Figure 4.10(b) illustrates a similar bifurcation diagram for larger α_0. Since the locations of the pitchfork bifurcations are determined by (4.47), increasing α_0 has the effect of promoting all non-trivial branches so that buckling can occur for smaller λ_G. For the parameter choice illustrated all bifurcations are supercritical. Type 1 deformations occur most readily, the onset of which is for $\lambda_G \simeq 1.2$ in this case. Examining the system numerically reveals that the result of increasing either α_0 or α_1 (analogous to decreasing the substrate's stiffness or increasing its extensibility respectively) is the promotion of a non-trivial configuration for a reduced degree of cellular growth. For fixed α_0, increasing α_1 results in a transition of the pitchfork bifurcations from supercritical to subcritical.

Finally, we discuss the effect of a pressure acting across the layer (appropriate bifurcation diagrams are displayed in figure 4.11). Comparing figure 4.11 with figure 4.10(a), we find that increasing p from zero has the effect of breaking the vertical symmetry in the problem, so that downward buckling is favoured. The flat configuration is no longer a valid solution in this regime and those bifurcations corresponding to configurations of odd type in figure 4.10(a) become imperfect, the result being that a type 1^- configuration is attainable even in the absence of cellular growth ($\lambda_G = 1$). As λ_G is increased (*c.f.* the onset of growth) this solution increases in amplitude. A configuration of type 1^+ is still attainable for sufficiently large λ_G; however, this configuration will be energetically unfavourable. Neutral curves corresponding to even-type branches remain symmetrical for $p > 0$ since the lateral symmetry of the problem results in configurations of even type occurring in pairs. In the case of type 2 profiles, these solutions are of the forms illustrated in figure 4.6. As p is further increased, the broken symmetry becomes more evident as illustrated by figure 4.11(b).

4.4 No cell–substrate adhesion – nonlinear analysis

Below we analyse deformations of the substrate under the assumption that the cells experience no resistance to sliding along the substrate. Once more, we assume uniform growth so that $\bar{\lambda}_G = \lambda_G$. Having used (4.36) to eliminate F from (4.34), we are left with the following system:

$$\frac{\mathrm{d}\theta}{\mathrm{d}\tilde{s}} = \lambda\kappa, \tag{4.58a}$$

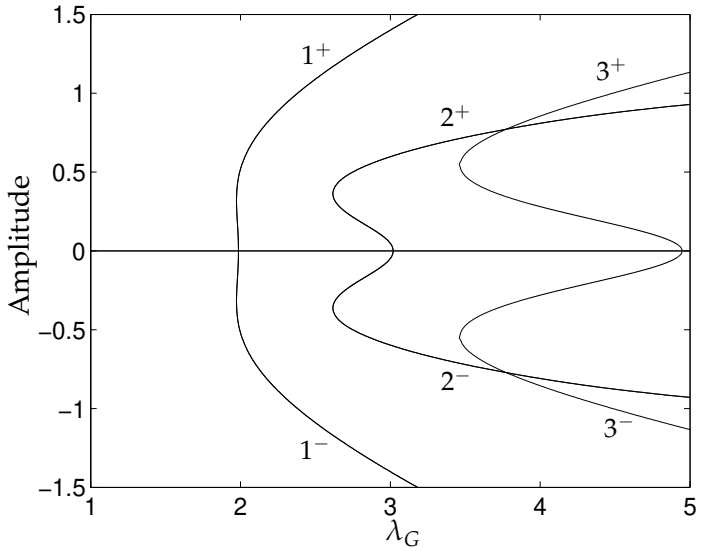

(a) $\alpha_0 = 10$, $\alpha_1 = 1$, $p = 0$.

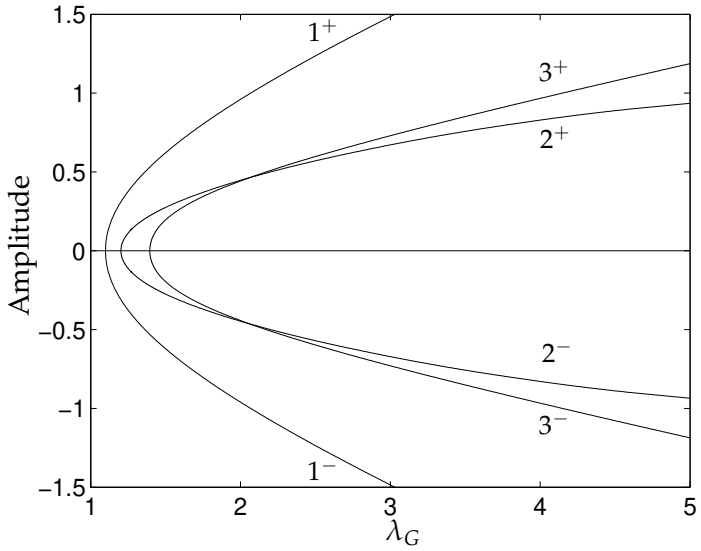

(b) $\alpha_0 = 100$, $\alpha_1 = 1$, $p = 0$.

Figure 4.10: Bifurcation diagrams illustrating the amplitudes of the configurations obtained for strong cell–substrate adhesion in the absence of pressure.

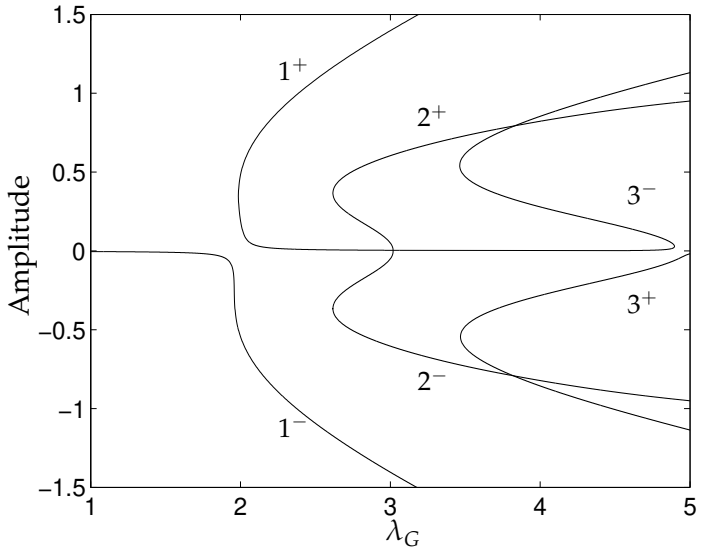

(a) $p = 0.01$.

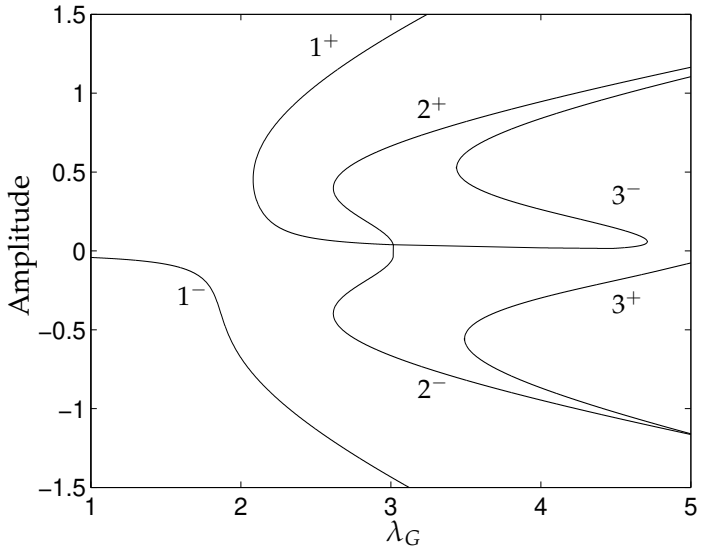

(b) $p = 0.1$.

Figure 4.11: Development of imperfect bifurcations as p is increased from zero in the regime of strong cell–substrate adhesion, for $\alpha_0 = 10$ and $\alpha_1 = 1$.

$$\frac{\mathrm{d}\kappa}{\mathrm{d}\tilde{s}} = \alpha_0 \lambda F_N, \tag{4.58b}$$

$$\frac{\mathrm{d}\lambda}{\mathrm{d}\tilde{s}} = -\frac{\alpha_1}{\alpha_1 + 1} \lambda \kappa F_N, \tag{4.58c}$$

$$\frac{\mathrm{d}F_N}{\mathrm{d}\tilde{s}} = \lambda\kappa \left(\frac{1}{\alpha_1} (\lambda - 1) + \bar{\lambda} - \lambda_G \right) - \lambda p, \tag{4.58d}$$

$$\frac{\mathrm{d}x}{\mathrm{d}\tilde{s}} = \lambda \cos\theta, \tag{4.58e}$$

$$\frac{\mathrm{d}y}{\mathrm{d}\tilde{s}} = \lambda \sin\theta, \tag{4.58f}$$

where

$$\bar{\lambda} = \frac{1}{2} \int_{-1}^{1} \lambda \mathrm{d}\tilde{s}. \tag{4.59}$$

For ease of computation we solve (4.58) using the method described in section 4.3, treating $\bar{\lambda} - \lambda_G$ as an input parameter which we prescribe. Having determined the configuration of the substrate, we use (4.59) to calculate the value of λ_G to which this configuration corresponds. Deploying the continuation scheme of section 4.3 once more, we trace out a series of bifurcation curves which track the amplitudes of the solutions as functions of λ_G.

Figure 4.12 illustrates typical solution profiles obtained in this regime, while figure 4.13 illustrates a typical distribution of stresses and stretches along the length of the domain. The illustrated configurations are highly similar to those of figure 4.8, in which cell–substrate adhesion was strong. This similarity results from the fact that, in the regime of strong adherence, variations in λ along the substrate are small (as figure 4.9(c) shows). Thus, the integral of λ over the entire domain is well approximated by λ itself. Numerical simulations reveal that as λ_G is increased variations in λ become larger. We suggest that geometric differences between the regimes are likely to be more significant for large amplitude configurations obtained for larger λ_G; however, the cellular compression required to generate such configurations is likely to be significantly greater than that generated by the cell layer *in vitro*.

Figures 4.14 and 4.15 illustrate the bifurcation diagrams obtained for $p = 0$ and $p > 0$ respectively. Once more, we observe a high degree of similarity with the corresponding figures in section 4.3.

4.5 Limiting cases

We now consider limiting solutions of (4.34–4.37) to determine the extent to which nonlinear buckled states depend upon the patterning of growth. Once more, we compare results in the case of strong cell–substrate adhesion to those obtained in the absence of

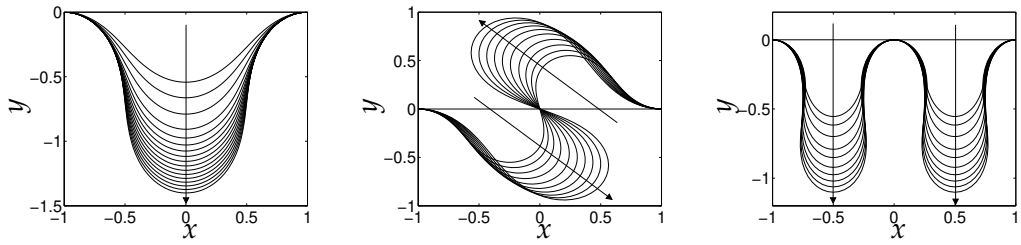

(a) Type 1^- solutions. (b) Type 2^- solutions. (c) Type 3^- solutions.

Figure 4.12: Profiles obtained in the absence of cell–substrate adhesion for $\alpha_0 = 10$, $\alpha_1 = 1$, $p = 0$ and increasing λ_G (indicated by arrows).

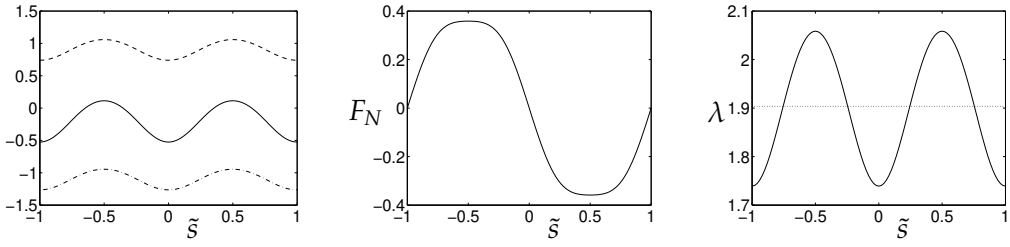

(a) (b) (c)

Figure 4.13: Stresses corresponding to the extremal configuration of figure 4.12(a), obtained for $\alpha_0 = 10$, $\alpha_1 = 1$, $p = 0$ and $\lambda_G = 3$. (a) In-plane stress in the substrate (dashed line), the cell layer (dash-dotted line) and the composite (solid line). (b) Normal stress in the substrate. (c) Substrate stretch (solid line) and cellular stretch (dotted line).

cell–substrate adhesion. Exploiting the fact that $\alpha_0 \gg \alpha_1$ for a thin substrate (see (4.38)), and assuming $p = 0$, we show how solutions are approximated by those of an incompressible beam, allowing growth to still be represented parametrically. We separately consider the two cases $\alpha_0 \gg 1$ and $\alpha_0 = O(1)$ below.

4.5.1 Soft substrate: $\alpha_0 \gg 1$, $\alpha_1 = O(1)$

We begin by considering a beam whose resistance to bending is small compared with the resistance to extension of the cells, for which $\alpha_0 \gg 1$. We rescale the dependent variables in (4.34) according to $F = \hat{F}/\alpha_0$, $F_N = \hat{F}_N/\alpha_0$, so that (4.34) becomes

$$\frac{\mathrm{d}\theta}{\mathrm{d}\tilde{s}} = \lambda\kappa, \qquad \frac{\mathrm{d}\kappa}{\mathrm{d}\tilde{s}} = \lambda\hat{F}_N, \qquad \frac{\mathrm{d}\hat{F}}{\mathrm{d}\tilde{s}} = -\lambda\kappa\hat{F}_N, \tag{4.60 a,b,c}$$

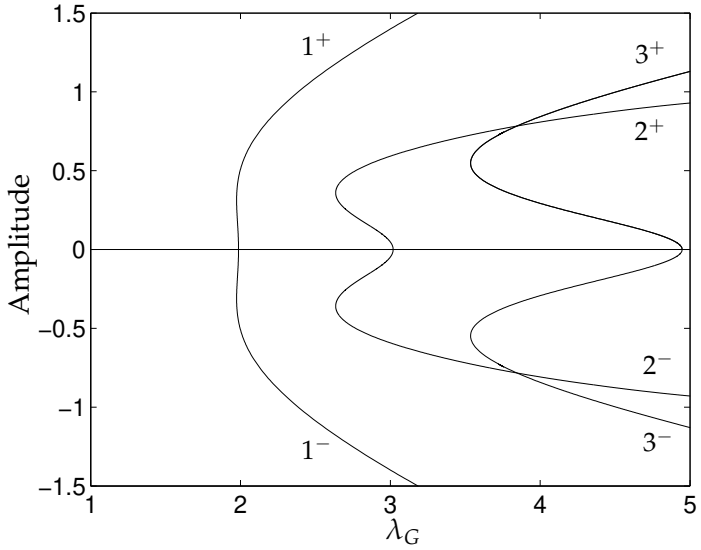

(a) $\alpha_0 = 10$, $\alpha_1 = 1$.

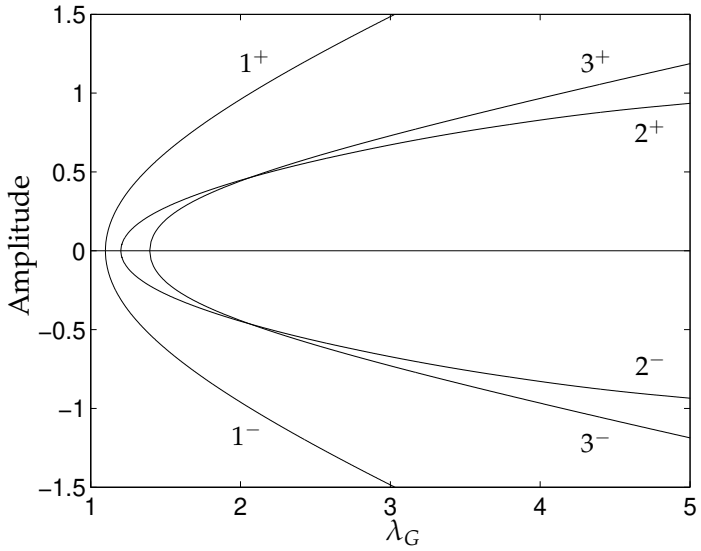

(b) $\alpha_0 = 100$, $\alpha_1 = 1$.

Figure 4.14: Bifurcation diagrams illustrating the amplitudes of configurations obtained for $p = 0$ in the absence of cell–substrate adhesion.

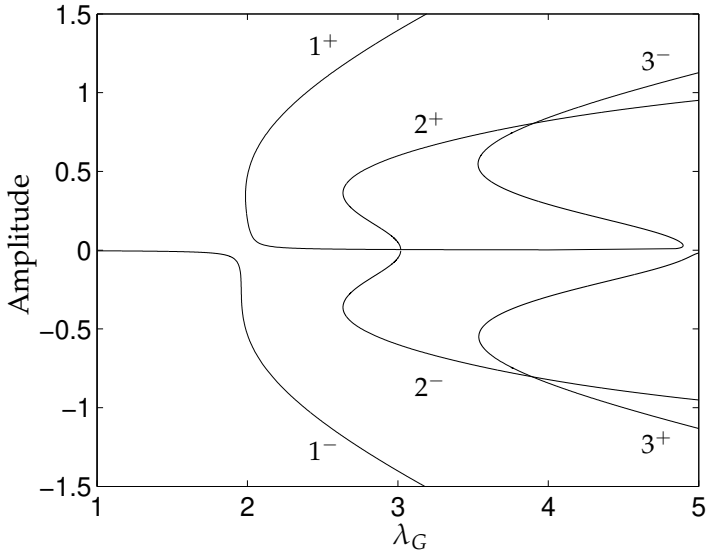

(a) $p = 0.01$.

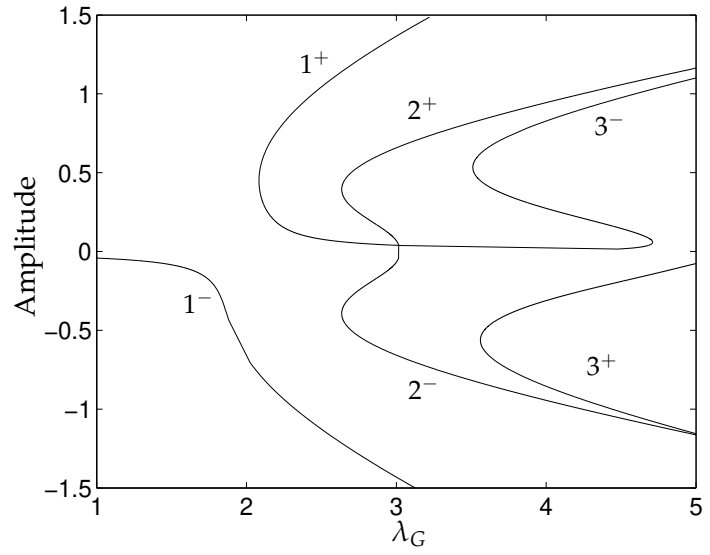

(b) $p = 0.1$.

Figure 4.15: Development of imperfect bifurcations as p is increased from zero in the regime of no cell–substrate adhesion, for $\alpha_0 = 10$ and $\alpha_1 = 1$.

$$\frac{\mathrm{d}\hat{F}_N}{\mathrm{d}\tilde{s}} = \lambda\kappa\hat{F}, \qquad \frac{\mathrm{d}x}{\mathrm{d}\tilde{s}} = \lambda\cos\theta, \qquad \frac{\mathrm{d}y}{\mathrm{d}\tilde{s}} = \lambda\sin\theta. \tag{4.60 d,e,f}$$

In the regime of strong cell–substrate adhesion, (4.35) implies that λ is determined by

$$0 = \frac{\lambda - 1}{\alpha_1} + (\lambda - \lambda_G) + O\left(\frac{1}{\alpha_0}\right). \tag{4.61}$$

Thus, to leading order

$$\lambda = \frac{1 + \alpha_1\lambda_G}{1 + \alpha_1}. \tag{4.62}$$

The degree to which cell growth leads to stretching of the substrate is parameterised by α_1. Since (4.62) allows us to regard λ as prescribed, we introduce a new spatial coordinate, Σ, defined according to

$$\frac{\mathrm{d}\Sigma}{\mathrm{d}\tilde{s}} = \lambda, \qquad \Sigma(-1) = -1. \tag{4.63}$$

Under this change of variable, (4.60) becomes

$$\frac{\mathrm{d}\theta}{\mathrm{d}\Sigma} = \kappa, \quad \frac{\mathrm{d}\kappa}{\mathrm{d}\Sigma} = \hat{F}_N, \quad \frac{\mathrm{d}\hat{F}}{\mathrm{d}\Sigma} = -\kappa\hat{F}_N, \quad \frac{\mathrm{d}\hat{F}_N}{\mathrm{d}\Sigma} = \kappa\hat{F}, \quad \frac{\mathrm{d}x}{\mathrm{d}\Sigma} = \cos\theta, \quad \frac{\mathrm{d}y}{\mathrm{d}\Sigma} = \sin\theta, \tag{4.64}$$

subject to

$$\theta = 0, \quad x = \pm 1, \quad y = 0 \quad \text{on } \Sigma = -1, -1 + 2\bar{\lambda}. \tag{4.65}$$

Substituting (4.64b) into (4.64c) and integrating, we determine $\hat{F}$ as

$$\hat{F} = C - \frac{1}{2}\kappa^2, \tag{4.66}$$

for some constant C. Noting (4.66), equations (4.64b) and (4.64d) then yield the classical problem of an incompressible Euler–Bernoulli beam, for which

$$\frac{\mathrm{d}^2\kappa}{\mathrm{d}\Sigma^2} + \frac{1}{2}\kappa^3 - C\kappa = 0. \tag{4.67}$$

Figure 4.16(a) illustrates the bifurcations exhibited by (4.64–4.65) as $\bar{\lambda}$ is increased through unity, alongside the equivalent curves obtained for $\alpha_0 = O(1)$. We have buckling driven by parametric growth as $\bar{\lambda}$ is increased through 1, or equivalently for $\bar{\lambda}_G > 1$ (which is consistent with (4.53) in the limit $\alpha_0 \gg 1$). Significantly, the shape of the deformed configuration is determined entirely by $\bar{\lambda}$ and is, therefore, independent of the patterning of cellular growth. Non-uniform growth, $\lambda_G(s)$, does determine the distribution of material along the layer, while (4.62) shows how substrate stretching resistance limits the degree of physical stretch relative to cell remodelling, λ_G. Figure 4.16(a) shows that, as a consequence of reducing the problem to that of an incompressible Euler–Bernoulli beam, bifurcations onto non-trivial branches collapse onto the point $\lambda_G = 1$. In contrast, for $\alpha_0 = O(1)$, the composite beam's compressibility

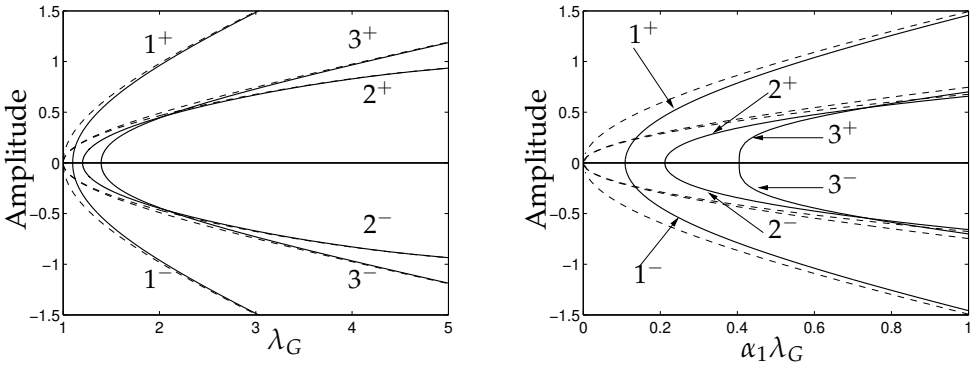

(a) (b)

Figure 4.16: Comparison of solutions to (4.34–4.37) to the limiting solutions of section 4.5, assuming uniform growth and strong cell–substrate adhesion. In (a) solid lines are for $\alpha_0 = 100$, $\alpha_1 = 1$ (representing a soft substrate) and dashed lines illustrate solutions to (4.64,4.65). In (b) $\alpha_0 = 1$, $\alpha_1 = 0.01$ (representing a stiff substrate) and dashed lines illustrate solutions to (4.75,4.76); note the rescaling of the horizontal axis.

results in the bifurcations lying in distinct locations and the non-trivial configuration attained first is of type 1.

Consider, now, the regime in which there is no adherence between the cells and the beam. From (4.36) at leading order in α_0^{-1}, we have

$$0 = \lambda - 1 + \alpha_1 \left(\bar{\lambda} - \bar{\lambda}_G\right). \tag{4.68}$$

Integrating over the length of the beam to determine $\bar{\lambda}$, it follows that

$$\lambda = \bar{\lambda} = \frac{1 + \alpha_1 \bar{\lambda}_G}{1 + \alpha_1}. \tag{4.69}$$

This case, therefore, differs from the fully-bound case only in the relationship between growth, λ_G, and stretch, λ; the remainder of the problem reduces to (4.64–4.65), a classical Euler–Bernoulli beam parameterised only by its length. These two extreme cases differ only in the Lagrangian displacement of material points.

4.5.2 Stiff substrate: $\alpha_0 = O(1)$, $\alpha_1 \ll 1$

Alternatively, when $\alpha_0 = O(1)$ and $\alpha_1 \ll 1$, the substrate has a high resistance to stretching and cellular growth needs to be powerful to induce buckling (figure 4.16(b)). Accordingly, we write $\lambda_G = \hat{\lambda}_G/\alpha_1$ where $\hat{\lambda}_G = O(1)$. Assuming F remains $O(1)$, (4.35)

and (4.36) imply that

$$F = \frac{\lambda - 1}{\alpha_1} + \lambda - \frac{\hat{\lambda}_G}{\alpha_1}, \quad \text{or} \quad F = \frac{\lambda - 1}{\alpha_1} + \bar{\lambda} - \frac{\bar{\hat{\lambda}}_G}{\alpha_1}, \tag{4.70}$$

in the strongly adhered and un-adhered regimes respectively. We expand λ as follows:

$$\lambda = 1 + \hat{\lambda}_G + \alpha_1 \hat{\lambda} + O\left(\alpha_1^2\right), \quad \text{or} \quad \lambda = 1 + \bar{\hat{\lambda}}_G + \alpha_1 \hat{\lambda} + O\left(\alpha_1^2\right), \tag{4.71}$$

so that F is given, to leading order, by

$$F = 1 + \hat{\lambda} + \hat{\lambda}_G, \quad \text{or} \quad F = 1 + \hat{\lambda} + \bar{\hat{\lambda}}_G. \tag{4.72}$$

We define the new spatial coordinate Σ according to

$$\frac{\mathrm{d}\Sigma}{\mathrm{d}\tilde{s}} = 1 + \hat{\lambda}_G, \quad \text{or} \quad \frac{\mathrm{d}\Sigma}{\mathrm{d}\tilde{s}} = 1 + \bar{\hat{\lambda}}_G, \tag{4.73}$$

with $\Sigma(-1) = -1$, from which it follows that

$$\Sigma = \tilde{s} + \int_{-1}^{\tilde{s}} \hat{\lambda}_G\left(s'\right) \mathrm{d}s'. \tag{4.74}$$

Under this change of variable (4.34) becomes

$$\frac{\mathrm{d}\theta}{\mathrm{d}\Sigma} = \kappa, \quad \frac{\mathrm{d}\kappa}{\mathrm{d}\Sigma} = \alpha_0 F_N, \quad \frac{\mathrm{d}F}{\mathrm{d}\Sigma} = -\kappa F_N, \quad \frac{\mathrm{d}F_N}{\mathrm{d}\Sigma} = \kappa F, \quad \frac{\mathrm{d}x}{\mathrm{d}\Sigma} = \cos\theta, \quad \frac{\mathrm{d}y}{\mathrm{d}\Sigma} = \sin\theta, \tag{4.75}$$

and is solved subject to

$$\theta = 0, \quad x = \pm 1, \quad y = 0 \quad \text{on } \Sigma = -1, 1 + 2\bar{\hat{\lambda}}_G. \tag{4.76}$$

Again, we recover (4.67) with

$$F = \frac{C}{\alpha_0} - \frac{\kappa^2}{2\alpha_0}, \tag{4.77}$$

for some constant C. The problem reduces to that of a classical Euler–Bernoulli beam one more, dependent only upon the beam's total length, $2 + 2\alpha_1 \bar{\lambda}_G$. As $\bar{\lambda}_G$ increases through zero we recover the sequence of buckled shapes parameterised by length alone. Each configuration has an associated in-plane stress $C(\bar{\hat{\lambda}}_G)$ and curvature κ, related to the beam's stretch via

$$\frac{1}{\alpha_0}\left(C\left(\bar{\hat{\lambda}}_G\right) - \frac{1}{2}\kappa^2\right) = 1 + \hat{\lambda} + \hat{\lambda}_G, \quad \text{or} \quad \frac{1}{\alpha_0}\left(C\left(\bar{\hat{\lambda}}_G\right) - \frac{1}{2}\kappa^2\right) = 1 + \hat{\lambda} + \bar{\hat{\lambda}}_G. \tag{4.78}$$

Figure 4.16(b) compares the solutions defined by (4.75–4.76) against numerical simulations obtained for $\alpha_0 = 1$ and $\alpha_1 = 0.01$. While reducing the problem to that of an incompressible beam fails to capture the disparate nature of the bifurcation points, for large deflections (4.75–4.76) are shown to be an accurate approximation of solutions to the full system for moderate parameter values. The profiles obtained are independent of both cellular adherence and patterning of growth.

4.6 Conclusions

In the above model we considered a confluent, homogeneous layer of proliferating cells upon an elastic substrate. The expansion and proliferation of the cells were considered to generate a compressive in-plane stress within the cell layer, the relief of which necessitates deformation of the underlying substrate. Two regimes of cell–substrate adhesion were considered: that in which cells are tightly bound, preventing any sliding of the cells against the substrate, and that in which cells experience no resistance to sliding. Numerical simulations revealed that the configurations obtained in each regime are highly similar, suggesting that the precise mechanism of cell–substrate adhesion may not be paramount in future models. However, our model does assume that the two layers remain in contact throughout deformation, which would, in reality, require some adhesion between the layers.

The model predicts that the shapes of nonlinear buckled states are controlled by the net cellular growth, rather than by localised patterning of growth. For a thin substrate ($\alpha_0 \gg \alpha_1$) the model reduces to the simpler problem of a growing, incompressible beam held between fixed supports (*c.f.* chapter 2). The compressibility of the substrate is important only in capturing the disparate nature of the bifurcation points (in comparison with an incompressible beam, for which all bifurcations coincide). Including the compression of the substrate in our analysis illustrates that an initial bifurcation to a low-order (type 1) mode is favoured. Nonlinear states of types 1 and 3 showed promising resemblance to colorectal crypts.

While this model has been derived to maximise relevance to the *in-vitro* study of chapter 3, we may also consider it as a refinement to the *in-vivo* model of chapter 2. Most notably, the two layer construct used here allows us to consider the epithelium and the lamina propria as distinct entities. Since our substrate is flexible, the points of cellular anchorage are displaced as the epithelium proliferates and bends. This improves upon the unrealistic aspects of the spring-based stroma model of chapter 2. The primary weakness of this model lies in the simplistic modelling of the cell layer, which neglects such aspects as cellular division and apoptosis. Our experimental studies observed that as the cell layer becomes confluent, older cells become apoptotic and detach from the substrate, leaving behind a void which is filled by other cells. This behaviour is neglected here. Furthermore, cells were observed to frequently exchange position during proliferation. Inclusion of such a phenomenon is not possible within the confines of a one-dimensional model and, as such, is omitted. We omit this from forthcoming two-dimensional models also, since it cannot easily by considered within a homogenised framework.

CHAPTER 5

Growth-Induced Buckling of a Two-Dimensional Substrate

In this chapter, we present a two-dimensional extension to the model of chapter 4. We consider an initially unstressed rectangular substrate which deforms due to forces induced by growing cell layers upon its upper or lower surfaces. Modelling the substrate as a thin plate, we begin with the equations of general, three-dimensional elasticity (written in Cartesian form) and apply the asymptotic scalings of Howell *et al.* (2009) to yield equations analogous to von Kármán's equations (von Kármán, 1910, 1940). Our equations exhibit key differences to the standard von Kármán equations, however. First, we incorporate surface stresses upon the upper and lower surfaces of the plate to capture the effects of a confluent proliferating cell layer upon either surface. Second, our derivation assumes that the substrate is spatially inhomogeneous, resulting in additional terms in the governing equations.

Dervaux & Ben Amar (2010) previously deployed von Kármán plate theory in their model of tissue growth. Their model differs from that presented here through its incorporation of a fully three-dimensional description of growth through a growth rate tensor, $\mathbf{g}$, whose components modify the standard strain–displacement relationship of linear elasticity to account for addition of mass. Buckling was mediated through tethering of the plate to an elastic Winkler foundation, representing underlying tissue. Spatial variations in the plate's mechanical response were incorporated via the assumption that the normal force exerted by the substrate can be written as a prescribed function of transverse displacement; however, their model does not explicitly incorporate variations in the plate's Young's modulus or Poisson's ratio, as studied here.

In this chapter, we focus upon a simplification of the derived model in which the plate is homogeneous. We examine a reduction of the full model to one-dimensional beam

theory, before reformulating the equations in terms of polar coordinates to facilitate the study of axisymmetric buckling. We examine fully two-dimensional solutions for inhomogeneous substrates in chapter 6, in which we address the question of how patterning of material properties can influence crypt frequency.

We close this chapter with a comparison of the von Kármán model with an alternative model presented of Pamplona & Calladine (1993). The formulation of the model of Pamplona & Calladine takes a different approach, in which the governing equations are determined by combining force balances with appropriate constitutive assumptions. We compare the results of these two models at both the onset of buckling and at large amplitudes, our goal being to determine the degree to which conclusions are sensitive to the modelling approach. Finally, we identify key differences between the constitutive assumptions in the model of Pamplona & Calladine and equivalent expressions arising from the scalings deployed in the derivation of the von Kármán model.

5.1 Notation and preliminaries

We consider the buckling of a three-dimensional, rectangular plate of in-plane dimensions $2L_1^*$ and $2L_2^*$, thickness h^*, Young's modulus E^* and Poisson's ratio ν. We assume that both E^* and ν vary spatially in the plane of the plate; however, we assume no variation in either parameter across the plate's thickness. We assume that the Poisson's ratio is positive since we expect the substrate, when stretched on one direction, to contract in another. As discussed in section 1.6.3, we further require $\nu \leq 0.5$ to ensure that the Lamé constants (defined in (1.45)) are both positive. For a perfectly incompressible, linearly elastic material, $\nu = 0.5$.

We use stars to distinguish dimensional quantities from their dimensionless counterparts throughout. Following the notation of section 1.6.1, we denote the position of a material point in the Lagrangian framework by $\left(X_1^*, X_2^*, X_3^*\right)$, relative to a fixed Cartesian coordinate system oriented so that X_1^* and X_2^* lie in the plane of the undeformed plate, and X_3^* is normal to the undeformed plate in a right-handed sense (figure 5.1). The plate's central plane lies at $X_3^* = 0$ in the undeformed configuration. Similarly, we denote the position of a material point in the deformed configuration by $\left(x_1^*, x_2^*, x_3^*\right)$. The plate undergoes a deformation with Cartesian components of displacement $\left(u_1^*, u_2^*, u_3^*\right)$, so that

$$x_i^* = X_i^* + u_i^*. \tag{5.1}$$

We describe stresses in terms of Piola–Kirchhoff stress tensors, as defined in section 1.6.1. We denote the first and second Piola–Kirchhoff stress tensors by $\mathbf{T}^*$ and $\mathbf{S}^*$ re-

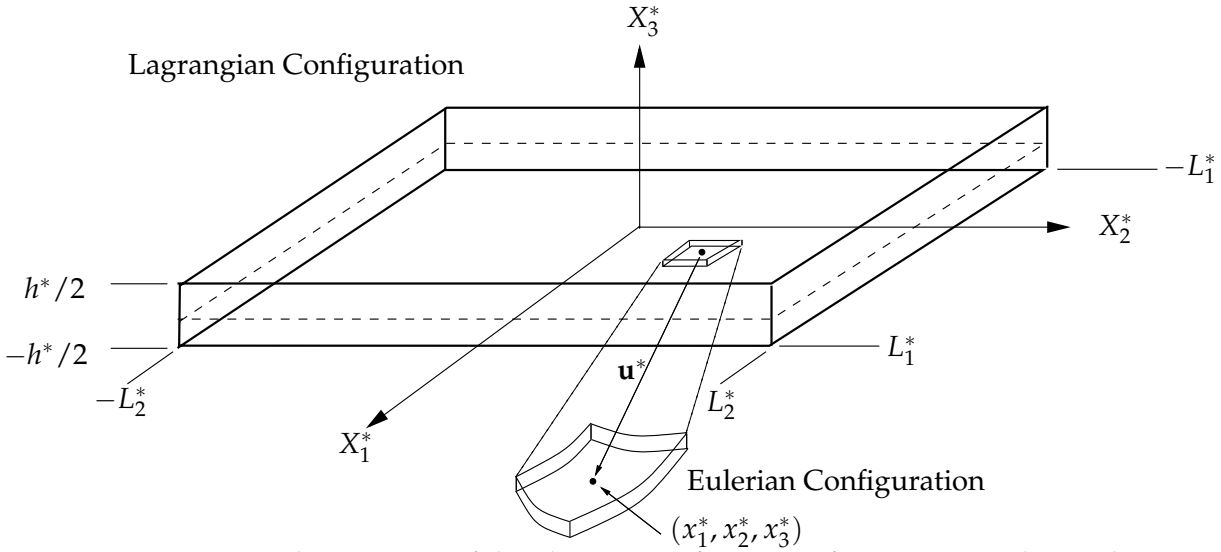

Figure 5.1: The geometry of the plate in its reference configuration. We denote the position of a material point in the Lagrangian frame by $\mathbf{X}^*$. Dotted lines illustrate the central plane, which lies at $X_3^* = 0$ in the undeformed configuration. Inset is an illustration of a typical volume element under deformation. The material point illustrated undergoes a displacement $\mathbf{u}^*$, and after displacement occupies position $\mathbf{x}^*$ in the Eulerian configuration.

spectively, the two measures being related by

$$\mathbf{S}^* = \mathbf{F}^{-1}\mathbf{T}^*, \tag{5.2}$$

for deformation gradient tensor $\mathbf{F}$. The senses of the components of $\mathbf{T}^*$ are as illustrated in figure 1.4. In general $\mathbf{T}^*$ is not symmetric; however, noting (1.4), its components are related via

$$\mathbf{T}^*\mathbf{F}^\top = \mathbf{F}\mathbf{T}^{*\top}. \tag{5.3}$$

The Lagrangian strain tensor is denoted by $\mathbf{e}$, and is given by

$$\mathbf{e} = \frac{1}{2}\left(\mathbf{F}^\top\mathbf{F} - \mathbf{I}\right). \tag{5.4}$$

We assume a neo-Hookean strain energy function and restrict attention to deflections of $O(h^*)$. It is, therefore, appropriate to restrict attention to small strains, for which we then have a linear stress–strain relationship (see chapter 1), *i.e.*

$$\mathbf{S}^* = \lambda^*\mathrm{Tr}(\mathbf{e})\mathbf{I} + 2\mu^*\mathbf{e}, \tag{5.5}$$

where (recalling (1.45)) the Lamé constants λ^* and μ^* are given by

$$\lambda^* = \frac{\nu E^*}{(1+\nu)(1-2\nu)}, \qquad \mu^* = \frac{E^*}{2\,(1+\nu)}, \tag{5.6}$$

provided $\nu \neq 0.5$. Dervaux *et al.* (2009) considered an arbitrary incompressible hyperelastic plate with $L^* \gg h^*$, whose transverse defelections are of $O(h^*)$, and illustrated that (to leading order in h^*/L^*) (5.5) is independent of the choice of strain energy function, up to addition of a material constant (Dervaux & Ben Amar, 2010). Since (5.6) suggests that λ^* becomes large in the incompressible limit ($\nu \to 0.5$), we expect that $\mathrm{Tr}(\mathbf{e}) \to 0$ as $\nu \to 0.5$ so that the stresses prescribed by (5.5) are bounded. We consider the limit $\nu \to 0.5$ in more detail in section 5.3.1.

In the following, we use the summation convention in presenting some of our equations. Any term containing a repeated index i or j should be summed over index values $1, 2, 3$. The starting point for the subsequent derivation is Cauchy's momentum equation which, in terms of Lagrangian variables (and in the absence of inertia) is

$$\frac{\partial T^*_{ij}}{\partial X^*_j} + \rho^*_0 b^*_i = 0, \tag{5.7}$$

where $\mathbf{b}^* = (b^*_1, b^*_2, b^*_3)$ captures any body forces acting upon the plate and ρ^*_0 is the initial density of the plate, related to ρ^* according to (Howell *et al.*, 2009)

$$\rho^*_0 = \rho^* \det(\mathbf{F}). \tag{5.8}$$

We select boundary conditions which are appropriate for modelling the cell culture substrate used in chapter 3. Consistent with earlier mathematical models, we impose clamping and zero displacement upon all four of the plate's boundaries, *i.e.*

$$u^*_i\left(\pm L^*_1, X^*_2, X^*_3\right) = u^*_i\left(X^*_1, \pm L^*_2, X^*_3\right) = 0 \qquad \text{for } i = 1, 2, 3, \tag{5.9a}$$

$$\frac{\partial u^*_3}{\partial X^*_1}\left(\pm L^*_1, X^*_2, X^*_3\right) = \frac{\partial u^*_3}{\partial X^*_2}\left(X^*_1, \pm L^*_2, X^*_3\right) = 0. \tag{5.9b}$$

We regard the plate as a cell culture substrate with confluent cell layers upon the upper and lower surfaces. As these cells proliferate, the cell layers are placed under compression. We consider the cell layers to be of negligible thickness, and formulate their governing equations in terms of in-plane stresses which are averaged across the cells' height. We write $\boldsymbol{\mathcal{T}}^{+*}$ and $\boldsymbol{\mathcal{T}}^{-*}$ to represent the averaged in-plane stresses of the upper and lower cell layers respectively; $\boldsymbol{\mathcal{T}}^{\pm *}$ are vectors of length 2 whose components have dimensions of force per unit length.

The in-plane stresses in the cell layer generate both normal and in-plane stresses upon the plate's surfaces, according to some constitutive law which describes assumptions of cell–substrate adhesion. We proceed through the derivation without considering a specific constitutive law, however, instead formulating a more general model appropriate for studying any imposed distributions of surface stresses. Rather than working

in terms of $\boldsymbol{\mathcal{T}}^{\pm *}$, we describe the model in terms of the stresses applied to the plate's surfaces, which we denote by $\mathbf{f}^{\pm *}$. The remaining boundary conditions are then given by

$$T^*_{i3}\left(X^*_1, X^*_2, \pm h^*/2\right) = \pm f_i^{\pm *}\left(X^*_1, X^*_2\right) \qquad \text{for } i = 1, 2, 3. \tag{5.10}$$

We return to the issue of selecting constitutive assumptions for cell–substrate adhesion in section 5.3.2, at which point we will also need to refer to the curvature of the substrate, κ^*, given by

$$\kappa^* = \nabla \cdot \left(\frac{\nabla u^*_3}{\sqrt{1 + |\nabla u^*_3|^2}} \right). \tag{5.11}$$

5.2 Nondimensionalisation and asymptotic scalings

We nondimensionalise the system via the following scalings which depend upon one small parameter $\varepsilon = h^*/L^*_1$, which captures the slenderness of the plate. We scale the coordinates according to

$$X^*_1 = L^*_1 X, \qquad X^*_2 = L^*_1 Y, \qquad X^*_3 = h^* Z. \tag{5.12}$$

In terms of dimensionless coordinates, the plate is bounded by $-1 \leq X \leq 1$, $-l \leq Y \leq l$ (where $l = L^*_2/L^*_1$) and $-1/2 \leq Z \leq 1/2$. Following Howell *et al.* (2009), we assume that deformations in the Z-direction are of small amplitude. Transverse displacements (*i.e.* those in the Z-direction) are assumed to be of $O(h^*)$ and the associated in-plane displacements are assumed to be of $O(\varepsilon h^*)$. We also retain an $O(\varepsilon^2 h^*)$ correction to the leading-order transverse displacement, setting

$$u^*_1 = \varepsilon h^* u, \qquad u^*_2 = \varepsilon h^* v, \qquad u^*_3 = h^*\left(w + \varepsilon^2 \tilde{w}\right). \tag{5.13}$$

For consistency with the Kirchhoff assumptions introduced in section 1.6.3, we regard w to be independent of Z; *i.e.* we assume that the thickness of the plate is unchanged to leading order during deformation. We scale the Young's modulus against its maximum, $E^*_{\max}$, setting

$$E^* = E^*_{\max} E. \tag{5.14}$$

We omit a derivation of the appropriate scalings of the stress tensor components, and simply follow those presented by Howell *et al.* (2009), which are:

$$\left\{T^*_{11}, T^*_{12}, T^*_{21}, T^*_{22}\right\} = \varepsilon^2 E^*_{\max}\left\{T_{11}, T_{12}, T_{21}, T_{22}\right\}, \tag{5.15a}$$

$$\left\{T^*_{13}, T^*_{23}, T^*_{31}, T^*_{32}\right\} = \varepsilon^3 E^*_{\max}\left\{T_{13}, T_{23}, T_{31}, T_{32}\right\}, \tag{5.15b}$$

$$T_{33}^* = \varepsilon^4 E_{\max}^* T_{33}, \tag{5.15c}$$

$$\{S_{11}^*, S_{12}^*, S_{21}^*, S_{22}^*\} = \varepsilon^2 E_{\max}^* \{S_{11}, S_{12}, S_{21}, S_{22}\}, \tag{5.15d}$$

$$\{S_{13}^*, S_{23}^*, S_{31}^*, S_{32}^*\} = \varepsilon^3 E_{\max}^* \{S_{13}, S_{23}, S_{31}, S_{32}\}, \tag{5.15e}$$

$$S_{33}^* = \varepsilon^4 E_{\max}^* S_{33}. \tag{5.15f}$$

The corresponding rescalings of the components of $\mathbf{f}^{\pm *}$ are

$$f_1^{\pm *} = \varepsilon^3 E_{\max}^* f_1^{\pm}, \qquad f_2^{\pm *} = \varepsilon^3 E_{\max}^* f_2^{\pm}, \qquad f_3^{\pm *} = \varepsilon^4 E_{\max}^* f_3^{\pm}, \tag{5.16}$$

while the averaged stresses in the cell layers are nondimensionalised according to

$$\mathcal{T}_i^{\pm *} = \varepsilon^3 E_{\max}^* L_1^* \mathcal{T}_i^{\pm}, \qquad \text{for } i = 1, 2. \tag{5.17}$$

When discussing cell–substrate adhesion assumptions in section 5.3.2, we will refer to dimensionless curvature, κ, given by

$$\kappa^* = \frac{\varepsilon}{L_1^*}\kappa. \tag{5.18}$$

Applying the scalings of (5.12), (5.13) and (5.18) to (5.11), we have

$$\kappa = \nabla^2 w + O\left(\varepsilon^2\right). \tag{5.19}$$

For compactness of notation, we abbreviate some of the equations below by denoting derivatives of displacements by addition of the appropriate subscripts. Noting (5.1), we substitute (5.12) and (5.13) into (1.1), to determine the form of the deformation gradient tensor as

$$\mathbf{F} = \begin{pmatrix} 1 + \varepsilon^2 u_X & \varepsilon^2 u_Y & \varepsilon u_Z \\ \varepsilon^2 v_X & 1 + \varepsilon^2 v_Y & \varepsilon v_Z \\ \varepsilon w_X + \varepsilon^3 \tilde{w}_X & \varepsilon w_Y + \varepsilon^3 \tilde{w}_Y & 1 + \varepsilon^2 \tilde{w}_Z \end{pmatrix}, \tag{5.20}$$

and from (5.4) we have the following expression for the Lagrangian strain:

$$\mathbf{e} = \frac{\varepsilon}{2}\begin{pmatrix} 0 & 0 & u_Z + w_X \\ 0 & 0 & v_Z + w_Y \\ u_Z + w_X & v_Z + w_Y & 0 \end{pmatrix} + \frac{\varepsilon^2}{2}\begin{pmatrix} 2u_X + w_X^2 & u_Y + v_X + w_X w_Y & 0 \\ u_Y + v_X + w_X w_Y & 2v_Y + w_Y^2 & 0 \\ 0 & 0 & 2\tilde{w}_Z + u_Z^2 + v_Z^2 \end{pmatrix} + O\left(\varepsilon^3\right). \tag{5.21}$$

Dimensionless boundary conditions are given by

$$u(\pm 1, Y, Z) = u(X, \pm l, Z) = 0, \tag{5.22a}$$

$$v(\pm 1, Y, Z) = v(X, \pm l, Z) = 0, \tag{5.22b}$$

$$w(\pm 1, Y, Z) = w(X, \pm l, Z) = 0, \tag{5.22c}$$

$$w_X(\pm 1, Y, 0) = w_Y(X, \pm l, 0) = 0, \tag{5.22d}$$

$$T_{i3}(X, Y, \pm 1/2) = \pm f_i^{\pm}(X, Y) \qquad \text{for } i = 1, 2, 3. \tag{5.22e}$$

5.3 Model derivation

Assuming the absence of body forces, applying the scalings of section 5.2 reduces the momentum equations of (5.7) to

$$\frac{\partial T_{11}}{\partial X} + \frac{\partial T_{12}}{\partial Y} + \frac{\partial T_{13}}{\partial Z} = 0, \tag{5.23a}$$

$$\frac{\partial T_{21}}{\partial X} + \frac{\partial T_{22}}{\partial Y} + \frac{\partial T_{23}}{\partial Z} = 0, \tag{5.23b}$$

$$\frac{\partial T_{31}}{\partial X} + \frac{\partial T_{32}}{\partial Y} + \frac{\partial T_{33}}{\partial Z} = 0. \tag{5.23c}$$

We integrate (5.23) with respect to Z to obtain expressions for the averaged stress components, denoted with overbars and defined according to

$$\bar{T}_{ij} = \int_{-1/2}^{1/2} T_{ij} \mathrm{d}Z. \tag{5.24}$$

Since the boundary conditions given by (5.22e) imply that

$$\frac{\partial \bar{T}_{i3}}{\partial Z} = \int_{-1/2}^{1/2} \frac{\partial T_{i3}}{\partial Z} \mathrm{d}Z = [T_{i3}]_{-1/2}^{1/2} = f_i^+ + f_i^-, \qquad i = \{1, 2, 3\}, \tag{5.25}$$

the expressions resulting from averaging (5.23) are as follows:

$$\frac{\partial \bar{T}_{11}}{\partial X} + \frac{\partial \bar{T}_{12}}{\partial Y} + f_1^+ + f_1^- = 0, \tag{5.26a}$$

$$\frac{\partial \bar{T}_{21}}{\partial X} + \frac{\partial \bar{T}_{22}}{\partial Y} + f_2^+ + f_2^- = 0, \tag{5.26b}$$

$$\frac{\partial \bar{T}_{31}}{\partial X} + \frac{\partial \bar{T}_{32}}{\partial Y} + f_3^+ + f_3^- = 0. \tag{5.26c}$$

Similarly, multiplying (5.23a) and (5.23b) by Z and integrating yields equations for the bending moments,

$$\frac{\partial M_{11}}{\partial X} + \frac{\partial M_{12}}{\partial Y} - \bar{T}_{13} + \frac{1}{2}\left(f_1^+ - f_1^-\right) = 0, \tag{5.27a}$$

$$\frac{\partial M_{21}}{\partial X} + \frac{\partial M_{22}}{\partial Y} - \bar{T}_{23} + \frac{1}{2}\left(f_2^+ - f_2^-\right) = 0, \tag{5.27b}$$

where, using the notation of Brush & Almroth (1975),

$$M_{ij} = \int_{-1/2}^{1/2} T_{ij} Z \mathrm{d}Z, \tag{5.28}$$

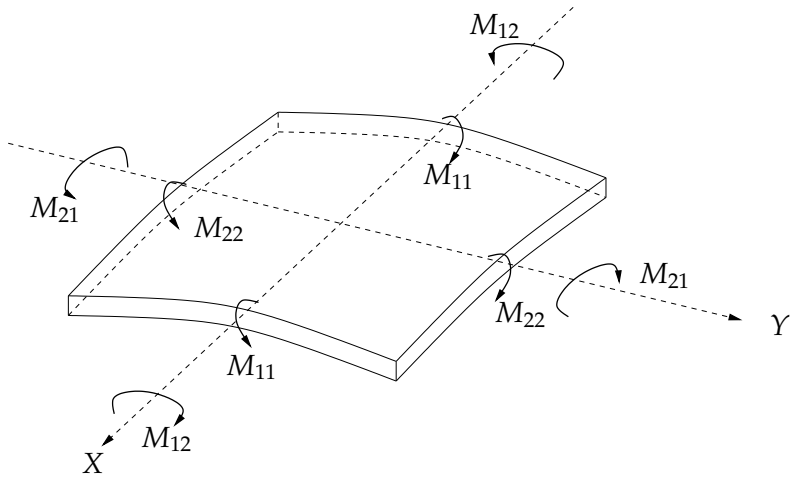

Figure 5.2: Bending moments acting upon a surface element, as defined by 5.28.

the senses of which are illustrated in figure 5.2. We regard M_{ij} as a bending moment which acts upon the side of a surface element whose normal is X_i, owing to internal forces directed parallel to X_j.

We can eliminate $\bar{T}_{21}$, $\bar{T}_{31}$ and $\bar{T}_{32}$ from the system since (5.3) and (5.20) imply that

$$\bar{T}_{21} = \bar{T}_{12} + O\left(\varepsilon^2\right), \tag{5.29a}$$

$$\bar{T}_{31} = \bar{T}_{13} + w_X \bar{T}_{11} + w_Y \bar{T}_{12} + O\left(\varepsilon^2\right), \tag{5.29b}$$

$$\bar{T}_{32} = \bar{T}_{23} + w_X \bar{T}_{21} + w_Y \bar{T}_{22} + O\left(\varepsilon^2\right). \tag{5.29c}$$

Equation (5.29a) states that averaged in-plane shear stresses are equal to leading order.

For notational convenience we define a vector $\boldsymbol{\mathcal{F}}$ with components given by

$$\mathcal{F}_i = f_i^+ + f_i^- \qquad \text{for } i = 1, 2. \tag{5.30}$$

The components of $\boldsymbol{\mathcal{F}}$ represent the net in-plane stresses acting in each coordinate direction due to forcing upon both upper and lower surfaces of the plate. Deploying the Helmholtz decomposition theorem, which states that any two-dimensional vector field can be written as the sum of a conservative component and a rotational component (Arfken & Webber, 2005), we write

$$\boldsymbol{\mathcal{F}} = \nabla\chi + \nabla \times (\psi \hat{\mathbf{z}}), \tag{5.31}$$

for scalar fields χ and ψ. Under this definition, (5.26a) and (5.26b) become

$$\frac{\partial}{\partial X}\left(\bar{T}_{11} + \chi\right) + \frac{\partial}{\partial Y}\left(\bar{T}_{12} + \psi\right) = 0, \tag{5.32a}$$

$$\frac{\partial}{\partial Y}\left(\bar{T}_{22} + \chi\right) + \frac{\partial}{\partial X}\left(\bar{T}_{12} - \psi\right) = 0. \tag{5.32b}$$

We seek to simplify (5.32) by writing the stress resultants in terms of some Airy stress function $\Phi(X, Y)$. However, we see from (5.32) that the definition of a self-consistent Airy stress function is not possible for non-zero ψ. We, thus, restrict our attention to the case $\psi \equiv 0$, under the assumption that cellular growth upon the upper and lower surfaces will not typically impose any twisting upon the substrate. From (5.32) we deduce the appropriate definition of $\Phi(X, Y)$ to be

$$\bar{T}_{11} = \frac{\partial^2 \Phi}{\partial Y^2} - \chi(X, Y), \tag{5.33a}$$

$$\bar{T}_{22} = \frac{\partial^2 \Phi}{\partial X^2} - \chi(X, Y), \tag{5.33b}$$

$$\bar{T}_{12} = -\frac{\partial^2 \Phi}{\partial X \partial Y}. \tag{5.33c}$$

Due to (5.33), (5.26a) and (5.26b) are satisfied trivially. For convenience, we define the vector $\mathbf{\Omega}$ to represent the couple induced by in-plane surface stresses, *i.e.*

$$\Omega_i = f_i^+ - f_i^- \qquad \text{for } i = 1, 2. \tag{5.34}$$

Also, we denote by $\mathcal{N}$ the net normal force upon the substrate due to the two cell layers, *i.e.*

$$\mathcal{N} = f_3^+ + f_3^-. \tag{5.35}$$

Using (5.27–5.35) to manipulate (5.26c), we obtain

$$\frac{\partial^2 M_{11}}{\partial X^2} + 2\frac{\partial^2 M_{12}}{\partial X \partial Y} + \frac{\partial^2 M_{22}}{\partial Y^2} + \frac{\partial^2 w}{\partial X^2}\frac{\partial^2 \Phi}{\partial Y^2} - 2\frac{\partial^2 w}{\partial X \partial Y}\frac{\partial^2 \Phi}{\partial X \partial Y} + \frac{\partial^2 w}{\partial Y^2}\frac{\partial^2 \Phi}{\partial X^2} + \frac{1}{2}\nabla \cdot \mathbf{\Omega} - \nabla \cdot (\chi \nabla w) + \mathcal{N} = 0. \tag{5.36}$$

For now, we restrict attention to the case $0 \leq \nu < 0.5$, returning to the case $\nu = 0.5$ in section 5.3.1. In terms of dimensionless quantities, (5.5) and (5.6) give

$$\mathbf{S} = \frac{\nu E}{(1+\nu)(1-2\nu)} \mathrm{Tr}(\mathbf{e})\mathbf{I} + \frac{E}{1+\nu}\mathbf{e}. \tag{5.37}$$

Following Howell *et al.* (2009), we use (5.2) and (5.37) to evaluate the components of $\mathbf{T}^*$. In particular, we find that

$$\varepsilon^2 T_{13} = E\left(\frac{w_X + u_Z}{2(1+\nu)}\right) + O(\varepsilon^2), \quad \varepsilon^2 T_{23} = E\left(\frac{w_Y + v_Z}{2(1+\nu)}\right) + O(\varepsilon^2), \tag{5.38}$$

to lowest order. Thus, to preserve the balance of terms in (5.38), we require

$$u = \bar{u}(X, Y) - Z w_X, \qquad v = \bar{v}(X, Y) - Z w_Y, \tag{5.39}$$

for some undetermined functions $\bar{u}$ and $\bar{v}$ which capture the displacement of the plate's central plane. Similarly, using (5.2) and (5.37) to evaluate T_{33}, and employing (5.39) to

simplify terms, we have

$$\varepsilon^2 T_{33} = E\left(\frac{w_X^2 + w_Y^2 + 2\nu\left(u_X + v_Y\right) + 2\left(1-\nu\right)\tilde{w}_Z}{2\left(1-\nu\right)}\right) + O\left(\varepsilon^2\right), \tag{5.40}$$

and to ensure consistency between the scalings of (5.15c) and (5.15f), we require

$$\tilde{w}_Z = -\frac{w_X^2 + w_Y^2 + 2\nu\left(u_X + v_Y\right)}{2(1-\nu)}. \tag{5.41}$$

To leading order, equations (5.39) and (5.41) enforce the *Kirchhoff assumptions*, which are commonly deployed in deriving plate theories directly from three-dimensional elasticity. The Kirchhoff assumptions state that (i) normals to the central plane in the undeformed configuration remain normal throughout deformation, which follows from (5.39), and (ii) transverse normal stresses are negligibly small in comparison with in-plane normal stress components, which follows from (5.41). The further requirement that normals are inextensible holds to leading order as a consequence of (5.13); however, transverse normals strains remain $O(\varepsilon^2)$.

Utilising (5.39) and (5.41), we calculate the remaining stress components as

$$T_{11} = E\left(\frac{2u_X + w_X^2 + \nu\left(2v_Y + w_Y^2\right)}{2\left(1-\nu^2\right)}\right) + O\left(\varepsilon^2\right), \tag{5.42a}$$

$$T_{12} = E\left(\frac{u_Y + v_X + w_X w_Y}{2\left(1+\nu\right)}\right) + O\left(\varepsilon^2\right), \tag{5.42b}$$

$$T_{22} = E\left(\frac{\nu\left(2u_X + w_X^2\right) + 2v_Y + w_Y^2}{2\left(1-\nu^2\right)}\right) + O\left(\varepsilon^2\right). \tag{5.42c}$$

Averaging (5.42), we obtain

$$\bar{T}_{11} \equiv \frac{\partial^2 \Phi}{\partial Y^2} - \chi = E\left(\frac{2\bar{u}_X + w_X^2 + \nu\left(2\bar{v}_Y + w_Y^2\right)}{2\left(1-\nu^2\right)}\right), \tag{5.43a}$$

$$\bar{T}_{12} \equiv -\frac{\partial^2 \Phi}{\partial X \partial Y} = E\left(\frac{\bar{u}_Y + \bar{v}_X + w_X w_Y}{2\left(1+\nu\right)}\right), \tag{5.43b}$$

$$\bar{T}_{22} \equiv \frac{\partial^2 \Phi}{\partial X^2} - \chi = E\left(\frac{\nu\left(2\bar{u}_X + w_X^2\right) + 2\bar{v}_Y + w_Y^2}{2\left(1-\nu^2\right)}\right). \tag{5.43c}$$

As a consequence of (5.39) and (5.43), the Lagrangian strain, $\mathbf{e}$, is $O(\varepsilon^2)$ with in-plane components given by

$$e_{11} = \varepsilon^2\left[\frac{1}{E}\left(\frac{\partial^2 \Phi}{\partial Y^2} - \nu\frac{\partial^2 \Phi}{\partial X^2} - \left(1-\nu\right)\chi\right) - \frac{1}{2}w_{XX}Z\right], \tag{5.44a}$$

$$e_{22} = \varepsilon^2\left[\frac{1}{E}\left(\frac{\partial^2 \Phi}{\partial X^2} - \nu\frac{\partial^2 \Phi}{\partial Y^2} - \left(1-\nu\right)\chi\right) - \frac{1}{2}w_{YY}Z\right], \tag{5.44b}$$

$$e_{12} = -\varepsilon^2\left(\frac{1+\nu}{E}\frac{\partial^2 \Phi}{\partial X \partial Y} + w_{XY}Z\right). \tag{5.44c}$$

Rearranging (5.43a) and (5.43c) gives that

$$\bar{u}_X + \frac{w_X^2}{2} = \frac{1}{E}\left(\frac{\partial^2\Phi}{\partial^2 Y} - \nu\frac{\partial^2\Phi}{\partial^2 X} - (1-\nu)\,\chi\right), \tag{5.45a}$$

$$\bar{v}_Y + \frac{w_Y^2}{2} = \frac{1}{E}\left(\frac{\partial^2\Phi}{\partial^2 X} - \nu\frac{\partial^2\Phi}{\partial^2 Y} - (1-\nu)\,\chi\right). \tag{5.45b}$$

We eliminate $\bar{u}$ and $\bar{v}$ from the system by differentiating (5.43b) with respect to X and Y and noting (5.45). For notational convenience we introduce the commutator of functions $\eta(X,Y)$ and $\Theta(X,Y)$, denoted $[\eta,\Theta]$ and defined according to

$$[\eta,\Theta] \equiv \frac{\partial^2\eta}{\partial X^2}\frac{\partial^2\Theta}{\partial Y^2} + \frac{\partial^2\Theta}{\partial X^2}\frac{\partial^2\eta}{\partial Y^2} - 2\frac{\partial^2\eta}{\partial X\partial Y}\frac{\partial^2\Theta}{\partial X\partial Y}. \tag{5.46}$$

In differentiating (5.43b) we note the following two identities:

$$\frac{\partial^2}{\partial X^2}\left(\eta\frac{\partial^2\Theta}{\partial X^2}\right) + \frac{\partial^2}{\partial Y^2}\left(\eta\frac{\partial^2\Theta}{\partial Y^2}\right) + 2\frac{\partial^2}{\partial X\partial Y}\left(\eta\frac{\partial^2\Theta}{\partial X\partial Y}\right) = \nabla^2\left(\eta\nabla^2\Theta\right) - [\eta,\Theta], \tag{5.47a}$$

$$\frac{\partial^2}{\partial Y^2}\left(\eta\frac{\partial^2\Theta}{\partial X^2}\right) + \frac{\partial^2}{\partial X^2}\left(\eta\frac{\partial^2\Theta}{\partial Y^2}\right) - 2\frac{\partial^2}{\partial X\partial Y}\left(\eta\frac{\partial^2\Theta}{\partial X\partial Y}\right) = [\eta,\Theta], \tag{5.47b}$$

which allow us to write (5.43b) as

$$\nabla^2\left(\frac{1}{E}\nabla^2\Phi\right) - \left[\frac{1+\nu}{E},\Phi\right] - \nabla^2\left(\frac{1-\nu}{E}\chi\right) + \frac{1}{2}[w,w] = 0. \tag{5.48}$$

The bending moments are evaluated by multiplying (5.42) by Z and integrating with respect to Z, yielding

$$M_{11} = -\frac{E}{12\,(1-\nu^2)}\left(\frac{\partial^2 w}{\partial X^2} + \nu\frac{\partial^2 w}{\partial Y^2}\right), \tag{5.49a}$$

$$M_{12} = -\frac{E}{12\,(1+\nu)}\frac{\partial^2 w}{\partial X\partial Y}, \tag{5.49b}$$

$$M_{22} = -\frac{E}{12\,(1-\nu^2)}\left(\frac{\partial^2 w}{\partial Y^2} + \nu\frac{\partial^2 w}{\partial X^2}\right). \tag{5.49c}$$

Substituting (5.49) into (5.36), and noting (5.47) once more, we obtain

$$\nabla^2\left(\frac{E}{12\,(1-\nu^2)}\nabla^2 w\right) = \left[\frac{E}{12\,(1+\nu)},w\right] + [w,\Phi] + \frac{1}{2}\nabla\cdot\boldsymbol{\Omega} - \nabla\cdot(\chi\nabla w) + \mathcal{N}. \tag{5.50}$$

The corresponding boundary conditions for (5.62) are as follows. Directly from (5.22), we have the following conditions on w:

$$w(X,\pm l) = w(\pm 1,Y) = 0, \tag{5.51a}$$

$$w_X(\pm 1,Y) = w_Y(X,\pm l) = 0. \tag{5.51b}$$

To obtain conditions upon $\Phi(X,Y)$, we substitute (5.22a) and (5.22b) into (5.45) and note that any partial derivatives of displacements along the boundary vanish. This yields the following boundary conditions:

$$\frac{\partial^2\Phi}{\partial X^2} - \nu\frac{\partial^2\Phi}{\partial Y^2} = (1-\nu)\,\chi \quad \text{on } X = \pm 1, \tag{5.52a}$$

$$\frac{\partial^2\Phi}{\partial Y^2} - \nu\frac{\partial^2\Phi}{\partial X^2} = (1-\nu)\,\chi \quad \text{on } Y = \pm l. \tag{5.52b}$$

We also impose the following condition, which enforces that there is no shear upon the boundaries:

$$\frac{\partial^2\Phi}{\partial X\partial Y}(\pm 1, Y) = \frac{\partial^2\Phi}{\partial X\partial Y}(X, \pm l) = 0. \tag{5.53}$$

Equations (5.48) and (5.50), together with the boundary conditions of (5.51–5.53), provide an extension to the standard von Kármán plate equations to incorporate surface forcing and material nonuniformity.

5.3.1 The incompressible limit

In the case of an incompressible substrate, for which $\nu = 0.5$, the expression for λ^* in (5.6) is invalid. For the stress–strain relationship of (5.5) to remain valid, we require $\mathrm{Tr}(\mathbf{e}) = 0$ in this limit. We consider this below.

From (5.20) and (5.21) we have

$$\det(\mathbf{F}) = 1 + \varepsilon^2\left(u_X + v_Y + \tilde{w}_Z - u_Z w_X - v_Z w_Y\right) + O\left(\varepsilon^4\right), \tag{5.54a}$$

$$\mathrm{Tr}(\mathbf{e}) = \varepsilon^2\left(u_X + v_Y + \tilde{w}_Z + \frac{1}{2}\left(w_X^2 + w_Y^2 + u_Z^2 + v_Z^2\right)\right) + O\left(\varepsilon^3\right). \tag{5.54b}$$

Noting the form of $\tilde{w}_Z$ given in (5.41), (5.54) reduces to

$$\det(\mathbf{F}) = 1 + \frac{\varepsilon^2(1-2\nu)}{1-\nu}\left(u_X + v_Y + \frac{1}{2}\left(w_X^2 + w_Y^2\right)\right) + O\left(\varepsilon^4\right), \tag{5.55a}$$

$$\mathrm{Tr}(\mathbf{e}) = \frac{\varepsilon^2(1-2\nu)}{1-\nu}\left(u_X + v_Y + \frac{1}{2}\left(w_X^2 + w_Y^2\right)\right) + O\left(\varepsilon^3\right). \tag{5.55b}$$

It follows, to leading order, that

$$\det(\mathbf{F}) = 1 + \mathrm{Tr}(\mathbf{e}). \tag{5.56}$$

Since an incompressible substrate satisfies $\det(\mathbf{F}) = 1$, it follows that $\mathrm{Tr}(\mathbf{e}) = 0$. Furthermore, noting (5.39) and (5.45), we can write $\mathrm{Tr}(\mathbf{e})$ as

$$\mathrm{Tr}(\mathbf{e}) = \varepsilon^2(1-2\nu)\left(\frac{\nabla^2\Phi - 2\chi}{E} - \frac{Z}{1-\nu}\nabla^2 w\right), \tag{5.57}$$

so that (5.37) becomes

$$\mathbf{S} = \frac{\nu}{1+\nu}\left(\nabla^2\Phi - 2\chi - \frac{EZ}{1-\nu}\nabla^2 w\right)\mathbf{I} + \frac{E}{1+\nu}\mathbf{e}. \tag{5.58}$$

Hence, (5.37) is regular in the limit $\nu \to 0.5$ and the equations derived in the previous section are valid for an incompressible substrate.

5.3.2 Cell layer assumptions

Motivated by the experimental set-up discussed in chapter 3, we consider deformations induced by the expansion of a cell layer upon the upper surface of the substrate. We assume that no cells are present upon the lower surface ($\boldsymbol{\mathcal{T}}^- = \mathbf{0}$). When studying the one-dimensional analogue of this model in chapter 4, we focused upon two regimes of cell–substrate adhesion: that in which cells are fully bound and that in which cells experience no resistance to sliding against the substrate. We observed that the resulting configurations were highly similar in each regime. In the analysis of this model we, therefore, restrict our attention to the simpler case, assuming that cells are free to slide across the substrate. This assumption implies that there is no in-plane shear upon the upper surface of the substrate, so that $\chi = 0$ and $\boldsymbol{\Omega} = \mathbf{0}$. Applying these assumptions to (5.48) and (5.50), we obtain

$$\nabla^2\left(\frac{1}{E}\nabla^2\Phi\right) - \left[\frac{1+\nu}{E}, \Phi\right] + \frac{1}{2}[w, w] = 0, \tag{5.59a}$$

$$\nabla^2\left(\frac{E}{12\,(1-\nu^2)}\nabla^2 w\right) = \left[\frac{E}{12\,(1+\nu)}, w\right] + [w, \Phi] + \mathcal{N}. \tag{5.59b}$$

Since no friction acts between the cell layer and the substrate, we expect cell growth to generate an isotropic compression $T < 0$ in the cell layer, *i.e.*

$$\mathcal{T}_1^+ = \mathcal{T}_2^+ = T < 0. \tag{5.60}$$

Extending the normal force balance given in (4.15b) to two dimensions, we expect the contribution from the stress in the cell layer to be proportional to the substrate's curvature, κ. We also include a contribution arising from a pressure, p, which acts to deform the substrate downwards. It follows that

$$\mathcal{N} = \kappa T - p \quad \text{where} \quad \kappa = \nabla^2 w. \tag{5.61}$$

Note that each of the terms in (5.61) has an opposing sign to the equivalent term in (4.15b) since the normal upon the upper surface is directed upwards.

For the remainder of this chapter we assume that the substrate is homogeneous, *i.e.* $E \equiv 1$ and ν is constant. In this limit, (5.59) reduces to

$$\nabla^4\Phi + \frac{1}{2}[w, w] = 0, \tag{5.62a}$$

$$\frac{\nabla^4 w}{12\,(1-\nu^2)} = [w, \Phi] + \mathcal{N}, \tag{5.62b}$$

with $\mathcal{N}$ given by (5.61). We return to the problem of an inhomogeneous substrate in chapter 6.

5.4 Comparison with earlier 1D models

Here, we examine solutions to (5.62) and (5.51–5.53) which are of long-wavelength in the Y-direction. Far from the boundaries at $Y = \pm l$, we expect solutions to be slowly-varying with respect to Y, reducing to the problem of a one-dimensional beam to leading order. We anticipate the existence of boundary layers close to $Y = \pm l$, in which the solution undergoes a rapid departure from the one-dimensional solution over a short lengthscale, so that boundary conditions applied on $Y = \pm l$ can be satisfied. In this section, we examine solutions in the outer region (*i.e.* far from the Y-boundaries), comparing results with previous one-dimensional models. Denoting $\delta = 1/l \ll 1$, we rescale Y according to

$$Y = \frac{y}{\delta}. \tag{5.63}$$

Since we expect T_{11} to be of $O(1)$ in general, (5.33a) motivates the following rescaling of Φ:

$$\Phi = \frac{\varphi}{\delta^2}. \tag{5.64}$$

Subject to (5.63) and (5.64), equations (5.62) become

$$\frac{\partial^4 \varphi}{\partial X^4} + 2\delta^2 \frac{\partial^4 \varphi}{\partial X^2 \partial y^2} + \delta^4 \frac{\partial^4 \varphi}{\partial y^4} + \delta^4 \frac{\partial^2 w}{\partial X^2}\frac{\partial^2 w}{\partial y^2} - \delta^4 \left(\frac{\partial^2 w}{\partial X \partial y}\right)^2 = 0, \tag{5.65a}$$

$$\frac{\partial^4 w}{\partial X^4} + 2\delta^2 \frac{\partial^4 w}{\partial X^2 \partial y^2} + \delta^4 \frac{\partial^4 w}{\partial y^4} = 12\left(1-\nu^2\right)\left[\frac{\partial^2 w}{\partial X^2}\frac{\partial^2 \varphi}{\partial y^2} + \frac{\partial^2 w}{\partial y^2}\frac{\partial^2 \varphi}{\partial X^2} - 2\frac{\partial^2 w}{\partial X \partial y}\frac{\partial^2 \varphi}{\partial X \partial y} + \mathcal{N}\right], \tag{5.65b}$$

and are solved subject to

$$w = \frac{\partial w}{\partial X} = \frac{\partial^2 \varphi}{\partial X^2} - \delta^2 \nu \frac{\partial^2 \varphi}{\partial y^2} = \frac{\partial^2 \varphi}{\partial X \partial y} = 0 \quad \text{on } X = \pm 1, \tag{5.66a}$$

$$w = \frac{\partial w}{\partial y} = \delta^2 \frac{\partial^2 \varphi}{\partial y^2} - \nu \frac{\partial^2 \varphi}{\partial X^2} = \frac{\partial^2 \varphi}{\partial X \partial y} = 0 \quad \text{on } y = \pm 1. \tag{5.66b}$$

We expand φ and w in powers of δ^2 as follows,

$$\varphi = \varphi_0 + \delta^2 \varphi_1 + \delta^4 \varphi_2 + \ldots, \tag{5.67a}$$

$$w = w_0 + \delta^2 w_1 + \delta^4 w_2 + \ldots \tag{5.67b}$$

We take a similar expansion for $\mathcal{N}(X, y)$ also. Considering $O(1)$ terms in (5.65a), we have

$$\frac{\partial^4 \varphi_0}{\partial X^4} = 0, \tag{5.68}$$

which suggests the following form for $\varphi_0(X, y)$:

$$\varphi_0(X, y) = \varphi_{00}(y) + \varphi_{01}(y)X + \varphi_{02}(y)X^2 + \varphi_{03}(y)X^3. \tag{5.69}$$

The boundary conditions of (5.66) require that $\varphi_{02}(y) = \varphi_{03}(y) = 0$ and that $\varphi_{01}(y)$ is constant, so that

$$\varphi_0(X, y) = \varphi_{00}(y) + \varphi_{01} X. \tag{5.70}$$

For deflections within the range of validity of this model, we expect in-plane stresses to be of a lower-order than the leading-order out-of-plane displacement. We therefore expect $\mathrm{d}^2\varphi_{00}/\mathrm{d}y^2 = 0$, and we have

$$\frac{1}{12\left(1-\nu^2\right)}\frac{\partial^4 w_0}{\partial X^4} = \mathcal{N}_0, \tag{5.71}$$

which is one form of the beam equation, subject to an applied normal force $\mathcal{N}_0$.

Under the cell layer assumptions of section 5.3.2, (5.61) motivates the following expression for $\mathcal{N}_0$:

$$\mathcal{N}_0 = T\frac{\mathrm{d}^2 w_0}{\mathrm{d}X^2} - p, \tag{5.72}$$

having neglected y-dependence. Substituting (5.72) into (5.71), we have

$$\frac{\mathrm{d}^4 w_0}{\mathrm{d}X^4} + \xi^2\frac{\mathrm{d}^2 w_0}{\mathrm{d}X^2} + 12\left(1-\nu^2\right)p = 0, \tag{5.73}$$

where $\xi^2 = -12\left(1-\nu^2\right)T$. Equation (5.73) recovers the linearisation of the model of chapter 4 (4.44) and, for $p = 0$, recovers that of section 2.1 in the limit of weak springs (2.35).

For $p = 0$, (5.73) suggests that buckling occurs for parameters which give $\xi = \xi_n$, where $\xi_n = (n+1)\pi/2$ for n odd and ξ_n is the $(n/2)^{\text{th}}$ positive root of $\xi = \tan(\xi)$ for n even; the corresponding forms of $w_0(X)$ are given by

$$w_0(X) = \begin{cases} A_n\left(\cos\left(\xi_n X\right) - \cos\xi_n\right) & \text{for } n \text{ odd}, \\ A_n\left(\sin\left(\xi_n X\right) - X\sin\xi_n\right) & \text{for } n \text{ even}, \end{cases} \tag{5.74}$$

where A_n are constants determining the solutions' amplitude, which are arbitrary since (5.73) is linear. Equation (5.74) describes solutions of types n^+ and n^-, attained without bias for $p = 0$; type n^- configurations are as illustrated in figure 4.4. In terms of dimensional quantities, buckling occurs for

$$T^* = -\frac{E^*_{\max} h^{*3}}{12\left(1-\nu^2\right)L_1^{*2}}\xi_n^2. \tag{5.75}$$

Recall the buckling condition of chapter 4 (4.53), in terms of dimensional quantities:

$$\frac{k^* L^{*2}}{D^*}\left(\lambda_G - 1\right) = \xi_n^2, \tag{5.76}$$

where (in the notation of chapter 4) k^* describes the stiffness of the cell layer, $2L^*$ is the substrate's undeformed length, $D^* = E^* h^{*3}/12\left(1-\nu^2\right)$ is the substrate's stiffness, λ_G

is a growth parameter and ξ_n is as defined above. The parametric description of growth used in chapter 4 stated that, for uniform growth in the absence of friction between the layers, the in-plane stress in the cell layer is given by $T^* = k^* \left(\bar{\lambda} - \lambda_G\right)$, where $\bar{\lambda}$ is the substrate's averaged in-plane stretch. For small deflections $\bar{\lambda} \sim 1$ (see (4.40)) and (5.76) becomes

$$T^* = -\frac{E^* h^{*3}}{12\left(1-\nu^2\right) L^{*2}} \xi_n^2, \tag{5.77}$$

which recovers (5.75), since $E^* = E^*_{\max}$ for homogeneous materials.

The leading-order solution given by (5.74) only determines the parameters which give rise to buckling instabilities, it does not provide any information regarding the nature of the bifurcations. Note that, in deriving (5.73), we do not explicitly assume small deflections; equation (5.73) holds in the weakly nonlinear regime also. In the weakly nonlinear regime, this one-dimensional reduction gives rise to solutions of arbitrary amplitude (although these amplitudes must be at most $O(h^*)$ for the model to remain valid). A bifurcation diagram plotting the amplitude of configurations as a function of T would show branches which are exactly vertical close to the bifurcation. Higher-order terms must be considered to identify the nature of the bifurcations; however, the one-dimensional model of chapter 4 predicts that bifurcations are likely to be super-critical for very slender plates.

As discussed in section 4.2, when $p > 0$ (5.73) has solutions for any $\xi \neq m\pi$ ($m \in \mathbb{Z}$) and cellular growth is no-longer solely responsible for inducing buckling. Solutions lose the vertical symmetry which they displayed for $p = 0$, instead becoming biased downwards; figures 4.5 and 4.6 illustrate typical configurations.

5.5 Axisymmetric buckling

We now consider (5.62) in terms of a Lagrangian polar coordinate system, denoted (r, φ). We distinguish quantities written with reference to polar coordinates by addition of hats where necessary; the hatted quantities below refer to variables averaged across the thickness of the plate in a manner consistent with section 5.3. Denoting radial and azimuthal displacements by $\hat{u}$ and $\hat{v}$ respectively, we have

$$\hat{u} = \bar{u}\cos\varphi + \bar{v}\sin\varphi, \tag{5.78a}$$

$$\hat{v} = -\bar{u}\sin\varphi + \bar{v}\cos\varphi. \tag{5.78b}$$

We denote the first Piola-Kirchhoff stress tensor by $\hat{\mathbf{T}}$ when written in terms of polar coordinates and denote its components by $\hat{T}_{\alpha\beta}$. We use Greek letters to distinguish indices in the polar formulation from those in the Cartesian formulation, signifying

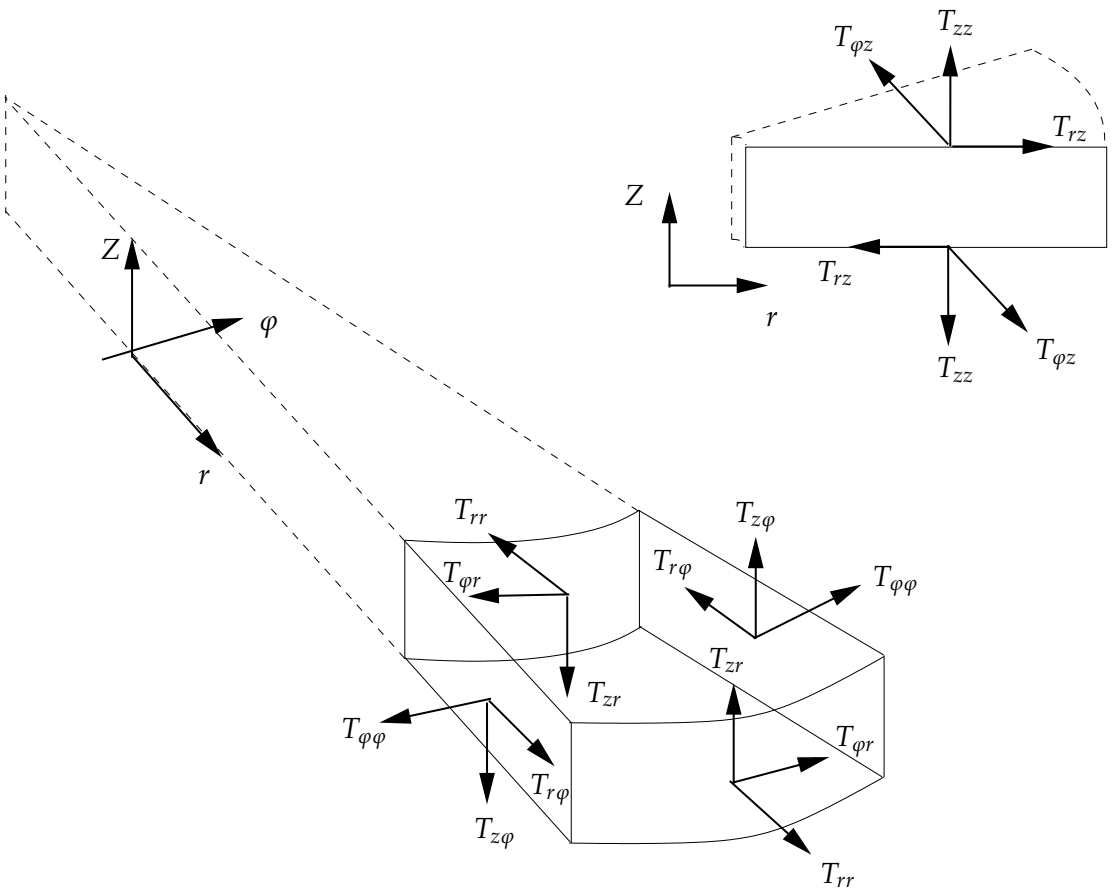

Figure 5.3: Distribution of stresses on a surface element, relative to polar coordinates.

that their values are to be taken from r, φ and z. The senses of these stress components are illustrated in figure 5.3. We begin by relating the components of $\hat{\mathbf{T}}$ to those of $\mathbf{T}$ via the following transformation law,

$$\hat{T}_{\alpha\beta} = \mathcal{M}_{\alpha i}\mathcal{M}_{\beta j}T_{ij}, \tag{5.79}$$

where $\mathcal{M}$ is the matrix given by (Riley *et al.*, 1997)

$$\mathcal{M} = \begin{bmatrix} \cos\varphi & \sin\varphi & 0 \\ -\sin\varphi & \cos\varphi & 0 \\ 0 & 0 & 1 \end{bmatrix}. \tag{5.80}$$

The resulting expressions for the in-plane components of $\hat{\mathbf{T}}$, in terms of Cartesian stresses, are as follows:

$$\hat{T}_{rr} = \bar{T}_{11}\cos^2\varphi + \bar{T}_{22}\sin^2\varphi + 2\bar{T}_{12}\sin\varphi\cos\varphi, \tag{5.81a}$$

$$\hat{T}_{\varphi\varphi} = \bar{T}_{11}\sin^2\varphi + \bar{T}_{22}\cos^2\varphi - 2\bar{T}_{12}\sin\varphi\cos\varphi, \tag{5.81b}$$

$$\hat{T}_{r\varphi} = \left(\bar{T}_{22} - \bar{T}_{11}\right)\sin\varphi\cos\varphi + \bar{T}_{12}\left(\cos^2\varphi - \sin^2\varphi\right). \tag{5.81c}$$

Cartesian derivatives appearing in section 5.3 may be transformed to polar coordinates via

$$\frac{\partial}{\partial X} = \cos\varphi\frac{\partial}{\partial r} - \frac{1}{r}\sin\varphi\frac{\partial}{\partial\varphi}, \qquad \frac{\partial}{\partial Y} = \sin\varphi\frac{\partial}{\partial r} + \frac{1}{r}\cos\varphi\frac{\partial}{\partial\varphi}, \tag{5.82}$$

while vector operators may be expanded as follows:

$$\nabla^2 = \frac{\partial^2}{\partial r^2} + \frac{1}{r}\frac{\partial}{\partial r} + \frac{1}{r^2}\frac{\partial^2}{\partial\varphi^2}, \tag{5.83}$$

$$\nabla^4 = \frac{\partial^4}{\partial r^4} + \frac{2}{r}\frac{\partial^3}{\partial r^3} - \frac{1}{r^2}\frac{\partial^2}{\partial r^2} + \frac{1}{r^3}\frac{\partial}{\partial r} + \frac{2}{r^2}\frac{\partial^4}{\partial\varphi^2\partial r^2} + \frac{1}{r^4}\frac{\partial^4}{\partial\varphi^4} - \frac{2}{r^3}\frac{\partial^3}{\partial\varphi^2\partial r} + \frac{4}{r^4}\frac{\partial^2}{\partial\varphi^2}. \tag{5.84}$$

Similarly, given any functions $\eta(r,\varphi)$ and $\Theta(r,\varphi)$, the commutator may be expanded as follows (Mansfield, 1962):

$$[\Theta,\eta] = \frac{\partial^2\eta}{\partial r^2}\left(\frac{1}{r}\frac{\partial\Theta}{\partial r} + \frac{1}{r^2}\frac{\partial^2\Theta}{\partial\varphi^2}\right) + \frac{\partial^2\Theta}{\partial r^2}\left(\frac{1}{r}\frac{\partial\eta}{\partial r} + \frac{1}{r^2}\frac{\partial^2\eta}{\partial\varphi^2}\right) - 2\frac{\partial}{\partial r}\left(\frac{1}{r}\frac{\partial\Theta}{\partial\varphi}\right)\frac{\partial}{\partial r}\left(\frac{1}{r}\frac{\partial\eta}{\partial\varphi}\right). \tag{5.85}$$

Noting (5.82) and assuming $\chi = 0$, we substitute (5.43) into (5.81) to obtain the following relationships between in-plane stresses and material displacements:

$$\hat{T}_{rr} = \frac{1}{r}\frac{\partial\Phi}{\partial r} + \frac{1}{r^2}\frac{\partial^2\Phi}{\partial\varphi^2} = \frac{E}{2(1-\nu^2)}\left(2\hat{u}_r + w_r^2 + \frac{2\nu}{r}\left(\hat{v}_\varphi + \hat{u}\right) + \nu\left(\frac{1}{r}w_\varphi\right)^2\right), \tag{5.86a}$$

$$\hat{T}_{\varphi\varphi} = \frac{\partial^2\Phi}{\partial r^2} = \frac{E}{2(1-\nu^2)}\left(2\nu\hat{u}_r + \nu w_r^2 + \frac{2}{r}\left(\hat{v}_\varphi + \hat{u}\right) + \left(\frac{1}{r}w_\varphi\right)^2\right), \tag{5.86b}$$

$$\hat{T}_{r\varphi} = -\frac{\partial}{\partial r}\left(\frac{1}{r}\frac{\partial\Phi}{\partial\varphi}\right) = \frac{E}{2(1+\nu)}\left(\hat{v}_r + \frac{1}{r}\left(\hat{u}_\varphi - \hat{v}\right) + \frac{1}{r}w_r w_\varphi\right). \tag{5.86c}$$

Under the cell layer assumptions discussed in section 5.3.2, axisymmetric configurations satisfy the following equations, which follow from (5.62):

$$\mathrm{D}^2\Phi + \frac{1}{2}[w,w] = 0, \tag{5.87a}$$

$$\mathrm{D}^2 w = 12\left(1-\nu^2\right)\left\{[w,\Phi] + \mathcal{N}\right\}, \tag{5.87b}$$

where D denotes the Laplacian operator under the assumption of axisymmetry, *i.e.*

$$\mathrm{D} = \frac{1}{r}\frac{\mathrm{d}}{\mathrm{d}r}\left(r\frac{\mathrm{d}}{\mathrm{d}r}\right). \tag{5.88}$$

Consistent with (5.61), we set $\mathcal{N} = \kappa T - p$ where $\kappa = \mathrm{D}w$, *i.e.*

$$\mathcal{N} = T\frac{\mathrm{d}^2 w}{\mathrm{d}r^2} + \frac{T}{r}\frac{\mathrm{d}w}{\mathrm{d}r} - p. \tag{5.89}$$

In section 5.6 below, we will show that the first term in (5.89) may be associated with curvature in the radial direction, while the second may be associated with curvature in the azimuthal direction; T represents an isotropic cellular compression which generates a normal force proportional to the curvatures in both directions.

5.5.1 Boundary conditions

We hold the rim of the plate fixed and clamped, so that

$$w = \frac{\mathrm{d}w}{\mathrm{d}r} = 0 \qquad \text{on } r = 1. \tag{5.90}$$

Manipulation of (5.86a) and (5.86b) gives the following expression for radial displacement:

$$\hat{u} = \frac{1}{E}\left(r\frac{\mathrm{d}^2\Phi}{\mathrm{d}r^2} - \nu\frac{\mathrm{d}\Phi}{\mathrm{d}r}\right). \tag{5.91}$$

Hence, we impose zero radial displacement at the rim ($r = 1$) via the following boundary condition:

$$\frac{\mathrm{d}^2\Phi}{\mathrm{d}r^2} - \nu\frac{\mathrm{d}\Phi}{\mathrm{d}r} = 0 \qquad \text{on } r = 1. \tag{5.92}$$

To determine the appropriate boundary conditions at the centre of the disc, we consider the relative scalings of Φ and w close to $r = 0$. We expand all dependent variables in terms of powers of r (for $r \ll 1$), setting

$$\Phi = \Phi_0 + r\Phi_1 + \ldots, \tag{5.93a}$$

$$w = w_0 + rw_1 + \ldots, \tag{5.93b}$$

$$\mathcal{N} = \mathcal{N}_0 + r\mathcal{N}_1 + \ldots. \tag{5.93c}$$

Since Φ only appears in the governing equations in differentiated form we assume, without loss of generality, that $\Phi_0 \equiv 0$. Substituting (5.93) into (5.87) and considering terms of $O(1/r^3)$, we find that

$$\Phi_1 = 0, \qquad w_1 = 0. \tag{5.94}$$

The equations yielded at $O(1/r^2)$ are satisfied trivially, while at $O(1/r)$ we have

$$\Phi_3 = 0, \qquad w_3 = 0. \tag{5.95}$$

Balancing $O(1)$ terms gives

$$\Phi_4 = -\frac{1}{16}w_2^2, \qquad w_4 = \frac{3}{16}\left(1-\nu^2\right)\left(8w_2\Phi_2 + \mathcal{N}_0\right). \tag{5.96}$$

Under our cell layer assumptions, (5.89) prescribes $\mathcal{N}_0$ as

$$\mathcal{N}_0 = 4Tw_2 - p, \tag{5.97}$$

assuming that $p = O(1)$. Balancing terms of $O(r)$ gives $\Phi_5 = w_5 = \mathcal{N}_1 = 0$, from which it follows that non-singular solutions have the following local expansion close to $r = 0$:

$$\Phi = \Phi_2 r^2 - \frac{1}{16}w_2^2 r^4 + O\left(r^6\right), \tag{5.98a}$$

$$w = w_0 + w_2 r^2 + \frac{3}{16}\left(1-\nu^2\right)\left(8w_2\Phi_2 + \mathcal{N}_0\right) r^4 + O\left(r^6\right). \tag{5.98b}$$

Local expansions close to $r = 0$ are, therefore, dependent upon three undetermined parameters: Φ_2, w_0 and w_2, which respectively capture the magnitudes of in-plane stresses, vertical deflection and curvature at the centre of the disc.

Since solutions of (5.87) can be singular at $r = 0$, we use the local expansion above to motivate approximate boundary conditions which we impose at $r = \delta$ for some $0 < \delta \ll 1$, suppressing singular solutions. Taking appropriate derivatives of (5.98) gives the following boundary conditions at $r = \delta$:

$$\Phi = \frac{\delta}{2}\frac{\mathrm{d}\Phi}{\mathrm{d}r}, \qquad \frac{\mathrm{d}\Phi}{\mathrm{d}r} = \delta\frac{\mathrm{d}^2\Phi}{\mathrm{d}r^2}, \qquad \frac{\mathrm{d}^3\Phi}{\mathrm{d}r^3} = -\frac{3\delta}{8}\left(\frac{\mathrm{d}^2 w}{\mathrm{d}r^2}\right)^2, \tag{5.99a}$$

$$\frac{\mathrm{d}w}{\mathrm{d}r} = \delta\frac{\mathrm{d}^2 w}{\mathrm{d}r^2}, \qquad \frac{\mathrm{d}^3 w}{\mathrm{d}r^3} = \frac{9\delta}{2}\left(1-\nu^2\right)\left[2\left(\frac{\mathrm{d}^2\Phi}{\mathrm{d}r^2} + T\right)\frac{\mathrm{d}^2 w}{\mathrm{d}r^2} - p\right], \tag{5.99b}$$

having neglected terms of $O(\delta^2)$.

5.5.2 Buckling instabilities due to cell growth

We identify the parameter values for which buckling instabilities occur via analysis of (5.87) for small deformations. We linearise by setting $w = \zeta\bar{w}$ for some $0 < \zeta \ll 1$, assuming that Φ can, in general, remain $O(1)$. We also set $p = \zeta\bar{p}$. For small amplitude deformations, we have

$$\kappa = \zeta \mathrm{D}\bar{w} \tag{5.100}$$

to leading order. Neglecting terms of $O\left(\zeta^2\right)$, (5.87) becomes

$$\mathrm{D}^2\Phi = 0, \tag{5.101a}$$

$$\mathrm{D}^2\bar{w} = 12\left(1-\nu^2\right)\left\{[\bar{w},\Phi] + T\mathrm{D}\bar{w} - \bar{p}\right\}. \tag{5.101b}$$

Solutions to (5.101a) are of the form

$$\Phi = \alpha_1 + \alpha_2 r^2 + \alpha_3 \log r + \alpha_4 r^2 \log r, \tag{5.102}$$

for constants of integration $\alpha_1, \ldots, \alpha_4$. Without loss of generality, we can assume $\alpha_1 = 0$ since only derivatives of Φ appear in (5.101). Enforcing that stresses must be bounded as $r \to 0$, we require $\alpha_3 = \alpha_4 = 0$, while the boundary condition of (5.92) forces $\alpha_2 = 0$. It follows that $\Phi = O\left(\zeta^2\right)$ to leading order. Thus (5.101b) reduces to

$$\mathrm{D}^2\bar{w} = 12T\left(1-\nu^2\right)\mathrm{D}\bar{w} - \bar{p}. \tag{5.103}$$

Assuming that solutions are bounded as $r \to 0$, it follows that $\bar{w}(r)$ takes the following form:

$$\bar{w}(r) = C\left(J_0\left(\sqrt{K}r\right) - J_0\left(\sqrt{K}\right)\right) - \frac{\bar{p}}{4K}\left(r^2 - 1\right), \tag{5.104}$$

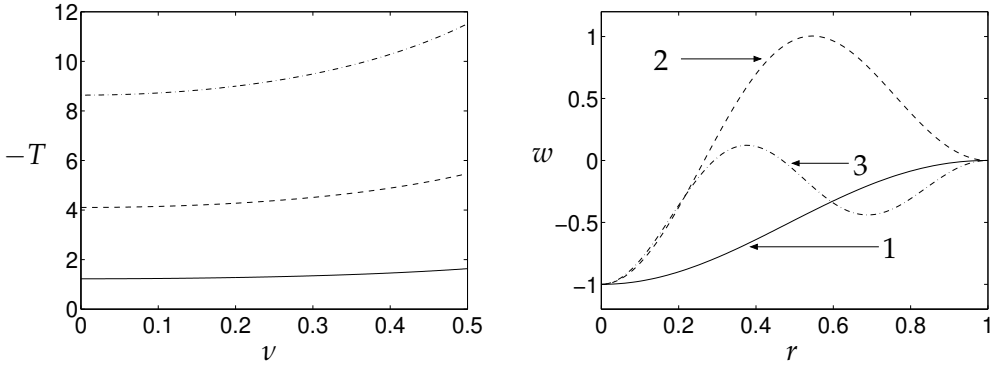

(a) (b)

Figure 5.4: (a) The first three neutral curves of the linear system given by (5.103,5.90), showing the critical degree of cellular compression required to stimulate buckling, as a function of the Poisson's ratio. In (b) the corresponding eigenmodes are shown, normalised so as to have unit amplitude.

where $K = -12(1-\nu^2)T$, C is an arbitrary constant and J_0 is the zero-order Bessel function of the first kind. Since $T < 0$ for a compressed cell layer, and $|\nu| < 1$, we will always have $K > 0$.

In the case $\bar{p} = 0$, setting $\mathrm{d}\bar{w}/\mathrm{d}r = 0$ on $r = 1$ requires that non-trivial solutions only exist for choices of K which satisfy

$$J_1\left(\sqrt{K}\right) = 0. \tag{5.105}$$

Taking the in-plane lengthscales of section 5.2 to be the undeformed disc radius R_0^*, we write (5.105) in terms of dimensional quantities to conclude that a non-trivial configuration can be obtained provided that the cell layer can generate the following degree of compression:

$$T^* = -\frac{E^* h^{*3} j_i^2}{12\left(1-\nu^2\right) R_0^{*2}}, \tag{5.106}$$

where j_i is the i^{th} positive root of $J_1(x) = 0$. The first three neutral curves defined by (5.105), and the corresponding eigenmodes, are illustrated in figure 5.4. In figure 5.4, eigenmodes are normalised in such a manner that they have unit amplitude. We classify solutions as "type $n^{\pm}$", where n is the number of local extrema in the interval $0 \leq r < 1$ and the superscript reflects the sign of w at $r = 0$. Since (5.104) exhibits the symmetry $w \mapsto -w$ when $\bar{p} = 0$, deformed configurations of both positive and negative type are attainable without bias.

For non-zero $\bar{p}$, a buckled configuration is attainable provided $J_1(\sqrt{K}) \neq 0$, with C

given by

$$C = -\frac{\bar{p}}{2K^{3/2}J_1\left(\sqrt{K}\right)}. \tag{5.107}$$

The configuration type is dependent upon K; for small K (5.104) and (5.107) describe a buckled configuration of type $1^{\pm}$. For larger K, (5.104) and (5.107) describe buckled configurations of higher order.

5.5.3 Nonlinear solutions

Here we examine solutions to the full nonlinear system defined by (5.87,5.89), together with the boundary conditions of section 5.5.1. The von Kármán model is valid for deflections of $O(h^*)$. In terms of dimensionless variables, it is appropriate for us to examine solutions for which w is no larger than $O(1)$. Solutions are sought numerically via the use of MATLAB's boundary value solver, bvp4c, in a similar manner to that discussed in chapters 2 and 4. Numerical solutions are validated through comparison with the linear analysis, and through verification that residual errors reported by the solver are sufficiently small. We restrict our attention to the case $\nu = 0.5$, since the cell culture experiments with which we compare our results utilised a silicon-based substrate which is highly hydrated and approximately incompressible. Solutions of type 1^- and 2^-, obtained for $p = 0$ and $\nu = 0.5$, are illustrated in figure 5.5 together with plots of typical radial and hoop stress distributions. The figure illustrates that plate stresses in both radial ($\hat{T}_{rr}$) and azimuthal ($\hat{T}_{\varphi\varphi}$) directions are tensile, since the plate is in extension. Note, however, that cellular growth generates both radial and azimuthal compression within the cell layer, the magnitudes of which are much larger than the tensions in the plate ($T = -3$ in figure 5.5(b), and $T = -7$ in figure 5.5(d)). The composite stresses across both layers are, therefore, compressive in both radial and azimuthal directions.

In figure 5.6, we track the development of the various configurations for $p = 0$, plotting the amplitudes of the profiles as functions of T. The continual growth of the cell layer is equivalent to traversing the bifurcation diagram in figure 5.6 from left to right. We see that initially the substrate will resist deformation until a critical level of compression is present in the cell layer. This behaviour is consistent with the linear analysis above. Once the required compression is achieved, the substrate can buckle into a type $1^{\pm}$ configuration whose amplitude increases as the compression in the cell layer continues to grow. For higher levels of compression, the substrate is able to adopt configurations of higher types.

For $p > 0$ the symmetry of the bifurcation diagram is broken in a manner analogous to

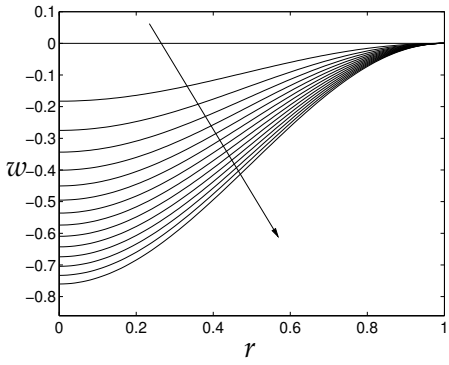

(a) Type 1^- deformations as T is decreased from -1.6 to -3, as indicated by the arrow.

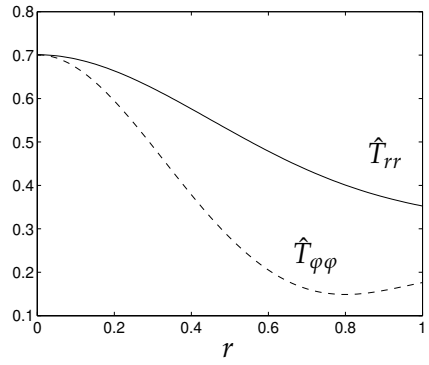

(b) Radial stress (solid line) and hoop stress (dashed line) corresponding to the extremal type 1^- configuration shown in (a), for which $T = -3$.

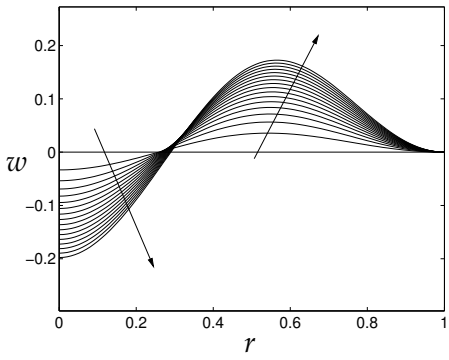

(c) Type 2^- deformations as T is decreased from -5.4 to -7, as indicated by arrows.

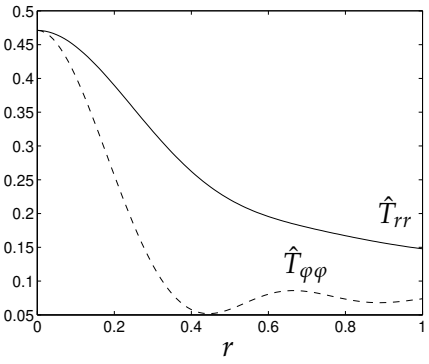

(d) Radial stress (solid line) and hoop stress (dashed line) corresponding to the extremal type 2^- configuration shown in (c), for which $T = -7$.

Figure 5.5: Type 1^- and type 2^- deformations for $\nu = 0.5$ and $p = 0$, together with the corresponding stress distributions.

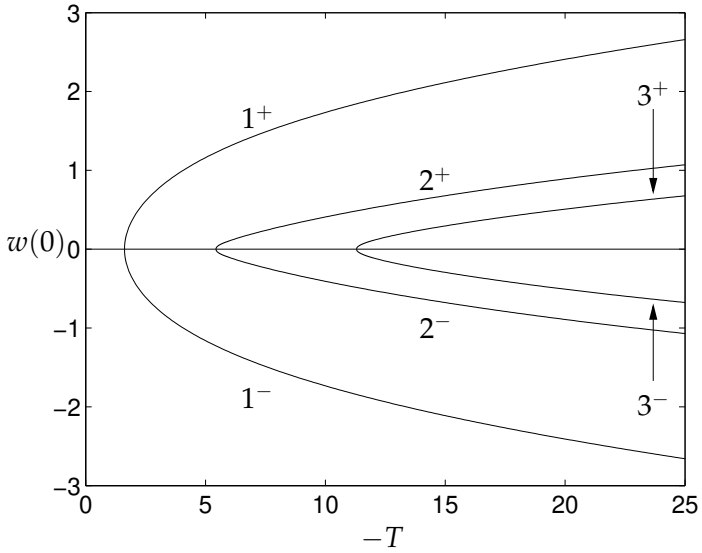

Figure 5.6: Bifurcation diagram illustrating deflections at $r = 0$ as a function of cell compression $(-T)$. Axisymmetric configurations of types $1^{\pm}$, $2^{\pm}$ and $3^{\pm}$ are shown, for an incompressible plate ($\nu = 0.5$), with $p = 0$. The dimensionless deflections plotted here are attained by scaling dimensional displacement against the plate thickness.

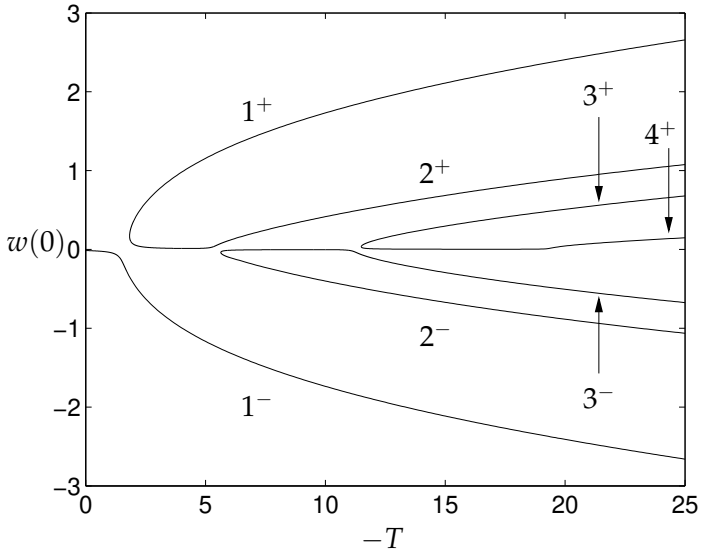

Figure 5.7: Bifurcation diagram illustrating deflections at $r = 0$ as a function of cell compression $(-T)$. Axisymmetric configurations of types $1^{\pm}$, $2^{\pm}$, $3^{\pm}$ and 4^{+} are shown, for an incompressible plate ($\nu = 0.5$), with $p = 0.1$. The dimensionless deflections plotted here are attained by scaling dimensional displacement against the plate thickness.

that of chapter 4, as illustrated in figure 5.7. Even in the absence of cellular growth, a type 1^- configuration is attained; the flat configuration is no longer valid. As growth of the cells induces compression of the cell layer, this configuration grows in amplitude. For sufficiently high compression there exist further unstable branches, the first of which is of type 1^+.

5.6 An alternative shell theory model

We now compare the above results to those of an alternative model based upon that of Pamplona & Calladine (1993). The model of Pamplona & Calladine considers axisymmetric configurations attained by an initially spherical vesicle under compression. The authors modelled the vesicle using nonlinear shell equations, derived via the selection of appropriate constitutive assumptions. We present a detailed derivation of the model in appendix B. We take, as our reference configuration, a disc of radius R^* (rather than the spherical reference configuration originally used by Pamplona & Calladine). The material has bending stiffness D^* and shear modulus H^*. In our adaptation of the model, buckling is driven by the compression required to confine the disc to a circular boundary of radius R_0^*. We deploy a parametric description of growth, examining the equilibrium configurations attained by a sequence of discs of increasing undeformed radius. Figure 5.8 illustrates how we may place the growth studied here into the framework of Rodriguez *et al.* (1994), discussed in section 1.6.2. Our unstressed reference configuration is a flat disc of radius R_0^*. This disc is mapped, via growth tensor $\mathbf{F}_g$, to a hypothetical intermediate configuration in which the disc is enlarged but remains flat and stress-free. In this configuration, the disc is larger than the boundary region to which it is ultimately confined. This enlarged configuration is then acted upon by an elastic deformation gradient tensor, $\mathbf{F}_e$, which acts to confine the rim of the disc to the specified boundary region, thus inducing buckling. Neither $\mathbf{F}$ nor $\mathbf{F}_g$ are prescribed here; however, this model is applicable only to the study of growth patterns which are compatible and result in an intermediate configuration of an unstressed disc. The nature of $\mathbf{F}_e$ is conveniently described in terms of (dimensionless) arc-length coordinates $\tilde{s}$ and s, which measure distance along a meridian from the centre of the disc in the intermediate and buckled configurations respectively. We denote the radial stretch resulting from elastic deformations by λ^{-1}. We show in appendix B that, under the assumption that deformations locally preserve the sheet's area, we have

$$\frac{1}{\lambda} = \frac{\mathrm{d}s}{\mathrm{d}\tilde{s}} = \frac{\tilde{s}}{r}, \tag{5.108}$$

where r denotes radial position in the deformed configuration.

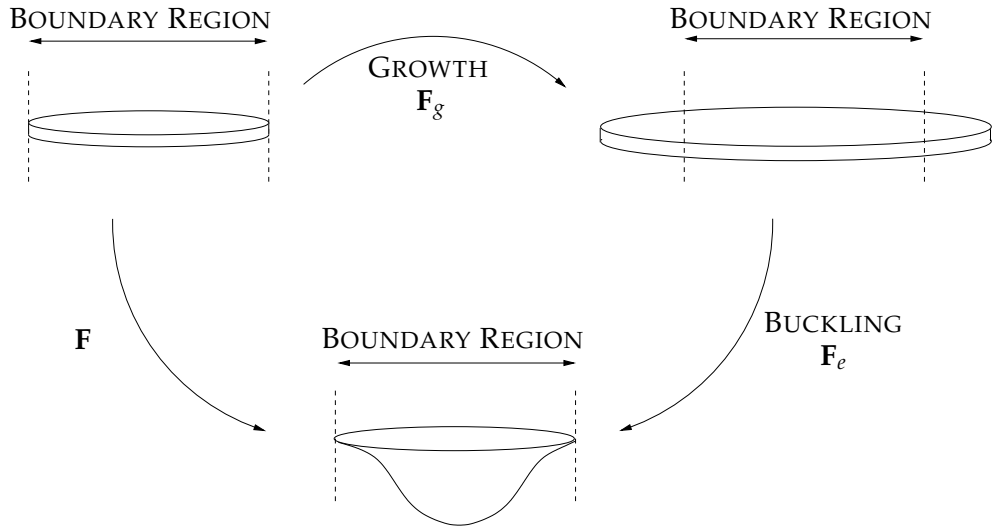

Figure 5.8: Decomposition of growth and buckling in the nonlinear shell model of Pamplona & Calladine (1993). See section 1.6.2 for further details.

In appendix B we derive the equations governing this model which, in terms of appropriate dimensionless variables, are as follows:

$$\frac{\mathrm{d}r}{\mathrm{d}\tilde{s}} = \frac{1}{\lambda}\cos\theta, \tag{5.109a}$$

$$\frac{\mathrm{d}z}{\mathrm{d}\tilde{s}} = \frac{1}{\lambda}\sin\theta, \tag{5.109b}$$

$$\frac{\mathrm{d}\theta}{\mathrm{d}\tilde{s}} = \frac{\kappa_\theta}{\lambda}, \tag{5.109c}$$

$$\frac{\mathrm{d}\kappa_\theta}{\mathrm{d}\tilde{s}} = \frac{1}{\lambda r^2}\sin\theta\cos\theta - \frac{F_n}{\lambda} - \frac{\kappa_\theta}{\lambda r}\cos\theta, \tag{5.109d}$$

$$\frac{\mathrm{d}F_n}{\mathrm{d}\tilde{s}} = \frac{1}{\lambda}\left[-\kappa_\theta\left(F + \alpha\frac{1}{\lambda}\right) - \frac{1}{r}\left(F + \alpha\lambda\right)\sin\theta - \frac{F_n}{r}\cos\theta\right], \tag{5.109e}$$

$$\frac{\mathrm{d}F}{\mathrm{d}\tilde{s}} = -\alpha\frac{\mathrm{d}}{\mathrm{d}\tilde{s}}\left(\frac{1}{\lambda}\right) + \alpha\frac{1}{r}\left(1 - \frac{1}{\lambda^2}\right)\cos\theta + \frac{\kappa_\theta F_n}{\lambda}, \tag{5.109f}$$

where z denotes vertical position, θ is the angle of inclination of the plate to the horizontal, κ_θ is the radial curvature, F is an isotropic in-plane stress resultant and F_n is the normal stress resultant. The system depends upon the dimensionless parameter $\alpha = H^* R_0^{*2}/D^*$, which captures the material's resistance to in-plane shearing relative to its resistance to bending.

Since solutions to (5.109) may be singular at $\tilde{s} = 0$, we use a local series expansion close to $\tilde{s} = 0$ to motivate the following approximate boundary conditions applied at $\tilde{s} = \delta$ (for some $0 < \delta \ll 1$), suppressing singular solutions:

$$r = \delta, \qquad \theta = \kappa_\theta\delta, \qquad F_n = -\kappa_\theta\left(F + \alpha\right)\delta \qquad \text{on } \tilde{s} = \delta. \tag{5.110}$$

A derivation of these approximate boundary conditions is given in appendix B. We

also apply the following conditions, which impose that the rim of the disc is held fixed and clamped:

$$r = 1, \qquad \theta = 0, \qquad z = 0 \qquad \text{on } \tilde{s} = R, \tag{5.111}$$

where $R = R^*/R_0^*$.

5.6.1 Linear analysis

We identify the onset of buckling via linearisation of (5.109–5.111) about the flat configuration. For small deflections $r \sim \tilde{s}$, $\lambda \sim 1$ and $F = F_0$ (for constant F_0) to leading order. We rescale the dependent variables according to

$$r = \tilde{s} + \zeta \bar{r}, \qquad \lambda = 1 + \zeta \bar{\lambda}, \qquad F = F_0 + \zeta \bar{F}, \tag{5.112a}$$

$$\theta = \zeta \bar{\theta}, \qquad z = \zeta \bar{z}, \qquad \bar{\kappa}_\theta = \zeta \bar{\kappa}_\theta, \qquad F_n = \zeta \bar{F}_n, \tag{5.112b}$$

for $0 < \zeta \ll 1$. Neglecting terms of $O(\zeta)$ and smaller, (5.109) becomes

$$\frac{\mathrm{d}\bar{r}}{\mathrm{d}\tilde{s}} = -\bar{\lambda}, \tag{5.113a}$$

$$\frac{\mathrm{d}\bar{z}}{\mathrm{d}\tilde{s}} = \bar{\theta}, \tag{5.113b}$$

$$\frac{\mathrm{d}\bar{\theta}}{\mathrm{d}\tilde{s}} = \bar{\kappa}_\theta, \tag{5.113c}$$

$$\frac{\mathrm{d}\bar{\kappa}_\theta}{\mathrm{d}\tilde{s}} = \frac{\bar{\theta}}{\tilde{s}^2} - \bar{F}_n - \frac{1}{\tilde{s}}\bar{\kappa}_\theta, \tag{5.113d}$$

$$\frac{\mathrm{d}\bar{F}_n}{\mathrm{d}\tilde{s}} = -\bar{\kappa}_\theta \left(F_0 + \alpha\right) - \frac{1}{\tilde{s}} \left(F_0 + \alpha\right) \bar{\theta} - \frac{1}{\tilde{s}} \bar{F}_n, \tag{5.113e}$$

$$\frac{\mathrm{d}\bar{F}}{\mathrm{d}\tilde{s}} = \alpha \frac{\mathrm{d}\bar{\lambda}}{\mathrm{d}\tilde{s}} + \frac{2\alpha\bar{\lambda}}{\tilde{s}}, \tag{5.113f}$$

with $\bar{\lambda} = \bar{r}/\tilde{s}$. We solve (5.113) subject to linearised boundary conditions given by

$$\bar{r} = 0, \qquad \bar{\theta} = \bar{\kappa}_\theta \delta, \qquad \bar{F}_n = -\bar{\kappa}_\theta \left(F_0 + \alpha\right) \delta \qquad \text{on } \tilde{s} = \delta, \tag{5.114a}$$

$$\bar{r} = 0, \qquad \bar{\theta} = 0, \qquad \bar{z} = 0 \qquad \text{on } \tilde{s} = 1, \tag{5.114b}$$

since for small deformations we have $R = 1 + O\left(\zeta^2\right)$. We note that (5.113c-e) decouple from the remainder of the system. For convenience, we define the operator D as

$$\mathrm{D} \equiv \frac{\mathrm{d}}{\mathrm{d}\tilde{s}} + \frac{1}{\tilde{s}} \tag{5.115}$$

and rewrite (5.113c-e) as follows:

$$\mathrm{D}\bar{\theta} = \bar{\kappa}_\theta + \frac{1}{\tilde{s}}\bar{\theta}, \tag{5.116a}$$

$$\mathrm{D}\bar{\kappa}_\theta = \frac{1}{\tilde{s}^2}\bar{\theta} - \bar{F}_n, \tag{5.116b}$$

$$\mathrm{D}\bar{F}_n = C\left(\bar{\kappa}_\theta + \frac{1}{\tilde{s}}\bar{\theta}\right), \tag{5.116c}$$

where $C = -(F_0 + \alpha)$. From (5.116a) and (5.116c) we deduce

$$\mathrm{D}\Psi = 0, \tag{5.117}$$

where $\Psi = \bar{F}_n - C\bar{\theta}$. We integrate (5.117) to obtain a solution of the form

$$\Psi = \frac{\Psi_0}{\tilde{s}}, \tag{5.118}$$

for arbitrary constant of integration Ψ_0. It follows that

$$\bar{F}_n - C\bar{\theta} = \frac{\Psi_0}{\tilde{s}}, \tag{5.119}$$

and from (5.114a) we require $\Psi_0 = 0$. From (5.113c) we have that

$$\frac{\mathrm{d}^2\bar{\theta}}{\mathrm{d}\tilde{s}^2} = \frac{1}{\tilde{s}^2}\bar{\theta} - \bar{F}_n - \frac{1}{\tilde{s}}\frac{\mathrm{d}\bar{\theta}}{\mathrm{d}\tilde{s}}. \tag{5.120}$$

Since (5.119) implies that $\bar{F}_n = C\bar{\theta}$, we rearrange (5.120) to obtain

$$\frac{\mathrm{d}^2\bar{\theta}}{\mathrm{d}\tilde{s}^2} + \frac{1}{\tilde{s}}\frac{\mathrm{d}\bar{\theta}}{\mathrm{d}\tilde{s}} + \left(C - \frac{1}{\tilde{s}^2}\right)\bar{\theta} = 0. \tag{5.121}$$

Since the disc is under compression, we can expect $F_0 < 0$ in general. Provided $F_0 < -\alpha$, so that $C > 0$, we can seek solutions to (5.121) via a change to new independent variable $S = C^{1/2}\tilde{s}$, reducing (5.121) to Bessel's equation of order 1:

$$S^2\frac{\mathrm{d}^2\bar{\theta}}{\mathrm{d}S^2} + S\frac{\mathrm{d}\bar{\theta}}{\mathrm{d}S} + \left(S^2 - 1\right)\bar{\theta} = 0. \tag{5.122}$$

Solutions to (5.122) are of the form

$$\bar{\theta}(S) = AJ_1(S) + BY_1(S), \tag{5.123}$$

where A and B are arbitrary constants of integration and $J_1(S)$ and $Y_1(S)$ are the order-1 Bessel functions of the first and second kind respectively. Since $Y_1 \to -\infty$ as $S \to 0$, we require $B = 0$ for consistency with (5.114a). Since (5.122) is linear, the constant A is arbitrary.

Since (5.114b) requires $\bar{\theta}\left(\sqrt{C}\right) = 0$, we have an eigenvalue problem in C. Non-trivial solutions only exist for those values of C satisfying

$$J_1\left(\sqrt{C}\right) = 0. \tag{5.124}$$

The first three neutral curves are plotted in figure 5.9, the corresponding eigenmodes recover those illustrated in figure 5.4(b).

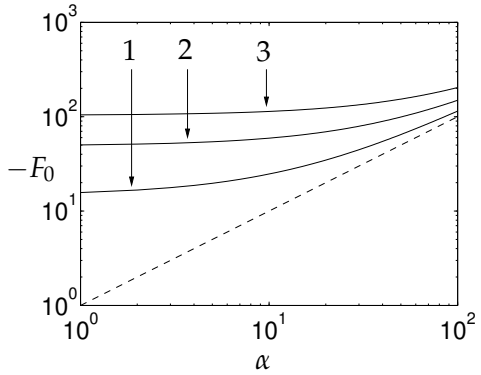

Figure 5.9: The first three neutral curves of the linear system defined by (5.113–5.114). The dashed line illustrates the line $F_0 = -\alpha$, above which (5.122) is valid. The corresponding eigenmodes are as illustrated in figure 5.4(b).

Writing (5.124) in terms of dimensional variables, we have the following condition for the onset of buckling:

$$J_1\left(\sqrt{12\left(1-\nu^2\right)\frac{R_0^*}{E^*h^{*3}}\left(-F_0^*-H^*\right)}\right)=0. \tag{5.125}$$

Denoting the i^{th} positive root of $J_1(x)$ by j_i, (5.125) requires that the force required to yield a buckling instability to a type i configuration is

$$F_0^*=-H^*-\frac{E^*h^{*3}j_i^2}{12\left(1-\nu^2\right)R_0^{*2}}. \tag{5.126}$$

5.6.2 Nonlinear buckling

We now examine solutions to the full nonlinear system given by (5.109–5.111). Solutions are determined using MATLAB's boundary value solver ('bvp4c') as described previously. Configurations upon modes 1 and 2, obtained for various α, are illustrated in figures 5.10–5.12. Figure 5.13 shows corresponding bifurcation diagrams, illustrating the amplitude of configurations, $z(0)$, as a function of R. Also plotted in figure 5.13 are curves illustrating $F(0)$ as a function of R. Consideration of a growing tissue equates to traversing the plots of figures 5.10–5.13 from left to right.

For R close to unity, nonlinear results recover those of the linear analysis above; since the sheet's area is preserved, an infinite family of buckled configurations appears at $R = 1$, each configuration being parameterised by the leading-order in-plane compression, F_0. The configurations with F_0 of smallest magnitude initially correspond to the first neutral curve, the corresponding configuration being similar to that labelled '1' in figure 5.4(b). Since F_0 is a measure of the compressive force required to induce buckling, we regard these configurations to be favoured energetically. For all parameters

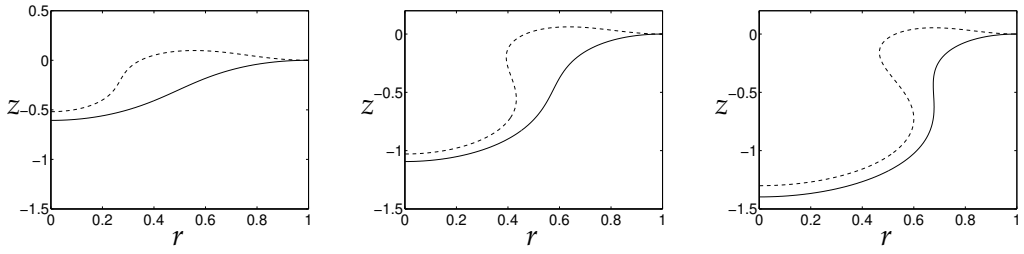

(a) $R = 1.1$ (b) $R = 1.3$ (c) $R = 1.5$

Figure 5.10: Nonlinear mode 1 (solid line) and mode 2 (dashed line) solutions of (5.109–5.111) for $\alpha = 10$.

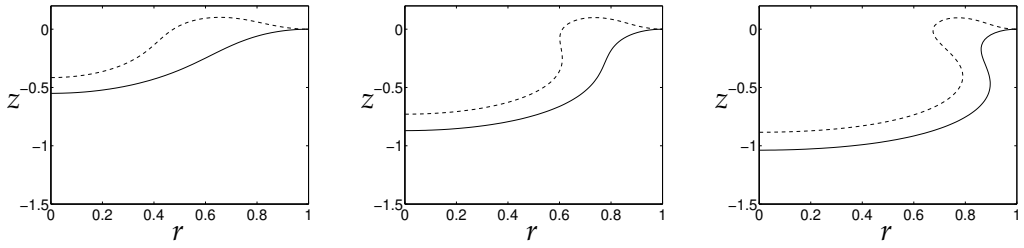

(a) $R = 1.1$ (b) $R = 1.3$ (c) $R = 1.5$

Figure 5.11: Nonlinear mode 1 (solid line) and mode 2 (dashed line) solutions of (5.109–5.111) for $\alpha = 100$.

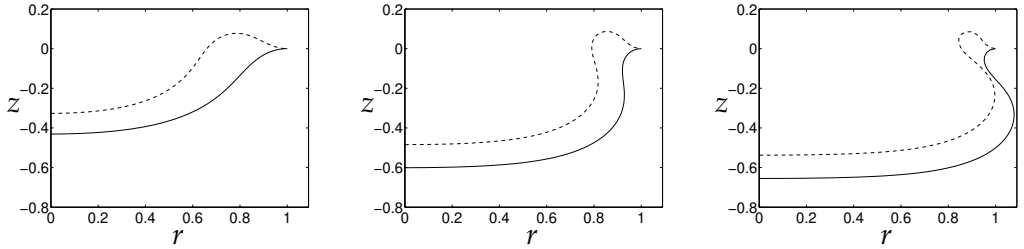

(a) $R = 1.1$ (b) $R = 1.3$ (c) $R = 1.5$

Figure 5.12: Nonlinear mode 1 (solid line) and mode 2 (dashed line) solutions of (5.109–5.111) for $\alpha = 1000$.

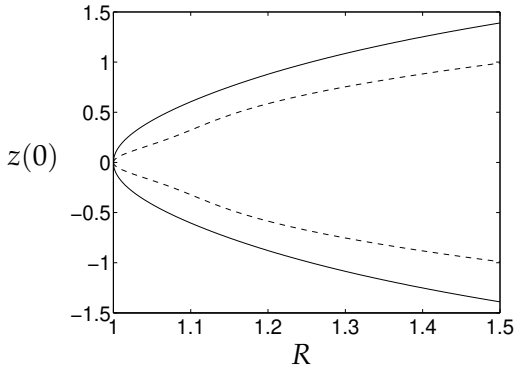

(a) $\alpha = 10$

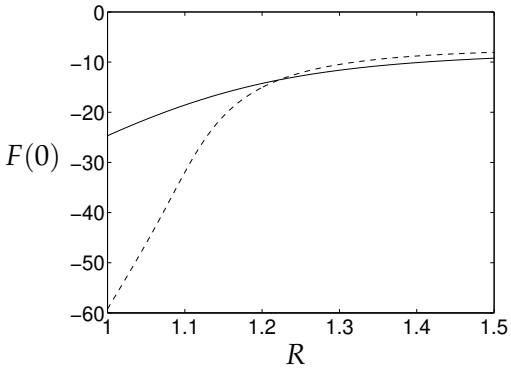

(b) $\alpha = 10$

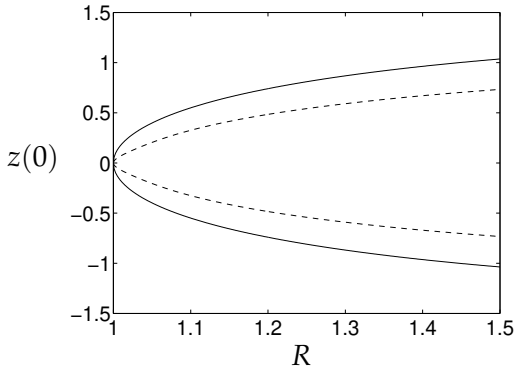

(c) $\alpha = 100$

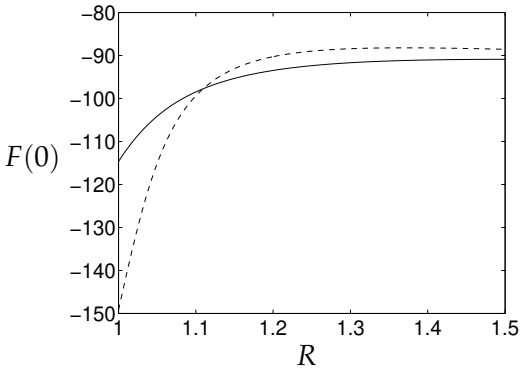

(d) $\alpha = 100$

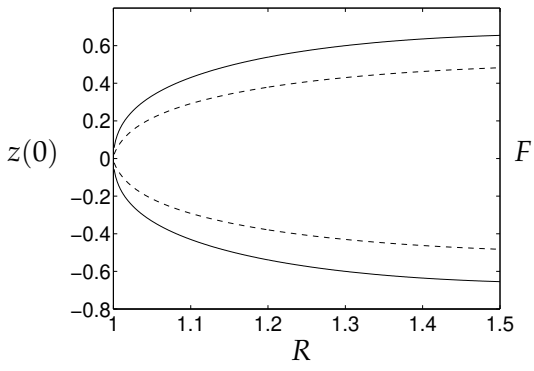

(e) $\alpha = 1000$

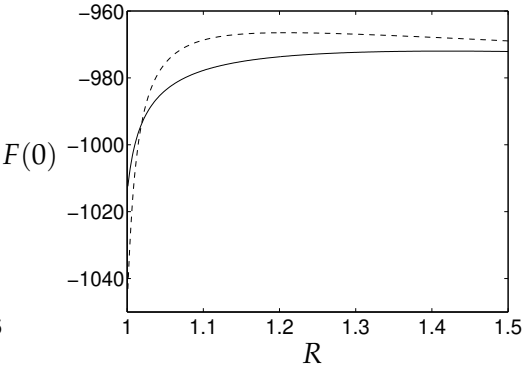

(f) $\alpha = 1000$

Figure 5.13: Bifurcation diagrams in which deflections at $\tilde{s} = 0$ are plotted as functions of R (a,c,e) alongside plots of the corresponding values of $F(0)$ (b,d,f). Solid lines represent mode 1 solutions, dashed lines represent mode 2.

studied, the lowest energy configuration becomes that of mode 2 for sufficiently large R (see figure 5.13(b,d,f)).

5.6.3 Comparison with the von Kármán model

As discussed in chapter 1, various authors have postulated constitutive assumptions relating stresses to strains and bending moments to principal curvatures *etc.* Selection of appropriate constitutive assumptions is a critical exercise which underlies the derivation of the model of Pamplona & Calladine (1993) (and others). Recall from (1.53–1.54) the following two constitutive assumptions, giving in-plane stress resultants (F^*_φ and F^*_θ) in terms of principal stretches (λ_φ and λ_θ):

$$F^*_\varphi - F^*_\theta = H^* \left(\lambda^2_\varphi - \lambda^2_\theta\right), \qquad F^*_\varphi - F^*_\theta = H^* \left(\lambda_\varphi - \lambda_\theta\right), \tag{5.127}$$

the first of which was proposed by Evans & Skalak (1980), while the second was proposed by Pamplona & Calladine (1993) and later used by authors including Parker & Winlove (1999), Preston *et al.* (2008) and Reboux *et al.* (2009). Evans & Skalak (1980) and Pozrikidis (2003) have also suggested the following constitutive assumptions, relating bending moments ($\mathscr{M}^*_\varphi$ and $\mathscr{M}^*_\theta$) to principal curvatures (κ^*_φ and κ^*_θ):

$$\mathscr{M}^*_\varphi = \mathscr{M}^*_\theta = D^* \left(\kappa^*_\varphi + \kappa^*_\theta\right), \tag{5.128a}$$

$$\mathscr{M}^*_\varphi = D^* \left(\kappa^*_\varphi - \tilde{\kappa}^*_\varphi\right), \qquad \mathscr{M}^*_\theta = D^* \left(\kappa^*_\theta - \tilde{\kappa}^*_\theta\right), \tag{5.128b}$$

where quantities with tildes refer to the reference configuration. In the above expressions, positive bending moments induce positive curvatures. This convention is used consistently by all of the above authors; however, this is inconsistent with the convention used in the derivation of the von Kármán model of this chapter. We use calligraphic notation to remind the reader that these bending moments are defined differently to those of (5.28).

Pamplona & Calladine deploy (5.127b) and (5.128a) in their model, choices which are believed to be appropriate for modelling lipid bilayers. These constitutive assumptions are retained in the adaptation of their model described above; here, we examine whether these constitutive assumptions are consistent with the von Kármán model. In the forthcoming comparison of the two models, we present equations in the notation of the von Kármán model. We identify the stress resultants of the model of Pamplona & Calladine (F^*_θ and F^*_φ) with the averaged stresses of the von Kármán model ($\hat{T}^*_{rr}$ and $\hat{T}^*_{\varphi\varphi}$). Principal stretches are denoted λ_r and λ_φ in the von Kármán model; we identify λ_r with λ_θ (the meridional stretch) in the model of Pamplona & Calladine. Similarly, when comparing bending moments, we identify M^*_{rr} and $M^*_{\varphi\varphi}$ in the von Kármán

model with $-\mathscr{M}_\theta^*$ and $-\mathscr{M}_\varphi^*$ respectively. We denote principal curvatures by κ_r^* and κ_φ^* in the von Kármán model. In appendix B, we derive expressions which relate the principal curvatures to the plate's displacement ((B.7) and (B.8)). Motivated by these, we give the following expressions for the principal curvatures of the von Kármán model, which hold at leading order for small deflections:

$$\kappa_r^* = \frac{\mathrm{d}^2 w^*}{\mathrm{d}r^{*2}}, \qquad \kappa_\varphi^* = \frac{1}{r^*}\frac{\mathrm{d}w^*}{\mathrm{d}r^*}. \tag{5.129}$$

We begin by evaluating the strain components of the von Kármán model for axisymmetric deformations. We determine these via an equation similar to (5.81), writing the polar strains in terms of their Cartesian counterparts. Noting (5.44), the in-plane strains upon the plate's central plane are given by

$$e_{rr} = \frac{\varepsilon^2}{E}\left(\frac{1}{r}\frac{\mathrm{d}\Phi}{\mathrm{d}r} - \nu\frac{\mathrm{d}^2\Phi}{\mathrm{d}r^2}\right), \qquad e_{\varphi\varphi} = \frac{\varepsilon^2}{E}\left(\frac{\mathrm{d}^2\Phi}{\mathrm{d}r^2} - \frac{\nu}{r}\frac{\mathrm{d}\Phi}{\mathrm{d}r}\right), \qquad e_{r\varphi} = 0. \tag{5.130}$$

It follows from (5.130) and (1.15) that the principal stretches, denoted λ_r and λ_φ in the notation of the von Kármán model, satisfy

$$\lambda_r^2 = 1 + \frac{2\varepsilon^2}{E}\left(\frac{1}{r}\frac{\mathrm{d}\Phi}{\mathrm{d}r} - \nu\frac{\mathrm{d}^2\Phi}{\mathrm{d}r^2}\right) = 1 + \frac{2\varepsilon^2}{E}\left(\hat{T}_{rr} - \nu\hat{T}_{\varphi\varphi}\right), \tag{5.131a}$$

$$\lambda_\varphi^2 = 1 + \frac{2\varepsilon^2}{E}\left(\frac{\mathrm{d}^2\Phi}{\mathrm{d}r^2} - \frac{\nu}{r}\frac{\mathrm{d}\Phi}{\mathrm{d}r}\right) = 1 + \frac{2\varepsilon^2}{E}\left(\hat{T}_{\varphi\varphi} - \nu\hat{T}_{rr}\right). \tag{5.131b}$$

It follows from (5.131) that

$$\lambda_r^2 - \lambda_\varphi^2 = \frac{2\varepsilon^2\,(1+\nu)}{E}\left(\hat{T}_{rr} - \hat{T}_{\varphi\varphi}\right). \tag{5.132}$$

Noting the scalings of (5.15a) and (5.14), we write (5.132) in terms of dimensional quantities given by

$$\hat{T}_{rr}^* = \varepsilon^2 h^* E_{\max}^* \hat{T}_{rr}, \qquad \hat{T}_{\varphi\varphi}^* = \varepsilon^2 h^* E_{\max}^* \hat{T}_{\varphi\varphi}, \qquad E^* = E_{\max}^* E, \tag{5.133}$$

where the additional h^* terms in (5.133) arise since $\hat{T}_{rr}$ and $\hat{T}_{\varphi\varphi}$ refer to quantities averaged across the thickness of the plate. Equation (5.132) then becomes

$$\hat{T}_{rr}^* - \hat{T}_{\varphi\varphi}^* = \frac{E^* h^*}{2\,(1+\nu)}\left(\lambda_r^2 - \lambda_\varphi^2\right), \tag{5.134}$$

which recovers the constitutive assumption posed by Evans & Skalak (1980) (5.127a) with $H^* = E^* h^*/2\,(1+\nu)$. Noting this expression for H^*, we may express the dimensionless parameter α (which appears in the model of Pamplona & Calladine) as follows:

$$\alpha = \frac{H^* R_0^{*2}}{D^*} = 6\,(1-\nu)\,\frac{R_0^{*2}}{h^{*2}} \gg 1, \tag{5.135}$$

which shows that α represents an inverse measure of the aspect ratio of the plate, identifiable with ε^{-2} in the von Kármán model.

While the model of Pamplona & Calladine treats H^* as an independent parameter, the von Kármán model states that this parameter is actually given as a combination of material parameters. Substituting the above form of H^* into (5.126), the model of Pamplona & Calladine predicts that buckling instabilities occur when the leading-order in-plane compression, F_0^*, satisfies

$$F_0^* = E^* h^* \left(-\frac{1}{2\left(1+\nu\right)} - \frac{\varepsilon^2 j_1^2}{12\left(1-\nu^2\right)} \right), \tag{5.136}$$

where $\varepsilon = h^*/R_0^*$ and j_1 denotes the first positive root of $J_1(x)$. The model of Pamplona & Calladine therefore predicts that the buckling threshold is dominated by the plate's resistance to shear.

Noting (5.81) and the expressions for bending moments in terms of Cartesian coordinates given by (5.49), we can determine the bending moments corresponding to axisymmetric deformations as

$$M_{rr} = -\frac{E}{12\left(1-\nu^2\right)} \left(\frac{\mathrm{d}^2 w}{\mathrm{d}r^2} + \frac{\nu}{r}\frac{\mathrm{d}w}{\mathrm{d}r} \right), \tag{5.137a}$$

$$M_{\varphi\varphi} = -\frac{E}{12\left(1-\nu^2\right)} \left(\nu\frac{\mathrm{d}^2 w}{\mathrm{d}r^2} + \frac{1}{r}\frac{\mathrm{d}w}{\mathrm{d}r} \right). \tag{5.137b}$$

It follows from (5.137) that

$$M_{rr} - M_{\varphi\varphi} = -\frac{E}{12\left(1+\nu\right)} \left(\frac{\mathrm{d}^2 w}{\mathrm{d}r^2} - \frac{1}{r}\frac{\mathrm{d}w}{\mathrm{d}r} \right). \tag{5.138}$$

In terms of dimensional variables given by

$$\{M_{rr}^*, M_{\varphi\varphi}^*\} = \varepsilon^2 h^{*2} E_{\max}^* \{M_{rr}, M_{\varphi\varphi}\}, \qquad w^* = h^* w, \qquad r^* = R_0^* r, \tag{5.139}$$

where R_0^* is the undeformed disc radius, (5.138) becomes

$$M_{rr}^* - M_{\varphi\varphi}^* = -D^* \left(\frac{\mathrm{d}^2 w^*}{\mathrm{d}r^{*2}} - \frac{1}{r^*}\frac{\mathrm{d}w^*}{\mathrm{d}r^*} \right), \tag{5.140}$$

where $D^* = E^* h^{*3}/12\left(1-\nu^2\right)$ is the plate's bending stiffness. Noting (5.129), we write (5.140) as

$$M_{rr}^* - M_{\varphi\varphi}^* = -D^* \left(\kappa_r^* - \kappa_\varphi^* \right). \tag{5.141}$$

The additional minus sign in (5.141) appears to ensure consistency with (5.28), in which positive bending moments generate negative curvatures. Equation (5.141) illustrates that the difference between bending moments in the von Kármán model is consistent with (5.128b), since the plate has zero curvature in the reference configuration; however, (5.137) states that the von Kármán model is not entirely consistent with either of

the constitutive assumptions of (5.128). Writing (5.137) in terms of dimensional quantities, we see that the von Kármán model suggests that the appropriate constitutive assumption for the bending moments should be as follows:

$$M^*_{rr} = -D^* \left(\kappa^*_r + \nu \kappa^*_\varphi \right), \qquad M^*_{\varphi\varphi} = -D^* \left(\kappa^*_\varphi + \nu \kappa^*_r \right). \tag{5.142}$$

Differences between the constitutive assumptions used in these models underpin any differences in the resulting configurations and corresponding distributions of stresses. Below, we compare typical stress distributions obtained at finite amplitude in the two models. Note the following expressions for the dimensional stresses in each model, which follow from the scaling above:

$$\text{von Kármán:} \qquad \{\hat{T}^*_{rr}, \hat{T}^*_{\varphi\varphi}, \mathcal{T}^*\} = 12\left(1-\nu^2\right) \frac{D^*}{R_0^{*2}} \{\hat{T}_{rr}, \hat{T}_{\varphi\varphi}, T\} \tag{5.143a}$$

$$\text{Pamplona \& Calladine:} \qquad F^*_\theta = \frac{D^*}{R_0^{*2}} F + \frac{H^*}{\lambda}, \qquad F^*_\varphi = \frac{D^*}{R_0^{*2}} F + H^* \lambda, \tag{5.143b}$$

where $\mathcal{T}^*$ is the isotropic stress in the cell layer of the von Kármán model. In figure 5.14, we consider a plate of aspect ratio $\varepsilon = 1/10$ and Poisson's ratio $\nu = 0.5$ to illustrate typical differences in stress distributions between the two models. The figure plots the dimensional stresses of (5.143), divided by D^*/R_0^{*2}, so as to be independent of dimensional parameters. Consistent with (5.135), we set $\alpha = 300$ in the model of Pamplona & Calladine. The figure shows stresses corresponding to configurations whose deflections are of magnitude h^* in both models. Note that these deflections are within the range of validity of both models; comparison of the models for deflections which are regarded as 'large' in the model of Pamplona & Calladine is not appropriate since these violate the asymptotic assumptions of the von Kármán model. In figure 5.14(a), we show the radial and hoop stresses in the plate in the von Kármán model (blue curves), together with the net stresses incorporating both the cell layer and plate (red curves). The figure illustrates that in this model the plate is in extension in both principal directions, although the composite stresses are both compressive. In figure 5.14(b), we show the equivalent stresses in the model of Pamplona & Calladine (F^*_θ and F^*_φ), showing that the plate is compressed in both radial and azimuthal directions. Comparing the two figures reveals that the stresses predicted by the two models differ.

The von Kármán model recovers (5.127a), while Pamplona & Calladine assume (5.127b): we identify this as one potential source for discrepency. However, numerical tests reveal that replacing (5.127b) with (5.127a) has only a minor effect upon stress distributions (details omitted). While Pamplona & Calladine deploy (5.128a) in their model (as opposed to (5.128b) or (5.142)), substitution of (5.128b) or (5.142) into (B.18a) reveals that additional terms cancel (provided that the reference configuration is flat).

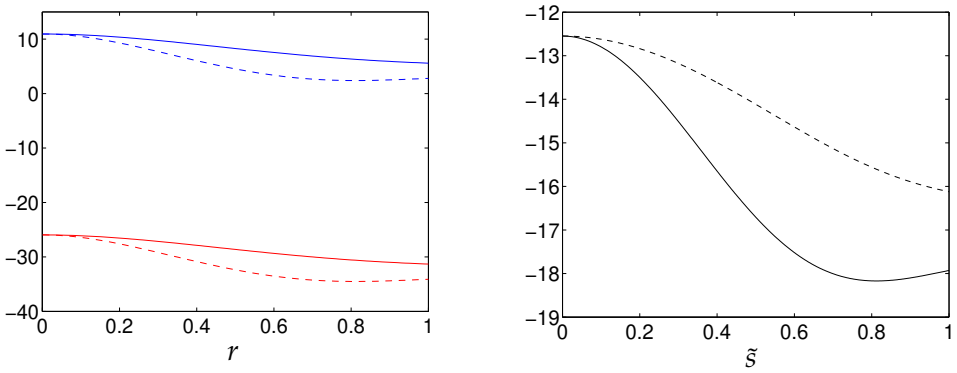

(a) (b)

Figure 5.14: A comparison of stress distributions in the von Kármán model and the model of Pamplona & Calladine, for a plate with aspect ratio $\varepsilon = 1/10$ and $\nu = 0.5$. Plots show dimensional stresses divided by D^*/R_0^{*2}, so as to be independent of dimensional quantities. Maximal dimensional deflections are of magnitude h^* in both panels. In (a) we show the radial (blue, solid line) and azimuthal (blue, dashed line) stresses in the plate, and the net radial (red, solid line) and azimuthal (red, dashed line) stresses incorporating both plate and cell layer, for $T = -4.1$. In (b) we show radial (solid line) and azimuthal (dashed line) stresses in the model of Pamplona & Calladine, for $R = 1.0003$ and $\alpha = 300$ (consistent with (5.135)).

While expressions for corresponding physical quantities will differ, the shapes of configurations predicted by this model are independent of the assumptions upon bending moments in this case. Furthermore, the model of Pamplona & Calladine assumes (in (B.20)) absolute inextensibility of the layer in the out-of-plane direction. While the von Kármán model is consistent with this to leading order, the transverse normal strain is of the same magnitude ($O(\varepsilon^2)$) as in-plane strains. This suggests that (B.21) may not be entirely appropriate; however, a suitable alternative does not readily present itself as a result of the von Kármán analysis.

5.7 Conclusions

In this chapter, we have considered two models for growth-induced deformations of a thin, two-dimensional layer. The first of these deployed von Kármán plate theory, considering deformations to be driven by the growth of a cell layer upon the plate's upper surface. In light of the results of chapter 4, we assumed that the cell layer experiences no resistance to sliding along the layer; a normal force proportional to curvature was

then transmitted to the substrate. Solutions were determined numerically for extensive cellular growth; however, the validity of underlying mechanical assumptions becomes questionable at large amplitude. While the primary motivation for the development of this model was centred around epithelial cell culture *in vitro*, we may also view the model as applicable to a buckling epithelium resting upon underlying tissue *in vivo*.

The above model was compared to the nonlinear shell model of Pamplona & Calladine (1993), derived through selection of appropriate constitutive assumptions. For small deflections, the two models predicted buckling instabilities for critical values of compression which differ in a manner proportional to the shear modulus of the material (H^*). For a material whose shear modulus is small, the two models are in agreement to leading order. The model of Pamplona & Calladine treats H^* as an independent parameter; however, comparison with the von Kármán model reveals that $H^* = E^*h^*/2(1+\nu)$ for linearly elastic materials. Differences between the two models were most apparent at large amplitude (*i.e.* after more prolonged growth). The von Kármán model motivates the use of the constitutive assumption upon stresses and strains used by Evans & Skalak (1980), rather than (5.127b). Motivated by the von Kármán model, we suggested a new constitutive assumption upon bending moments in (5.142). However, brief analyses reveal that results are relatively insensitive to these choices provided that the reference configuration is flat. The derivation of the model of Pamplona & Calladine assumes, in (B.20), that there is no change in the thickness of the plate during deformation: a valid assumption for their study of a lipid bilayer whose thickness is necessarily fixed. Since the von Kármán model states that transverse normal strains are of similar magnitude to in-plane strains, we may regard the validity of (B.20) as questionable for some materials; however, identification of a suitable alternative remains as further work. It is notable that (B.20) is justifiable in that it facilitates modelling progress, and can be thought to provide a reasonable approximation of the full system. Comparison of the two models has highlighted the sensitivity of results to the choice of underlying constitutive assumptions. Importantly, the validity of both models is questionable for large amplitude configurations which exhibit large strains.

Neither of the models presented in this chapter incorporate patterned growth; however, the models of chapters 2 and 4 suggest that patterning of growth is largely insignificant in determining the shapes of buckled configurations. For such a patterning to be of any significance at all, cell–substrate adhesion must be strong. The analyses presented in this chapter focus upon one-dimensional (planar and axisymmetric) reductions of the von Kármán model for homogeneous plates. We examine fully two-dimensional solutions for inhomogeneous plates in the following chapter.

CHAPTER 6

Tissue Patterning as a Mechanism of Crypt Frequency Control

In this chapter, we seek solutions to the von Kármán model of chapter 5 for plates whose material properties vary spatially. We seek to establish the extent to which variations in the material properties of the substrate control buckling patterns.

Recall that the equations governing the buckling of the substrate due to a cell layer upon the upper surface, assuming that the cell layer experiences no resistance to sliding against the substrate, are

$$\nabla^2\left(\frac{1}{E}\nabla^2\Phi\right) - \left[\frac{1+\nu}{E},\Phi\right] + \frac{1}{2}\left[w,w\right] = 0, \tag{6.1a}$$

$$\nabla^2\left(\frac{E}{12\left(1-\nu^2\right)}\nabla^2 w\right) = \left[\frac{E}{12\left(1+\nu\right)},w\right] + \left[w,\Phi\right] + T\kappa, \tag{6.1b}$$

where $T < 0$ is the isotropic tension in the cell layer and the curvature of the substrate, κ, is given by

$$\kappa = \nabla^2 w, \tag{6.2}$$

to leading order. In this chapter, we assume that no external pressure acts across the layer, setting $p = 0$ in (5.61).

We solve (6.1) subject to boundary conditions given by (5.51–5.53), in the case of a Cartesian formulation, or by (5.90,5.92,5.99) when studying axisymmetric deformations in a polar coordinate system. We begin this chapter with an analysis of long wavelength solutions on a rectangular domain, allowing (6.1) to be reduced from a PDE system to an ODE system. We then repeat the same analysis for axisymmetric deformations of a circular substrate to examine the restrictions placed upon deformation by the generation of a non-zero hoop stress resultant. We will then examine fully two-dimensional patternings of a rectangular substrate.

6.1 Long wavelength solutions on a rectangular domain

Assuming that variations in the Y-direction occur over a long wavelength, we exploit the small parameter $\delta = 1/l$ to recover a one-dimensional beam problem to leading order. Deploying the rescalings of (5.63,5.64) and expanding dependent variables in powers of δ^2, as in (5.67), (6.1a) implies that Φ is $O(\delta^2)$ to leading order. From (6.1b), the leading-order problem is then given by

$$\frac{\partial^2}{\partial X^2}\left(\frac{E}{12\left(1-\nu^2\right)}\frac{\partial^2 w}{\partial X^2}\right) = T\frac{\partial^2 w}{\partial X^2}, \tag{6.3}$$

where T is the leading-order compression in the cell layer. We solve (6.3) numerically using a shooting method. For simplicity we solve on half of the domain, assuming either odd or even symmetry conditions on $X = 0$. Thus, we solve (6.3) subject to

$$w = 0, \quad \frac{\partial w}{\partial X} = 0, \quad \frac{\partial^2 w}{\partial X^2} = 1 \quad \text{on } X = -1, \tag{6.4}$$

and adjust T until the resulting solution also satisfies

$$\frac{\partial w}{\partial X} = \frac{\partial^3 w}{\partial X^3} = 0 \quad \text{on } X = 0, \tag{6.5}$$

in the case of odd modes, or

$$w = \frac{\partial^2 w}{\partial X^2} = 0 \quad \text{on } X = 0, \tag{6.6}$$

for even modes. Since the problem is linear, we normalise all eigenmodes such that their maximal deflections are of unit magnitude.

We restrict attention to non-uniformities of the Young's modulus of the form

$$E(X) = \frac{1 + c - c\exp\left(p\left(X-a\right)^m\right)}{1 + c - c\exp\left(p\left(1-a\right)^m\right)}, \tag{6.7}$$

for $p = -100$ and $m = 4$. Setting $c = 0$ in (6.7) corresponds to a homogeneous substrate, while increasing c increases the magnitude of inhomogeneities. We examine two cases below: $a = 0$, which represents a softened region in the centre of the substrate, and $a = -0.5$, which yields a distinct softened region in each half of the domain. Note that the denominator in (6.7) appears simply to ensure consistency with the nondimensionalisation of (5.14). Throughout all of the analysis below, the Poisson's ratio remains fixed at $\nu = 0.5$.

The first three modes attained in each of the above cases are illustrated (for $c = 10000$) in figure 6.1, alongside their homogeneous counterparts. With $a = 0$ the solution obtained upon mode 1 is reminiscent of a single crypt in the centre of the substrate, while

with $a = -0.5$ a two-crypt configuration appears upon mode 3. The first three neutral curves in each regime are illustrated in figure 6.2. The effect of imposing a softening of the substrate is that the magnitude of cellular compression required to deform the substrate is reduced. While imposing a patterning with $a = -0.5$ does not result in a transition of the primary buckling mode from type 1 to type 3 for parameters investigated, the mode 3 configuration is more easily attained with such a softening than in the homogeneous case.

6.2 Axisymmetric solutions

Here, we briefly examine the axisymmetric analogue of the solutions above. Following our analysis of homogeneous materials in chapter 5, we linearise (6.1) via the assumption that if $w \sim \zeta$ for some $0 < \zeta \ll 1$, then $\Phi \sim \zeta^2$. Under these scalings (6.1b) reduces to

$$\frac{1}{r}\frac{\mathrm{d}}{\mathrm{d}r}\left(r\frac{\mathrm{d}}{\mathrm{d}r}\left(\frac{E}{12\left(1-\nu^2\right)r}\frac{\mathrm{d}}{\mathrm{d}r}\left(r\frac{\mathrm{d}w}{\mathrm{d}r}\right)\right)\right) = \frac{1}{r}\left(\frac{\mathrm{d}}{\mathrm{d}r}\left(\frac{E}{12\left(1+\nu\right)}\right)\frac{\mathrm{d}^2w}{\mathrm{d}r^2} + \frac{\mathrm{d}^2}{\mathrm{d}r^2}\left(\frac{E}{12\left(1+\nu\right)}\right)\frac{\mathrm{d}w}{\mathrm{d}r}\right) + \frac{T}{r}\frac{\mathrm{d}}{\mathrm{d}r}\left(r\frac{\mathrm{d}w}{\mathrm{d}r}\right), \tag{6.8}$$

and (following from (5.90) and (5.99)) is solved subject to

$$w = -1, \qquad \frac{\mathrm{d}w}{\mathrm{d}r} = \delta\frac{\mathrm{d}^2w}{\mathrm{d}r^2}, \qquad \frac{\mathrm{d}^3w}{\mathrm{d}r^3} = 9\delta T\left(1-\nu^2\right)\frac{\mathrm{d}^2w}{\mathrm{d}r^2}, \quad \text{on } r = \delta, \tag{6.9a}$$

$$w = 0 \qquad \text{on } r = 1. \tag{6.9b}$$

The first condition in (6.9a) is a normalisation condition which we can select arbitrarily since (6.8) is linear. We deploy a shooting method once more, adjusting T until the configuration also satisfies

$$\frac{\mathrm{d}w}{\mathrm{d}r} = 0 \quad \text{on } r = 1. \tag{6.10}$$

We restrict attention to a softening in the centre of the substrate here, prescribing the Young's modulus according to

$$E(r) = \frac{1 + c - c\exp\left(pr^m\right)}{1 + c - c\exp\left(p\right)}, \tag{6.11}$$

for $p = -100$ and $m = 4$. Once more, we fix $\nu = 0.5$. Furthermore, we restrict attention to type 1 solutions in this regime.

Solution of (6.8–6.11) allows us to determine the degree of cellular compression required to stimulate a buckling instability. The resulting neutral curve is illustrated (for

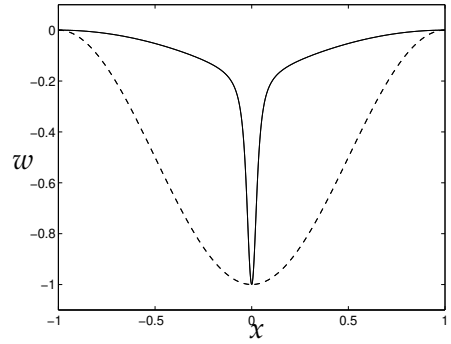

(a) Mode 1 solution, $a = 0$.

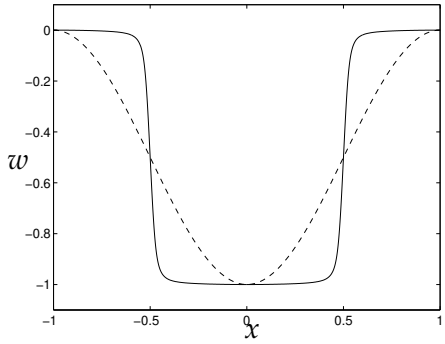

(b) Mode 1 solution, $a = -0.5$.

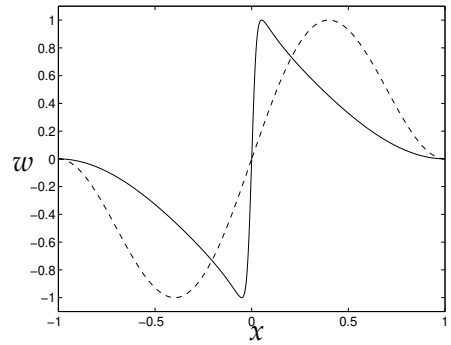

(c) Mode 2 solution, $a = 0$.

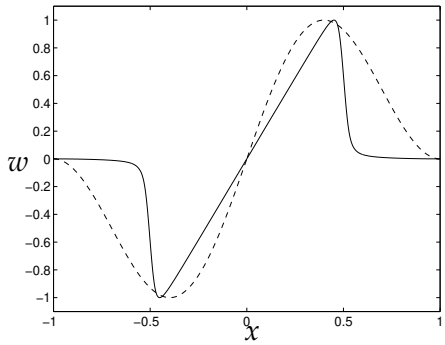

(d) Mode 2 solution, $a = -0.5$.

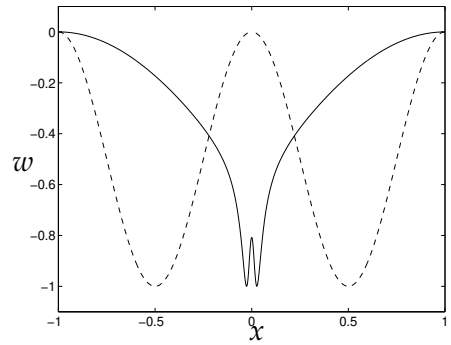

(e) Mode 3 solution, $a = 0$.

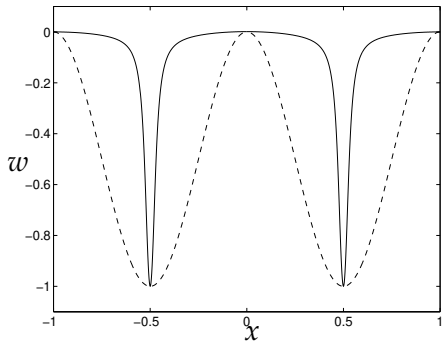

(f) Mode 3 solution, $a = -0.5$.

Figure 6.1: Eigenmodes obtained in the one-dimensional reduction of the von Kármán model, for incompressible, inhomogeneous plates patterned according to (6.7) with $c = 10000$ (solid lines). In (a,c,e), the plate has a reduced resistance to bending in the centre of the plate, while in (b,d,f) the plate is softened close to $x = \pm 0.5$. Dashed lines illustrate equivalent solutions for homogeneous plates ($c = 0$).

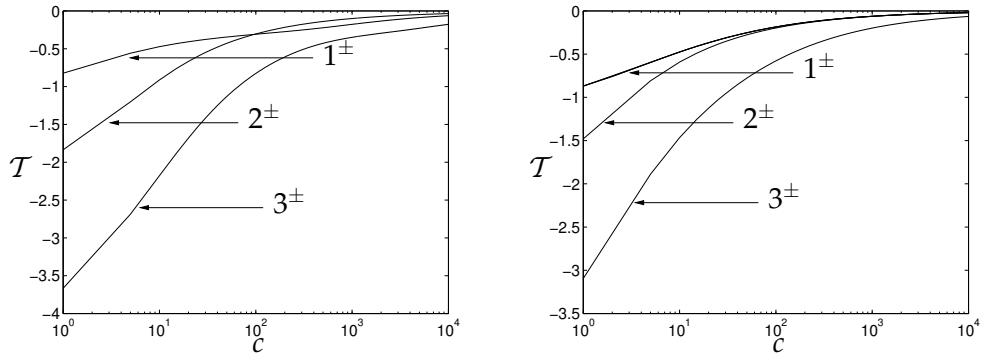

(a) $a = 0$ (b) $a = -0.5$

Figure 6.2: The first three neutral curves of the one-dimensional reduction of the von Kármán model given by (6.3–6.7), for $\nu = 0.5$.

$\nu = 0.5$) in figure 6.3, alongside the corresponding eigenmodes for $c = 0$ (a homogeneous layer) and $c = 10000$. For a homogeneous layer with $\nu = 0.5$, buckling occurs for $T = -1.63$. As c is increased from zero, exaggerating the softening in the centre of the disc, the cellular compression required to stimulate buckling is reduced (see figure 6.3(a)).

Having determined the region of parameter space in which nontrivial solutions exist, we are then able to examine solutions to the full nonlinear problem defined by (6.1,5.90,5.92,5.99), for a strongly inhomogeneous substrate. Taking $c = 10000$, the substrate remains in its flat configuration while $T \gtrsim -0.1$. As figure 6.4 shows, decreasing T from -0.1 yields a configuration which resembles a single crypt in the centre of the substrate, whose amplitude increases with cellular compression. The configuration shown at the onset of buckling in figure 6.4(a) recovers that of figure 6.3(b) (however, since the solution is weakly nonlinear, it is no longer normalised).

6.3 Buckling instabilities on a square domain

We begin with a linearisation of (6.1), setting $w = \zeta\bar{w}$ and $\Phi = \zeta^2\bar{\Phi}$ for some $0 < \zeta \ll 1$, which (omitting bars) yields

$$\nabla^2\left(\frac{E}{12\,(1-\nu^2)}\nabla^2 w\right) = \left[\frac{E}{12\,(1+\nu)}, w\right] + T\nabla^2 w, \tag{6.12}$$

to leading order in ζ. For simplicity we restrict attention to a square domain (setting $l = 1$) and seek solutions to (6.12) subject to the following clamped boundary conditions,

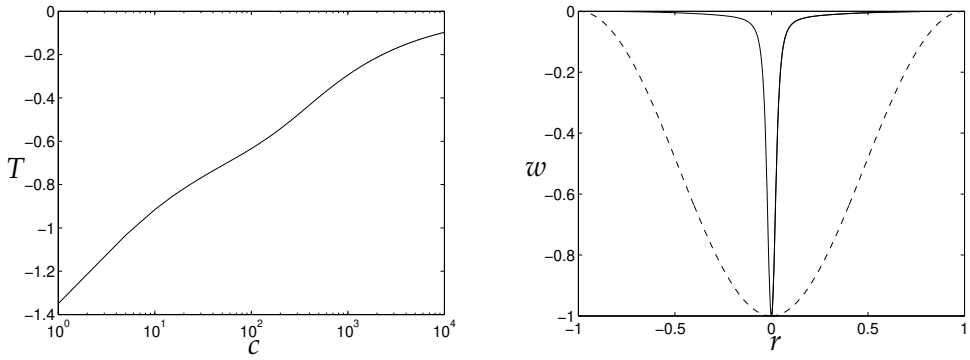

(a) (b)

Figure 6.3: (a) The first neutral curve corresponding to axisymmetric solutions of the von Kármán model given by (6.8–6.11), for $\nu = 0.5$. (b) The corresponding eigenmodes for a homogeneous substrate ($c = 0$, dashed line) and a substrate with a strongly softened region in the centre ($c = 10000$, solid line).

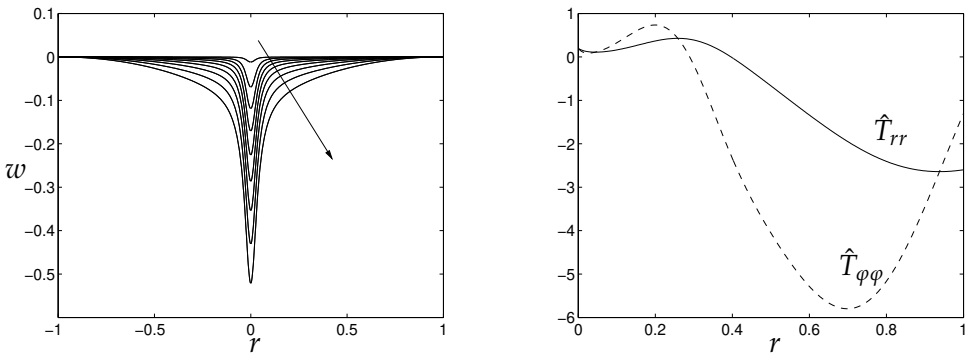

(a) (b)

Figure 6.4: Nonlinear solutions to the axisymmetric von Kármán model, for a plate with Young's modulus prescribed by (6.11) with $c = 10000$. In (a) we plot the substrate's deflection as cell growth induces increasing compression in the cell layer. The arrow indicates T decreasing from -0.1 to -0.5. In (b) the radial (solid line) and azimuthal (dashed line) stress resultants corresponding to the extremal configuration are shown.

which carry directly from the previous chapter:

$$w = 0, \quad \frac{\mathrm{d}w}{\mathrm{d}X} = 0 \quad \text{on } X = \pm 1, \tag{6.13a}$$

$$w = 0, \quad \frac{\mathrm{d}w}{\mathrm{d}Y} = 0 \quad \text{on } Y = \pm 1. \tag{6.13b}$$

Solutions to (6.12–6.13) are determined numerically using the spectral methods described by Trefethen (2000), which we discuss in more detail in appendix C. The domain is discretised onto an $(N+1) \times (N+1)$ Chebyshev mesh, whose mesh points cluster near the boundaries; Trefethen (2000) states that such a choice of mesh maximises the accuracy of the numerical code. Since Dirichlet conditions are imposed upon the boundaries, the boundary mesh points can be removed from the system. For ease of computation, the remaining meshpoints are stored in a vector $\mathbf{v}$ (of length $(N-1)^2$), allowing (6.12) to be written in the form of the following generalised eigenvalue problem:

$$\mathbf{A} \cdot \mathbf{v} = \xi \mathbf{L} \cdot \mathbf{v}, \tag{6.14}$$

where the matrix $\mathbf{A}$ is constructed by taking the appropriate combination of differentiation matrices given in appendix C, $\mathbf{L}$ is the Laplacian operator given by (C.10) and ξ is as defined below. We then deploy MATLAB's built-in eigenvalue solvers to determine solutions to (6.14).

In the case of homogeneity, we validate our numerical code by comparison of results with those published by Leriche & Labrosse (2004). In the case of an inhomogeneous substrate, we validate the spectral code by solving (6.3–6.7) as a test case and comparing results with those of figure 6.2(a). Figure C.1 illustrates this comparison. For $N = 50$, the maximal error is of $O(10^{-5})$; we set $N = 50$ in all forthcoming simulations.

6.3.1 Buckling of a homogeneous substrate

Assuming homogeneity ($E \equiv 1$), (6.12) reduces to

$$\nabla^4 w = \xi \nabla^2 w, \tag{6.15}$$

where $\xi = 12T\left(1-\nu^2\right) < 0$. We solve (6.15) subject to the clamped boundary conditions of (6.13). Analytical solution of (6.15,6.13) is not possible, since the clamped boundary conditions do not permit the existence of a separable solution (Leriche & Labrosse, 2004). We seek solutions of (6.15,6.13) numerically, using the methods described above.

The solutions of (6.15,6.13) discussed below exhibit various symmetries, all of which are characterised by the elements of the eighth-order *dihedral group*, denoted $\mathcal{D}_4$ (Hoyle,

2006). Before examining these solutions, we take a brief aside to summarise some pertinant ideas from group theory which will aid the characterisation of our solutions.

The eighth-order dihedral group, $\mathcal{D}_4$, has two generators: a reflection, m, about the line $X = 0$; and an anticlockwise rotation, ρ, by $\pi/2$ radians about the origin. The orders of these generators are two and four respectively, by which we mean that applying m twice or ρ four times yields the identity. We can present the group as follows:

$$\mathcal{D}_4 = \left\langle m, \rho \middle| m^2, \rho^4, (m\rho)^2 \right\rangle, \tag{6.16}$$

the expressions to the left of the vertical bar being the generators, and those to the right (termed *relators*) being a list of combinations of the generators which yield the identity. We determine the elements of $\mathcal{D}_4$ by taking all possible combinations of m and ρ, subject to cancellation via any of the relators of (6.16). We are left with the following eight elements:

$$\mathbb{1}, \quad \rho, \quad \rho^2, \quad \rho^3, \quad m, \quad m\rho, \quad m\rho^2, \quad m\rho^3, \tag{6.17}$$

where $\mathbb{1}$ represents the identity. The elements ρ^2 and ρ^3 represent rotations by π and $3\pi/2$ radians respectively, while $m\rho^2$ represents reflection about $Y = 0$ and $m\rho$ and $m\rho^3$ are reflections about the square diagonals (Hoyle, 2006). To make further progress we require the following two definitions.

Definition 6.1. *Consider a group G with elements g_1 and g_2. The elements g_1 and g_2 are said to be in the same* conjugacy class *if there exists some $\gamma \in G$ such that*

$$\gamma g_1 \gamma^{-1} = g_2. \tag{6.18}$$

Definition 6.2. *Consider a finite group G and a field $\mathbb{F}$. Let the group comprised of all $n \times n$ invertible matrices whose elements are taken from $\mathbb{F}$ be denoted $GL_n(\mathbb{F})$. A* representation *of G over $\mathbb{F}$ is a homomorphism, $\vartheta : G \mapsto GL_n(\mathbb{F})$. Denoting $\vartheta(g)$ by M_g for any $g \in G$, we require*

$$M_g M_h = M_{gh} \quad \forall g, h \in G, \tag{6.19}$$

since ϑ is a homomorphism. The dimension *of the representation is n. The representation reflects the action of G upon the vector space $\mathbb{F}^n$ (Hoyle, 2006). We refer to a representation as* irreducible *if it cannot be equivalently expressed in terms of matrices of smaller dimension.*

Since we are interested in real solutions to (6.15,6.13), we restrict attention to $\mathbb{F} = \mathbb{R}$. It can be shown (Cornwell, 1984) that $\mathcal{D}_4$ has five conjugacy classes, given by:

$$\{\mathbb{1}\}, \quad \{\rho, \rho^3\}, \quad \{m, m\rho^2\}, \quad \{m\rho, m\rho^3\}, \quad \{\rho^2\}. \tag{6.20}$$

Cornwell (1984) proves that, for any finite group, the number of irreducible representations over a given field is equal to the number of conjugacy classes. We therefore know

	$\{\mathbb{1}\}$	$\{\rho, \rho^3\}$	$\{m, m\rho^2\}$	$\{m\rho, m\rho^3\}$	$\{\rho^2\}$
R_1	1	1	1	1	1
R_2	1	-1	1	-1	1
R_3	1	1	-1	-1	1
R_4	1	-1	-1	1	1

Table 6.1: The four one-dimensional representations of $\mathcal{D}_4$. The table lists the scalars associated with each group element under each representation, as derived by (6.22). Column headings list the conjugacy classes of $\mathcal{D}_4$; for one-dimensional representations, the scalars associated with any two elements in the same conjugacy class are equal.

that $\mathcal{D}_4$ has five irreducible representations over $\mathbb{R}$. Each of the solutions to (6.15,6.13) determined in this section conforms to exactly one representation of $\mathcal{D}_4$. Consider, first, the possible one-dimensional representations, defined entirely by scalars M_m and M_ρ (*i.e.* the elements of $GL_1(\mathbb{R})$ associated with group elements m and ρ under the homomorphism ϑ of definition 6.2). From (6.16) we require

$$M_m^2 = 1, \quad M_\rho^4 = 1, \quad \left(M_m M_\rho\right)^2 = 1. \tag{6.21}$$

It follows that

$$M_m = \pm 1, \qquad M_\rho = \pm 1, \tag{6.22}$$

yielding the four representations of $\mathcal{D}_4$ given in table 6.1, which we label $R_1, \ldots, R_4$. We can interpret the values given in table 6.1 as the action of the given symmetry upon our solutions to (6.15). If the value presented in table 6.1 for a given group element were 1, the solution would be unchanged under the corresponding symmetry. If the same value were -1, the solution would be negated under this symmetry. Solutions to (6.15,6.13) can, thus, be associated with one of the representations of $\mathcal{D}_4$ on the basis of whether the configuration is preserved or negated under anticlockwise rotation by $\pi/2$ radians (M_ρ) and reflection about $X = 0$ (M_m). If the configuration is invariant under both of these actions, then it belongs to the R_1 solution family. If it is negated under rotation but preserved under reflection, then it belongs to the R_2 classification. Similarly, negation under reflection and invariance under rotation implies the R_3 family, and negation under both actions implies R_4. Since $R_1, \ldots, R_4$ are one-dimensional representations, configurations belonging to these representations exhibit the same symmetries in X as in Y. R_1 and R_2 solutions are even in both X and Y, while R_3 and R_4 are odd in both X and Y.

Having determined four representations, we have one remaining. Any eigenmode which does not obey one of the above four symmetry rules must belong to this final

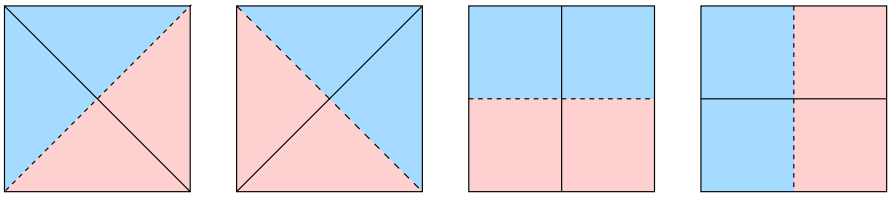

Figure 6.5: Eigenmodes corresponding to the two-dimensional representation of $\mathcal{D}_4$. Solid lines represent lines of symmetry; dashed lines represent lines of anti-symmetry.

family, which we now determine. We consider the natural two-dimensional representation given by Hoyle (2006), defined by associating each group element with the matrix used to make the corresponding transformation to the Cartesian plane, *i.e.*

$$M_{\mathbb{1}} = \begin{pmatrix} 1 & 0 \\ 0 & 1 \end{pmatrix}, \quad M_m = \begin{pmatrix} -1 & 0 \\ 0 & 1 \end{pmatrix}, \quad M_\rho = \begin{pmatrix} 0 & -1 \\ 1 & 0 \end{pmatrix}, \tag{6.23a}$$

$$M_{\rho^2} = \begin{pmatrix} -1 & 0 \\ 0 & -1 \end{pmatrix}, \quad M_{\rho^3} = \begin{pmatrix} 0 & 1 \\ -1 & 0 \end{pmatrix}, \tag{6.23b}$$

$$M_{m\rho} = \begin{pmatrix} 0 & 1 \\ 1 & 0 \end{pmatrix}, \quad M_{m\rho^2} = \begin{pmatrix} 1 & 0 \\ 0 & -1 \end{pmatrix}, \quad M_{m\rho^3} = \begin{pmatrix} 0 & -1 \\ -1 & 0 \end{pmatrix}. \tag{6.23c}$$

It can be confirmed that the matrices of (6.23) satisfy (6.19) and, thus, that these matrices define a representation of $\mathcal{D}_4$. We refer to this two-dimensional representation as R_5. As figure 6.5 illustrates, R_5 encompasses solutions which are even in X and odd in Y (labelled R_{5c} in the figure), and solutions which are odd in X and even in Y (labelled R_{5d}). Modes corresponding to R_{5c} and R_{5d} are linearly independent. Taking linear combinations of these modes yields two further subcategories (which we label R_{5a} and R_{5b}) each of which is symmetrical about one of the square diagonals. These four subclassifications of R_5 recover those given by Hoyle (2006). Below, we present solutions belonging to the R_{5a} and R_{5b} families only, but use the more general terminology "R_5" to refer to any of these four eigenmodes or linear combinations thereof. We also introduce the terminology "eigenmode $R_i^{(j)}$" to describe the j^{th} eigenmode in the R_i family ($i \in [1,5]$, $j \in [1,\infty)$); $R_i^{(1)}$ refers to the mode corresponding to the least negative eigenvalue in family R_i, for example.

Solutions to (6.15,6.13) are determined numerically, by writing the problem as

$$\mathbf{B} \cdot \mathbf{w} = \xi \mathbf{L} \cdot \mathbf{w}, \tag{6.24}$$

where $\mathbf{B}$ and $\mathbf{L}$ are given by (C.16) and (C.10) respectively. Table 6.2 gives the first seven eigenvalues for each of the five representations of $\mathcal{D}_4$ described above. These

R_1	R_2	R_3	R_4	R_5
[1] -13.0862	[5] -38.5314	[12] -67.2802	[4] -32.0524	[2*] -23.0311
[6] -41.7573	[16] -87.329	[25] -125.2549	[13] -69.7698	[7*] -47.393
[11] -61.5818	[21] -106.3548	[32] -155.4244	[20] -100.9667	[9*] -61.5806
[17] -90.6878	[33] -156.164	[46] -203.5528	[28] -127.9746	[14*] -81.6609
[22] -108.6967	[38] -173.6856	[53] -232.2052	[34] -157.611	[18*] -95.0768
[31] -150.212	[49] -214.4493	[68] -283.3951	[47] -206.1533	[23*] -120.422
[35] -159.672	[57] -244.8421	[73] -301.8406	[48] -209.7246	[26*] -125.9873

Table 6.2: The first seven eigenvalues, ξ, of (6.15,6.13) for each symmetry family. The numbers in square brackets denote the ordering of the eigenvalues, [1] being the eigenvalue of smallest magnitude. Stars denote eigenvalues with multiplicity 2 – the corresponding eigenmodes are identical, subject to a rotation through $\pi/2$ radians.

data recover the equivalent results of Leriche & Labrosse (2004). The eigenmodes corresponding to the eigenvalues listed in table 6.2 are illustrated in figure 6.6. As the onset of cellular growth generates a compression in the cell layer, a normal force is transmitted to the substrate, inducing buckling instabilities for values of T which correspond to eigenvalues of (6.24). The configuration attained for the lowest magnitude force is mode $R_1^{(1)}$, which exhibits a single extremum in the centre of the domain. For an incompressible substrate ($\nu = 0.5$), this instability occurs for $T = -1.45$. We may regard this configuration as most reminiscent of a single crypt. For greater degrees of compression (*i.e.* more prolonged cellular growth) we see higher modes; the next mode to appear is of the R_5 family. Solutions which correspond to R_5 arise for eigenvalues of multiplicity 2, enabling us to select two linearly independent eigenmodes to treat as basis functions, the linear combination of which (under normalisation) gives rise to a one-parameter family of R_5 modes for each eigenvalue pair. For values of T of large magnitude we obtain highly wrinkled configurations.

Mode selection via a Winkler foundation

As an aside, we now briefly illustrate the manner in which mode selection can be controlled by addition of a supporting foundation attached to the underside of the plate. We model this support as a *Winkler foundation*, *i.e.* a series of elastic springs connecting points on the plate to a series of reference points. Such elastic foundations have previously been used to mediate buckling patterns: examples include Audoly & Boudaoud (2008), Sultan & Boudaoud (2008) and Coman (2010). The one-dimensional models of chapter 2 illustrated that strengthening of such springs promoted highly wrinkled modes, while weaker springs facilitated 'type 1' modes, for example. For small deflec-

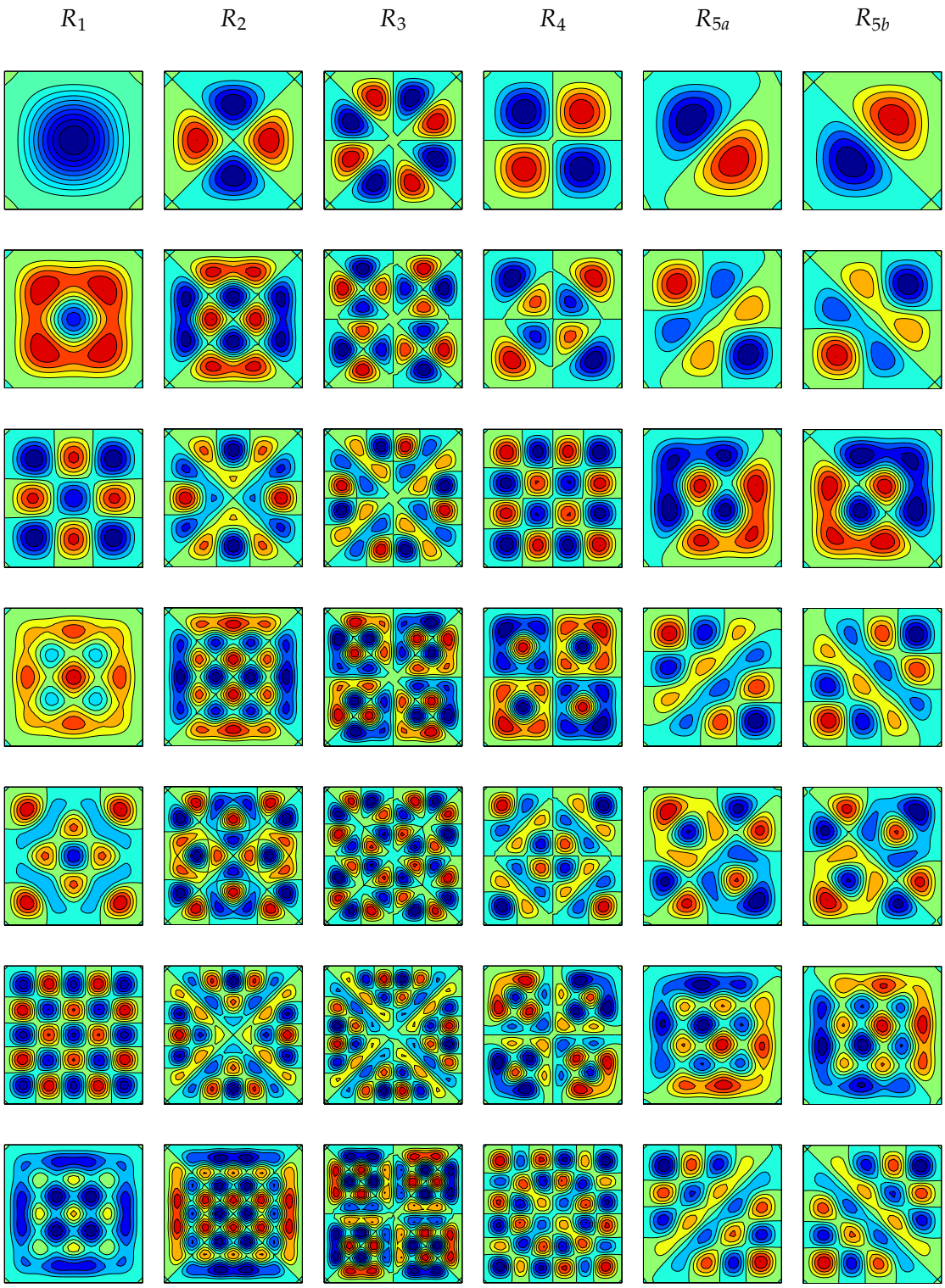

Figure 6.6: The first seven eigenmodes of (6.15,6.13) for each representation of $\mathcal{D}_4$, corresponding to the eigenvalues given in table 6.2. Solutions are categorised according to their symmetries under reflection about $X = 0$ and rotation about $\pi/2$ radians, as discussed above.

tions, adding such a construct to this model requires the addition of a term linear in w to $\mathcal{N}$, *i.e.*

$$\mathcal{N} = T\nabla^2 w + kw, \tag{6.25}$$

where the parameter k captures the stiffness of the foundation. Noting (6.25), (6.15) is replaced by

$$\nabla^4 w = \xi \nabla^2 w + \eta w, \tag{6.26}$$

where $\eta = 12k\left(1-\nu^2\right)$ and ξ is defined as following (6.15).

In figure 6.7 we examine the first eigenmode (*i.e.* that obtained for the least degree of compression in the cell layer) as k is varied. As figure 6.7(a) shows, increasing η results in crossings of the neutral curves, resulting in transitions of the first eigenmode from symmetry family R_1 to R_5 (at $\eta = 134$), followed by R_4 (at $\eta = 448$) *etc.* As we traverse along any specific neutral curve, we see transitions of the corresponding eigenmode which preserve the symmetry properties. Starting with the first neutral curve for $\eta = 0$, for example, we initially see mode $R_1^{(1)}$ as illustrated in figure 6.6. As we increase η, the eigenmode on this curve will progress continuously through a sequence of configurations similar to those illustrated in the left-hand column of figure 6.6 in turn.

6.3.2 Buckling of an inhomogeneous substrate

We now consider a substrate whose Young's modulus varies spatially. We consider, firstly, a plate which is softened in its centre with Young's modulus prescribed according to

$$E(X,Y) = \frac{1+c-c\exp\left(pX^m + pY^m\right)}{1+c-c\exp\left(2p\right)}, \tag{6.27}$$

where $p = -100$ and $m = 4$. Once more, the denominator in (6.27) is introduced to ensure consistency with (5.14). As c is increased from zero, the magnitude of variations in the substrate's stiffness is increased. The first eigenmode of (6.12,6.13,6.27) is illustrated in figure 6.8 for increasing values of c. For a strongly softened central region, buckling is restricted to the centre of the plate. The resulting configuration bears some similarity to a single colorectal crypt.

Consider, now, a plate whose Young's modulus is given by

$$E(X,Y) = \frac{1+c-c\exp\left(p\left(X^2-a^2\right)^m + p\left(Y^2-a^2\right)^m\right)}{1+c-c\exp\left(p\left(1-a^2\right)^m + p\left(1-a^2\right)^m\right)}, \tag{6.28}$$

for $a = 0.5$, which exhibits a distinct softened region in each quadrant. Figure 6.9 illustrates the first eigenmode obtained under the patterning of (6.28). We find that,

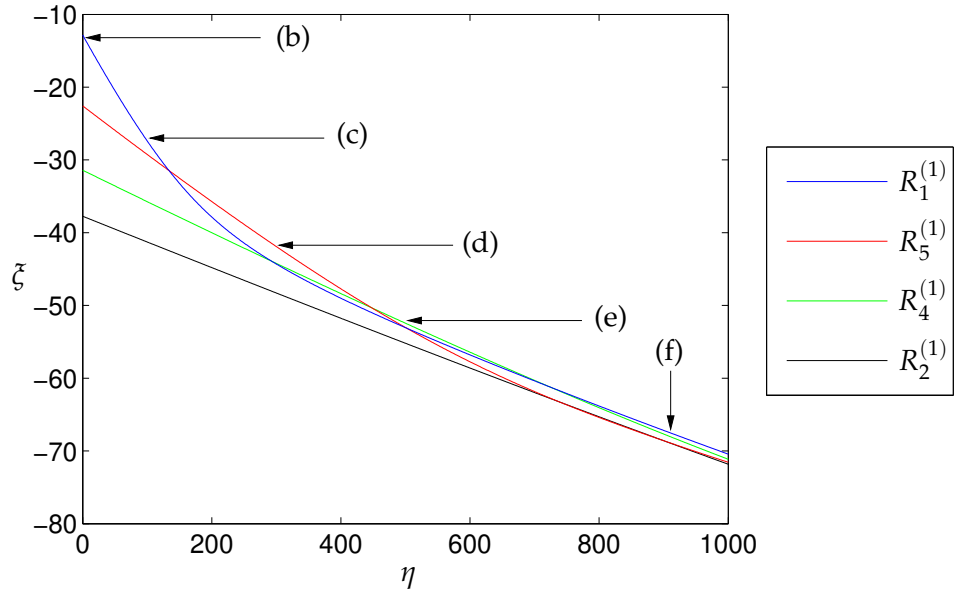

(a) Neutral curves.

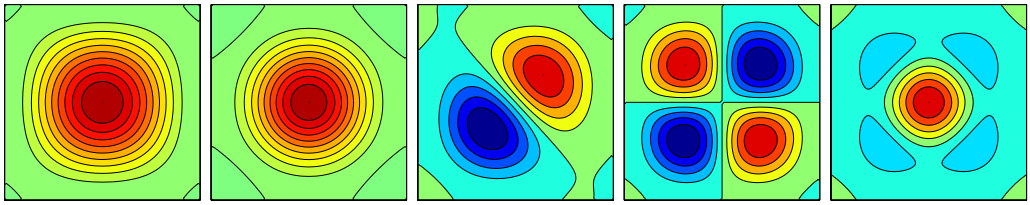

(b) $\eta = 0$ (c) $\eta = 100$ (d) $\eta = 300$ (e) $\eta = 500$ (f) $\eta = 900$

Figure 6.7: Configurations selected by a homogeneous substrate attached to a Winkler foundation. In (a) we show the first four neutral curves, illustrating the cellular compression, T, required to buckle the substrate as a function of foundation stiffness, η. In (b-f) we illustrate the first eigenmode for various η.

while we can encourage buckling within the four softened regions, the resulting configuration also exhibits a large dome in its centre. Our numerical simulations do not reveal a clear 'four crypt' profile in the manner illustrated in previous one-dimensional model analyses. Within the confines of this linear analysis, the existence of a configuration with four clear downward-pointing crypts would be required to exhibit the symmetries of an R_1-configuration; it appears that the closest such profile which we can obtain is that corresponding to mode $R_1^{(2)}$ in figure 6.6. Note, in particular, that the nature of the symmetry group respresentations suggests that the first solution in the R_4 family cannot be biased to yield four downward-pointing crypts.

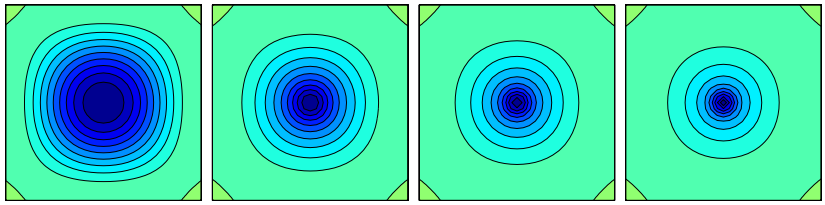

(a) $c = 0$ (b) $c = 30$ (c) $c = 100$ (d) $c = 300$

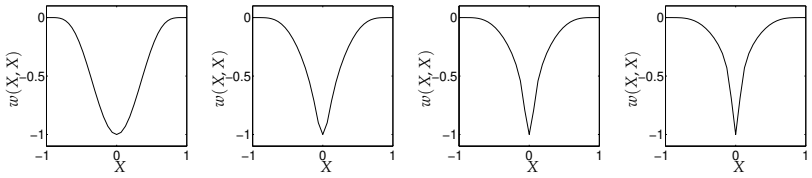

(e) $c = 0$ (f) $c = 30$ (g) $c = 100$ (h) $c = 300$

Figure 6.8: Lowest-order configuration of a plate with a softened region in the centre, with Young's modulus given by (6.27) (for increasing c) and $\nu = 0.5$. Panels (e)-(h) show cross-sections of the configurations in (a)-(d), taken along the line $Y = X$.

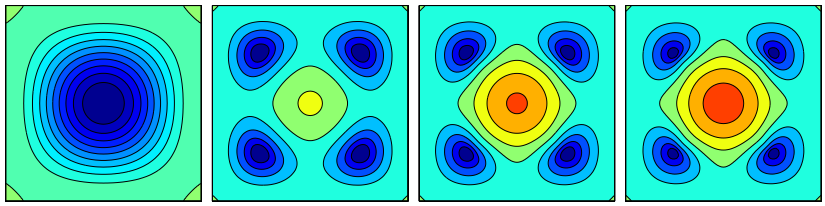

(a) $c = 0$ (b) $c = 30$ (c) $c = 100$ (d) $c = 300$

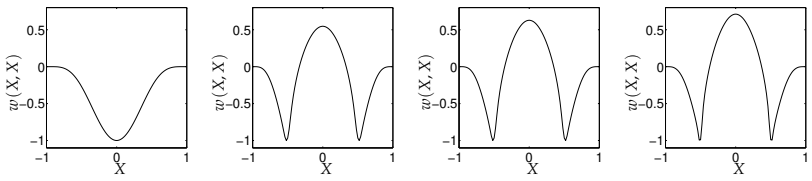

(e) $c = 0$ (f) $c = 30$ (g) $c = 100$ (h) $c = 300$

Figure 6.9: Lowest-order configuration of a plate with a softened region in each quadrant, with Young's modulus given by (6.28) (for increasing c) and $\nu = 0.5$. Panels (e)-(h) show cross-sections of the configurations in (a)-(d), taken along the line $Y = X$.

6.4 Conclusions

In this chapter we have presented an analysis of the buckling of a two-dimensional plate, with a focus placed upon the manner in which variations in mechanical properties determine the preferred configuration. Our numerical simulations reveal that we are able to control the buckled configuration by prescribing variations in the plate's stiffness; however, for the effects to be sufficiently significant to yield crypt-like profiles, we require variations in the Young's modulus to be substantial. A one-thousand-fold change in the Young's modulus has been shown to yield crypt-like profiles; however, biological evidence to support the existence of such sizeable inhomogeneities is currently lacking. We discuss this in further detail in the following chapter.

Attempts to generate configurations with multiple crypts exhibited less success in the two-dimensional framework than in the analogous one-dimensional models. While prescribing softened regions in each quadrant of the plate did facilitate the generation of crypt shapes therein, large deflections were also observed in the centre of the plate. The goal of attaining a configuration with a large number of crypts by imposing high frequency variations in plate stiffness seems optimistic; for such patternings buckling seems to be controlled by the average plate stiffness and configurations with few extrema remain attainable.

While patterning of material properties does not appear to be a sufficient mechanism to control crypt-frequency independently, we have shown that more wrinkled configurations can be promoted by addition of a supporting foundation (modelled in section 6.3.1 as a series of springs). We can regard such a foundation to represent the sub-epithelial mucosa *in vivo*, or as a support for a cell culture substrate *in vitro*. Stiffening of the supporting foundation has been shown to bias wrinkled configurations in preference to single-crypt modes.

In general, we expect buckling modes to be controlled by a combination of material properties, stiffness of the supporting foundation and boundary conditions. The clamped boundary conditions imposed above are largely motivated by the *in-vitro* studies discussed earlier. Buckling patterns *in vivo* may be more accurately described using periodic boundary conditions, for example, which naturally provide a mechanism by which high-frequency modes are attained. While mode selection seems to be a more complicated task in two dimensions, many of the patterns of figure 6.6 display a reassuring resemblance to multiple-crypt configurations.

CHAPTER 7

Conclusions & Further Work

In this study, we have presented mathematical and experimental models which investigate the mechanisms underlying colorectal crypt formation *in vivo*, motivated by the long-term goal of replicating intestinal tissue *in vitro*. An understanding of crypt formation is key to successfully engineering intestinal tissue, since the crypts house stem cells which are responsible for the maintenance of a healthy epithelium. Our focus throughout has been placed upon one previously postulated mechanism of crypt formation: that during development, the growth of cells in the epithelial layer generates a compressive stress within the layer itself, resulting in buckling instabilities which initiate crypt formation.

In chapter 2, we examined an extention to the model of Edwards & Chapman (2007), in which the epithelium is modelled as a growing extensible beam tethered to underlying tissue via a series of springs. To incorporate the effects of cellular migration, spring stresses were considered elastic over short timescales but exhibited viscous relaxation over longer times. Focussing on the incompressible limit throughout, our studies extended those of the original authors, who addressed only linear solutions for a limited range of parameters. We expanded upon their results through a more thorough consideration of post-buckled states; identification of a simplified version of their model, in which growth can be modelled parametrically; quantification of the energies corresponding to both linear and large-amplitude solutions, in terms of the force exerted at the boundaries; and a greater focus placed upon the geometric effects of spatial inhomogeneities of growth and mechanical properties. Under parametric growth, we examined the sequence of equilibrium configurations attained by beams of increasing length, and demonstrated that tuning the stiffness of the beam relative to that of stromal adhesion selects the wavelength of the primary buckling instability: stronger adhesion to the stroma predisposes the system to a more wrinkled configuration. Numerical simulations of the full time-dependent model illustrated how non-uniform growth

(together with relaxation of adhesive bonds) influences the sequence of intermediate states through which the system passes; however, the ultimate states were shown to be relatively insensitive to spatial growth patterns. Patterning can instead be manipulated via localised softening of the beam, which we modelled by locally reducing its bending stiffness, to produce multiple crypt-like shapes.

In chapter 3, we presented an *in-vitro* proof-of-principle experiment which validated the claim that compressive stresses generated by the growth of an epithelial cell layer can be sufficient to generate out-of-plane deformations. A rat intestinal epithelial cell line (IEC6) was cultured to confluence upon a flexible silicon substrate. Under standard culture conditions, upon a rigid surface, cell proliferation ceases due to contact inhibition as the cells reach confluence. However, upon our flexible substrate, proliferation was shown to continue beyond confluence since deflection of the substrate resulted in an enlarged culture surface area. The amplitudes and modes of deformations were strongly sample-dependent; further studies are required to elucidate the reasons for such variations. Substrate deflections were shown to be attributable to the cells alone, since deflections were enhanced on addition of a suitable growth factor, reduced on addition of a cell lysis buffer, and were negligible in the absence of the cells.

In chapter 4, we developed a one-dimensional mathematical model of the *in-vitro* study of chapter 3, modelling the substrate as an extensible beam covered by a confluent monolayer of cells, each modelled as a linear spring. A discrete representation of the cell layer was presented and homogenised following Fozard *et al.* (2010). The model compared two regimes of attachment between the cell layer and the substrate: that in which cells are fully bound, preventing any sliding along the substrate, and that in which cells experience no resistance to sliding. The model predicted that, while adhesion between the layers is essential in transmitting the compressive stress in the cell layer to bending of the underlying substrate, the resulting buckled shapes are highly similar in each regime. For a thin substrate, we exploited the small parameter α_1/α_0 (which captures beam bending resistance relative to beam stretching resistance) to reduce the model to that of an incompressible beam parameterised by its total length alone. Large-amplitude solutions were accurately approximated in this limit; the beam's compressibility is important only in separating the bifurcations of different modes, favouring an initial bifurcation to a low-order configuration. For an incompressible substrate, all bifurcation points coinside; this observation is consistent with our *in-vitro* study, in which the mode of buckling varied between samples. Shapes of configurations were shown to be solely determined by the net cell growth, and were insensitive to non-uniformities in growth patterns.

In chapter 5, we extended the studies of chapter 4 to two-dimensions, modelling the substrate as a thin plate which may deform due to surface stresses applied by the cells. The model constituted an extension to von Kármán plate theory which accounts for material inhomogeneities in the plate, and for non-zero surface stresses on both upper and lower surfaces. Since the model of chapter 4 suggested that buckled profiles are relatively insensitive to cell–substrate adhesion assumptions, we restricted attention to a confluent cell layer which experiences no resistance to sliding against the plate. Growth of the cell layer was considered to generate an isotropic compression in the cell layer, which was transmitted to the substrate as a normal surface stress proportional to the curvature of the layer. Restricting attention to axisymmetric configurations on a disc initially, large-amplitude solutions were determined and compared with the results of an adaptation of the model of Pamplona & Calladine (1993), which was derived from the alternative perspective of a thin-shell balance-of-forces formulation. Growth was incorporated into the latter model parametrically via examination of the equilibrium configurations of discs of increasing radius confined to a prescribed boundary region. Comparison of these two models illustrated discrepancies in configurations and distributions of stresses, for example, highlighting the degree to which such two-dimensional models are sensitive to the constitutive assumptions inherent in their derivation. Analysis of the von Kármán model motivates the constitutive assumption proposed by Evans & Skalak (1980) above that of Pamplona & Calladine (1993), while suggesting the new constitutive assumption upon the bending moments given by (5.142). However, variations in results owing to these choices are small in magnitude for plates with a flat reference configuration. A potential source for more significant discrepancies lies in the assumption of absolute inextensibility in the out-of-plane direction in the model of Pamplona & Calladine. While this holds to leading order in the von Kármán model, the out-of-plane normal strain was shown to be of the same order of magnitude as in-plane strains. This suggests that replacing (B.20) with a more realistic alternative might allow the models to agree; however, identification of a suitable candidate remains a target for future investigation.

In chapter 6, we considered how we may promote buckled configurations which exhibit multiple crypts within the confines of the von Kármán plate model of chapter 5. A focus was placed upon localised softening of discrete regions of the plate – an approach which showed some success in the one-dimensional model of chapter 2. Within planar and axisymmetric reductions of the von Kármán model, such localised softening acted as an effective way of determining crypt placement; however, mode selection via localised softening was shown to be less effective when applied to fully two-dimensional solutions on a square domain. Considering a softened region in each quadrant of the

plate, for example, we were able to generate crypt-like downward deformations in these regions, but only at the expense of some upward deformation at the centre of the plate. We suggest that this behaviour may partially be a consequence of the clamped boundary conditions deployed here, which are more easily motivated with regard to our *in-vitro* study than in the developing intestine *in vivo*. Periodic boundary conditions may be considered more appropriate when modelling crypt formation *in vivo*; configurations with multiple crypts would appear more readily under such assumptions. We also demonstrated that mode selection can be influenced by tethering of the plate to an elastic Winkler foundation. Stiffer foundations promote higher-modes which, in some cases, show promising resemblance to an array of colorectal crypts (see figures 6.6 and 6.7).

The models presented in this thesis consistently point to localised tissue softening as a plausible mechanism for controlling crypt distribution *in vivo*. While much is known about the role of various signalling factors and chemical gradients in crypt development and function (Sancho *et al.*, 2004; Barker *et al.*, 2008), little information upon the role of matrix stiffness is currently available, particularly with reference to the possible existence of localised regions with reduced stiffness. However, TGF-β is known to stimulate collagen deposition in tissues, resulting in a stiffening of the matrix (Wells & Discher, 2008). In the intestine, TGF-β is expressed in abundance near the top of the crypt and barely at all near the base (Avery *et al.*, 1993). This suggests that the extracellular matrix which surrounds the stem cells may be less stiff than that elsewhere in the crypt. Previous studies (such as that of Engler *et al.* (2006), for example) have also linked variations in matrix stiffness to differentiated cell behaviour, suggesting that matrix stiffness may play a role in determining the patterning of cell function up the crypt axis. One currently unanswered question is that of whether significant variations in matrix stiffness are present in an under-developed intestine prior to crypt formation and, if so, whether the location of softened regions is linked to stem cell position.

A recent study by Dervaux & Ben Amar (2010) considered a model for three-dimensional growth with the von Kármán plate framework. The authors showed that on reducing their model to unidirectional growth, the geometry of buckled profiles was controlled by mechanical properties alone, becoming independent of localised growth patterns. This conclusion recovers those of the one-dimensional models of chapters 2 and 4. However, the authors state that the growth process plays a more important role in determining fully three-dimensional configurations since more complex energetic constraints then apply. The two-dimensional models pre-

sented here have focused upon uniform growth; the extension of these models to study growth patterning is an area for future examination. Future mathematical modelling might also incorporate reaction-diffusion-driven pattern formation mechanisms, such as those previously studied in the embryo (Thieffry & Sanchez, 2003), in developing organs such as the heart (Smith & Armstrong, 1993), and in relation to tumour growth (Gatenby & Gawlinski, 1996; Ferreira *et al.*, 2002), for example. Such models would require identification of relevant stimulants (such as those discussed in section 1.1.2), although information upon the signalling, growth and mechanical behaviour in an under-developed gut is currently much less extensive than that of the developed tissue. Reaction and diffusion of extracellular signals may by linked to the models of this study via direct coupling to either tissue growth or mechanical properties.

One of the goals of this study was to answer the question of whether replication of intestinal tissue *in vitro* requires a complex preformed scaffold which imposes the crypt geometry, or whether we can exploit the cells' ability to form crypts unaided, given the appropriate environment. Previous intestinal tissue engineering has been heavily focused around *in-vivo* approaches, due to the complex structure and function of the tissue (Day, 2006). Much of our understanding of intestinal cell function, particularly with regard to the stem cell niche, has been as a result of animal studies. An *in-vitro* approach would provide a valuable tool for cancer and stem-cell biologists, and others, providing protocols which have the potential to yield functional tissues for transplantation. Relatively few previous studies have investigated approaches by which intestinal epithelial cells may form crypts unaided, although the studies of Sato *et al.* (2009) and Viney *et al.* (2009) each enjoyed some success in this area. Our experimental model has validated the hypothesis that the growth of intestinal epithelial cells can generate sufficient force to induce out-of-plane deflections of a flexible substrate. We suggest, therefore, that future replication of intestinal tissue *in vitro* might exploit this ability. The conclusions of our mathematical models suggest that a next generation of tissue engineering scaffolds might comprise a deformable substrate with an array of locally softened regions which can be deformed more readily. The design of such scaffolds remains the focus of future research.

APPENDIX A

Chapter 2 Derivations

A.1 Energy considerations

A.1.1 Buckling under imposed forcing at the boundaries

We define a dimensionless energy functional of the form:

$$\begin{aligned}\mathcal{E} = \int_{-1}^{1} \mathcal{F} d\tilde{s} = \int_{-1}^{1} \Big\{ & -\frac{1}{2}\left(T_x^2 + T_y^2\right) + T_x\left(x - \tilde{s}\right) + T_y y \\ & - \frac{1}{2\beta_1}\Sigma^2 + \Sigma\left(\frac{\mathrm{d}s}{\mathrm{d}\tilde{s}} - 1\right) \\ & + \frac{1}{2\beta_0}\left(\frac{\mathrm{d}\theta}{\mathrm{d}\tilde{s}}\right)^2 - \left(F_x\cos\theta + F_y\sin\theta\right)\frac{\mathrm{d}s}{\mathrm{d}\tilde{s}} \\ & + F_x\frac{\mathrm{d}x}{\mathrm{d}\tilde{s}} + F_y\frac{\mathrm{d}y}{\mathrm{d}\tilde{s}} + F_0\frac{\mathrm{d}x}{\mathrm{d}\tilde{s}}\Big\}\mathrm{d}\tilde{s}, \end{aligned} \tag{A.1}$$

where Σ is the tension in the beam and $\tilde{s}$ is the Lagrangian arc-length. We use a variational approach to illustrate that this energy is pertinent to the system defined by (2.21–2.22). In (A.1), the first line represents energy due to the stretching of the springs, the second represents stretching or compression of the beam, the third represents beam bending and the forth encompasses geometric relations and work done at the boundaries.

Following the notation of Arfken & Webber (2005), we describe variations of the nine dependent variables in terms of the new $O(1)$ functions $\eta_i(\tilde{s})$ and a scale factor α which captures the magnitude of the variation. We define

$$\theta(\tilde{s},\alpha) = \theta(\tilde{s},0) + \alpha\eta_1(\tilde{s}), \tag{A.2a}$$

$$x(\tilde{s},\alpha) = x(\tilde{s},0) + \alpha\eta_2(\tilde{s}), \tag{A.2b}$$

$$y(\tilde{s},\alpha) = y(\tilde{s},0) + \alpha\eta_3(\tilde{s}), \tag{A.2c}$$

$$s(\tilde{s},\alpha) = s(\tilde{s},0) + \alpha\eta_4(\tilde{s}), \tag{A.2d}$$

$$F_x(\tilde{s},\alpha) = F_x(\tilde{s},0) + \alpha\eta_5(\tilde{s}), \tag{A.2e}$$

$$F_y(\tilde{s},\alpha) = F_y(\tilde{s},0) + \alpha\eta_6(\tilde{s}), \tag{A.2f}$$

$$T_x(\tilde{s},\alpha) = T_x(\tilde{s},0) + \alpha\eta_7(\tilde{s}), \tag{A.2g}$$

$$T_y(\tilde{s},\alpha) = T_y(\tilde{s},0) + \alpha\eta_8(\tilde{s}), \tag{A.2h}$$

$$\Sigma(\tilde{s},\alpha) = \Sigma(\tilde{s},0) + \alpha\eta_9(\tilde{s}). \tag{A.2i}$$

The variation of θ, denoted $\delta\theta$, is given by

$$\delta\theta = \theta(\tilde{s},\alpha) - \theta(\tilde{s},0) = \alpha\eta_1(\tilde{s}). \tag{A.3}$$

Similar expressions hold for the other eight dependent variables. Now $\mathcal{E}$ is a functional which depends upon α, and the condition for selecting an extremum of $\mathcal{E}$ is

$$\left[\frac{\delta\mathcal{E}}{\delta\alpha}\right]_{\alpha=0} = 0. \tag{A.4}$$

We evaluate this is follows:

$$\frac{\delta\mathcal{E}}{\delta\alpha} = \int_{-1}^{1}\frac{\delta\mathcal{F}}{\delta\alpha}d\tilde{s} = \int_{-1}^{1}\left(\frac{\delta\mathcal{F}}{\delta\theta}\frac{\partial\theta}{\partial\alpha} + \frac{\delta\mathcal{F}}{\delta\theta_{\tilde{s}}}\frac{\partial\theta_{\tilde{s}}}{\partial\alpha} + \frac{\delta\mathcal{F}}{\delta x}\frac{\partial x}{\partial\alpha} + \frac{\delta\mathcal{F}}{\delta x_{\tilde{s}}}\frac{\partial x_{\tilde{s}}}{\partial\alpha} + \ldots\right)\partial\tilde{s}, \tag{A.5}$$

where additional $\tilde{s}$-subscripts denote derivatives of the dependent variables with respect to $\tilde{s}$. Since $\mathcal{F}$ exhibits no dependence upon the derivatives of Σ, $F_{x,y}$ or $T_{x,y}$, the corresponding terms in (A.5) vanish. From (A.3) we have that $\delta\theta/\delta\alpha = \eta_1$ *etc.* Substituting these expressions into (A.5) yields

$$\frac{\delta\mathcal{E}}{\delta\alpha} = \int_{-1}^{1}\left(\frac{\delta\mathcal{F}}{\delta\theta}\eta_1 + \frac{\delta\mathcal{F}}{\delta x}\eta_2 + \ldots + \frac{\delta\mathcal{F}}{\delta\theta_{\tilde{s}}}\frac{\mathrm{d}\eta_1}{\mathrm{d}\tilde{s}} + \frac{\delta\mathcal{F}}{\delta x_{\tilde{s}}}\frac{\mathrm{d}\eta_2}{\mathrm{d}\tilde{s}}\ldots\right)\mathrm{d}\tilde{s}. \tag{A.6}$$

Integrating the second set of terms by parts, we obtain the η_i as common factors. For example, we have:

$$\int_{-1}^{1}\frac{\delta\mathcal{F}}{\delta\theta_{\tilde{s}}}\frac{\mathrm{d}\eta_1}{\mathrm{d}\tilde{s}}\mathrm{d}\tilde{s} = \left[\eta_1\frac{\delta\mathcal{F}}{\delta\theta_{\tilde{s}}}\right]_{-1}^{1} - \int_{-1}^{1}\eta_1(\tilde{s})\frac{\mathrm{d}}{\mathrm{d}\tilde{s}}\frac{\delta\mathcal{F}}{\delta\theta_{\tilde{s}}}\mathrm{d}\tilde{s}. \tag{A.7}$$

Noting (A.7), (A.6) yields

$$\frac{\delta\mathcal{E}}{\delta\alpha} = \left[\eta_1\frac{\delta\mathcal{F}}{\delta\theta_{\tilde{s}}} + \eta_2\frac{\delta\mathcal{F}}{\delta x_{\tilde{s}}} + \ldots\right]_{-1}^{1} + \int_{-1}^{1}\left[\frac{\delta\mathcal{F}}{\delta\theta} - \frac{\mathrm{d}}{\mathrm{d}\tilde{s}}\frac{\delta\mathcal{F}}{\delta\theta_{\tilde{s}}}\right]\eta_1 + \left[\frac{\delta\mathcal{F}}{\delta x} - \frac{\mathrm{d}}{\mathrm{d}\tilde{s}}\frac{\delta\mathcal{F}}{\delta x_{\tilde{s}}}\right]\eta_2 + \ldots\mathrm{d}\tilde{s}. \tag{A.8}$$

Of the integrated terms in (A.8), non-zero contributions arise from those terms pertaining to θ, x, y and s only; yielding

$$\left[\frac{1}{\beta_0}\frac{\mathrm{d}\theta}{\mathrm{d}\tilde{s}}\eta_1 + (F_x + F_0)\,\eta_2 + F_y\eta_3 + \left(\Sigma - F_x\cos\theta - F_y\sin\theta\right)\eta_4\right]_{-1}^{1}. \tag{A.9}$$

We select boundary conditions which result in (A.9) vanishing. Imposing $\theta = 0$ and $y = 0$ on $\tilde{s} = \pm 1$ forces $\eta_1 = \eta_3 = 0$ on the boundaries and (A.9) reduces to

$$\left[(F_x + F_0)\, \eta_2 + (\Sigma - F_x)\, \eta_4 \right]_{-1}^{1}. \tag{A.10}$$

Since η_2 and η_4 are non-zero at the boundaries in general, we prescribe $F_x = \Sigma = -F_0$ at $\tilde{s} = \pm 1$. In doing so, (A.10) vanishes.

Considering the remaining non-zero terms in (A.8), we have that the nine bracketed terms are each equal to zero since the η_i are arbitrary and independent. The resultant equations are known as the Euler–Lagrange equations. Evaluating the Euler–Lagrange equations with $\mathcal{F}$ prescribed according to (A.1), we have

$$\frac{\delta \mathcal{F}}{\delta \theta} - \frac{\mathrm{d}}{\mathrm{d}\tilde{s}} \frac{\delta \mathcal{F}}{\delta \theta_{\tilde{s}}} = 0 \quad \Longrightarrow \left(F_x \sin\theta - F_y \cos\theta \right) \frac{\mathrm{d}s}{\mathrm{d}\tilde{s}} - \frac{1}{\beta_0} \frac{\mathrm{d}}{\mathrm{d}\tilde{s}} \left(\frac{\mathrm{d}\theta}{\mathrm{d}\tilde{s}} \right) = 0, \tag{A.11a}$$

$$\frac{\delta \mathcal{F}}{\delta x} - \frac{\mathrm{d}}{\mathrm{d}\tilde{s}} \frac{\delta \mathcal{F}}{\delta x_{\tilde{s}}} = 0 \quad \Longrightarrow T_x - \frac{\mathrm{d}}{\mathrm{d}\tilde{s}} \left(F_x + F_0 \right) = 0, \tag{A.11b}$$

$$\frac{\delta \mathcal{F}}{\delta y} - \frac{\mathrm{d}}{\mathrm{d}\tilde{s}} \frac{\delta \mathcal{F}}{\delta y_{\tilde{s}}} = 0 \quad \Longrightarrow T_y - \frac{\mathrm{d}}{\mathrm{d}\tilde{s}} F_y = 0, \tag{A.11c}$$

$$\frac{\delta \mathcal{F}}{\delta s} - \frac{\mathrm{d}}{\mathrm{d}\tilde{s}} \frac{\delta \mathcal{F}}{\delta s_{\tilde{s}}} = 0 \quad \Longrightarrow \frac{\mathrm{d}}{\mathrm{d}\tilde{s}} \left(-F_x \cos\theta - F_y \sin\theta + \Sigma \right) = 0, \tag{A.11d}$$

$$\frac{\delta \mathcal{F}}{\delta F_x} - \frac{\mathrm{d}}{\mathrm{d}\tilde{s}} \frac{\delta \mathcal{F}}{\delta F_{x\tilde{s}}} = 0 \quad \Longrightarrow -\cos\theta \frac{\mathrm{d}s}{\mathrm{d}\tilde{s}} + \frac{\mathrm{d}x}{\mathrm{d}\tilde{s}} = 0, \tag{A.11e}$$

$$\frac{\delta \mathcal{F}}{\delta F_y} - \frac{\mathrm{d}}{\mathrm{d}\tilde{s}} \frac{\delta \mathcal{F}}{\delta F_{y\tilde{s}}} = 0 \quad \Longrightarrow -\sin\theta \frac{\mathrm{d}s}{\mathrm{d}\tilde{s}} + \frac{\mathrm{d}y}{\mathrm{d}\tilde{s}} = 0, \tag{A.11f}$$

$$\frac{\delta \mathcal{F}}{\delta T_x} - \frac{\mathrm{d}}{\mathrm{d}\tilde{s}} \frac{\delta \mathcal{F}}{\delta T_{x\tilde{s}}} = 0 \quad \Longrightarrow -T_x + (x - \tilde{s}) = 0, \tag{A.11g}$$

$$\frac{\delta \mathcal{F}}{\delta T_y} - \frac{\mathrm{d}}{\mathrm{d}\tilde{s}} \frac{\delta \mathcal{F}}{\delta T_{y\tilde{s}}} = 0 \quad \Longrightarrow -T_x + y = 0, \tag{A.11h}$$

$$\frac{\delta \mathcal{F}}{\delta \Sigma} - \frac{\mathrm{d}}{\mathrm{d}\tilde{s}} \frac{\delta \mathcal{F}}{\delta \Sigma_{\tilde{s}}} = 0 \quad \Longrightarrow -\frac{1}{\beta_1} \Sigma + \left(\frac{\mathrm{d}s}{\mathrm{d}\tilde{s}} - 1 \right) = 0. \tag{A.11i}$$

Rearranging, (A.11e) and (A.11f) yield

$$\frac{\mathrm{d}x}{\mathrm{d}s} = \cos\theta, \qquad \frac{\mathrm{d}y}{\mathrm{d}s} = \sin\theta, \tag{A.12}$$

while (A.11g) and (A.11h) prescribe spring tensions according to

$$T_x = x - \tilde{s}, \qquad T_y = y, \tag{A.13}$$

and (A.11b) and (A.11c) relate spring tensions to beam stress resultants according to

$$\frac{\mathrm{d}F_x}{\mathrm{d}\tilde{s}} = T_x, \qquad \frac{\mathrm{d}F_y}{\mathrm{d}\tilde{s}} = T_y. \tag{A.14}$$

Integrating (A.11d) subject to the constraint that $\Sigma = F_x = -F_0$ at the boundaries (where $\theta = 0$), we obtain

$$\Sigma = F_x \cos\theta + F_y \sin\theta, \tag{A.15}$$

and substituting this into (A.11i) we obtain

$$F_x \cos\theta + F_y \sin\theta = \beta_1 \left(\frac{\mathrm{d}s}{\mathrm{d}\tilde{s}} - 1 \right). \tag{A.16}$$

Finally, from (A.11a) we have

$$\frac{\mathrm{d}^2\theta}{\mathrm{d}\tilde{s}^2} + \beta_0 \frac{\mathrm{d}s}{\mathrm{d}\tilde{s}} \left(F_y \cos\theta - F_x \sin\theta \right) = 0. \tag{A.17}$$

For an incompressible beam, $\beta_1 \to \infty$ while $\Sigma = O(1)$. Therefore, $s \sim \tilde{s}$ to leading order. Expanding s in the form $s = \tilde{s} + \beta_1^{-1}\hat{s}$, (A.16) gives the local stretch as

$$\frac{\mathrm{d}\hat{s}}{\mathrm{d}\tilde{s}} = F_x \cos\theta + F_y \sin\theta. \tag{A.18}$$

In this limit (A.12–A.17) yield

$$\frac{\mathrm{d}^2\theta}{\mathrm{d}s^2} + \beta_0 \left(F_y \cos\theta - F_x \sin\theta \right) = 0, \tag{A.19a}$$

$$\frac{\mathrm{d}F_x}{\mathrm{d}s} = T_x, \qquad \frac{\mathrm{d}F_y}{\mathrm{d}s} = T_y, \tag{A.19b}$$

$$T_x = x - s, \qquad T_y = y, \tag{A.19c}$$

$$\frac{\mathrm{d}x}{\mathrm{d}s} = \cos\theta, \qquad \frac{\mathrm{d}y}{\mathrm{d}s} = \sin\theta, \tag{A.19d}$$

which reduce directly to (2.24). In the incompressible limit, given that the first variation of $\mathcal{E}$ vanishes, we can simplify the expression for $\mathcal{E}$ given in (A.1). From (A.19), (A.1) reduces to

$$\mathcal{E} = \int_{-1}^{1} \left\{ \frac{1}{2} \left(T_x^2 + T_y^2 \right) + \frac{1}{2\beta_0} \left(\frac{\mathrm{d}\theta}{\mathrm{d}s} \right)^2 + F_0 \frac{\mathrm{d}x}{\mathrm{d}s} \right\} \mathrm{d}s, \tag{A.20}$$

in which we have energy contributions from stretching of the springs, bending of the beam and work done at the boundaries respectively.

A.1.2 Parametric growth

We now look to derive a similar expression for the energy corresponding to the formulation of section 2.1.4. Motivated by (A.1), and assuming incompressibility from the outset, we consider an energy functional of the form

$$\begin{aligned} \mathcal{E} = \int_{-1}^{1} \mathcal{F} d\tilde{s} = \int_{-1}^{1} \Big\{ & -\frac{1}{2} \left(\hat{T}_x^2 + \hat{T}_y^2 \right) + \hat{T}_x \left(\hat{x} - \frac{\hat{s}}{L} \right) + \hat{T}_y \hat{y} \\ & + \frac{1}{2\hat{\beta}_0} \left(\frac{\mathrm{d}\theta}{\mathrm{d}\hat{s}} \right)^2 + \hat{F}_x \left(\frac{\mathrm{d}\hat{x}}{\mathrm{d}\hat{s}} - \cos\theta \right) + \hat{F}_y \left(\frac{\mathrm{d}\hat{y}}{\mathrm{d}\hat{s}} - \sin\theta \right) \Big\} \mathrm{d}\hat{s}, \end{aligned} \tag{A.21}$$

where $\{\hat{T}_x, \hat{T}_y\} = \{T_x, T_y\}/L$ and all other variables are as defined in section 2.1.4. For convenience we define $\bar{x} = \hat{x} - \hat{s}/L$ and denote variations of the seven dependent

variables θ, $\bar{x}$, $\hat{y}$, $\hat{F}_x$, $\hat{F}_y$, $\hat{T}_x$ and $\hat{T}_y$ by $\eta_1, \ldots, \eta_7$ respectively. Following the approach of the previous section, (A.9) is replaced by the following:

$$\left[\frac{1}{\hat{\beta}_0}\frac{\mathrm{d}\theta}{\mathrm{d}\hat{s}}\eta_1 + \hat{F}_x\eta_2 + \hat{F}_y\eta_3\right]_{-1}^{1}, \tag{A.22}$$

which vanishes since θ, $\bar{x}$ and $\hat{y}$ are all prescribed on the boundaries (and, hence, their variations must vanish). Evaluating the Euler–Lagrange equations yields the following, for $\eta_1, \ldots, \eta_7$ respectively:

$$\hat{F}_x \sin\theta - \hat{F}_y \cos\theta = \frac{1}{\hat{\beta}_0}\frac{\mathrm{d}^2\theta}{\mathrm{d}\hat{s}^2}, \quad \hat{T}_x = \frac{\mathrm{d}\hat{F}_x}{\mathrm{d}\hat{s}}, \quad \hat{T}_y = \frac{\mathrm{d}\hat{F}_y}{\mathrm{d}\hat{s}}, \tag{A.23 a,b,c}$$

$$\frac{\mathrm{d}\hat{x}}{\mathrm{d}\hat{s}} = \cos\theta, \quad \frac{\mathrm{d}\hat{y}}{\mathrm{d}\hat{s}} = \sin\theta, \quad \hat{T}_x = \left(\hat{x} - \frac{\hat{s}}{L}\right), \quad \hat{T}_y = \hat{y}, \tag{A.23 d,e,f,g}$$

which reduces directly to (2.52). Assuming that the first variation of (A.21) vanishes, we can write the energy expression more compactly as follows:

$$\mathcal{E} = \frac{1}{2}\int_{-1}^{1}\left(\frac{\mathrm{d}\hat{F}_x}{\mathrm{d}\hat{s}}\right)^2 + \left(\frac{\mathrm{d}\hat{F}_y}{\mathrm{d}\hat{s}}\right)^2 + \frac{1}{\hat{\beta}_0}\left(\frac{\mathrm{d}\theta}{\mathrm{d}\hat{s}}\right)^2 \mathrm{d}\hat{s}. \tag{A.24}$$

We now consider the form of (A.24) for small deflections, setting $L = 1 + \varepsilon^2$ and

$$\theta = \varepsilon\theta_0 + \ldots, \qquad \hat{x} = \hat{x}_0 + \varepsilon^2\hat{x}_1 + \ldots, \qquad \hat{y} = \varepsilon\hat{y}_0 + \ldots, \tag{A.25}$$

for some $0 < \varepsilon \ll 1$. From (A.23d,e), we have

$$\frac{\mathrm{d}\hat{x}_0}{\mathrm{d}\hat{s}} = 1, \qquad \frac{\mathrm{d}\hat{x}_1}{\mathrm{d}\hat{s}} = -\frac{\theta_0^2}{2}, \qquad \frac{\mathrm{d}\hat{y}_0}{\mathrm{d}\hat{s}} = \theta_0. \tag{A.26}$$

Since $\hat{x} = \pm 1/L$ on $\hat{s} = \pm 1$, we require $\hat{x}_0 = \pm 1$ and $\hat{x}_1 = \mp 1$ on $\hat{s} = \pm 1$. We, thus, have $\hat{x}_0 = \hat{s}$ and

$$\hat{x}_1 = A - \int_0^{\hat{s}} \frac{\theta_0^2}{2}\mathrm{d}\hat{s}, \tag{A.27}$$

for some constant A. It follows from (A.26) and (A.27) that

$$\int_0^1 \frac{\theta_0^2}{2}\mathrm{d}\hat{s} - \int_{-1}^0 \frac{\theta_0^2}{2}\mathrm{d}\hat{s} = 2A. \tag{A.28}$$

Equivalently, we can write (A.28) as

$$\frac{1}{2}\int_0^1 \theta_0^2(\hat{s}) - \theta_0^2(-\hat{s})\,\mathrm{d}\hat{s} = 2A. \tag{A.29}$$

All the configurations which are presented in section 2.1 have θ either odd or even in $\hat{s}$. For such configurations $\theta_0^2(-\hat{s}) = \theta_0^2(\hat{s})$ and the integral in (A.29) vanishes, giving $A = 0$. From (A.26) and (A.27) we then have

$$\int_0^1 \frac{\theta_0^2}{2}\mathrm{d}\hat{s} = 1, \tag{A.30}$$

which provides a normalisation condition which must be satisfied for our asymptotic expansions to be valid.

Now, it follows from (A.23) that spring stresses satisfy

$$\frac{\mathrm{d}\hat{T}_x}{\mathrm{d}\hat{s}} = 1 - \frac{\varepsilon^2\theta_0^2}{2} - \frac{1}{1+\varepsilon^2} + \ldots = \varepsilon^2\left(1 - \frac{\theta_0^2}{2}\right) + \ldots, \qquad \frac{\mathrm{d}\hat{T}_y}{\mathrm{d}\hat{s}} = \varepsilon\theta_0 + \ldots, \tag{A.31}$$

which motivates the following expansions of beam stress resultants:

$$\hat{F}_x = -F_0 + \varepsilon^2\hat{F}_{x1} + \ldots, \qquad \hat{F}_y = \varepsilon\hat{F}_{y0} + \ldots \tag{A.32}$$

From (A.23b,c), we have

$$\frac{\mathrm{d}^2\hat{F}_{x1}}{\mathrm{d}\hat{s}^2} = 1 - \frac{\theta_0^2}{2}, \qquad \frac{\mathrm{d}^2\hat{F}_{y0}}{\mathrm{d}\hat{s}^2} = \theta_0 = \frac{\mathrm{d}\hat{y}_0}{\mathrm{d}\hat{s}}. \tag{A.33}$$

It follows, either from (A.33) or directly from (A.23), that

$$\frac{\mathrm{d}\hat{F}_{y0}}{\mathrm{d}\hat{s}} = \hat{y}_0. \tag{A.34}$$

Leading order terms in (A.24) are as follows:

$$\mathcal{E} = \frac{\varepsilon^2}{2}\int_{-1}^{1}\left(\left(\frac{\mathrm{d}\hat{F}_{y0}}{\mathrm{d}\hat{s}}\right)^2 + \frac{1}{\hat{\beta}_0}\frac{\mathrm{d}\theta_0}{\mathrm{d}\hat{s}}\right)\mathrm{d}\hat{s}. \tag{A.35}$$

Note, in particular, that the expansion of $\hat{F}_x$ in (A.32) implies that the $\hat{F}_x$ term does not contribute at leading order. Given the above results, (A.35) can be written as

$$\mathcal{E} = \frac{\varepsilon^2}{2}\int_{-1}^{1}\left(\hat{y}_0^2 + \frac{1}{\hat{\beta}_0}\frac{\mathrm{d}^2\hat{y}_0}{\mathrm{d}\hat{s}^2}\right)\mathrm{d}\hat{s} \tag{A.36}$$

Now consider the following integral:

$$\begin{aligned}\int_{-1}^{1}\left(\frac{\mathrm{d}^2\hat{y}_0}{\mathrm{d}\hat{s}^2}\right)^2\mathrm{d}\hat{s} &= \left[\frac{\mathrm{d}\hat{y}_0}{\mathrm{d}\hat{s}}\frac{\mathrm{d}^2\hat{y}_0}{\mathrm{d}\hat{s}^2}\right]_{-1}^{1} - \int_{-1}^{1}\frac{\mathrm{d}\hat{y}_0}{\mathrm{d}\hat{s}}\frac{\mathrm{d}^3\hat{y}_0}{\mathrm{d}\hat{s}^3}\mathrm{d}\hat{s} \\ &= \left[\frac{\mathrm{d}\hat{y}_0}{\mathrm{d}\hat{s}}\frac{\mathrm{d}^2\hat{y}_0}{\mathrm{d}\hat{s}^2} - \frac{\mathrm{d}\hat{y}_0}{\mathrm{d}\hat{s}}\frac{\mathrm{d}^3\hat{y}_0}{\mathrm{d}\hat{s}^3}\right]_{-1}^{1} + \int_{-1}^{1}\hat{y}_0\frac{\mathrm{d}^4\hat{y}_0}{\mathrm{d}\hat{s}^4}\mathrm{d}\hat{s}.\end{aligned} \tag{A.37}$$

Since $\mathrm{d}\hat{y}/\mathrm{d}\hat{s}$ vanishes on the boundaries, the integrated terms are all zero. The leading-order terms of (A.23a) give

$$\frac{\mathrm{d}^4\hat{y}_0}{\mathrm{d}\hat{s}^4} + \hat{\beta}_0 F_0\frac{\mathrm{d}^2\hat{y}_0}{\mathrm{d}\hat{s}^2} + \hat{\beta}_0\hat{y}_0 = 0, \tag{A.38}$$

which we substitute into (A.37) to obtain

$$\frac{1}{\hat{\beta}_0}\int_{-1}^{1}\left(\frac{\mathrm{d}^2\hat{y}_0}{\mathrm{d}\hat{s}^2}\right)^2\mathrm{d}\hat{s} = -\int_{-1}^{1}\left(F_0\hat{y}_0\frac{\mathrm{d}^2\hat{y}_0}{\mathrm{d}\hat{s}^2} + \hat{y}_0^2\right)\mathrm{d}\hat{s}. \tag{A.39}$$

Noting (A.39) and that $\varepsilon^2 = L - 1$, (A.36) becomes

$$\mathcal{E} = -\frac{1}{2}(L-1)F_0 \int_{-1}^{1} \hat{y}_0 \frac{\mathrm{d}^2\hat{y}_0}{\mathrm{d}\hat{s}^2}\mathrm{d}\hat{s}. \tag{A.40}$$

Integrating by parts once again, we obtain

$$\mathcal{E} = -\frac{1}{2}(L-1)F_0 \left\{ \left[\hat{y}_0 \frac{\mathrm{d}\hat{y}_0}{\mathrm{d}\hat{s}}\right]_{-1}^{1} - \int_{-1}^{1} \left(\frac{\mathrm{d}\hat{y}_0}{\mathrm{d}\hat{s}}\right)^2 \mathrm{d}\hat{s} \right\}. \tag{A.41}$$

The integrated term vanishes once more, since $\hat{y} = 0$ on the boundaries, while the integral equals four as a consequence of (A.30). So, for small deflections we have

$$\mathcal{E} = 2(L-1)F_0, \tag{A.42}$$

which is precisely the total work done at the two boundaries.

A.2 Maxwell viscoelasticity

The model of section 2.2 considers T_x and T_y as viscoelastic in order to capture the migration of cells along the lamina propria, and the consequent relaxation of stress in the layer. Here we return to dimensional variables in order to derive the equations which govern this relaxation. Our derivation is presented in terms of T_x^*, and we simply note that a corresponding equation holds for T_y^*. We represent the viscoelastic component of T_x^* by a dashpot, and place this in series with a linear spring with spring constant k^*, as illustrated in figure A.1. Under tension T_x^*, the linear spring extends by a length u_1^* according to

$$T_x^* = k^* u_1^*. \tag{A.43}$$

Under the same tension, the extension of the dashpot (u_2^*) is governed by

$$T_x^* = \nu^* \frac{\partial u_2^*}{\partial \tau^*}, \tag{A.44}$$

where ν^* is the coefficient of viscosity, and τ^* is time measured in the reference frame (Bland, 1960). The total extension of the layer is then given by

$$u^* = u_1^* + u_2^*, \tag{A.45}$$

and it follows from (A.43) and (A.44) that

$$\frac{\partial u^*}{\partial \tau^*} = \frac{1}{k^*}\frac{\partial T_x^*}{\partial \tau^*} + \frac{1}{\nu^*}T_x^*. \tag{A.46}$$

We nondimensionalise (A.46) in a manner consistent with section 2.2, setting $u^* = L^* u$, $\tau^* = T^*\tau$ and $T_x^* = k^* L^* T_x$. The timescale T^* is left arbitrary here; however, in section

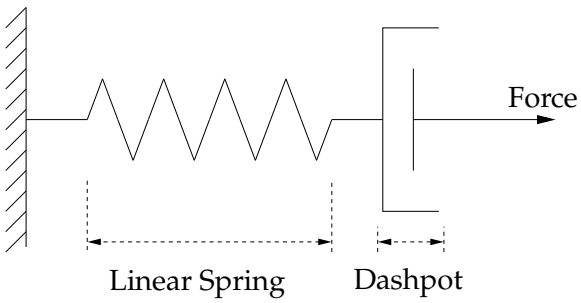

Figure A.1: Schema of the Maxwell model showing a linear spring and a dashpot in series.

2.2 we choose T^* to represent a characteristic growth timescale, which we introduce in the following section. It follows from (A.46) that

$$\frac{\partial u}{\partial \tau} = \frac{\partial T_x}{\partial \tau} + \frac{T^* k^*}{\nu^*} T_x. \tag{A.47}$$

The quantity ν^*/k^* is known as the *relaxation time* of the layer. This is the timescale over which the layer gradually relaxes after a sudden deformation. The equation governing T_x is dependent upon one dimensionless parameter: $\beta_T = T^* k^*/\nu^*$, which characterises the relative timescales of growth (T^*) and viscous relaxation of stresses (ν^*/k^*). For $\beta_T \ll 1$, or equivalently $T^* \ll \nu^*/k^*$, (A.47) reduces to Hooke's law and the springs behave linearly. It is this linearly elastic behaviour over short times which motivates the use of the Maxwell model above other viscoelastic models.

Returning to the notation of section 2.2, in which the horizontal displacement of the point X (in the reference configuration) at time τ is given by

$$\int_{g(0)}^{g(X,\tau)} \cos\theta\left(s'\right) \mathrm{d}s' - X, \tag{A.48}$$

we rewrite (A.47) as

$$\frac{\partial T_x}{\partial \tau} + \beta_T T_x = \frac{\partial}{\partial \tau} \int_{g(0)}^{g(X,\tau)} \cos\theta\left(s'\right) \mathrm{d}s'. \tag{A.49}$$

The corresponding expression for T_y is as follows:

$$\frac{\partial T_y}{\partial \tau} + \beta_T T_y = \frac{\partial}{\partial \tau} \int_{g(-1)}^{g(X,\tau)} \sin\theta\left(s'\right) \mathrm{d}s'. \tag{A.50}$$

A.3 Derivation of the conservation of mass equation in 2.2.

We regard growth to be a density-preserving process which simply generates an increase in the length (or equivalently mass) of material line elements over a given time

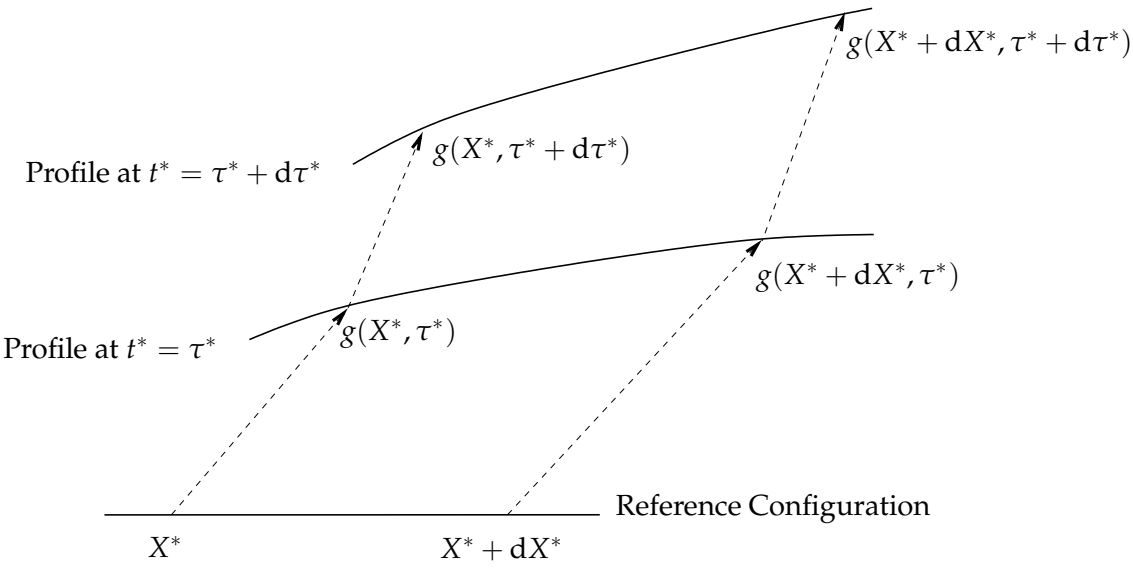

Figure A.2: Deformation of a line element of length $\mathrm{d}X^*$ over time $\mathrm{d}\tau^*$.

interval. Returning briefly to dimensional variables, we consider an element of the beam whose length in the reference configuration is $\mathrm{d}X^*$. As illustrated in figure A.2, the length of the element at time $t^* = \tau^*$ is

$$g^*(X^* + \mathrm{d}X^*, \tau^*) - g^*(X^*, \tau^*) = \mathrm{d}X^* \frac{\partial g^*}{\partial X^*}(X^*, \tau^*), \tag{A.51}$$

Similarly, the length of the same element at time $t^* = \tau^* + \mathrm{d}\tau^*$ is given, by

$$\mathrm{d}X^* \frac{\partial g^*}{\partial X^*}(X^*, \tau^* + \mathrm{d}\tau^*). \tag{A.52}$$

Thus, the following expression holds for the change in the length of the element over time $\mathrm{d}\tau^*$:

$$\mathrm{d}X^* \left(\frac{\partial g}{\partial X^*}(X^*, \tau^* + \mathrm{d}\tau^*) - \frac{\partial g}{\partial X^*} \right) = \mathrm{d}X^* \mathrm{d}\tau^* \frac{\partial}{\partial \tau^*} \frac{\partial g}{\partial X^*}(X^*, \tau^*). \tag{A.53}$$

This change in the element's length is solely due to the growth of the element over time $\mathrm{d}\tau^*$, which is precisely $\gamma^*(s^*)$ multiplied by the length of the line element (as a function of time). Thus, the total growth over time $\mathrm{d}\tau^*$ is

$$\begin{aligned}
\gamma^*(s^*) \int_{\tau^*}^{\tau^* + \mathrm{d}\tau^*} g^*(X^* + dX^*, t^*) - g^*(X^*, t^*) \mathrm{d}t^* & \\
&= \gamma^*(s) \mathrm{d}X^* \int_{\tau^*}^{\tau^* + \mathrm{d}\tau^*} \frac{\partial g^*}{\partial X^*}(X^*, \tau^*) \mathrm{d}t^*, \\
&= \gamma^*(s^*) \mathrm{d}X^* \int_0^{\mathrm{d}\tau^*} \frac{\partial g^*}{\partial X^*}(X^*, \tau^* + \bar{t}^*) \mathrm{d}\bar{t}^*, \\
&= \gamma^*(s^*) \mathrm{d}X^* \int_0^{\mathrm{d}\tau^*} \frac{\partial g^*}{\partial X^*}(X^*, \tau^*) + O(\bar{t}^*) \mathrm{d}\bar{t}^*,
\end{aligned}$$

$$= \gamma^*(s^*)\mathrm{d}X^*\mathrm{d}\tau^*\frac{\partial g^*}{\partial X^*}(X^*,\tau^*), \tag{A.54}$$

to leading order. Equating (A.53) and (A.54), the following conservation of mass equation is obtained:

$$\frac{\partial^2 g^*}{\partial \tau^* \partial X^*} = \gamma^*(s^*)\frac{\partial g^*}{\partial X^*}. \tag{A.55}$$

We solve (A.55) subject to the symmetry condition $g^*(0,\tau^*) = 0$, and the condition imposing that the layer is flat initially, $g^*(X^*,0) = X^*$. Equation (A.55) is nondimensionalised by setting $X = X^*/L_0^*$, $s = s^*/L_0^*$, $g = g^*/L_0^*$, $\gamma(s) = \gamma^*(s^*)/\gamma_{\max}^*$ and $\tau = \gamma_{\max}^*\tau^*$ (where $\gamma_{\max}^*$ is the maximal value which γ^* obtains). These changes of variable reduce (A.55) to

$$\frac{\partial^2 g}{\partial \tau \partial X} = \gamma(s)\frac{\partial g}{\partial X}, \tag{A.56}$$

which is solved subject to $g(0,\tau) = 0$ and $g(X,0) = X$.

APPENDIX B

The Model of Pamplona & Calladine (1993)

Here we adapt the nonlinear shell model for the buckling of a compressed spherical vesicle presented by Pamplona & Calladine (1993), to derive an alternative two-dimensional model to the von Kármán model of chapter 5. Rather than the spherical reference configuration used by Pamplona & Calladine, we consider a sheet of epithelial tissue whose reference configuration is a flat disc. The rim of the disc is compressed to reside within a specified circular boundary. We deploy a parametric description of epithelial growth, considering the equilibrium configurations attained by a sequence of discs of increasing undeformed radius. We restrict our attention to axisymmetric deformations here. Below, we summarise the model's derivation (which deploys many of the constitutive assumptions discussed in section 1.6.3), boundary conditions and appropriate nondimensionalisation.

B.1 Model derivation

We consider a sheet of epithelial tissue whose undeformed configuration is a disc of radius R^* and thickness h^*. The sheet is compressed within a circular boundary of radius $R_0^* < R^*$ which, under appropriate conditions, induces buckling. We assume that $h^* \ll R^*$ and characterise the profile of the deformed tissue layer by that of its central plane. We define a right-handed cylindrical polar coordinate system with unit vectors $\hat{\mathbf{r}}$, $\hat{\boldsymbol{\varphi}}$ and $\hat{\mathbf{z}}$ which are respectively directed radially from the centre of the disc, azimuthally in the plane of the undeformed disc, and vertically upwards, as illustrated in figure B.1. We also define the unit vectors $\hat{\mathbf{n}}$, normal to the surface and directed downwards when in the reference configuration, and $\hat{\boldsymbol{\theta}}$, tangential to the surface in the

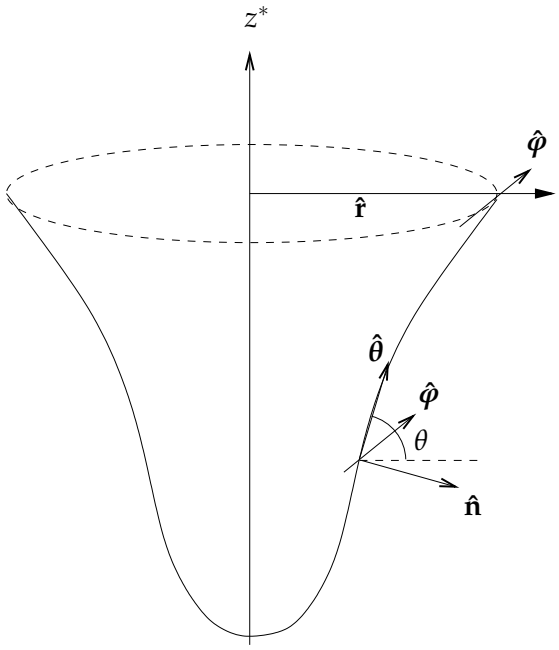

Figure B.1: Coordinate system used in our adaptation of the model presented by Pamplona & Calladine (1993).

$(\hat{\mathbf{r}}, \hat{\mathbf{z}})$-plane. The angle of inclination of $\hat{\boldsymbol{\theta}}$ to the horizontal is denoted θ.

For later use, we note the following relationships between the unit vectors described above:

$$\hat{\mathbf{n}} = \hat{\mathbf{r}} \sin\theta - \hat{\mathbf{z}} \cos\theta, \tag{B.1a}$$

$$\hat{\boldsymbol{\theta}} = \hat{\mathbf{r}} \cos\theta + \hat{\mathbf{z}} \sin\theta, \tag{B.1b}$$

and the corresponding inverse relations:

$$\hat{\mathbf{r}} = \hat{\mathbf{n}} \sin\theta + \hat{\boldsymbol{\theta}} \cos\theta, \tag{B.2a}$$

$$\hat{\mathbf{z}} = -\hat{\mathbf{n}} \cos\theta + \hat{\boldsymbol{\theta}} \sin\theta. \tag{B.2b}$$

From the definition of the polar coordinate system, we have

$$\frac{\partial \hat{\mathbf{r}}}{\partial \theta} = 0, \qquad \frac{\partial \hat{\mathbf{z}}}{\partial \theta} = 0, \qquad \frac{\partial \hat{\mathbf{r}}}{\partial \varphi} = \hat{\boldsymbol{\varphi}}, \qquad \frac{\partial \hat{\mathbf{z}}}{\partial \varphi} = 0, \tag{B.3}$$

and (B.1–B.3) imply that

$$\frac{\partial \hat{\mathbf{n}}}{\partial \theta} = \hat{\boldsymbol{\theta}}, \qquad \frac{\partial \hat{\boldsymbol{\theta}}}{\partial \theta} = -\hat{\mathbf{n}}, \qquad \frac{\partial \hat{\boldsymbol{\varphi}}}{\partial \theta} = 0, \tag{B.4a}$$

$$\frac{\partial \hat{\mathbf{n}}}{\partial \varphi} = \sin\theta \hat{\boldsymbol{\varphi}}, \qquad \frac{\partial \hat{\boldsymbol{\varphi}}}{\partial \varphi} = -\hat{\mathbf{r}}, \qquad \frac{\partial \hat{\boldsymbol{\theta}}}{\partial \varphi} = \cos\theta \hat{\boldsymbol{\varphi}}. \tag{B.4b}$$

We denote the two principal radii of curvature by r^*_θ (representing the curvature of a cross-section of constant φ) and r^*_φ (representing the curvature of a cross-section of

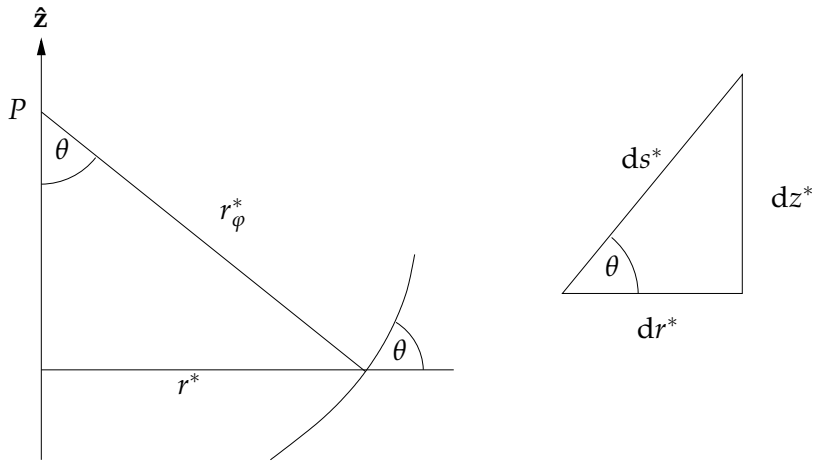

Figure B.2: Orientation of normals to a surface element inclined at angle θ to the horizontal.

constant θ). The corresponding curvatures are denoted κ^*_θ and κ^*_φ respectively, and satisfy

$$\kappa^*_\theta = 1/r^*_\theta, \qquad \kappa^*_\varphi = 1/r^*_\varphi. \tag{B.5}$$

We introduce the spatial variable s^* as a measure of arclength along a meridian from the centre of the disc, and note the following geometric relations between s^*, r^* and z^* (see figure B.2):

$$\frac{\mathrm{d}r^*}{\mathrm{d}s^*} = \cos\theta, \quad \frac{\mathrm{d}z^*}{\mathrm{d}s^*} = \sin\theta. \tag{B.6}$$

For axisymmetric deformations the normals to the surface, for fixed θ, intersect at some point on the $\hat{\mathbf{z}}$-axis, marked as P in figure B.2. Noting the geometry illustrated in figure B.2, it follows that

$$r^* = r^*_\varphi \sin\theta. \tag{B.7}$$

Figure B.3 shows a typical surface element, bounded by meridians separated by $\mathrm{d}\varphi$ and parallel circles separated by $\mathrm{d}\theta$. Inspection of figure B.3 reveals that

$$\mathrm{d}s^* = r^*_\theta \mathrm{d}\theta. \tag{B.8}$$

We derive equilibrium equations via consideration of the forces and moments acting upon a small surface element such as that illustrated in figure B.3. We denote the in-plane stress resultants by F^*_θ and F^*_φ (acting in the meridional and azimuthal directions respectively), and denote the out-of-plane stress resultant by F^*_n. Since we assume axisymmetry, we have only two non-zero bending moments: $\mathscr{M}^*_\theta$, which acts to bend the surface in the $(\hat{\mathbf{n}}, \hat{\boldsymbol{\theta}})$-plane; and $\mathscr{M}^*_\varphi$, which acts to bend the surface in the $(\hat{\mathbf{n}}, \hat{\boldsymbol{\varphi}})$-plane. The geometries of these stress resultants and bending moments are illustrated in figure B.3.

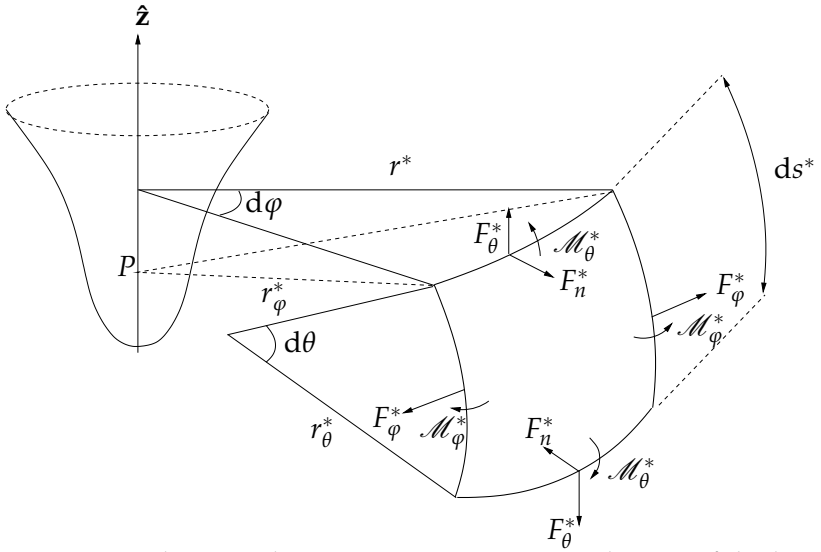

Figure B.3: Stress resultants and moments acting upon an element of the layer. The element is bounded by the meridians at φ and $\varphi + \mathrm{d}\varphi$ and the parallel circles located at θ and $\theta + \mathrm{d}\theta$. Thus the edges of the element are of lengths $r^*\mathrm{d}\varphi$ and $r^*_\theta \mathrm{d}\theta$ respectively.

Variations in F^*_φ across the surface element produce a net force given by

$$\left(F^*_\varphi r^*_\theta \mathrm{d}\theta \hat{\boldsymbol{\varphi}}\right)\Big|_{\varphi+\mathrm{d}\varphi} - \left(F^*_\varphi r^*_\theta \mathrm{d}\theta \hat{\boldsymbol{\varphi}}\right)\Big|_{\varphi} = \frac{\partial}{\partial \varphi}\left(F^*_\varphi r^*_\theta \mathrm{d}\theta \hat{\boldsymbol{\varphi}}\right)\mathrm{d}\varphi$$
$$= \left[\frac{\partial}{\partial \varphi}\left(F^*_\varphi r^*_\theta\right)\hat{\boldsymbol{\varphi}} - F^*_\varphi r^*_\theta \hat{\mathbf{r}}\right]\mathrm{d}\theta \mathrm{d}\varphi, \tag{B.9}$$

in which we have Taylor expanded, discarded terms of $O(\mathrm{d}\varphi^2)$ and utilised (B.3) to differentiate $\hat{\boldsymbol{\varphi}}$. Resolving the radial term in (B.9) into its normal and azimuthal components, we write the force owing to variations in F^*_φ as

$$\left[\frac{\partial}{\partial \varphi}\left(F^*_\varphi r^*_\theta\right)\hat{\boldsymbol{\varphi}} - F^*_\varphi r^*_\theta \sin\theta \hat{\mathbf{n}} - F^*_\varphi r^*_\theta \cos\theta \hat{\boldsymbol{\theta}}\right]\mathrm{d}\theta \mathrm{d}\varphi. \tag{B.10}$$

Under the assumption of axisymmetry, the first term in (B.10) vanishes. The following force is also generated as a result of variations in F^*_θ across the element:

$$\left(F^*_\theta r^* \mathrm{d}\varphi \hat{\boldsymbol{\theta}}\right)\Big|_{\theta+\mathrm{d}\theta} - \left(F^*_\theta r^* \mathrm{d}\varphi \hat{\boldsymbol{\theta}}\right)\Big|_{\theta} = \frac{\partial}{\partial \theta}\left(F^*_\theta r^* \mathrm{d}\varphi \hat{\boldsymbol{\theta}}\right)\mathrm{d}\theta$$
$$= \left[\frac{\partial}{\partial \theta}\left(F^*_\theta r^*\right)\hat{\boldsymbol{\theta}} - F^*_\theta r^* \hat{\mathbf{n}}\right]\mathrm{d}\theta \mathrm{d}\varphi. \tag{B.11}$$

Similarly, variations in the out-of-plane stress resultant F^*_n generate a net force given by

$$\left(-F^*_n r^* \mathrm{d}\varphi \hat{\mathbf{n}}\right)\Big|_{\theta+\mathrm{d}\theta} - \left(-F^*_n r^* \mathrm{d}\varphi \hat{\mathbf{n}}\right)\Big|_{\theta} = \frac{\partial}{\partial \theta}\left(-F^*_n r^* \mathrm{d}\varphi \hat{\mathbf{n}}\right)\mathrm{d}\theta$$
$$= -\left[\frac{\partial}{\partial \theta}\left(F^*_n r^*\right)\hat{\mathbf{n}} + F^*_n r^* \hat{\boldsymbol{\theta}}\right]\mathrm{d}\theta \mathrm{d}\varphi. \tag{B.12}$$

The net moment upon the element due to $\mathscr{M}_\varphi^*$ is

$$\left(-\mathscr{M}_\varphi^* r_\theta^* \mathrm{d}\theta\hat{\boldsymbol{\theta}}\right)\Big|_{\varphi+\mathrm{d}\varphi} - \left(-\mathscr{M}_\varphi^* r_\theta^* \mathrm{d}\theta\hat{\boldsymbol{\theta}}\right)\Big|_{\varphi} = \frac{\partial}{\partial\varphi}\left(-\mathscr{M}_\varphi^* r_\theta^* \hat{\boldsymbol{\theta}}\right)\mathrm{d}\theta\mathrm{d}\varphi$$
$$= -\mathscr{M}_\varphi^* r_\theta^* \cos\theta\hat{\boldsymbol{\varphi}}\mathrm{d}\theta\mathrm{d}\varphi, \tag{B.13}$$

where we have truncated terms of $O(\mathrm{d}\varphi^2)$ and have utilised (B.4b) in the differentiation step. Similarly the net moment due to $\mathscr{M}_\theta^*$ is

$$\left(\mathscr{M}_\theta^* r^* \mathrm{d}\varphi\hat{\boldsymbol{\varphi}}\right)\Big|_{\theta+\mathrm{d}\theta} - \left(\mathscr{M}_\theta^* r^* \mathrm{d}\varphi\hat{\boldsymbol{\varphi}}\right)\Big|_{\theta} = \frac{\partial}{\partial\theta}\left(\mathscr{M}_\theta^* r^* \hat{\boldsymbol{\varphi}}\right)\mathrm{d}\theta\mathrm{d}\varphi$$
$$= \frac{\partial}{\partial\theta}\left(\mathscr{M}_\theta^* r^*\right)\hat{\boldsymbol{\varphi}}\mathrm{d}\theta\mathrm{d}\varphi. \tag{B.14}$$

Finally, the moment generated by the out-of-plane stress resultant F_n^* is

$$F_n^* r^* r_\theta^* \mathrm{d}\theta\mathrm{d}\varphi\hat{\boldsymbol{\varphi}}. \tag{B.15}$$

In equilibrium the net moment must vanish, and (B.13–B.15) yield

$$\frac{\partial}{\partial\theta}\left(\mathscr{M}_\theta^* r^*\right) - \mathscr{M}_\varphi^* r_\theta^* \cos\theta - F_n^* r^* r_\theta^* = 0, \tag{B.16}$$

having divided by the common factor $\mathrm{d}\theta\mathrm{d}\varphi$. Equilibrium of forces implies (from the meridional and normal components of (B.10–B.12)) that

$$\hat{\boldsymbol{\theta}}\text{:} \qquad \frac{\partial}{\partial\theta}\left(F_\theta^* r^*\right) - F_n^* r^* - F_\varphi^* r_\theta^* \cos\theta = 0, \tag{B.17a}$$

$$\hat{\boldsymbol{n}}\text{:} \qquad \frac{\partial}{\partial\theta}\left(F_n^* r^*\right) + F_\theta^* r^* + F_\varphi^* r_\theta^* \sin\theta = 0. \tag{B.17b}$$

We utilise (B.8) to rewrite (B.16–B.17) as follows:

$$\frac{\mathrm{d}}{\mathrm{d}s^*}\left(\mathscr{M}_\theta^* r^*\right) - \mathscr{M}_\varphi^* \cos\theta + F_n^* r^* = 0, \tag{B.18a}$$

$$\frac{\mathrm{d}}{\mathrm{d}s^*}\left(F_\theta^* r^*\right) - \kappa_\theta^* F_n^* r^* - F_\varphi^* \cos\theta = 0, \tag{B.18b}$$

$$\frac{\mathrm{d}}{\mathrm{d}s^*}\left(F_n^* r^*\right) + \kappa_\theta^* F_\theta^* r^* + F_\varphi^* \sin\theta = 0. \tag{B.18c}$$

The above equations recover those given in by Pamplona & Calladine (1993).

We now relate the stress resultants in the sheet to the principal stretches, through some elastic constitutive law. The stretch of a surface element, in some principal direction, is precisely its length in that direction when deformed divided by the corresponding length in the reference configuration. We distinguish the variables required to describe the reference configuration by an over-tilde, denoting the arclength and radial poisition of a point in the reference configuration by $\tilde{s}^*$ and $\tilde{r}^*$ respectively. We define the two principal stretches, λ_θ and λ_φ as follows:

$$\lambda_\theta = \frac{r_\theta^* \mathrm{d}\theta}{\tilde{r_\theta}^* \mathrm{d}\tilde{\theta}} = \frac{\mathrm{d}s^*}{\mathrm{d}\tilde{s}^*}, \qquad \lambda_\varphi = \frac{r^* \mathrm{d}\varphi}{\tilde{r}^* \mathrm{d}\tilde{\varphi}} = \frac{r^*}{\tilde{r}^*}, \tag{B.19}$$

where the latter equality utilises the fact that $\mathrm{d}\varphi/\mathrm{d}\tilde{\varphi} = 1$ for axisymmetric deformations. Following such authors as Pamplona & Calladine (1993), Preston *et al.* (2008) and Reboux *et al.* (2009), we make the constitutive assumption that deformations of the sheet locally preserve the area of the surface element. We thus write

$$\lambda_\theta = \frac{1}{\lambda_\varphi} = \frac{1}{\lambda}, \quad \text{where} \quad \lambda = \frac{\mathrm{d}\tilde{s}^*}{\mathrm{d}s^*} = \frac{r^*}{\tilde{r}^*}. \tag{B.20}$$

It is then convenient to write F^*_φ and F^*_θ in terms of an isotropic stress resultant, denoted F^*, and relate principal tensions to principal stretches via the assumption that each of F^*_φ and F^*_θ differs from F^* in a manner proportional to the corresponding principal stretch. We write

$$F^*_\varphi = F^* + H^*\lambda, \quad F^*_\theta = F^* + \frac{H^*}{\lambda}, \tag{B.21}$$

where H^* is the *shear modulus* of the sheet – a measure of the resistance to changes in shape in the plane of the surface. We also require a constitutive relationship between the bending moments, $\mathscr{M}^*_\theta$ and $\mathscr{M}^*_\varphi$, and the principal curvatures, κ^*_θ and κ^*_φ. Following Evans & Skalak (1980), we assume that bending moments are isotropic and proportional to the mean curvature of the surface:

$$\mathscr{M}^*_\varphi = \mathscr{M}^*_\theta = D^*\left(\kappa^*_\varphi + \kappa^*_\theta\right), \tag{B.22}$$

where $D^* = E^*h^{*3}/12(1-\nu^2)$ is the bending stiffness of the sheet. We have now determined 13 equations for the 13 unknowns $\mathscr{M}^*_\theta$, $\mathscr{M}^*_\varphi$, F^*_θ, F^*_φ, F^*_n, F^*, κ^*_θ, κ^*_φ, r^*, θ, z^* and $\tilde{s}$; noting that $\tilde{r}$ is a prescribed function of $\tilde{s}$. Algebraic manipulations of these equations reduce the system to:

$$\frac{\mathrm{d}r^*}{\mathrm{d}s^*} = \cos\theta, \tag{B.23a}$$

$$\frac{\mathrm{d}z^*}{\mathrm{d}s^*} = \sin\theta, \tag{B.23b}$$

$$\frac{\mathrm{d}\theta}{\mathrm{d}s^*} = \kappa^*_\theta, \tag{B.23c}$$

$$\frac{\mathrm{d}\kappa^*_\theta}{\mathrm{d}s^*} = \frac{1}{r^{*2}}\sin\theta\cos\theta - \frac{F^*_n}{D^*} - \frac{\kappa^*_\theta}{r^*}\cos\theta, \tag{B.23d}$$

$$\frac{\mathrm{d}F^*_n}{\mathrm{d}s^*} = -\kappa^*_\theta\left(F^* + \frac{H^*}{\lambda}\right) - \frac{1}{r^*}\left(F^* + H^*\lambda\right)\sin\theta - \frac{1}{r^*}F_n\cos\theta, \tag{B.23e}$$

$$\frac{\mathrm{d}F^*}{\mathrm{d}s^*} = -H^*\frac{\mathrm{d}}{\mathrm{d}s^*}\left(\frac{1}{\lambda}\right) + \frac{H^*}{r^*}\left(\lambda - \frac{1}{\lambda}\right)\cos\theta + \kappa_\theta F_n, \tag{B.23f}$$

with λ prescribed according to

$$\lambda = \frac{r^*}{\tilde{s}^*}, \tag{B.24}$$

derived as a consequence of (B.20), having noted that the reference configuration satisfies $\tilde{r}^* = \tilde{s}^*$. It is convenient to re-express (B.23), treating $\tilde{s}^*$ as the independent variable,

to yield:

$$\frac{\mathrm{d}r^*}{\mathrm{d}\tilde{s}^*} = \cos\theta/\lambda, \tag{B.25a}$$

$$\frac{\mathrm{d}z^*}{\mathrm{d}\tilde{s}^*} = \sin\theta/\lambda, \tag{B.25b}$$

$$\frac{\mathrm{d}\theta}{\mathrm{d}\tilde{s}^*} = \kappa_\theta^*/\lambda, \tag{B.25c}$$

$$\frac{\mathrm{d}\kappa_\theta^*}{\mathrm{d}\tilde{s}^*} = \frac{1}{\lambda r^{*2}}\sin\theta\cos\theta - \frac{F_n^*}{\lambda D^*} - \frac{\kappa_\theta^*}{\lambda r^*}\cos\theta, \tag{B.25d}$$

$$\frac{\mathrm{d}F_n^*}{\mathrm{d}\tilde{s}^*} = \frac{1}{\lambda}\left[-\kappa_\theta^*\left(F^* + \frac{H^*}{\lambda}\right) - \frac{1}{r^*}\left(F^* + H^*\lambda\right)\sin\theta - \frac{1}{r^*}F_n^*\cos\theta\right], \tag{B.25e}$$

$$\frac{\mathrm{d}F^*}{\mathrm{d}\tilde{s}^*} = -H^*\frac{\mathrm{d}}{\mathrm{d}\tilde{s}^*}\left(\frac{1}{\lambda}\right) + \frac{H^*}{r^*}\left(1 - \frac{1}{\lambda^2}\right)\cos\theta + \frac{1}{\lambda}\kappa_\theta^* F_n^*. \tag{B.25f}$$

Subject to the differing form of λ given in (B.24) (owing to the change in reference configuration), (B.25) recovers equivalent equations given by both Pamplona & Calladine (1993) and Preston *et al.* (2008).

B.1.1 Boundary conditions

Following Preston *et al.* (2008), we derive the appropriate boundary conditions, to which (B.24–B.25) are solved, as follows. Since (B.25) is singular at the centre of the disc, where $\tilde{s}^* = r^* = 0$, we impose boundary conditions at a point $\tilde{s}^* = \delta^*$ for some $\delta^* \ll 1$. To ensure that solutions are smooth at $\tilde{s}^* = 0$, we must have that $\theta \to 0$ as $\tilde{s}^* \to 0$. Hence, for small $\tilde{s}^*$, $r^* = \tilde{s}^*$ and $\lambda = 1$ to leading order. We expand the remainder of the dependent variables in powers of $\tilde{s}^*$, denoting

$$z^* = z_0^* + \tilde{s}^* z_1^* + \tilde{s}^{*2} z_2^* + \ldots, \tag{B.26}$$

for constants z_i^* ($i = 0, 1, 2, \ldots$). Similar expansions are adopted for θ, κ_θ^*, F^* and F_n^*. Expanding (B.25c) yields

$$\theta_1 = \kappa_0^* + O(\tilde{s}^*), \tag{B.27}$$

and hence $\theta = \kappa_0^*\tilde{s}^*$ to leading order. Similar expansions of (B.25e-f) give $F_{n0}^* = 0$ and

$$F_n^* \sim -\kappa_0^*\left(F_0^* + H^*\right)\tilde{s}^*. \tag{B.28}$$

Noting the forms of the dependent variables in the limit $\tilde{s}^* \ll 1$, we suppress singular solutions by imposing the following approximate boundary conditions:

$$r^* = \delta^*, \qquad \theta = \kappa_\theta^*\delta^*, \qquad F_n^* = -\kappa_\theta^*\left(F^* + H^*\right)\delta^* \qquad \text{on } \tilde{s}^* = \delta^*, \tag{B.29}$$

which are equivalent to those of Preston *et al.* (2008). To close our sixth order system, we thus require three further boundary conditions. We impose that the rim of the disc is

held fixed at $r^* = R_0^*$, for some prescribed R_0^*. Upon the rim, the sheet is held clamped. We, thus, impose:

$$\theta = 0, \qquad r^* = R_0^*, \qquad z^* = 0 \qquad \text{on } \tilde{s}^* = R^*. \tag{B.30}$$

We regard growth as a mechanism by which the layer adopts a sequence of equilibrium configurations corresponding to discs of increasing radius. We, thus, examine buckled states as R^* is increased above R_0^*.

B.1.2 Nondimensionalisation

We nondimensionalise the system by scaling all lengths against the boundary radius, R_0^*, and all stress resultants against D^*/R_0^{*2}. Under these scalings, (B.25) becomes

$$\frac{\mathrm{d}r}{\mathrm{d}\tilde{s}} = \frac{1}{\lambda}\cos\theta, \tag{B.31a}$$

$$\frac{\mathrm{d}z}{\mathrm{d}\tilde{s}} = \frac{1}{\lambda}\sin\theta, \tag{B.31b}$$

$$\frac{\mathrm{d}\theta}{\mathrm{d}\tilde{s}} = \frac{\kappa_\theta}{\lambda}, \tag{B.31c}$$

$$\frac{\mathrm{d}\kappa_\theta}{\mathrm{d}\tilde{s}} = \frac{1}{\lambda r^2}\sin\theta\cos\theta - \frac{F_n}{\lambda} - \frac{\kappa_\theta}{\lambda r}\cos\theta, \tag{B.31d}$$

$$\frac{\mathrm{d}F_n}{\mathrm{d}\tilde{s}} = \frac{1}{\lambda}\left[-\kappa_\theta\left(F + \alpha\frac{1}{\lambda}\right) - \frac{1}{r}\left(F + \alpha\lambda\right)\sin\theta - \frac{F_n}{r}\cos\theta\right], \tag{B.31e}$$

$$\frac{\mathrm{d}F}{\mathrm{d}\tilde{s}} = -\alpha\frac{\mathrm{d}}{\mathrm{d}\tilde{s}}\left(\frac{1}{\lambda}\right) + \alpha\frac{1}{r}\left(1 - \frac{1}{\lambda^2}\right)\cos\theta + \frac{\kappa_\theta F_n}{\lambda}, \tag{B.31f}$$

where $\lambda = r/\tilde{s}$ and the dimensionless parameter $\alpha = H^* R_0^{*2}/D^*$ is a measure of the sheet's resistance to in-plane shearing relative to its resistance to bending. We solve (B.31) subject to the nondimensionalised boundary conditions, given by

$$r = \delta, \qquad \theta = \kappa_\theta\delta, \qquad F_n = -\kappa_\theta\left(F + \alpha\right)\delta^* \qquad \text{on } \tilde{s} = \delta, \tag{B.32a}$$

$$r = 1, \qquad \theta = 0, \qquad z = 0 \qquad \text{on } \tilde{s} = R, \tag{B.32b}$$

where $\delta = \delta^*/R_0^*$ and $R = R^*/R_0^*$. Growth of the layer corresponds to a progressive increase in R from $R = 1$.

APPENDIX C

Summary of the Spectral Methods Deployed in Chapter 6

We determine solutions to (6.12–6.13) numerically, utilising the spectral methods described by Trefethen (2000). We briefly introduce these methods below.

Consider, by way of example, a second order ODE of the form

$$\frac{\mathrm{d}^2 u}{\mathrm{d}x^2} = \lambda u, \qquad u(\pm 1) = 0, \tag{C.1}$$

for eigenvalue λ. Following Trefethen (2000), we seek solutions to (C.1) by discretising the system onto meshpoints denoted $x_0, x_1, \ldots, x_N$ (where x_0 and x_N are the boundaries of our domain). Trefethen states that for systems whose solutions are not necessarily periodic, we can construct a spectral method based upon polynomials with maximal accuracy obtained by choosing meshpoints which "lie in a minimal-energy configuration associated with inverse linear repulsion between points", rather than in a regular distribution. We, thus, define our mesh according to

$$x_j = \cos\left(j\pi/N\right), \qquad j = 0, 1, \ldots, N. \tag{C.2}$$

Let us denote $u(x_j)$ by u_j. Our numerical scheme will be as follows:

- Let $p(x)$ be the unique polynomial of degree at most N with $p(x_j) = u_j$ for all $0 \leq j \leq N$.
- We approximate the derivative of u at x_j, denoted u'_j, by $p'(x_j)$.

It then follows that the process of taking one derivative equates to the following matrix multiplication:

$$\mathbf{u}' = \mathbf{D}_N \mathbf{u}, \tag{C.3}$$

where $\mathbf{D}_N$ is an $(N+1) \times (N+1)$ matrix with elements given by the following rules:

$$(D_N)_{00} = \frac{2N^2+1}{6}, \qquad (D_N)_{NN} - \frac{2N^2+1}{6}, \tag{C.4a}$$

$$(D_N)_{jj} = -\frac{x_j}{2\left(1-x_j^2\right)}, \quad j = 1, \ldots, N-1, \tag{C.4b}$$

$$(D_N)_{ij} = \frac{c_i}{c_j}\frac{(-1)^{i+j}}{(x_i - x_j)}, \quad i \neq j, \quad i, j = 0, \ldots, N, \tag{C.4c}$$

where

$$c_i = \begin{cases} 2 & i = 0 \text{ or } N, \\ 1 & \text{otherwise.} \end{cases} \tag{C.5}$$

Given the Dirichlet boundary conditions of (C.1), we have $u_0 = u_N = 0$ and the first and last columns of $\mathbf{D}_N$ take no effect when computing (C.3). Similarly, since we have no interest in u_0' or u_N' we can ignore these entries. The linear algebra can, therefore, be simplified by stripping $\mathbf{D}_N$ of its first and last rows and columns, and working only with $u_1, \ldots, u_{N-1}$. We denote this reduced matrix by $\widetilde{\mathbf{D}}_N$.

We can represent the second derivative in (C.1) by repeated multiplication by $\widetilde{\mathbf{D}}_N$, reducing the problem to

$$\widetilde{\mathbf{D}}_N^2 \mathbf{u} = \lambda \mathbf{u}. \tag{C.6}$$

We determine the values of λ for which non-trivial solutions exist by simply deploying an in-built MATLAB routine to calculate the eigenvalues of $\widetilde{\mathbf{D}}_N^2$.

Now consider the two-dimensional analogue of (C.1), given by

$$\nabla^2 u = \lambda u, \qquad u = 0 \qquad \text{on } x = \pm 1 \text{ and } y = \pm 1. \tag{C.7}$$

We now denote by u_{ij} the solution to (C.7) evaluated at $x = x_i$, $y = y_j$, for $0 \leq i, j \leq N$. Our two-dimensional mesh will be defined according to the natural extension of (C.2):

$$x_i = \cos\left(i\pi/N\right), \qquad i = 0, 1, \ldots, N, \tag{C.8a}$$

$$y_j = \cos\left(j\pi/N\right), \qquad j = 0, 1, \ldots, N. \tag{C.8b}$$

Once more, we can ignore all boundary points and work solely with $1 \leq i, j \leq N-1$. For ease of computation we place all of our two-dimensional mesh points into a vector $\mathbf{v}$ of length $(N-1)^2$, arranging elements according to

$$u_{ij} \mapsto v_{(i-1)(N-1)+j}. \tag{C.9}$$

All that remains in solving (C.7) is to construct the appropriate $(N-1)^2 \times (N-1)^2$ differentiation matrix. We utilise *Kronecker products* for this. Consider a $p \times q$ matrix

A and an $r \times s$ matrix **B**. The Kronecker product of **A** and **B**, denoted $\mathbf{A} \otimes \mathbf{B}$, is a $pr \times qs$ matrix with block form, the ij-block being given by $a_{ij}\mathbf{B}$. Taking the Kronecker products of $\widetilde{\mathbf{D}}_N$ with the identity, **I**, we can quickly construct matrices representing second derivatives with respect to each independent variable. To differentiate $u(x, y)$ twice with respect to x, we simply pre-multiply **v** by $\mathbf{I} \otimes \widetilde{\mathbf{D}}_N^2$. Similarly, to take two y-derivatives, we pre-multiply by $\widetilde{\mathbf{D}}_N^2 \otimes \mathbf{I}$. We can then define a Laplacian operator, **L**, according to

$$\mathbf{L} = \mathbf{I} \otimes \widetilde{\mathbf{D}}_N^2 + \widetilde{\mathbf{D}}_N^2 \otimes \mathbf{I}, \tag{C.10}$$

allowing (C.7) to be written as

$$\mathbf{L}\mathbf{v} = \lambda \mathbf{v}. \tag{C.11}$$

Once more, identifying solutions can be achieved by determining the eigenvalues of **L**.

Finally, we consider the eigenvalue problem defined by the following fourth order ODE:

$$\frac{\mathrm{d}^4 u}{\mathrm{d}x^4} = \lambda u, \qquad u(\pm 1) = u'(\pm 1) = 0. \tag{C.12}$$

Since the Neumann boundary conditions in (C.12) are not incorporated in our standard differentiation matrix above, we cannot evaluate derivatives using $\mathbf{D}_N$ directly. However, if we choose a $p(x)$ of the form

$$p(x) = \left(1 - x^2\right) q(x), \tag{C.13}$$

where $q(\pm 1) = 0$, then the Neumann boundary conditions are satisfied automatically. We evaluate derivatives of u by differentiation of (C.13), *i.e.*

$$u_j' = \left(1 - x_j^2\right) q'(x_j) - 2x_j q(x_j), \tag{C.14a}$$

$$u_j'' = \left(1 - x_j^2\right) q''(x_j) - 4x_j q'(x_j) - 2q(x_j), \tag{C.14b}$$

$$u_j''' = \left(1 - x_j^2\right) q'''(x_j) - 6x_j q''(x_j) - 6q'(x_j), \tag{C.14c}$$

$$u_j'''' = \left(1 - x_j^2\right) q''''(x_j) - 8x_j q'''(x_j) - 12q''(x_j). \tag{C.14d}$$

Since $q(x)$ is constructed to satisfy $q(\pm 1) = 0$ only, we can compute the derivatives of $q(x)$ in (C.14) via multiplication by $\mathbf{D}_N$ as above. Our numerical strategy now becomes

- Let $q(x)$ by the unique polynomial of degree at most N with $q(\pm 1) = 0$ and $q(x_j) = u_j/(1 - x_j^2)$.
- Approximate derivatives of u using the formulae of (C.14).

It follows that the appropriate fourth order differentiation matrix (satisfying the boundary conditions of (C.12)) is

$$\widehat{\mathbf{D}}_N^{(4)} = \left[\mathrm{diag}\left(1 - x_j^2\right) \widetilde{\mathbf{D}}_N^4 - 8\mathrm{diag}\left(x_j\right) \widetilde{\mathbf{D}}_N^3 - 12\widetilde{\mathbf{D}}_N^2\right] \times \mathrm{diag}\left(\frac{1}{1 - x_j^2}\right), \tag{C.15}$$

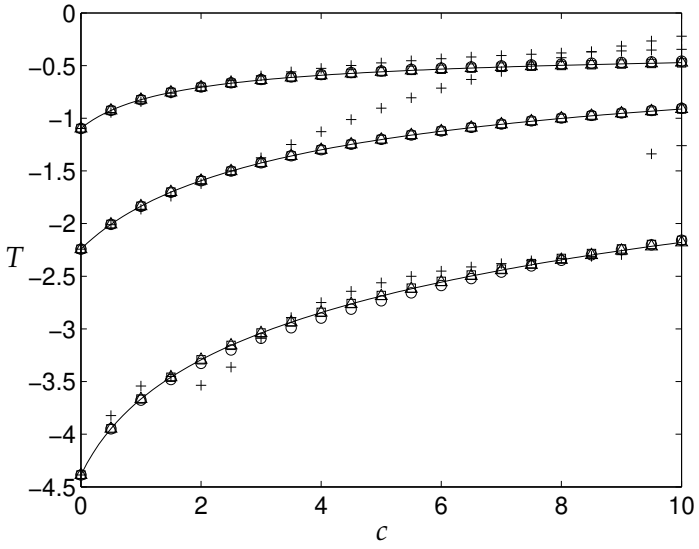

Figure C.1: The first three neutral curves of the one-dimensional reduced model of (6.3–6.7), obtained with the spectral code described in appendix C, for $a = 0$, $m = 4$ and $p = -100$. Solutions obtained via spectral methods are plotted for $N = 20$ (crosses), $N = 30$ (triangles), $N = 40$ (squares) and $N = 50$ (circles). Solid lines represent the results of section 6.1, as illustrated in figure 6.2a. For $N = 50$ the maximal error between the two methods is $O(10^{-5})$.

where diag (x_j) represents a diagonal matrix whose j^{th} element is x_j. The equivalent operators for lower derivatives follow immediately from (C.14) and are omitted for brevity.

We can extend this idea to two spatial dimensions via the natural extension of (C.10). Thus, we may define a spectral biharmonic operator by

$$B = \left(\mathbf{I} \otimes \widehat{\mathbf{D}}_N^{(4)}\right) + \left(\widehat{\mathbf{D}}_N^{(4)} \otimes \mathbf{I}\right) + 2\left(\mathbf{I} \otimes \widehat{\mathbf{D}}_N^{(2)}\right) \times \left(\widehat{\mathbf{D}}_N^{(2)} \otimes \mathbf{I}\right) \tag{C.16}$$

We deploy the methods of (C.14–C.16) to solve (6.12–6.13) numerically. In the case of homogeneity we validate our numerical code by comparison of results with those published by Leriche & Labrosse (2004). We confirm agreement with their results in section 6.3.1. In the case of an inhomogeneous substrate, we validate the spectral code by solving (6.3–6.7) as a test case and comparing results with those of figure 6.2(a). Figure C.1 compares the results of these two numerical methods, with $a = 0$, $m = 4$ and $p = -100$. For $N = 20$ agreement between the two codes appears relatively poor, with a maximal error of $O(10^{-1})$ over the range plotted. However, as N is increased the results of the codes converge rapidly with the magnitude of errors reducing to $O(10^{-3})$ for $N = 30$ and $O(10^{-5})$ for $N = 50$. In the simulations chapter of 6, we fix $N = 50$.

References

D. Ambrosi and F. Mollica. On the mechanics of a growing tumour. *Int. J. Eng. Sci.*, 40: 1297–1316, 2002.

G.B. Arfken and H.J. Webber. *Mathematical Methods for Physicists, 6th Ed.* Elsevier, 2005.

S. Artavanis-Tsakonas, M.D. Rand and R.J. Lake. Notch signaling: cell fate control and signal integration in development. *Science*, 284:770–776, 1999.

A. Atala, S.B. Bauer, S. Soker, J.J. Yoo and A.B. Retik. Tissue-engineered autologous bladders for patients needing cystoplasty. *The Lancet*, 367:1241–1246, 2006.

R.J. Atkin and N. Fox. *An introduction to the theory of elasticity*. Longman, New York, 1980.

B. Audoly and A. Boudaoud. Buckling of a stiff film bound to a compliant substrate – part I: Formulation, linear stability of cylindrical patterns, secondary bifurcations. *J. Mech. Phys. Solids*, 56:2401–2421, 2008.

A. Avery, C. Paraskeva, P. Hall, K.C. Flanders, M. Sporn and M. Moorghen. TGF-β expression in the human colon: differential immunostaining along crypt epithelium. *Br. J. Cancer*, 68:137–139, 1993.

S.P. Bach, A.G. Renehan and C.S. Potten. Stem cells: the intestinal cell as a paradigm. *Carcinogenesis*, 21:469–476, 2000.

N. Barker and H. Clevers. Tracking down the stem cells of the intestine: strategies to identify adult stem cells. *Gastroenterology*, 133:1755–1760, 2007.

N. Barker and H. Clevers. Leucine-rich repeat-containing G-protein–coupled receptors as markers of adult stem cells. *Gastroenterology*, 138:1681–1696, 2010.

N. Barker, M. van de Wetering and H. Clevers. The intestinal stem cell. *Genes & Dev.*, 22:1856–1864, 2008.

J.J.A. Barry, M.M.C.G. Silva, K.A. Shakesheff, S.M. Howdle and M.R. Alexander. Using plasma deposits to promote cell population of the porous interior of three-dimensional poly(d,l-lactic acid) tissue engineering scaffolds. *Adv. Funct. Mater.*, 15: 1134–1140, 2005.

E. Batlle, J.T. Henderson, H. Beghtel, M.M.W. van den Born, E. Sancho, G. Huls, J. Meeldijk, J. Robertson, M. van de Wetering, T. Pawson and H. Clevers. β-catenin and TCF mediate cell positioning in the intestinal epithelium by controlling the expression of EphB/EphrinB. *Cell*, 111:251–263, 2002.

L.E. Batts, D.B. Polk, R.N. Dubois and H. Kulessa. BMP signaling is required for intestinal growth and morphogenesis. *Developmental Dynamics*, 235:1563–1570, 2006.

R.D. Beauchamp, H.M. Sheng, J.Y. Shao, E.A. Thompson and T.C. Ko. Intestinal cell cycle regulation. interactions of cyclin d1, cdk4 and $p21^{cip1}$. *Annals of Surgery*, 223(5): 620–627, 1996.

M.R. Begley and T.J. Mackin. Spherical indentation of freestanding circular thin films in the membrane regime. *J. Mech. Phys. Solids*, 52:2005–2023, 2004.

M. Ben Amar and E. Brener. Theory of pattern selection in three-dimensional nonaxisymmetric dendritic growth. *Phys. Rev. Lett.*, 71(4):589–592, 1993.

M. Ben Amar and A. Goriely. Growth and instability in elastic tissues. *J. Mech. Phys. Solids*, 53:2284–2319, 2005.

P. Bianco and P.G. Robey. Stem cells in tissue engineering. *Nature*, 414:118–121, 2001.

M. Bjerknes and H. Cheng. Clonal analysis of mouse intestinal epithelial progenitors. *Gastroenterology*, 116:7–14, 1999.

D.R. Bland. *The theory of Linear Viscoelasticity*. Pergamon Press, 1960.

C. Booth, G. Brady and C.S. Potten. Crowd control in the crypt. *Nat. Med.*, 8(12):1360–1361, 2002.

A. Boudaoud, P. Patrício, Y. Couder and M. Ben Amar. Dynamics of singularities in a constrained elastic plate. *Nature*, 407:718–720, 2000.

G. Bouma and W. Strober. The immunological and genetic basis of inflammatory bowel disease. *Nature*, 3:521–533, 2003.

M. Brittan and N. A. Wright. Gastrointestinal stem cells. *J. Pathol.*, 197:492–509, 2002.

M. Brittan and N.A. Wright. The gastrointestinal stem cell. *Cell Prolif.*, 37:35–53, 2004.

D.O. Brush and B.O. Almroth. *Buckling of bars, plates and shells*. McGraw-Hill, New York, 1975.

S. Caddemi and I. Caliò. Exact solution of the multi-cracked Euler–Bernoulli column. *Int. J. Solids Struct.*, 45:1332–1351, 2008.

C.R. Calladine. *Theory of shell structures*. Cambridge University Press, 1989.

M.K. Chen and S.F. Badylak. Small bowel tissue engineering using small intestinal submucosa as a scaffold. *J. Surg. Res.*, 99:352–358, 2001.

M.K. Chen and E.A. Beierle. Animal models for intestinal tissue engineering. *Biomaterials*, 25:1675–1681, 2004.

R.S. Choi and J.P. Vacanti. Preliminary studies of tissue-engineered intestine using isolated epithelial orgnoid units on tubular synthetic biodegradable scaffolds. *Transplant. Proc.*, 29:848–851, 1997.

A.M. Collinsworth, S. Zhang, W.E. Kraus and G.A. truskey. Apparent elastic modulus and hysteresis of skeletal mucle cells throughout differentiation. *Am. J. Physiol. Cell Physiol.*, 283:1219–1227, 2002.

C.D. Coman. Localized elastic buckling: non-linearities versus inhomogeneities. *IMA J. Appl. Math.*, 75:461–474, 2010.

J.F. Cornwell. *Group theory in physics (Volume 1)*. Academic Press, 1984.

S.C. Cowin. Tissue growth and remodelling. *Annu. Rev. Biomed. Eng.*, 6:07.1–07.31, 2004.

S.C. Cowin and D.H. Hegedus. Bone remodeling I: theory of adaptive elasticity. *J. Elast.*, 6:313–326, 1976.

R.W. Cox and M.A. Peacock. The velocity field of growing ear cartlidge. *J. Anat.*, 126: 555–566, 1978.

R.W. Cox and M.A. Peacock. The growth of elastic cartlidge. *J. Anat.*, 128:207–213, 1979.

C. Crosnier, D. Stamataki and J. Lewis. Organizing cell renewal in the intestine: stem cells, signals and combinatorial control. *Nature*, 7:349–359, 2006.

R.M. Day. Epithelial stem cells and tissue engineered intestine. *Curr. Stem Cell Res. Ther.*, 1(1):113–120, 2006.

C. Dehili, P. Lee, K.M. Shakesheff and M.R. Alexander. Comparison of primary rat hepatocyte attachment to collagen and plasma-polymerised allylamine on glass. *Plasma Process. Polym.*, 3(6-7):474–484, 2006.

H. Demiray. A note on the elasticity of soft biological tissues. *J. Biomech.*, 5(3):309–311, 1972.

J. Dervaux and M. Ben Amar. Morphogenesis of growing soft tissues. *Phys. Rev. Lett.*, 101:068101 (4pp), 2008.

J. Dervaux and M. Ben Amar. Localized growth of layered tissues. *IMA J. Appl. Math.*, 75:571–580, 2010.

J. Dervaux, P. Ciarletta and M. Ben Amar. Morphogenesis of thin hyperelastic plates: a constitutive theory of biological growth in the Föppl–von Kármán limit. *J. Mech. Phys. Solids*, 57:458–471, 2009.

H. Diken. Vibration control of a rotating Euler–Bernoulli Beam. *J. Sound Vib.*, 232(3): 541–551, 2000.

D.E. Discher, P. Janmey and Wang Y-L. Tissue cells feel and respond to the stiffness of their substrate. *Science*, 310:1139–1143, 2005.

S. Doll and K. Schweizerhof. On the development of volumetric strain energy functions. *J. Appl. Mech.*, 67:17–21, 2000.

D. Drasdo. Buckling instabilities of one-layered growing tissues. *Phys. Rev. Lett.*, 84: 4244–4247, 2000.

D. Drasdo and G. Forgacs. Modeling the interplay of generic and genetic mechanisms in cleavage, blastulation and gastrulation. *Dev. Dynam.*, 219:182–191, 2000.

D. Drasdo and M. Loeffler. Individual-based models to growth and folding in one-layered tissues: intestinal crypts and early development. *Nonlinear Analysis*, 47:245–256, 2001.

O. Du Roure, A. Saez, A. Buguin, R.H. Austin, P. Chavrier, P. Siberzan and B. Ladoux. Force mapping in epithelial cell migration. *PNAS*, 102(7):2390–2395, 2005.

J. Dumais. Can mechanics control pattern formation in plants? *Curr. Opin. Plant Biol.*, 10:58–62, 2007.

C.M. Edwards and S.J. Chapman. Biomechanical modelling of colorectal crypt budding & fission. *Bull. Math. Biol.*, 69:1927–1942, 2007.

A. Engler, L. Bacakova, C. Newman, A. Hategan, M. Griffin and D. Discher. Substrate compliance versus ligand density in cell on gel responses. *Biophys. J.*, 86:617–628, 2004.

A.J. Engler, S. Sem, H.L. Sweeney and D.E. Discher. Matrix elasticity directs stem cell lineage specification. *Cell*, 126:677–689, 2006.

E.A. Evans and R. Skalak. *Mechanics and thermodynamics of biomembranes*. CRC Press. Boca Raton, Florida, 1980.

G.S. Evans, N. Flint, A.S. Somers, B. Eyden and C.S. Potten. The development of a method for the preparation of rat intestinal epithelial cell primary cultures. *J. Cell Science*, 101:219–231, 1992.

A.W. Feinberg, A. Feigel, S.S. Shevkoplyas, S. Sheehy, G.M. Whitesides and K.K. Parker. Muscular thin films for building actuators and powering devices. *Science*, 317:1366–1370, 2007.

S.C. Ferreira, M.L. Martins and M.J. Vilela. Reaction-diffusion model for the growth of avascular tumor. *Phys. Rev. E.*, 65(2):021907 (8pp), 2002.

J.E. Flaherty and J.B. Keller. Contact problems involving a buckled elastica. *SIAM J. Appl. Math.*, 24(2):215–225, 1973.

J.A. Fozard, H.M. Byrne, O.E. Jensen and J.R. King. Continuum approximation of individual-based models for epithelial monolayers. *Math. Med. Biol.*, 27(1):39–74, 2010.

Y.C.B. Fung. Elasticity of soft tissues in simple elongation. *Am. J. Physiol.*, 213(6):1532–1544, 1967.

J. Galle, M. Loeffler and D. Drasdo. Modeling the effect of deregulated proliferation and apoptosis on the growth dynamics of epithelial cell populations in vitro. *Biophys. J.*, 88:62–75, 2005.

R.A. Gatenby and E.T. Gawlinski. A reaction-diffusion model of cancer invasion. *Cancer Res.*, 56(24):5745–5753, 1996.

M.D. Gordon and R. Nusse. Wnt signaling: multiple pathways, multiple receptors and multiple transcription factors. *J. Biol. Chem.*, 281:22429–22433, 2006.

A. Goriely, M. Destrade and M. Ben Amar. Instabilities in elastomers and in soft tissues. *Q. J. Mech. Appl. Math.*, 59(4):615–630, 2006.

A. Goriely, M. Robertson-Tessi, M. Tabor and R. Vandiver. Elastic growth models. *Appl. Optimizat.*, 102:1–44, 2008.

P.B. Green, C.S. Steele and S.C. Rennich. Phyllotactic patterns: a biophysical mechanism for their origin. *Annals of Botany*, 77:515–527, 1996.

L.G. Griffith and G. Naughton. Tissue engineering – current challenges and expanding opportunities. *Science*, 295:1009–1014, 2002.

T.C. Grikscheit, J.B. Ogilvie, E.R. Ochoa, E. Alsberg, D. Mooney and J.P. Vacanti. Tissue-engineered colon exhibits function in vivo. *Surgery*, 132(2):200–204, 2002.

W-H. Guo, M.T. Frey, N.A. Burnham and Y-L. Wang. Substrate rigidity regulates the formation. *Biophys. J.*, 90:2213–2220, 2006.

A. Gutowska, B. Jeong and M. Jasionowski. Injectable gels for tissue engineering. *The anatomical record*, 263:342–349, 2001.

X.C. He, J. Zhang, W.G. Tong, O. Tawfik, J. Ross, D.H. Scoville, Q. Tian, X. Zeng, X. He, L.M. Wiedemann, Y. Mishina and L. Li. BMP signaling inhibits intestinal stem cell self-renewal through suppression of Wnt-β-catenin signaling. *Nat. Genet.*, 36(10): 1117–1121, 2004.

G.A. Holzapfel, T.C. Gasser and R.W. Ogden. A new constitutive framework for arterial wall mechanics and a comparitive study of material models. *J. Elast.*, 61:1–48, 2000.

P. Howell, G. Kozyreff and J. Ockendon. *Applied solid mechanics*. Cambridge University Press, 2009.

R.B. Hoyle. *Pattern formation: an introduction to methods*. Cambridge University Press, 2006.

F-H. Hsu. The influences of mechanical loads on the form of a growing elastic body. *J. Biomech.*, 1:303–311, 1968.

C. Hu, Y. Ding, J. Chen, D. Liu, Y. Zhang, M. Ding and G. Wang. Basic fibroblast growth factor stimulates epithelial cell growth and epithelial wound healing in canine corneas. *Vet. Ophthalmol.*, 12(3):170–175, 2009.

R. Huang and Z. Suo. Wrinkling of a compressed elastic film on a viscous layer. *J. Appl. Phys.*, 91(3):1135–1142, 2002.

J.D. Humphrey. Continuum biomechanics of soft biological tissues. *Proc. R. Soc. Lond. A*, 459:3–46, 2003.

J.D. Humphrey and K.R. Rajagopal. A constrained mixture model for growth and remodeling of soft tissues. *Math. Mod. Meth. Appl. Sci.*, 12:407–430, 2002.

G.W. Jones and S.J. Chapman. Modelling apical constriction in epithelia using elastic shell theory. *Biomech. Mod. Mechanobiol.*, 9:247–261, 2009.

S.M. Karam. Lineage commitment and maturation of epithelial cells in the gut. *Front. Biosci.*, 4:286–298, 1999.

P. Kaur and C.S. Potten. Circadian variation in migration velocity in small intestinal epithelium. *Cell Tissue Kinet.*, 19(6):591–599, 1986.

J. Kierzenka and L.F. Shampine. A BVP solver based on residual control and the matlab PSE. *ACM Trans. Math. Software*, 27:299–316, 2001.

R. Langer and J.P. Vacanti. Tissue engineering. *Science*, 260:920–926, 1993.

R. Lanza, R. Langer and J. Vacanti. *Principles of tissue engineering*. Elsevier, 2007.

E. Leriche and G. Labrosse. Stokes eigenmodes in square domain and the stream function–vorticity correlation. *J. Comp. Phys.*, 200:489–511, 2004.

J. Lidmar, L. Mirny and D.R. Nelson. Virus shapes and buckling transitions in spherical shells. *Phys. Rev. E*, 68(5):051910, 2003.

C-M. Lo, H-B. Wang, M. Dembo and Y-L. Wang. Cell movement is guided by the rigidity of the substrate. *Biophys. J.*, 79:144–152, 2000.

M. Loeffler, C.S. Potten, U. Paulus, J. Glatzer and S. Chwalinski. Intestinal crypt proliferation. II. computer modelling of mitotic index data provides further evidence for lateral and vertical cell migration in the absence of mitotic activity. *Cell Tissue Kinet.*, 19:247–258, 1988.

M. Loeffler, R. Stein, H.E. Wichmann, C.S. Potten, P. Kaur and S. Chwalinski. Intestinal crypt proliferation. I. a comprehensive model of steady-state proliferation in the crypt. *Cell Tissue Kinet.*, 19:627–245, 1986.

P. Macchiarini, P. Jungebluth, T. Go, M.A. Asnaghi, L.E. Rees, T.A. Cogan, A. Dodson, J. Martorell, S. Bellini, P.P. Parnigotto, S.C. Dickinson, A.P. Hollander, S. Mantero, M.T. Conconi and M.A. Birchall. Clinical transplantation of a tissue-engineered airway. *The Lancet*, 372(9655):2023–2030, 2008.

E.H. Mansfield. Bending, buckling and curling of a heated thin plate. *Proc. Roy. Soc. London. A, Mathematical and Physical Sciences*, 268:316–327, 1962.

E. Marshman, C. Booth and C.S. Potten. The intestinal epithelial stem cell. *BioEssays*, 24(1):91–98, 2002.

F.A. Meineke, C.S. Potten and M. Loeffler. Cell migration and organization in the intestinal crypt using a lattice-free model. *Cell Prolif.*, 34:253–266, 2001.

T. Mora and A. Boudaoud. Buckling of swelling gels. *Eur. Phys. J. E*, 20:119–124, 2006.

D. Morel, R. Marcelpoil and G. Brugal. A proliferation control network model: the simulation of two-dimensional epithelial homeostasis. *Acta Biotheoretica*, 49:219–234, 2001.

O. Morgul. Dynamic boundary control of a Euler–Bernoulli beam. *IEEE Trans. Automat. Contr.*, 37(5):639–642, 1992.

P.J. Morin, B. Vogelstein and K.W. Kinzler. Apoptosis and APC in colorectal tumorigenesis. *Proc. Natl. Acad. Sci. USA*, 93:7950–7954, 1996.

G.M. Odell, G. Oster, P. Alberch and B. Burnside. The mechanical basis of morphogenesis. i. epithelial folding and invagination. *Dev. Biol.*, 85(2):446–462, 1981.

J.M. Osborne, A. Walter, S.K. Kershaw, G.R. Mirams, A.G. Fletcher, P. Pathmanathan, D. Gavaghan, O.E. Jensen, P.K. Maini and H.M. Byrne. A hybrid approach to multiscale modelling of cancer. *Phil. Trans. Roy. Soc. A*, to appear, 2010.

D.C. Pamplona and C.R. Calladine. The mechanics of axially symmetric liposomes. *J. Biomech. Eng.*, 115:149–159, 1993.

D.C. Pamplona, J.A. Greenwood and C.R. Calladine. The buckling of spherical liposomes. *Transactions of the ASME*, 127:1062–1069, 2005.

K.H. Parker and C.P. Winlove. The deformation of spherical vesicles with permeable, constant-area membranes: application to the red blood cell. *Biophys. J.*, 77:3096–3107, 1999.

U. Paulus, M. Loeffler, J. Zeidler, G. Owen and C.S. Potten. The differentiation and lineage development of goblet cells in the murine small intestinal crypt: experimental and modelling studies. *J. Cell Sci.*, 106:473–484, 1993.

D. Pinto and H. Clevers. Wnt control of stem cells and differentiation in the intestinal epithelium. *Exp. Cell Res.*, 306:357–363, 2005.

L. Pocivavsek, R. Dellsy, A. Kern, S. Johnson, B. Lin, K.Y.C. Lee and E. Cerda. Stress and fold localization in thin elastic membranes. *Science*, 320:912–916, 2008.

C.S. Potten. Stem cells in gastrointestinal epithelium: numbers, characteristics and death. *Phil. Trans. R. Soc. B.*, 353:821–830, 1998.

D.W. Powell, Mifflin R.C., Valentich J.D., Crowe S.E., J.I. Saada and A.B. West. Myofibroblasts ii: Intestinal subepithelial myofibroblasts. *Am. J. Physiol. Cell Physiol.*, 277: 183–201, 1999.

C. Pozrikidis. Deformed shapes of axisymmetric capsules enclosed by elastic membranes. *J. Eng. Math.*, 45:169–182, 2003.

S.P. Preston, O.E. Jensen and G. Richardson. Buckling of an axisymmetric vesicle under compression: the effects of resistance to shear. *Q. J. Mech. Appl. Math.*, 61(1):1–24, 2008.

A. Quaroni, J. Wands, R.L. Trelstad and K.J. Isselbacher. Epithelioid cell cultures from rat small intestine. *J. Cell Biol.*, 80:248–265, 1979.

A. Rachev, N. Stergiopuos and J-J. Meister. A model for geometric and mechanical adaptation of arteries to sustained hypertension. *J. Biomech. Eng.*, 120:9–17, 1998.

F. Radtke and H. Clevers. Self-renewal and cancer of the gut: two sides of a coin. *Science*, 307:1904–1909, 2005.

M. Ramalho-Santos, D.A. Melton and A.P. McMahon. Hedgehog signals regulate multiple aspects of gastrointestinal development. *Development*, 127:2763–2772, 2000.

S. Reboux, G. Richardson and O.E. Jensen. An asymptotic analysis of the buckling of a highly shear-resistant vesicle. *Eur. J. Appl. Math.*, 20(6):479–518, 2009.

A.G. Renehan, S.T. O'Dwyer, N.J. Haboubi and C.S. Potten. Early cellular events in colorectal carcinogenesis. *Colorectal Dis.*, 4:76–89, 2002.

T. Reya and H. Clevers. Wnt signalling in stem cells and cancer. *Nature*, 434:843–850, 2005.

K.F. Riley, M.P. Hobson and B.J. Bence. *Mathematical methods for physics and engineering*. Cambridge University Press, 1997.

F. G. Rocha and E. E. Whang. Intestinal tissue engineering: from regenerative medicine to model systems. *J. Surg. Res.*, 120:320–325, 2004.

E.K. Rodriguez, A. Hoger and A.D. McCulloch. Stress-dependent finite growth in soft elastic tissues. *J. Biomech.*, 27:455–467, 1994.

M.H. Ross, G.I. Kaye and W. Pawlina. *Histology: A Text & Atlas*. Lippincott, Williams & Wilkins, Philadelphia, 2003.

A. Saez, E. Anon, M. Ghibaudo, O. Du Roure, J-M. Di Meglio, P. Hersen, P. Silberzan, A. Buguin and B. Ladoux. Traction forces exerted by epithelial cell sheets. *J. Phys.: Condens. Matter*, 22:194119 (9pp), 2010.

E. Sancho, E. Batlle and H. Clevers. Signalling pathways in intestinal development and cancer. *Annu. Rev. Cell. Dev. Biol.*, 20:695–723, 2004.

T. Sato, R.G. Vries, H.J. Snippert, M. van de Wetering, N. Barker, D.E. Strange, J.H. van Es, A. Abo, P. Kujala, P.J. Peters and H. Clevers. Single Lgr5 stem cells build crypt–villus structures in vitro without a mesenchymal niche. *Nature*, 459:262–266, 2009.

S-J. Shieh, S. Terada and J.P. Vacanti. Tissue engineering auricular reconstruction: in vitro and in vivo studies. *Biomaterials*, 25:1545–1557, 2004.

R. Skalak. Growth as a finite displacement field. In *Proceedings of the IUTAM Symposium on Finite Elasticity: Held at Lehigh University, Bethlehem, PA, USA, August 10-15*, 1980.

S.C. Smith and J.B. Armstrong. Reaction–diffusion control of heart development: evidence for activation and inhibition in precardiac mesoderm. *Dev. Biol.*, 160:535–542, 1993.

J. Solon, I. Levental, K. Sengupta, P.C. Georges and P.A. Janmey. Fibroblast adaptation and stiffness matching to soft elastic substrates. *Biophys. J.*, 93:4453–4461, 2007.

A.J.M. Spencer. *Continuum Mechanics*. Wiley & Sons, New York, 1980.

C.R. Steele. Shell stability related to pattern formation in plants. *J. Appl. Mech.*, 67: 237–247, 2000.

M.M. Stevens, R.P. Marini, D. Schaefer, J. Aronson, R. Langer and V.P. Shastri. In vivo engineering of organs: the bone bioreactor. *PNAS*, 102(32):11450–11455, 2005.

B.W. Stewart and P. Kleihues. *World Cancer Report*. IARC, 2003.

J.J. Stoker. Mathematical problems connected with the bending and buckling of elastic plates. *Bull. Amer. Math. Soc.*, 48:247–261, 1942.

E. Sultan and A. Boudaoud. The buckling of a swollen thin gel layer bound to a compliant substrate. *J. Appl. Mech.*, 75:051002–1–051002–5, 2008.

M. Swat, A. Kel and H. Herzel. Bifurcation analysis of the regulatory modules of the mammalian G_1/S transition. *Bioinformatics*, 20:1506–1511, 2004.

L.A. Taber. Biomechanics of growth, remodeling and morphogenesis. *Appl. Mech. Rev.*, 48:487–545, 1995.

L.A. Taber. A model for aortic growth based on fluid shear and fiber stresses. *Transactions of the ASME*, 120:348–354, 1998.

G.A. Thibodeau and K.T. Patton. *Anatomy and Physiology, 6th Ed.* Elsevier, 2007.

D. Thieffry and L. Sanchez. Dynamical modelling of pattern formation during embryonic development. *Curr. Opin. Genet. Dev.*, 13(4):326–330, 2003.

D.W. Thompson. *On growth and form*. Cambridge University Press, Cambridge, 1942.

G.J. Tortora and S.R. Grabowski. *Principles of Anatomy and Physiology, 8th Ed.* Harper Collins College Publishers, 1996.

L.N. Trefethen. *Spectral methods in Matlab*. SIAM, 2000.

J.P. Vacanti, M.A. Morse, W.M. Saltzman, A.J. Domb, A. Perez-Atayde and R. Langer. Selective cell transplantation using bioabsorbable artificial polymers as matrices. *Journal of Pediatric Surgery*, 23(1):3–9, 1988.

M. van de Wetering, E. Sancho, C. Verweij, W. de Lau, I. Oving, A. Hurlstone, K. van der Horn, E. Batlle, D. Coudreuse, A.P. Haramis, M. Tjon-Pon-Fong, M. Moerer, P. andvan den Born, G. Soete, S. Pals, M. Eilers, R. Medema and H. Clevers. The β-catenin/TCF-4 complex imposes a crypt progenitor phenotype on colorectal cancer cells. *Cell*, 111:241–250, 2002.

G.R. van den Brink, S.A. Bleuming, J.C.H. Hardwick, B.L. Schepman, G.J. Offerhaus, J.J. Keller, C. Nielsen, W. Gaffield, S.J.H. van Deventer, D.J. Robers and M.P. Peppelenbosch. Indian hedgehog is an antagonist of Wnt signalling in colonic crypt epithelium. *Nat. Genet.*, 36(3):277–282, 2004.

I.M.M. van Leeuwen, H.M. Byrne, O.E. Jensen and J.R. King. Crypt dynamics & colorectal cancer: Advances in mathematical modelling. *Cell Prolif.*, 39:157–181, 2006.

I.M.M. van Leeuwen, C.M. Edwards, M. Ilyas and H.M. Byrne. Towards a multiscale model of colorectal cancer. *World J. Gastroenterol.*, 13(9):1399–1407, 2007.

I.M.M. van Leeuwen, G.R. Mirams, A. Walter, A. Fletcher, P. Murray, J. Osbourne, S. Varma, S.J. Young, J. Cooper, B. Doyle, J. Pitt-Francis, L. Momtahan, P. Pathmanathan, J.P. Whiteley, S.J. Chapman, D.J. Gavaghan, O.E. Jensen, J.R. King, P.K. Maini, S.L. Waters and H.M. Byrne. An integrative computational model for intestinal tissue renewal. *Cell Prolif.*, 42:617–636, 2009.

J.A. Vanderhoof and A.N. Langnas. Short-bowel syndrome in children and adults. *Gastroenterology*, 113:1767–1778, 1997.

M.E. Viney, A.J. Bullock, M.J. Day and S. MacNeil. Co-culture of intestinal epithelial and stromal cells in 3d collagen-based environments. *Regen. Med.*, 4(3):397–406, 2009.

T. von Kármán. Festigkeitsprobleme im maschinenbau. *Encyklopädie der Mathematischen Wissenschaften*, pages 311–385, 1910.

T. von Kármán. The engineer grapples with nonlinear problems. *Bull. Amer. Math. Soc.*, 46(8):615–683, 1940.

A. Walter. *A comparison of continuum and cell-based models of colorectal cancer*. PhD thesis, University of Nottingham, 2009.

R.G. Wells and D.E. Discher. Matrix elasticity, cytoskeletal tension, and TGF-β: the insoluble and soluble meet. *Science Signalling*, 1(10), 2008.

A. Wilson and F. Radtke. Multiple functions of notch signaling in self-renewing organs and cancer. *FEBS Letters*, 580:2860–2868, 2006.

M.H. Wong. Regulation of intestinal stem cells. *J. Investig. Dermatol. Symp. Proc.*, 9: 224–228, 2004.

M.H. Wong, B. Rubinfeld and J.I. Gordon. Effects of forced expression of an NH_2-terminal truncated β-catenin on mouse intestinal epithelial homeostasis. *J. Cell Biol.*, 141(3):765–777, 1998.

M. Zelzer, R. Majani, J.W. Bradley, F.R.A.J. Rose, M.C. Davies and M.R. Alexander. Investigation of cell–surface interactions using chemical gradients formed from plasma polymers. *Biomaterials*, 29:172–184, 2008.